THERMOMECHANICS AND HYDROLOGY OF A DETACHMENT SHEAR ZONE

A DISSERTATION SUBMITTED TO THE FACULTY OF THE GRADUATE SCHOOL OF THE UNIVERSITY OF MINNESOTA BY

Raphaël Gottardi

IN PARTIAL FULFILLMENT OF THE REQUIREMENTS FOR THE DEGREE OF DOCTOR OF PHILOSOPHY

Christian Teyssier, Donna L. Whitney, Advisers

JULY 2012

Acknowledgments

In middle school, one of my teachers said about me *"pourrait briller, mais se contente de luire"* (*"he could shine, but is satisfied by glowing"*). Fortunately for me, I have met during my education numerous people that have encouraged me to go further than I would have on my own, allowing me to shine. By the end of my undergraduate studies in Grenoble, I was still undecided about my future, and Henriette Lapierre encouraged me to broaden my horizons, and she pushed me to find what my true motivation was. Her passion and enthusiasm convinced me to apply for a Master at the University of Lausanne. Though she never saw me graduate, I am grateful for her swift kick in the butt that led me to where I am today.

Once in Lausanne, I had to find a master's research project and an advisor. Christian Teyssier opened his door for me (literally since I shared his office for two years!). After our initial talk, I did not completely understand the project, all I remembered was that it was in the USA, in a remote mountains range, and that was enough to convince me! I do love a good mountain range... Christian gave

me the opportunity to visit the USA for the first time. With Christian and Andreas Mulch, the few days of fieldwork we spent in the Raft River Mountains were an eye opener: I knew I had found my niche.

My scientific awakening was also stimulated by other students in Lausanne, like Christine Authemayou, Gilles Brocard and Thibaud Simon-Labric, who welcomed me and shared their research with me. By the end of my masters I wasn't really thinking about a PhD, even less about applying for one, and Christian encouraged me to apply for graduate schools in the USA. Doubting my chances, I filled the application a couple of days before the deadlines. I did get accepted at the UMN, and here I am, four years later! Upon my arrival in Minneapolis, I met other fellow STAMP members, including Erkan Toraman, Rory McFadden, Seth Kruckenberg and Eric Goergen, whose scientific maturity inspired my work. I would like to thank the STAMP group in Minneapolis, especially William Nachlas and Matthew Carter for sharing thoughts and providing necessary feedback. I owe special thanks to Will for running the electron microprobe for me, Nick Seaton for the EBSD work, Po-Hao Kao for making the modeling possible, and Matt for taking me skiing out West! I would also like to thank Antoine Quilichini for memorable days (and nights) in the field, and for which I am in debt of many stable isotope analyses, that he kindly ran for me. I also have to thank Benita Putlitz and Anne-Lise Jourdan for introducing me to the stable isotope lab in Lausanne and teaching me how to use it.

I thank the members of my written, oral, and final examination, Christian Teyssier, Donna Whitney, Martin Saar, and David Kohlstedt, for reading through my work. I acknowledge my funding sources, including the University of Minnesota Department of Earth Sciences, and the National Science foundation. I thank the staff of the Department of Earth Sciences, Sharon Kressler, Greg Gambeski, and Doug Johnson for keeping me out of trouble more than once!

I have a thought for all my family in France, especially my parents, Marie-Claire and Pierre, and my brother Frédéric, for their encouragement and constant support throughout my work. At last, I would like to thank my future wife, Susan Close, for being so supportive at all times and having a rock collection that even I am jealous of...

To both of my grandfathers,
René Gottardi and Pierre Guillermet,
for instilling in me the love of learning,
and who never got a chance to see my work completed.

Abstract

The Raft River-Grouse Creek-Albion metamorphic core complex (NW Utah) is bound to the east by the Miocene Raft River detachment shear zone that is localized in a ~100 m thick quartzite mylonite. By performing combined structural, microstructural, $^{40}Ar/^{39}Ar$ geochronology, and oxygen and hydrogen stable isotope geochemistry of the well-exposed quartzite mylonite, we are provided with insight on the thermomechanical evolution of the continental crust during extension associated with the exhumation of metamorphic core complex.

Microstructural, electron backscattered diffraction, strain, and vorticity results show an increase in intensity of the rock fabrics from west to east, along the transport direction, compatible with observed finite strain markers (Compton, 1980; Wells, 2001; Sullivan 2008). The results fit in a model of "necking" of the shear zone proposed by Wells (2001) and Sullivan (2008). Microstructural evidences (quartz microstructures and deformation lamellae) suggest that the detachment shear zone evolved at its peak strength, close to the dislocation creep/exponential creep transition, where meteoric fluids played an important role on strain hardening, embrittlement and eventually seismic failure.

Two empirically calibrated paleopiezometers, the quartz recrystallized grain size paleopiezometer of Hirth et al. (2001), and a deformation lamellae spacing based paleopeizometer of Koch and Christie (1981), show very similar results,

indicating that the shear zone in question developed under stress ranging from 40 MPa to 60 MPa. Application of a quartzite dislocation creep flow law (Hirth et al., 2001) reveals that the detachment shear zone quartzite mylonite developed at a strain rate between 10^{-12} and 10^{-14} s^{-1}. We suggest that compressed geothermal gradient (Gottardi et al., 2011), produced by a combination of ductile shearing, heat advection and enhanced cooling by meteoric fluids, can trigger significant mechanical instabilities, and strongly influences the rheology of the detachment shear zone.

Combined geochronological and stable isotope data of quartz/muscovite pairs from the quartzite mylonite reveal that ductile deformation, and infiltration of meteoric fluids in the detachment shear zone, occurred between 26 and 20 Ma. $^{40}Ar/^{39}Ar$ release spectra are complex, but plateau ages decrease systematically from 31.1 $\pm$ 0.8 Ma at the top to 20.2 $\pm$ 0.6 Ma at the bottom of the quartzite mylonite. Throughout the studied area, hydrogen stable isotope values of syn-kinematic muscovite are low, ranging from -123 ‰ to 88 ‰, suggesting that meteoric fluids were infiltrating the detachment shear zone over the time scale of mylonite formation. Hydrogen stable isotope analyses from both muscovite and fluid inclusions show that the fluid infiltrating the detachment shear zone was meteoric in origin, with a low D/H and low $^{18}O/^{16}O$ composition. Quartz and muscovite oxygen isotope analyses show different degree of oxygen isotope depletion, suggesting different time-integrated interaction of the minerals with meteoric fluid; these fluids would be channelized in preferential layers, or shear zones, within the deforming system. The variability in oxygen stable isotope of both quartz and muscovite can be explained by variations in permeability in the basement units (confined versus diffuse flow), and strain variations along the transport direction of detachment shear zone (from flattening to constriction), resulting in different fluid-rock exchange patterns.

Based on our geochemical analyses and other published data, we conduct continuum - scale (i.e., large-scale, partial-bounceback) lattice-Boltzman fluid, heat, and oxygen isotope transport simulations of an idealized cross-section of a metamorphic core complex. The simulations investigate the effects of crustal and fault permeability and buoyancy driven flow on two-way coupled fluid and heat transfer and resultant exchange of oxygen isotopes between fluid and rock. The results show that fluid migration to mid- to lower-crustal levels has to be fault controlled and depends primarily on the permeability contrast between the fault zone and the crustal rock. High fault/crust permeability contrasts lead to channelized flow in the fault and shear zones, while lower contrasts allow leakage of the fluids from the fault into the crust. Channelized fluid flow in the shear zone leads to strong vertical and horizontal thermal gradients, comparable to field observations. The oxygen isotope results show profound oxygen depletion (starting value of $\delta^{18}O$ = +13 ‰ down to 4 ‰) concentrated along the faults and shear zone, similar to field data.

Contents

List of Figures

List of Tables

Chapter 1

INTRODUCTION

The size and shape of continents is constantly changing over time. They rift apart, collide, and coalesce as part of a grand tectonic cycle. Although the architecture of this cycle is known, the deformation of continental rocks themselves is poorly understood. The deformation of the crust is controlled by several parameters (geotherm, fluid flow, strain rate, etc...) and it is difficult to study each of them independently due to the feedback they exert on each other.

This dissertation addresses the fundamental problems of thermomechanical behavior of the continental crust in zones of extension. The research focuses on crustal-scale extension in the context of orogenic collapse, which leads to the development of metamorphic core complexes.

During orogenic collapse, the thickened continental crust is divided into two layers with contrasting thermal and rheological behaviors (Kuznir and Park, 1987). The upper crust thins by brittle faulting, and is separated from the ductile lower crust by a mylonitic detachment zone (Brun et al., 1994; Rey et al., 2001; Teyssier et al., 2005). Localization of extension in the upper crust leads to the formation of metamorphic core complexes that expose sections of upper and lower crust through

detachment zones. Thermochronological and thermomechanical studies conducted on metamorphic core complexes have established that detachment zones record high strain rates; rapid cooling rates (100°C/Ma) and that fluid play an important role in their thermal and mechanical history.

Recent stable isotope studies have shown that, at the time of extension, meteoric water permeates the brittle upper crust down to the detachment zone, where meteoric fluid signatures are preserved in metamorphic minerals (Fricke et al., 1992; Morrison and Anderson, 1994; Holk et al., 1997, 2000; Mulch et al., 2004, 2006; Gébelin et al., 2011; Gottardi et al., 2011). This context depicts the complex interplay among temperature, strain rate, and fluid-rock interaction, because fluid flow is enhanced by brittle faulting (and vice versa) and can be driven by high geotherm.

Regional setting of the Raft River metamorphic core complex

Following a Mesozoic protracted tectonic history of compression, accretion, and crustal thickening that built the North American Cordillera, extensional detachments evolved rapidly during Paleocene-Eocene time along crustal scale low-angle shear zones (Armstrong, 1992; Coney and Harms, 1984; Brown et al., 1986; Price, 1986; Parrish et al., 1988; Carr, 1992; Vanderhaeghe and Teyssier, 1997; Crowley et al., 2001, Bird, 2002). Thermochronological and geochemical studies of core complexes shows two groups (Fig. 1.1): North of the Snake River plain, from British Columbia to Washington State, the Omineca belt comprises the largest region of Cordilleran metamorphic core complexes (Armstrong, 1985; Coney et al., 1987; Brown et al., 1986). In this belt, the $^{40}Ar/^{39}Ar$ ages of fabric-forming, synkinematic white mica concentrate narrowly between 49 and 46 Ma. These metamor-

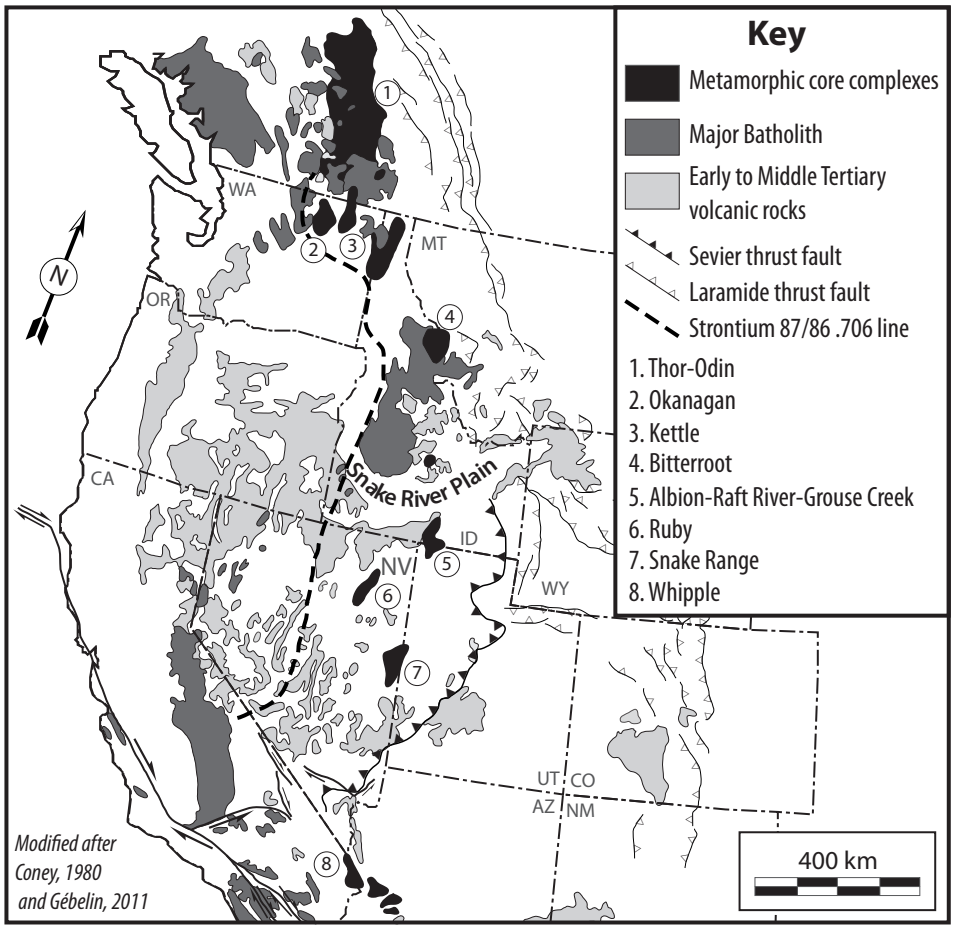

Figure 1.1: **Map of North American metamorphic core complexes.**

phic core complexes are characterized, below the detachment zone, by significant partial melting, granite intrusion, and flow of the lower crust synchronous with extensional activity (Parrish et al., 1988; Vanderhaeghe and Teyssier, 1997; Vanderhaeghe et al., 1999; Vanderhaeghe and Teyssier, 2001; Foster et al., 2001; Foster and Raza, 2002; Teyssier et al., 2005). In contrast, south of the Snake River plain (Fig. 1.1), the southern core complexes of the Raft River-Grouse Creek-Albion Mountains, Ruby-East Humboldt Range, Snake Range, and Whipple Mountain show a more prolonged extension history from Eocene to recent Basin-and-Range extension, with a pulse of mylonite development in Oligo-Miocene time.

The east-rooted, Miocene Raft River shear zone (Malavieille, 1987; Wells et al., 2000; Wells, 2001) is localized in the Proterozoic Elba Quartzite that rests unconformably on an Archean basement complex (Compton, 1972, 1975). Cenozoic $^{40}Ar/^{39}Ar$ white mica ages from the quartzite define a west to east age gradient from 47 to 15 Ma (Wells et al., 2000). This study focuses on the easternmost exposure of the Miocene shear zone (Clear Creek Canyon; Wells, 2001; Sullivan, 2008), where the shear zone is localized in a $\approx$100 m thick quartzite-dominated shear zone (Fig. 1.2).

Organization and Synopsis of Thesis

This thesis is divided into four chapters that aim at constraining the different parameters of deformation. In the first chapter, microstructural and stable isotope (hydrogen and oxygen) data of quartz and muscovite mineral pairs reveal how deformation and fluid flow influence the transient geotherm and the thermomechanics of extensional detachment systems. Hydrogen isotope analysis of muscovite and fluid inclusions in quartz suggests the presence of meteoric fluids throughout the detachment. Oxygen isotope thermometry data of recrystallized quartz-muscovite

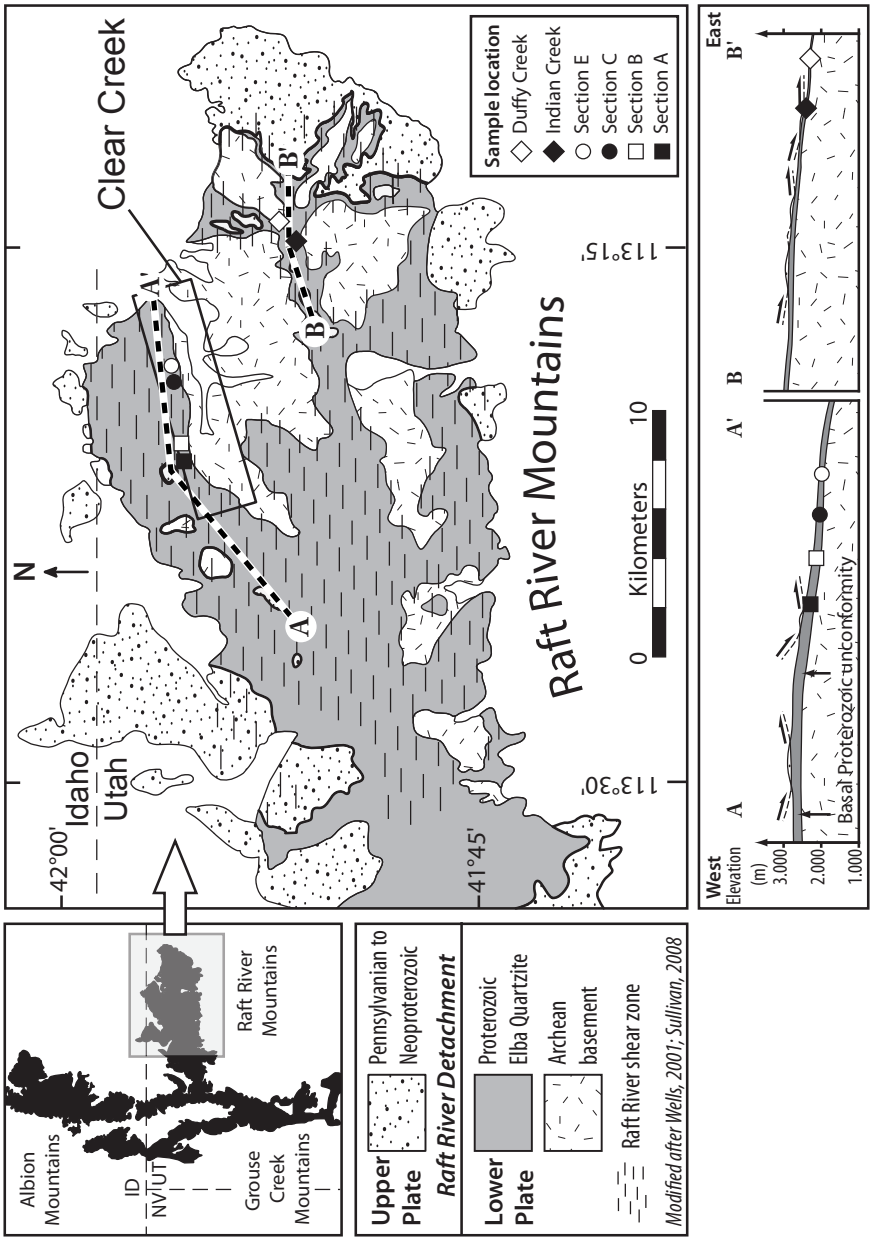

Figure 1.2: **Geological map of the Raft River metamorphic core complex.**

pairs shows a smooth thermal gradient (140°C) across the 100 m thick detachment shear zone. Recrystallized grain-shape fabrics and quartz c-axis fabric patterns reveal a strong coaxial (pure shear) strain component, consistent with considerable thinning of the mylonitic quartzite section. Therefore, we propose that the high thermal gradient preserved in the Raft River detachment is related not only to extensional shearing, as proposed for other detachments, but also to a strong component of coaxial flow that thinned the detachment zone, while the detachment zone was kept cool by presumably convective circulation of meteoric fluids.

In the second chapter, detailed structural and microstructural analysis of the Raft River detachment shear zone provides insight into the thermomechanical evolution of the continental crust during extension associated with the exhumation of metamorphic core complexes. Combined microstructural, electron backscattered diffraction, strain, and vorticity analyses of the very well exposed quartzite mylonite show a strengthening of the rock fabrics from west to east, along the transport direction, and compatible with observed finite strain markers (Compton, 1980; Wells, 2001; Sullivan 2008), that fits in a model of necking of the shear zone as has been proposed by Wells (2001) and Sullivan (2008). Microstructural evidence (quartz microstructures and deformation lamellae) suggest that the detachment shear zone evolved at its peak strength, close to the dislocation creep/exponential creep transition, where meteoric fluids played an important role on strain hardening, embrittlement, and eventually seismic failure. Two empirically calibrated paleopiezometers: the quartz recrystallized grain size paleopiezometer of Hirth et al. (2001) and a deformation lamellae spacing based paleopeizometer of Koch and Christie (1981), show very similar results, indicating that the shear zone developed under stress ranging from 40 MPa to 60 MPa. Using a quartzite dislocation creep flow law (Hirth et al., 2001) we further estimate that the detachment shear zone quartzite mylonite developed at a strain rate between 10^{-12} and 10^{-14} s^{-1}. We

suggest that a compressed geothermal gradient (Gottardi et al., 2011), produced by a combination of ductile shearing, heat advection and enhanced cooling by meteoric fluids, can trigger significant mechanical instabilities and strongly influences the rheology of the detachment shear zone.

In the third chapter, we use geochronological and extensive stable isotope analyses to explore the role of fluid and the permeability and hydrology of the Raft River detachment shear zone. Additional muscovite $^{40}Ar/^{39}Ar$ ages range from 26 to 20 Ma and decrease systematically with depth in the detachment. Combined with hydrogen stable isotope composition, these data suggest that meteoric fluids were infiltrating the detachment shear zone over the time scale of mylonite formation. Based on hydrogen stable isotope analyses from both muscovite and fluid inclusions we show that the fluid infiltrating the detachment shear zone was meteoric in origin, with a low D/H and low $^{18}O/^{16}O$ composition. Quartz and muscovite oxygen isotope analyses show different degree of oxygen isotope depletion, suggesting different time-integrated interaction of the minerals with meteoric fluid; these fluids would be channelized in preferential layers or shear zones within the deforming system. To explain the data, we propose that variation in permeability in the basement units (confined versus diffuse flow) might affect the flow pattern: may be responsible for the different degrees of isotopic depletion. Finally, we suggest that finite strain variations from flattening (planes) to constriction (pipes) along the transport direction might affect fluid pathways resulting in different fluid-rock exchange patterns.

In the fourth and final chapter, we conduct continuum-scale (i.e., large - scale, partial - bounceback) lattice-Boltzman fluid, heat, and oxygen isotope transport simulations of an idealized cross-section of a metamorphic core complex. The simulations investigate the effects of crustal and fault permeability and buoyancy driven flow on two-way coupled fluid and heat transfer and resultant exchange of

oxygen isotopes between fluid and rock. Our results show that fluid migration to mid- to lower-crustal levels has to be fault controlled and depends primarily on the permeability contrast between the fault zone and the crustal rock. High fault/crust permeability contrasts lead to channelized flow in the fault and shear zones while lower contrasts allow leakage of the fluids from the fault into the crust. Buoyancy affects mainly the flow patterns (more upward directed) and to a lesser extent the temperature distribution (disturbance by the geothermal field of about 25°C). Channelized fluid flow in the shear zone leads to strong vertical and horizontal thermal gradients, comparable to field observations. The oxygen isotope results show profound oxygen depletion (starting value of $\delta^{18}O$ = +13 ‰, down to 4 ‰) concentrated along the faults and shear zone, similar to field data.

Chapter 2

PRESERVATION OF AN EXTREME TRANSIENT GEOTHERM IN THE RAFT RIVER DETACHMENT SHEAR ZONE

Raphaël Gottardi[1], Christian Teyssier[2], Andreas Mulch[2,3], Torsten W. Vennemann[4], and Michael L. Wells[5]

[1] *Department of Geology and Geophysics, University of Minnesota, Minneapolis, Minnesota 55455, USA*

[2]*Institut für Geologie, Universität Hannover, 30167 Hannover, Germany*

[3]*Biodiversity and Climate Research Centre (BiK-F), 60325 Frankfurt, Germany. and Institut für Geowissenschaften, Goethe Universität Frankfurt, 60348 Frankfurt, Germany*

[4]*Institut de Minéralogie et Géochimie, Université de Lausanne, 1015 Lausanne, Switzerland*

[5]*Department of Geoscience, University of Nevada Las Vegas, 4505 S. Maryland Parkway, Las Vegas, Nevada 89154, USA*

Published in GEOLOGY, volume 39, p. 759-762.

Extensional detachment systems separate hot footwalls from cool hanging walls, but the degree to which this thermal gradient is the product of ductile/brittle deformation or a preserved original transient geotherm is unclear. Oxygen isotope thermometry using recrystallized quartz-muscovite pairs indicates a smooth thermal gradient (140°C/100 m) across the gently dipping, quartzite-dominated detachment zone that bounds the Raft River core complex in northwest Utah. Hydrogen isotope values of muscovite (δD_{ms} ~100 ‰) and fluid inclusions in quartz (δD_{Fluid} ~85 ‰) indicate the presence of meteoric fluids during detachment dynamics. Recrystallized grain-shape fabrics and quartz c-axis fabric patterns reveal a large component of coaxial strain (pure shear), consistent with thinning of the detachment section. Therefore, the high thermal gradient preserved in the Raft River detachment reflects the transient geotherm that developed owing to shearing, thinning, and the potentially prominent role of convective flow of surface fluids.

2.1 Introduction

Extensional detachment systems are critical interfaces that typically separate the cool, brittle upper crust from high-grade lower and middle crust exhumed in metamorphic core complexes. Detachments are zones of localized deformation, fluid flow, and thermal exchange (Nesbitt and Muehlenbachs, 1989, 1995; Wickham et al., 1993; Morrison, 1994; Morrison and Anderson, 1998; Holk and Taylor, 2000; Mulch et al., 2006; Mulch et al., 2007; Person et al., 2007), but the interplay among these processes is poorly understood. Here, the focus is on the footwall shear zone of the Raft River detachment system in northwest Utah (United States). The shear zone is dominantly in quartzite, such that quartz microfabrics provide a useful record on the kinematics and thermomechanics of this detachment system. Hydrogen isotope ratios of quartz fluid inclusions and of fabric-forming, recrystal-

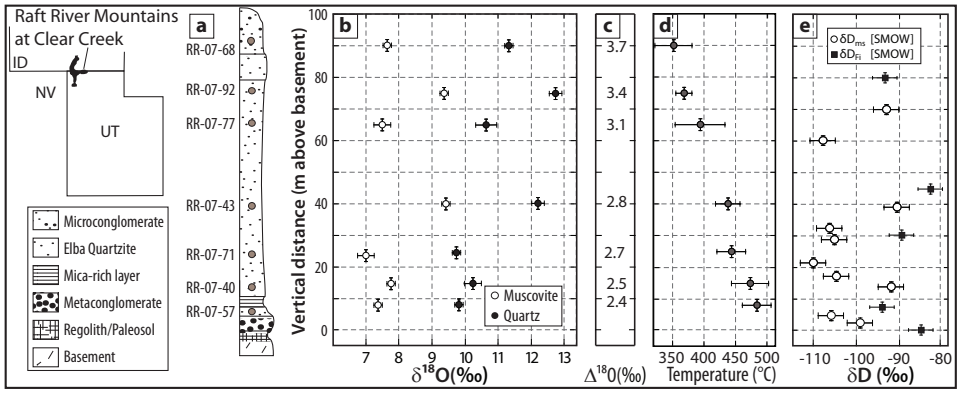

Figure 2.1: **(b) Oxygen isotope compositions of quartz and muscovite and (d) temperatures calculated from quartz/muscovite fractionation (c) with a synthetic vertical profile for scale (a). Hydrogen stable isotope compositions (e).**

lized white mica demonstrate that surface fluids permeated the shear zone during deformation. Oxygen isotope thermometry based on recrystallized quartz-mica pairs uncovers an extremely high gradient of metamorphic temperatures preserved in the 100 m thick shear zone. The influx of cool surface fluids likely produced and preserved the high geotherm that developed during detachment tectonics.

2.2 The Raft River Detachment

The east-rooted, Miocene Raft River shear zone (Malavieille, 1987; Wells et al., 2000; Wells, 2001) is localized in the Proterozoic Elba Quartzite that rests unconformably on an Archean basement complex (Compton, 1972, 1975). Cenozoic $^{40}Ar/^{39}Ar$ white mica ages from the quartzite define a west to east age gradient from 47 to 15 Ma (Wells et al., 2000). This study focuses on the easternmost exposure of the Miocene shear zone (Clear Creek Canyon; Wells, 2001; Sullivan, 2008), where the shear zone is localized in a ~100 m thick quartzite-dominated

shear zone.

The Elba Quartzite includes, from bottom to top, a basal quartzite-cobble metaconglomerate, an alternating sequence of white quartzite and muscovite-quartzite schist, a distinctive layer of red quartzite, and a pebble-metaconglomerate that includes alternating feldspar-rich quartzite, pure quartzite, and quartz-pebble metaconglomerate (Fig. 2.1) (Wells et al., 1998; Sullivan, 2008). Paleozoic metasedimentary rocks are preserved as a few scattered klippen above the quartzite and overlying schist unit and define the hanging wall of the Miocene Raft River detachment (Compton, 1975, Wells, 1997, 2001, 2009; Wells et al., 1998).

2.3 Quartz microfabrics

The well-developed mylonitic foliation and lineation are constant in orientation throughout the quartzite and are defined by flattened and elongated quartz and white mica grains. The strongly deformed quartzite shows two populations of quartz grains, including coarse (> 1000 μm long) elongated grains that define the macroscopic fabric, and finer recrystallized grains (50-100 μm) along the boundaries of coarser grains. Large grains commonly display strong undulose extinction, deformation bands, and even deformation lamellae, indicating that quartz deformed under high flow stress conditions (Hirth and Tullis, 1992). The fine recrystallized grains are commonly equant to slightly elongate and have a direct relation to subgrains present in large grains, suggesting that the dominant process of recrystallization was subgrain rotation (Regime II; Hirth and Tullis, 1992). Recrystallized grains may form an oblique secondary foliation, indicating top-to-east sense of shear, but their long axes are locally subparallel to the foliation planes defined by aligned mica, suggesting some component of coaxial flow (Wells, 2001; Sullivan, 2008).

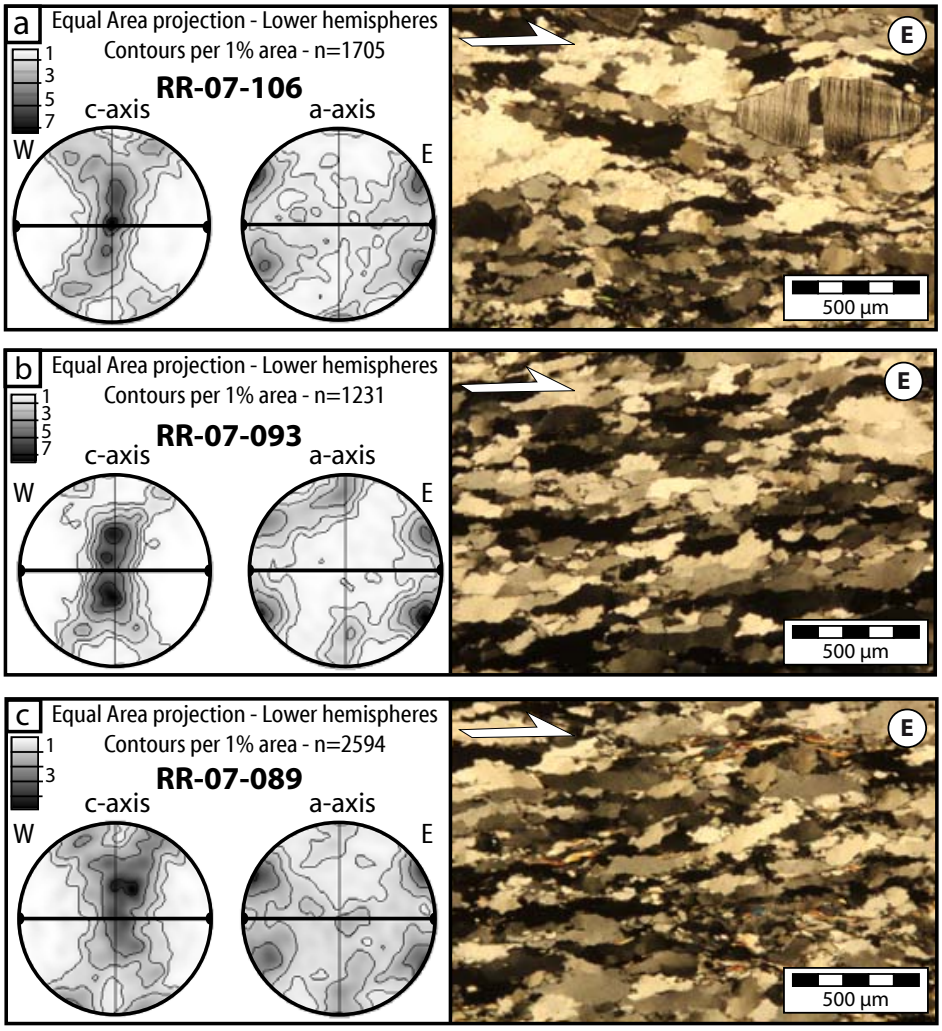

Figure 2.2: **(a-c) Characteristic microstructures of the deformed Elba quartzite, position of samples indicated by squares boxes and gray label in Figure 1. Thin sections cut perpendicular to foliation and parallel to lineation. Top-to-east sense of shear indicated by white arrows. Typical Regime II microstructures of Hirth and Tullis (1992), with formation of subgrains by subgrain rotation recrystallization processes. EBSD Pole figures display symmetrical type-I crossed girdles (Lister, 1977), suggesting strong coaxial strain (Lister and Hobbs, 1980, Schmid and Casey, 1986).**

Electron backscattered diffraction analyses of quartz across the detachment zone reveal strong lattice-preferred orientations developed in the dislocation creep regime (Fig. 2.2). Quartz c-axes define Type-I cross-girdles (Lister, 1977), and a-axis maxima are nearly symmetrical, indicating a strong coaxial component of deformation during fabric development, which was also documented by Compton (1980), Wells (2001) and Sullivan (2008). The opening angles measured on 16 c-axis fabric patterns are 50-60°, indicating deformation temperatures of 400-475 $\pm$ 50°C using the Kruhl (1998) geothermometer, with no clear trend across the sampled section.

2.4 Muscovite microstructures

The mylonitic Elba Quartzite typically contains 5-10 % muscovite. Muscovite grains are 50-200 μm long and a few tens of microns thick. White mica defines the mylonitic foliation in the shear zone, is distributed uniformly on the thin section scale, is in general blocky, and shows little evidence of deformation; mica fish are rare. These observations suggest that mica recrystallized during deformation by dissolution-precipitation creep, which facilitates oxygen and hydrogen isotope exchange between mica and fluid at elevated temperature (e.g., Mulch et al., 2005, 2006).

2.5 Stable isotope analyses

Oxygen ($\delta^{18}O$) and hydrogen (δD) isotopic compositions were measured at the University of Lausanne, Switzerland, and Stanford University, California (Appendix in the GSA Data Repository). Results of oxygen isotope analyses (Fig. 2.1 and Table 2.1) of quartz-muscovite pairs sampled across the shear zone in-

dicate that absolute $\delta^{18}O$ values of quartz and muscovite are variable and range from 9.8 ‰ to 12.7 ‰ for quartz and 7.1 ‰ to 9.4 ‰ for muscovite, without any systematic relationship to position in the vertical profile (Fig. 2.1). However, the temperature-dependent quartz-muscovite oxygen isotope fractionation ($\Delta^{18}O_{Qtz-Musc}$) increases systematically from 2.4 ‰ ~10 m from the basement / quartzite contact, to 3.7 ‰ at the top of the section, irrespective of the absolute $\delta^{18}O$ values of both quartz and muscovite. Using the calibration of Chacko et al. (1996), and assuming isotopic equilibrium between quartz and mica, this increase in the $\Delta^{18}O_{Qtz-Musc}$ values indicates a decrease in temperature from 485°C near the base to 345°C at the top of the ~100 m thick shear zone section (Fig. 2.1).

Hydrogen isotope compositions measured from muscovite (δD_{ms}) (Fig. 2.1 and Table 2.2) display values from 90 ‰ to 120 ‰, with no clear trend in the section. The isotopic value of the fluid present during hydrogen isotope exchange at the temperatures estimated using quartz-muscovite oxygen isotope thermometry, is δD_{Fluid} = -100 ‰ to 70 ‰ (Suzuoki and Epstein, 1976), which is in the range for meteoric fluids (e.g., Taylor, 1977).

Similarly, δD values of quartz fluid inclusions (δD_{FI}) analyzed in five samples over the entire thickness of the shear zone (Fig. 2.1 and Table 2.3) have a narrow range from 94 ‰ to 82 ‰ with no systematic variation in the section. These values are in good agreement with those calculated from δD_{ms} values, and are also consistent with meteoric fluids.

2.6 Discussion

Analyses of finite strain, kinematic vorticity (Wells, 2001; Sullivan, 2008), deformation mechanisms, and thermometry results from a quartzite-dominated section of the Raft River shear zone are integrated to evaluate the role of deformation

and fluids in the thermomechanics of detachment systems. The smooth change in isotopic fractionation between quartz and mica across the section, independent of the absolute $\delta^{18}O$ values of quartz and mica pairs, is likely related to an increase in temperature of equilibration downward through the 100 m thick shear zone. Even though absolute temperature estimates are biased depending on the choice of the calibration used for fractionation, relative temperature trends across the detachment are robust. Despite an analytical error of 20-30°C on temperatures determined from each quartz-mica pair, the high apparent linear metamorphic gradient (140°C/100 m) indicated by our $\delta^{18}O$ measurements is incompatible with a conductive structure and requires a compressed thermal gradient.

The quartzite microstructure is quite constant over the Clear Creek section, in apparent conflict with the temperature gradient revealed by oxygen isotope thermometry. However, in dislocation creep, quartz microstructure is controlled by flow stress, which is dependent on temperature / strain rate relations (Hirth and Tullis, 1992). At Clear Creek, microstructures reflect relatively high flow stress during detachment tectonics, irrespective of temperature, which suggests that temperature and strain rate self-adjusted to maintain near-constant stress. Given the relatively uniform finite strain documented by Sullivan (2008) on this section, the thermal gradient revealed by mineral pair thermometry may indicate that microstructure at the bottom of the section developed at higher strain rate for a shorter time compared to the top of the section. This scenario necessitates migration of the deformation front through the shear zone, with a tendency for strain to localize downward (toward higher temperature), which could be tested, for instance, by dating synkinematic micas.

Three factors can perturb syndeformational geotherms in detachment systems such as the Raft River shear zone (Fig. 2.3). First, the dipping shear zone advects and juxtaposes hot rocks from the footwall and cold rocks from the hanging wall,

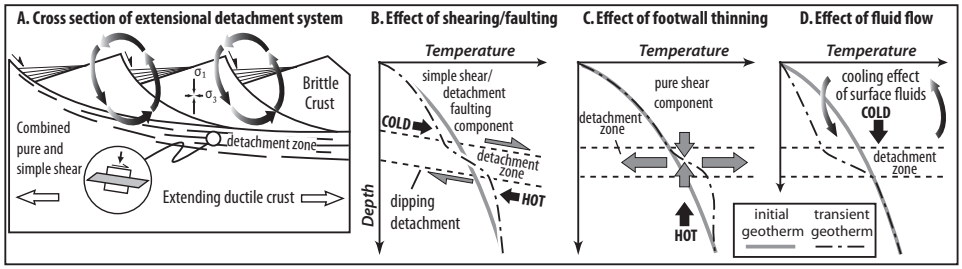

Figure 2.3: **(A) Conceptual diagrams of the transient effects of extensional shearing; (B), (C), and (D), schematic representation of effects of deformation and fluid flow on geotherm.**

such that a steep transient geotherm is established (Fig. 2.3B). For the Raft River shear zone, which probably evolved at shallow dip angles (Wells, 2001), this effect may account for the high metamorphic gradient only if the shear zone accommodated large displacements (Wells et al., 2000). Second, thinning of the footwall shear zone may also lead to heat advection (Fig. 2.3C). Coaxial flow was an important component of deformation in the Raft River shear zone (Compton, 1980; Wells, 2001; Sullivan, 2008), and our quartz crystallographic data support this conclusion (Fig. 2.2). Hence, the isotopic ratios and temperatures determined for the Raft River shear zone are likely to have been preserved during synkinematic thinning. However, given the original thickness of the Elba Quartzite, thinning alone cannot account for the preserved thermal gradient. Finally, the influx of cool surface fluids down to the detachment can maintain a steep transient geotherm over the timescale of shearing/exhumation (Fig. 2.3D).

Hydrogen isotope ratios measured in quartz fluid inclusions and white micas indicate that the fluids present during deformation were of meteoric origin. Fluid inclusion D values are constant throughout the section and are similar to the mean of the values calculated to be in equilibrium with the white mica in the Elba Quartzite at their temperatures of formation. Therefore, it is reasonable to infer that cool

surface fluids reached the detachment shear zone and therefore likely played a role in the thermal evolution of this detachment system. While simple shear and pure shear strain in the detachment shear zone is capable of creating a steep isotherm, we propose that cooling induced by fluid flow is the dominant process by which a transient geotherm develops and remains preserved across detachment shear zones. What is true for the Raft River shear zone is likely the case for other detachment systems in which the presence of meteoric fluids has been recognized (Morrison and Anderson, 1998; Holk and Taylor, 1997, 2000, 2007; Mulch et al., 2004, 2006, 2007).

In extensional detachment systems, fluid circulation in the upper crust is driven by surface topographic gradients and by heat flux from below, which drives fluid flow by buoyancy (Person et al., 2007; Saar, 2011). Crustal extension associated with orogenic collapse is a setting in which high amplitude topography creates a hydraulic head, for example through domino-style tilting of upper crustal blocks (e.g., Basin and Range). This hydraulic forcing develops at the same time as hot crust is brought in contact with cool crust by detachment tectonics. In the upper crust subvertical fracture patterns enhance the transfer of fluids, and normal faults are natural fluid conduits that provide pathways for upward and downward fluid flow (Fig. 2.3A). Studies of mineral isotopic compositions show that surface fluids do not, in general, penetrate the deep footwall of detachment systems (Fricke et al., 1992; Holk and Taylor, 2007) but do penetrate detachment shear zones (Mulch et al., 2004, 2006, 2007). This circulation of surface fluids must participate in cooling the detachment system (Person et al., 2007). Yet, time-integrated water-rock ratios typically diminish downward, which indicates that larger-scale conductive cooling of the detachment footwall is limited to the detachment shear zone (Mulch et al., 2006, 2007). In conclusion, thermal structure, thermal exchange regime, fluid flow, and strain critically control the dynamics and transient geotherm of ex-

tensional detachment systems. The high thermal gradient of ~140 °C/100 m across the Raft River shear zone revealed by isotope thermometry was probably generated by displacement across the detachment system, including coaxial thinning of the footwall shear zone, and more critically by the circulation of surface fluids, which produced a transient geotherm that was likely sustained over the duration of detachment tectonics.

[0]**Acknowledgments:** Gottardi, Vennemann, and Teyssier acknowledge support from the Swiss Science Foundation FNS-117694 and a U.S. National Science Foundation (NSF) grant EAR-0838541; Mulch acknowledges NSF grant EAR 0609649 support through Stanford University, laboratory support through German Science Foundation DFG-INST-187/400-1FUGG, and through the LOEWE funding program (Landes - Offensive zur Entwicklung Wissenschaftlich - ökonomischer Exzellenz) of Hesse's Ministry of Higher Education, Research, and the Arts. Wells acknowledges support from NSF grant EAR 061009. We thank F. Rossetti, W. Sullivan, and an anonymous reviewer, as well as Editor Sandra Wyld, for their helpful comments.

Elevation (m above basement)	Sample	$\delta^{18}O_{qtz}$ (‰)	$\delta^{18}O_{ms}$ (‰)	$\Delta^{18}O_{qtz-ms}$ (‰)	Temperature (°C)
90	RR07-068	11.3 ± 0.2	7.7 ± 0.2	3.7 ± 0.2	345 ± 45
75	RR07-092	12.7 ± 0.2	9.4 ± 0.2	3.4 ± 0.1	370 ± 10
65	RR07-077	10.6 ± 0.2	7.5 ± 0.2	3.1 ± 0.4	395 ± 40
40	RR07-043	12.2 ± 0.2	9.4 ± 0.2	2.8 ± 0.1	440 ± 20
25	RR07-071	9.8 ± 0.2	7.1 ± 0.2	2.7 ± 0.1	445 ± 20
15	RR07-040	10.2 ± 0.2	7.8 ± 0.2	2.5 ± 0.1	475 ± 25
8	RR07-057	9.8 ± 0.2	7.4 ± 0.2	2.4 ± 0.1	485 ± 20
90	RR07-068	11.3 ± 0.2	7.7 ± 0.2	3.7 ± 0.2	345 ± 45
90	RR07-068	11.3 ± 0.2	7.7 ± 0.2	3.7 ± 0.2	345 ± 45

Table 2.1: **Oxygen Isotope data (Clear Creek section, Raft River). Temperatures obtained using the calibration of Chacko et al. (1996), where $\Delta^{18}O_{Qtz-Musc}$ = 1.350 x + 0.042 x^2 - 0.0086 x^3 (x = 10^6 T^{-2}). UTM coordinates of samples: RR07-040 and RR07-043 come from Profile 1 (base at 0306737 - 4647194) RR07-071 and RR07-077come from Profile 3 (base at 0307245 - 4647473) RR07-057 and RR07-068 come from Profile 4 (base at 0307297 - 4647476) RR07-092 comes from Profile 5 (base at 0307720 - 4647533).**

Elevation (m above basement)	Sample	H_2O (μL)	Actual value δ (‰) vs. SMOW
80	RR07-068	0.129	-93
45	RR07-046	0.188	-83
30	RR07-041	0.134	-89
8	RR07-057	0.247	-94
0	RR07-087	0.229	-84

Table 2.2: **Hydrogen Isotope data - Fluid Inclusions (Clear Creek Section, Raft River).**

Elevation (m above basement)	Sample	δD_{ms} (‰)
70	RR09-103	-93
60	RR09-86	-108
38	RR0-158	-91
31	RR09-80	-106
28	RR09-78	-106
21	RR09-98	-110
18	RR09-96	-103
14	RR09-94	-92
6	RR09-74	-106
3	RR09-90	-99

Table 2.3: **Hydrogen isotope data on muscovite (Clear Creek section, Raft River).**

Chapter 3

THERMOMECHANICS OF AN EXTENSIONAL SHEAR ZONE

(RAFT RIVER METAMORPHIC CORE COMPLEX, NW UTAH)

A detailed structural and microstructural analysis of the Miocene Raft River detachment shear zone (NW Utah) provides insight into the thermomechanical evolution of the continental crust during extension associated with the exhumation of metamorphic core complexes. Combined microstructural, electron backscattered diffraction, strain, and vorticity analysis of the very well exposed quartzite mylonite show an increase in intensity of the rock fabrics from west to east, along the transport direction, compatible with observed finite strain markers (Compton, 1980; Wells, 2001; Sullivan 2008). The results are consistent with a model of "necking" of the shear zone, as proposed by Wells (2001) and Sullivan (2008). Microstructural evidence (quartz microstructures and deformation lamellae) suggest that the detachment shear zone evolved at its peak strength, close to the dislocation creep/exponential creep transition, where meteoric fluids played an important role on strain hardening, embrittlement, and eventually seismic failure.

Two empirically calibrated paleopiezometers: the quartz recrystallized grain size paleopiezometer of Hirth et al. (2001) and a deformation lamellae spacing based paleopeizometer of Koch and Christie (1981), show very similar results, indicating that the shear zone developed under stress ranging from 40 MPa to 60 MPa. Using a quartzite dislocation creep flow law (Hirth et al., 2001) we further estimate that the detachment shear zone quartzite mylonite developed at a strain rate between 10^{-12} and 10^{-14} s^{-1}. We suggest that compressed geothermal gradient (Gottardi et al., 2011), produced by a combination of ductile shearing, heat advection and enhanced cooling by meteoric fluids, can trigger significant mechanical instabilities and strongly influences the rheology of the detachment shear zone.

3.1 Introduction

The strength of the lithosphere during continental extension has been debated for decades (e.g., Kusznir and Park, 1987, Afonso and Ranalli, 2004). Numerical models have provided first-order tests of the bulk strength of the lithosphere over the time scale of lithospheric extension and collapse (e.g., Huismans and Beaumont, 2005; Tirel et al., 2004, 2008; Rey et al., 2009, 2011; Huet et al., 2011), and the effects of crustal thickness, mechanical layering, metamorphism, and melting have been evaluated. However, field-based analyses of the thermomechanical properties of extensional structures have lagged behind (Mulch et al., 2006). In this paper, we focus on the quartzite-dominated detachment shear zone that bounds the Miocene Raft River metamorphic core complex (MCC); we use the microstructural, thermal, and fluid-rock record preserved in this shear zone to infer its thermomechanical history.

At the onset of extension that leads to the formation of Cordilleran MCC, orogenic crust is thick and formed of essentially two layers with contrasting thermal

and rheological properties. The deformation of the cold brittle upper crust by normal faulting can be episodic and follows a Coulomb frictional failure criterion (Brace and Kohlstedt, 1980; Sibson, 1983). Rocks in the hot ductile lower crust are deforming ductilely, where deformation is controlled by stress, strain rate, temperature, grain size, fluid activity, and deformation mechanisms of the rheologically significant mineral species (Brace and Kohlstedt, 1980). Extensive studies of MCC show that brittle and ductile deformation is localized in a detachment zone that separates these two layers of contrasting mechanical behaviors.

In the classic model of MCC development (Lister and Davis, 1989), the detachment zone acts as a continental stress guide, where the strength of the continental crust reaches a maximum at the depth of the brittle-ductile transition. This model is supported by the distribution of seismic activity observed in the continental crust (Lister and Reynolds, 1989). The kinematics and rheology of low-angle detachment zones that accommodate most of the extension of the continental lithosphere have been debated (Davis and Lister, 1988; Lister and Davis, 1989; Axen et al., 1990; Planke and Smith, 1991; Axen, 1992; Wernicke, 1992; Manning and Bartley, 1994; Collettini and Barchi, 2002; Healy, 2009), but it appears that motion on the low-angle normal fault is primarily controlled by excess pore fluid pressure (Axen, 1992; Collettini and Barchi, 2002), weakening of the fault rock through reaction softening (Taylor and Huchon, 2002), stress increase (Axen, 1992), or the development of a high transient geotherm across the detachment zone (Gottardi et al., 2011). In some cases, the detachment zone contains rocks that have been subjected to high stress followed by creep during stress relaxation (Lister and Davis, 1989; Axen and Selverstone, 1994; Küster and Stöckhert, 1999; Trepmann and Stöckhert, 2001, 2002, 2003).

While deviatoric stress can be measured via boreholes in the upper crust, plastic flow stress in the lower crust is usually estimated based on experimentally cal-

ibrated flow laws, and by careful comparison with field observations of exposed sections of lower crust. Here, we focus on the Miocene Raft River detachment (Utah), that is localized dominantly in quartzite, and where quartz microfabrics provide useful information about the kinematics and thermomechanics of extensional detachment systems.

Combined quartz crystallographic preferred orientation, detailed microstructural, strain and vorticity analysis show an increase in intensity of the quartzite mylonite fabrics along the transport direction. We apply two different experimental paleopiezometers to evaluate the flow stress under which the rock fabric developed: the recrystallized grain size piezometer of Stipp and Tullis (2003) and the deformation lamellae of Koch and Christie (1981). Both yield stress estimates between 40 and 60 MPa, comparable with previous published data obtained from other extensional settings (Behr et al., 2011; Trepmann and Stöckhert, 2003; Gueydan et al., 2003). Using the geochemical data of Gottardi et al. (2011), reporting the preservation of an extreme geothermal gradient and the presence of meteoric fluids in the Raft River shear zone, we further combine these temperature data with the dislocation creep flow law of Hirth et al. (2001) to calculate the strain rate experienced by the shear zone during its development.

3.2 The Raft River detachment shear zone

The Raft River Mountains form the eastern limb of the Albion-Raft River-Grouse Creek metamorphic core complex in NW Utah (Fig. 3.1) and expose amphibolite- to greenschist-facies Archean to Permian rocks. These rocks experienced alternating crustal thickening and thinning during the Sevier orogeny (Wells, 1997; Wells et al., 1998; Hoisch et al., 2002; Harris et al., 2007), followed by episodes of extension on the west-rooted Eocene to early Oligocene Middle Mountain shear zone

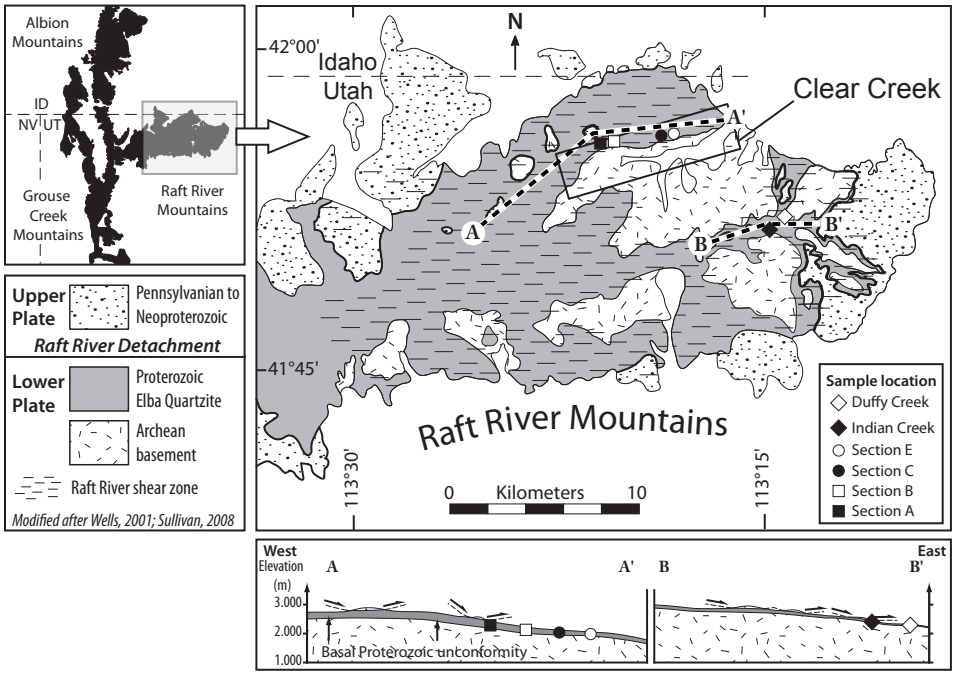

Figure 3.1: **Geological map and cross section of the Raft River Mountains and location of sampled sections, modified after Wells (2001) and Sullivan (2008).**

(Compton, 1983; Saltzer and Hodges, 1988; Wells, 1997; Wells et al. 2000), that was accompanied by a period of magmatism, including intrusion of the 32 Ma Middle Mountain gneiss (Strickland et al, 2011), 30 Ma Almo pluton (Strickland et al, 2011), 29 to 28 Ma Vipont pluton (Strickland et al, 2011), 25 Ma Red Butte pluton (Compton et al., 1977; Egger et al., 2003).

The east-rooted Raft River detachment (Malavieille, 1987) studied here shows muscovite $^{40}Ar/^{39}Ar$ ages as young as 15 Ma (Wells et al., 2000; Wells, 2001). Apatite fission-track ages record progressive east-directed unroofing along the detachment fault between 13.6 and 7.4 Ma (Wells et al., 2000). Here we focus on this Miocene detachment zone exposed at Clear Creek (Fig. 3.2), which has in-

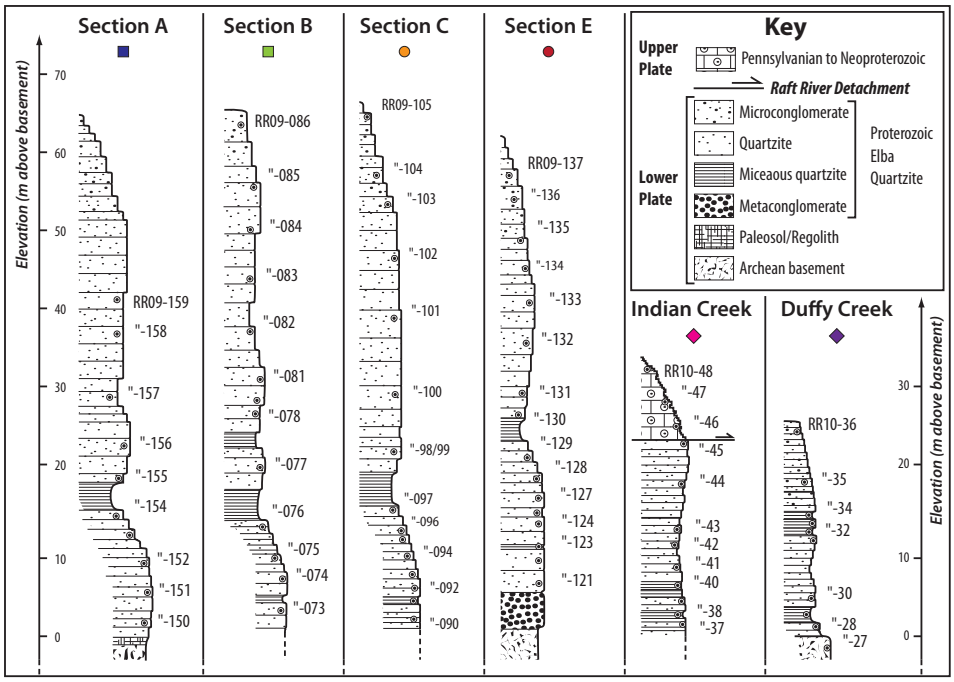

Figure 3.2: **Sections with positions of samples.**

cised a continuous section through the detachment (Compton, 1975; Wells, 2001; Sullivan, 2008).

The Green Creek Complex (Armstrong and Hills, 1967; Armstrong, 1968) is the lowest unit in the detachment zone and consists of ca. 2.55 Ga gneissic monzogranite (metamorphosed adamellite of Compton, 1972) that intrudes metatrondhjemite, metagabbro, and hornblende-biotite schist (Armstrong, 1968; Compton et al., 1977; Todd, 1980; Miller, 1980). These basement units are separated from the overlying Elba Quartzite by a conspicuous schist unit that has been interpreted as a metamorphosed paleosol/regolith (Armstrong, 1968) or a metamorphosed basement-derived arkose (Compton, 1975). The overlying Elba quartzite and schist (Wells et al., 1998; Sullivan, 2008) display a distinct stratigraphy that

includes, from bottom to top, a basal quartzite-cobble metaconglomerate, an alternating sequence of white quartzite and muscovite-quartzite schist, a very distinctive layer of red quartzite, and a sequence of alternating feldspar-rich micaceous quartzite, pure quartzite, and pebble-gravel metaconglomerate, which we refer to as microconglomerate, to contrast with the large-clast metaconglomerate. Paleozoic metasedimentary rocks are preserved as a few scattered klippen above the quartzite and schist and define the hanging wall of the Miocene Raft River detachment (Compton, 1975, Wells, 1997, 2001, 2009; Wells et al., 1998).

3.3 Microstructural analysis

Throughout the detachment shear zone in the Clear Creek area, the quartzite mylonite fabrics are generally similar (Fig. 3.3). The mylonitic foliation and lineation are well developed and constant in orientation throughout the quartzite. Field and thin section observations indicate that flattened and elongate muscovite grains define the foliation. Previous microstructural work on the Raft River detachment shear zone has reported clear evidence of top-to-east sense of shear, including type-II S-C fabrics, asymmetric tails around feldspar porphyroclasts, shear bands, asymmetric quartz c-axis crossed-girdles and single-girdles (Compton, 1980; Sabisky, 1985; Malavieille, 1987a, 1987b; Wells, 1997, 2001, Sullivan, 2008).

3.3.1 Quartz Microstructures

The quartzite is strongly deformed and shows two populations of grains. The first population consists of coarse elongated (>500 μm long) grains that define the macroscopic fabric (Fig. 3.3 a, b). Those grains have strong undulose extinction and exhibit features such as crossed deformation bands (Fig. 3.3f) and deformation lamellae (Fig. 3.11 and see section 3.2. below), indicating that quartz deformed un-

der high flow stress conditions (Hirth and Tullis, 1992). Quartz grains are usually crosscut by deformation bands oriented parallel near the trace of the c-axis.

The second population consists of finer recrystallized grains (25-100 μm) that are along the boundaries of coarser grains (Fig. 3.3b). The fine recrystallized grains are commonly equant to slightly elongate and have a direct relation to subgrains present in large grains, suggesting that the dominant process of recrystallization was subgrain rotation (Fig. 3.5), where recovery is accommodated by dislocation climb (Regime II of Hirth and Tullis, 1992). Recrystallized grains may form a low angle oblique secondary foliation, indicating top-to-east sense of shear, but their long axes are locally subparallel to the foliation planes defined by aligned mica, suggesting some component of coaxial flow (Wells, 2001; Sullivan, 2008). Shear bands at shallow angle to foliation (up to 15°) are locally present (Fig. 3.3g) and display complex grain geometry: the grain size reduces considerably closer to the shear band and the asymmetric shape of the grains clearly indicates the sense of shear.

In the easternmost sampled localities (Indian and Duffy Creek), where the quartzite mylonite is much attenuated, there is a sharper contrast between the two grain populations. The relic grains become very elongated (>2000 μm) with very high aspect ratio, forming single grain ribbons, typically asymmetric, indicating the sense of shear. These large grains are oriented such that their crystallographic basal plane is usually oriented close to the trace of the foliation. The recrystallized grains are more equant than in the western region, and triple junctions are observed at the grain boundaries. A larger area (up to ~50%) of the thin section is occupied by recrystallized grains.

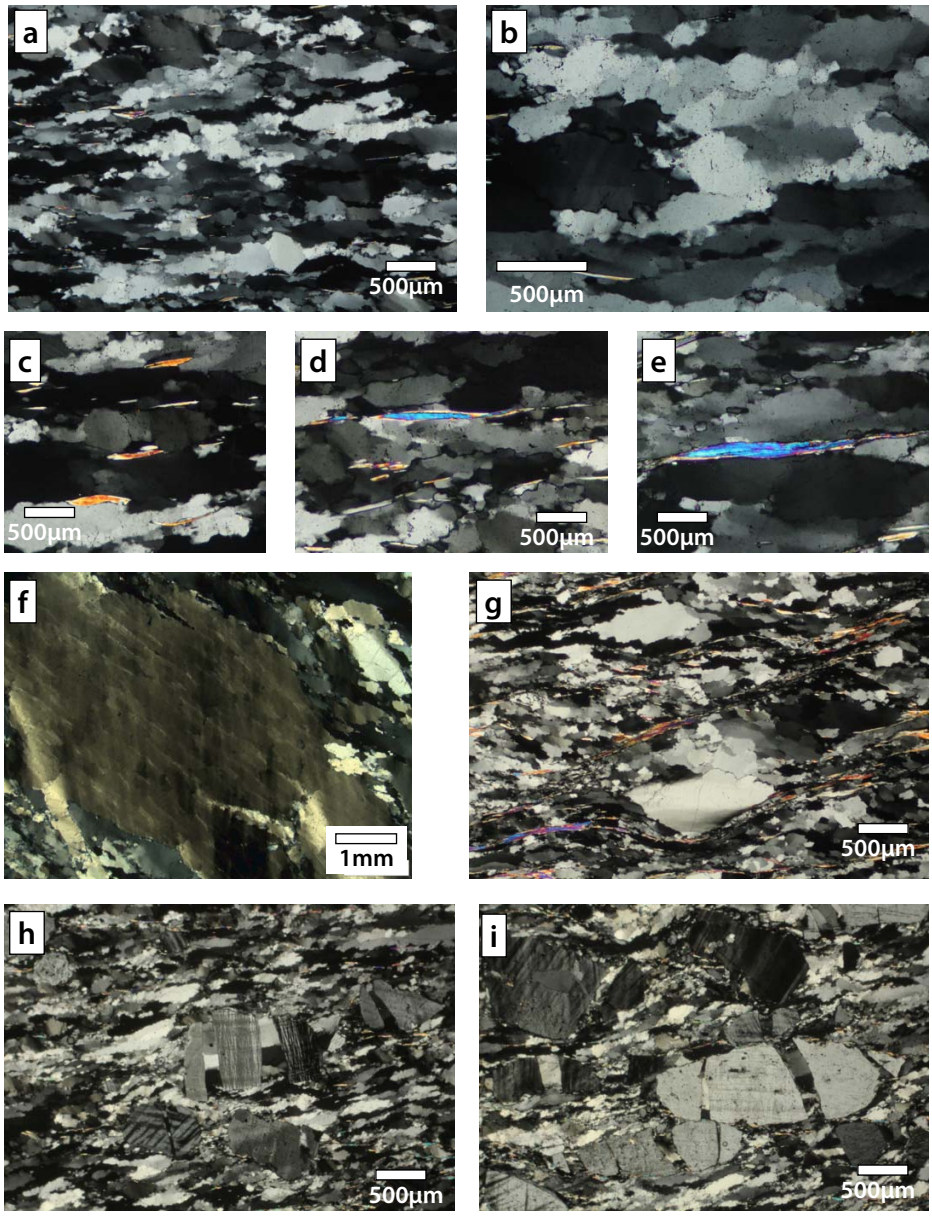

Figure 3.3: **Cross-polarized thin section pictures showing typical quartzite microstructures (a, b), mica microstructures (c, d, e), quartz chessboard structures (f), shear bands (g) and feldspar microstructures (h, i). Thin sections cut perpendicular to foliation and parallel to lineation, the pictures are taken oriented top to the East.**

3.3.2 Deformation lamellae

Characterization

The nature and occurrence of planar deformation features (PDFs) in quartz have been recognized since the pioneering work of Böhm (1883) and numerous others (see reviews by Christie and Raleigh, 1959; Drury, 1993; and references therein). Among all PDFs, deformation lamellae, with high optical relief and distinct preferred orientation, are commonly observed in quartz crystals deformed at low temperature (Fairbairn, 1941; Ingerson and Tuttle, 1945; Carter, 1971; Christie and Ardell, 1974; Drury, 1993). Deformation lamellae are crystallographically orientated, narrow sub-planar structures that occupy a part or the complete area of a grain and generally are only found with one orientation in any grain. In fact, many PDFs can be associated with deformation lamellae. In naturally deformed quartz, extensive TEM work has shown that lamellae consist of dislocations tangles, elongated subgrains (Mc Laren and Hobbs, 1972; White, 1973; Blenkinsop and Drury, 1988; McLaren, 1991; Trepmann and Stöckhert, 2003), subgrain walls (White, 1973), and zones of different concentrations of dislocations and/or fluid inclusions (McLaren and Hobbs, 1972; White 1973; Christie and Ardell, 1974; Blenkinsop and Drury, 1988). Deformation lamellae are particularly common in quartz, where they usually have a sub-basal orientation. Quartz deformation lamellae have been interpreted as planes of high resolved shear stress (Heard and Carter, 1968) and they were also used to determine paleostress directions for small strain deformation directions in a way similar to calcite e-twins (Carter and Friedman, 1965; Carter and Raleigh, 1969; Pavlis and Bruhn, 1988; Law 1990; Twiss and Moores, 1992). Blenkinsop and Drury (1988) have shown an inverse relationship between the dislocation density along subgrain wall forming lamellae and fluid inclusion density.

Deformation lamellae have also been produced experimentally on metals, alloys and ionic materials, in the exponential creep or cold working regime (see Drury, 1993 for review). Deformation lamellae have been produced experimentally on quartz at high temperatures (800 to 1000°C), various strain rates (10^{-7} to 10^{-4} s^{-1}) and particularly at high stress (above 1 GPa). By correlation to other studies on alloys, it has been proposed that a critical stress has to be overcome for their development, although interpretation of quartz rheological data is more complicated and it is not clear if the development of deformation lamellae is related to the transition from power law creep to exponential creep over a critical stress value (see Drury, 1993, for more detailed discussion).

Description

Throughout the detachment shear zone, deformation lamellae affect 20 to 50% of quartz grains in the mylonite. In thin sections cut perpendicular to foliation and parallel to lineation, deformation lamellae are oriented between 30 and 50° with respect to foliation and are nearly perpendicular to basal shear bands (Fig. 4). Lamellae are straight to slightly curved (0 to 10° of orientation change), show up well in cathodoluminescence imaging (Fig. 5), and appear to have formed late relative to quartz deformation-recrystallization as they crosscut subgrain boundaries. They are very well developed in large quartz clasts oriented at a high angle to foliation. Also, quartz grains close to mica grains tend to display well defined sets of deformation lamellae.

Two orientations of lamellae are commonly observed (~30-50° and ~130-150°) with respect to foliation, Fig. 3.4b, c), and locally, two neighbor grains may display different lamellae orientation (Fig. 3.4d, c). Lamellae planes cut trough subgrain boundaries (Fig. 3.4f, g) but not across grain boundaries, suggesting that they

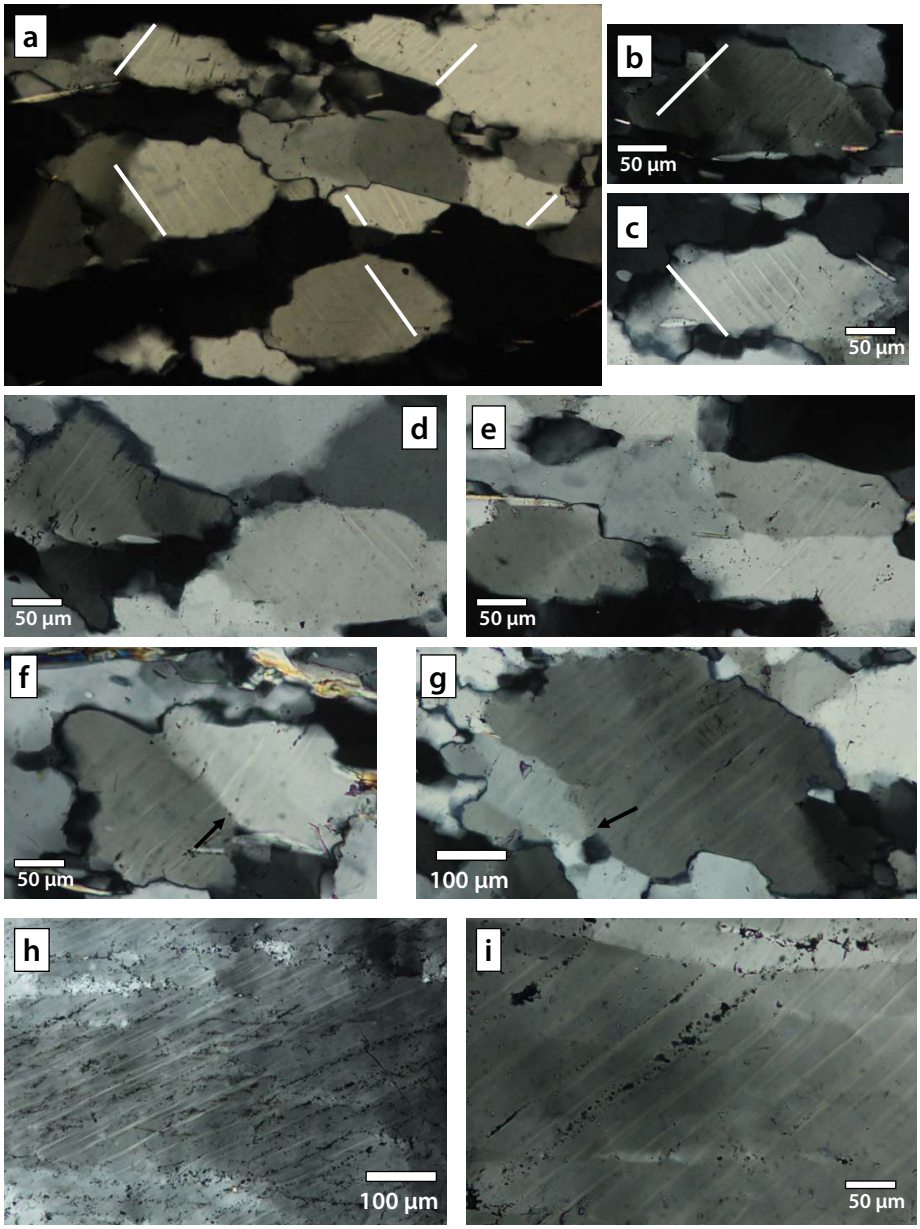

Figure 3.4: **Crossed polarized pictures of deformation lamellae, showing two conjugate orientations (a, b, c, d, e). Deformation lamellae commonly cross subgrain boundaries (f, g, back arrows). Note the deformation band oriented at a high angle (almost 90°) of the deformation lamellae. (h, i) show lamellae decorated with fluid inclusions. Thin sections cut perpendicular to foliation and parallel to lineation, pictures oriented top to the East.**

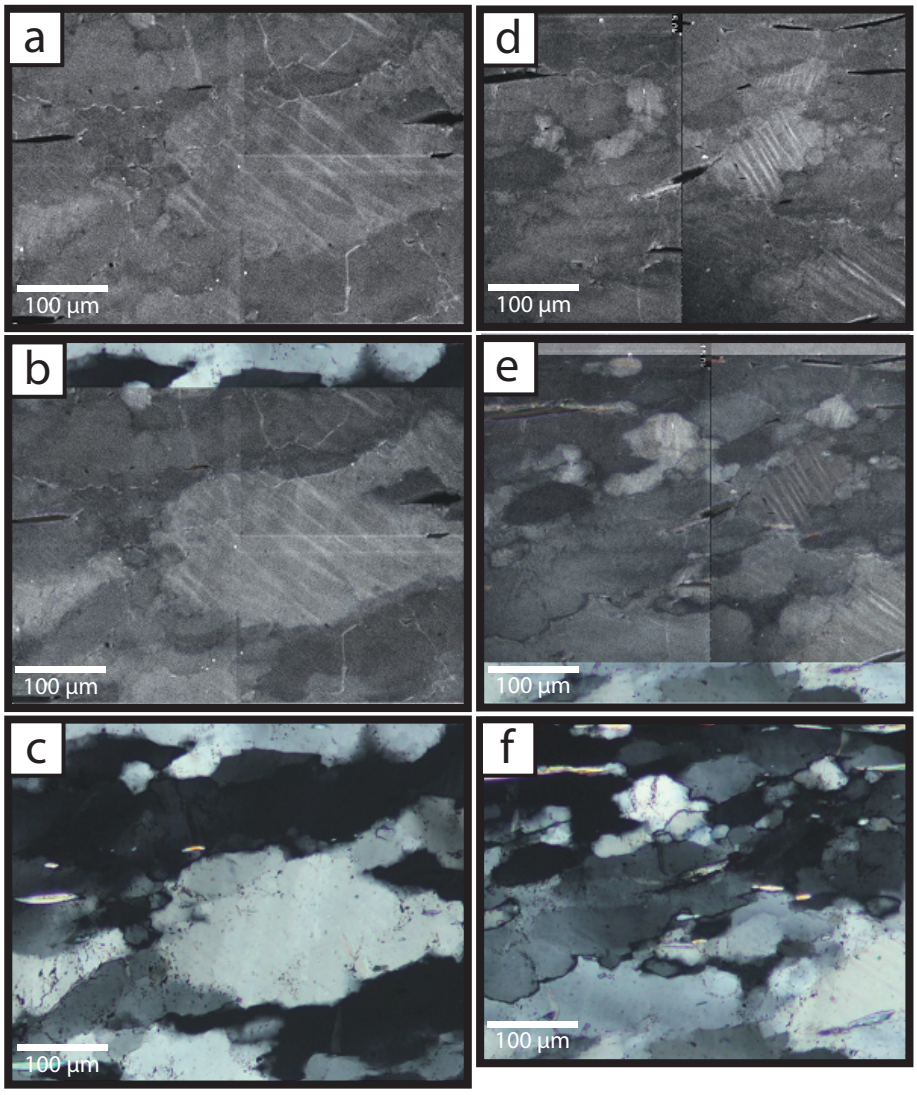

Figure 3.5: **Cathodoluminescence images of deformation lamellae (a and d) and crossed polarized image of the same area (c and f). When the CL image is superimposed to the crossed-polarized image (b and e), the CL contrast correlates very well with the microstructure. All pictures are oriented top-to-the-East.**

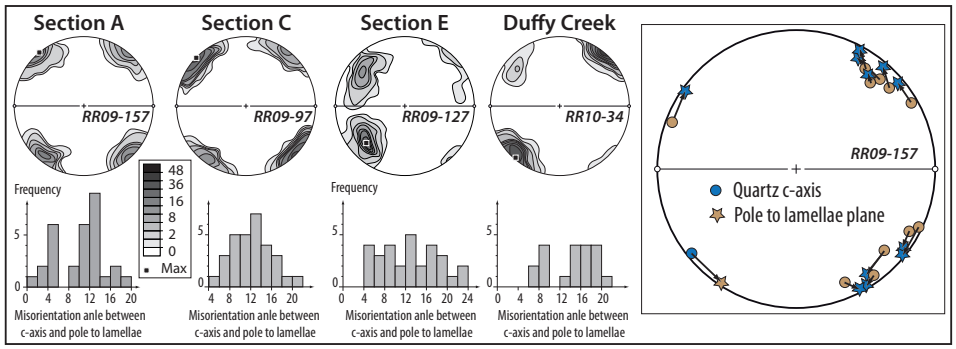

Figure 3.6: **Orientation of lamellae with respect to quartz c-axis. The c-axis and pole to lamellae where measured for individual quartz grain, at least 30 per sample. The misorientation angle between the pole to the lamellae and the c-axis, ranges between 0 and 25°, with a maximum around 12°, showing that the lamellae have a sub-basal orientation.**

formed while recrystallization was proceeding. Deformation lamellae are commonly decorated by fluid inclusions. In some cases the inclusions are sufficiently large (micron size) to be observed under the microscope (Fig. 3.4h, i), and deformation lamellae and fluid inclusion trails have usually a very similar orientation (Fig. 3.4h, i).

Cathodoluminescence imaging

Cathodoluminescence (CL) has been classically used on quartz in a descriptive way to reveal its origin and processes of crystal growth, recrystallization, alteration or diagenesis, and also to image lattice defects. Differences in CL band contrast are related to extrinsic (trace elements) or intrinsic (lattice defects) point defects in minerals, and thereby can be associated to variations in trace elements (substitution of Si in the crystal lattice), crystal lattice defects, and fluid inclusions (see review by Gotze et al., 2001 and references therein).

CL imaging was performed on 4 thin sections in which deformation lamellae are well developed; strong CL contrast was obtained (Fig. 3.5) across grains with deformation lamellae. Fig. 3.5 illustrates this correlation clearly: Fig. 3.5a (and d) are the CL images and Fig. 3.5c (and f) are a cross-polar image of the same area, and Fig. 3.5b (and e) shows the overlap of the CL image over the microstructure image. There is a direct correlation between the microstructure and the CL image. The different grains have different CL and the change is CL follows sharply the grain boundary. The lamellae always appear very bright on the CL image and form sharp and narrow planar domains. Deformation lamellae walls have high dislocation density and also contain fluids or voids, three features that can cause bright CL emission perturbations, although the exact significance of the observed CL contrast is not entirely clear.

Orientation

The orientation of deformation lamellae was measured using the universal stage, and poles to the planes are represented on stereographic projections (Fig. 3.6 and 3.10). 120 grains with lamellae were measured in each sample sample on two sets of thin sections: one set cut perpendicular to foliation and parallel to lineation (set A), another set cut perpendicular to foliation and lineation (set B). While lamellae affect 20 to 50% of the grains in thin sections from set A, they are almost absent in set B. To understand the orientation of the lamellae with respect to their host-grain, we measured their orientation and that of the c-axis of their host grain on one thin section per sample (Fig. 3.6). Therefore, the misorientation between the c-axis and the pole to lamellae planes was evaluated. Results are shown on Fig. 3.6.

The orientation of the lamellae is constrained between 30° and 50° with respect to the foliation. The poles to lamellae planes revolve in a cone around the lineation

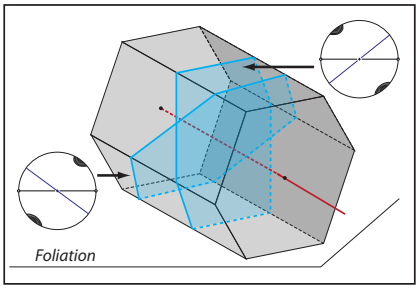

Figure 3.7: **Schematic diagram showing the orientation of deformation lamellae planes.**

direction. The misorientation angle between the c-axis and pole to lamellae of single grains encompasses also a very narrow range of values, between 0 and 25°, with a peak around ~14° (Fig. 3.6). These observations show that the lamellae are likely sub-basal planes with respect to the quartz crystal (Fig. 3.7).

3.3.3 Feldspar microstructures

In the microconglomerate, feldspar represents up to 40% of the grains and their size ranges from tens of microns to millimeter. In thin section, feldspar grains exhibit clear evidence of brittle deformation (Fig. 3.3h, i). Single feldspar grains are broken into angular fragments and display patchy undulose extinction. Cracks between broken feldspars are at high angle to the foliation, usually follow cleavage planes, and are filled with finely recrystallized quartz. This suggests that feldspar deformed during the recrystallization of the quartzite. “Domino” and “bookshelf” structures are commonly observed and are reliable indicators of the sense of shear (Fig. 3.3). The pressure shadows are composed of finely recrystallized grains. The lack of mica at the sides of the clasts suggests that pressure solution and/or retrograde reactions didn’t play a major role in the development of these porphyroclasts.

3.3.4 Muscovite microstructures

The mylonitic Elba Quartzite typically contains 5-10% muscovite. Muscovite grains are 50-200 μm long and a few tens of microns thick and define the mylonitic foliation in the shear zone (Fig. 3.3c, d, e). Distribution of muscovite grains on the thin section scale is quite uniform. The grains have a blocky texture and show little evidence of deformation; they occur as recrystallized grains along quartz grain boundaries. Mica grains locally form fish-shape clasts but are more commonly concentrated in thin layers (10 to ~75 μm thick) that define the foliation, with their long axes parallel to the mylonitic lineation. Large mica grains with high aspect ratios tend to form inverted stair stepping, which correlates to the Group 6 of the morphological grouping of mica fish proposed by ten Grotenhuis et al. (2003). The rare mica grains that do form fish correlate with the Group 2 of ten Grotenhuis et al. (2003). These observations suggest that mica recrystallized during deformation by dissolution-precipitation creep (e.g. Vernon, 2004).

3.4 Recrystallized quartz grain size analysis

3.4.1 Method

The goal of this analysis was to perform a statistical characterization of grainsize in large populations of quartz grains. Grain boundary maps were obtained using a chemical etching technique. Chips of oriented samples were mechanically polished down to 1 μm and chemically etched with ammonium fluoride ($NH_4F{\cdot}HF$, Wegener and Christie, 1983). Ammonium fluoride is a strong etching solution that nicely reveals grain and subgrain boundaries of quartz. After chemical etching, high resolution photographs were taken in reflected light (Fig. 3.8a). Finally, grain boundary maps were drawn using image software, allowing a sub-micron resolu-

tion (Fig. 3.8b). The grain boundary map processing was carried out using *Image SXM* (Barett, 2008). The processing of grain boundary maps yields basic parameters such as grain area, short and long axis of grains, and orientation of the long axis of grains that are necessary parameters to conduct a grain population analysis. The grain diameter was calculated assuming that it is the diameter of a sphere that equals the area of the grain, and geometrically corrected.

From one sample to another, the histogram of grain diameter relative frequency is very consistent: there is a peak in relative frequency around 10-25 μm, and then an abrupt exponential decay for larger sizes (Fig. 3.8c). The microstructural analysis reveals that regime II fabrics have a distinct population of recrystallized grains that reach up to 75 μm in diameter. Based on microstructural observation, a threshold value of 60 μm was chosen: all the grains smaller than 60 μm are considered recrystallized and all the grains above 60 μm are considered non-recrystallized or "relic" grains (Fig 3.8c). Changing this value to a 70 or 80 μm threshold doesn't affect significantly the the average recrystallized grain diameter and would change its value by a 1 to 5%. Also, this threshold value of recrystallized grains for regime II microstructures is in agreement with other studies of grain population analysis (Stipp and Tullis, 2003).

3.4.2 Results

In the Clear Creek area the range of harmonic mean recrystallized grain size values for each sample is relatively restricted, comprised between 20 and 30. μm (with stereological correction, Table 3.1 and Fig. 3.9). The harmonic mean over each section doesn't show any particular geographic variation: 23.0 ± 1.9 μm for Section A, 21.8 ± 1.4 μm for Section B, 28.8 ± 1.8 μm for Section C, 24.3 ± 1.6 μm for Section E, 23.2 ± 1.9 μm for Indian Creek and 23.2 ± 1.5 μm for Duffy Creek

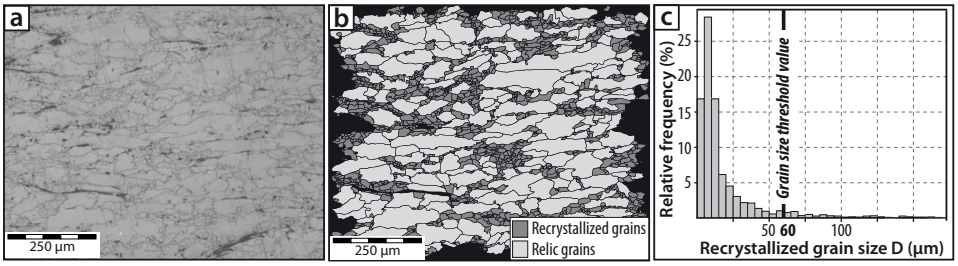

Figure 3.8: **Microstructural analysis procedure: (a) chips of rocks were polished and etched, (b) pictures were taken in reflected light and grain boundary maps were traced using Photoshop ®. (c) shows a typical grain population histogram)**

(Table 3.1 and Fig. 3.9).

The spread in percent of recrystallized area is quite large depending on the sample. The average value for each section shows an increase (above the error from one sample to another), from west to east, along the transport direction, with the following progression: 22 $\pm$ 9% for Section A, 28 $\pm$ 6% for Section B, 34 $\pm$ 8% for Section C, 39 $\pm$ 8% for Section E. The easternmost localities show larger recrystallized area: 50 $\pm$ 11% for Indian Creek and 50 $\pm$ 12% for Duffy Creek (Table 3.1 and Fig. 3.9). Combined recrystallized grain size and recrystallized area show that there is little variation in the grain size along the transport direction, but there is an increase in recrystallized area.

3.5 Quartz crystallographic orientation

The crystallographic preferred orientation (CPO) of quartz was investigated on thin sections cut perpendicular to foliation and parallel to lineation using the Electron Backscattered Diffraction method. The EBSD detector is mounted on a JEOL JSM-6500F SEM that incorporates a HKL Nordlys II EBSD camera; the diffraction

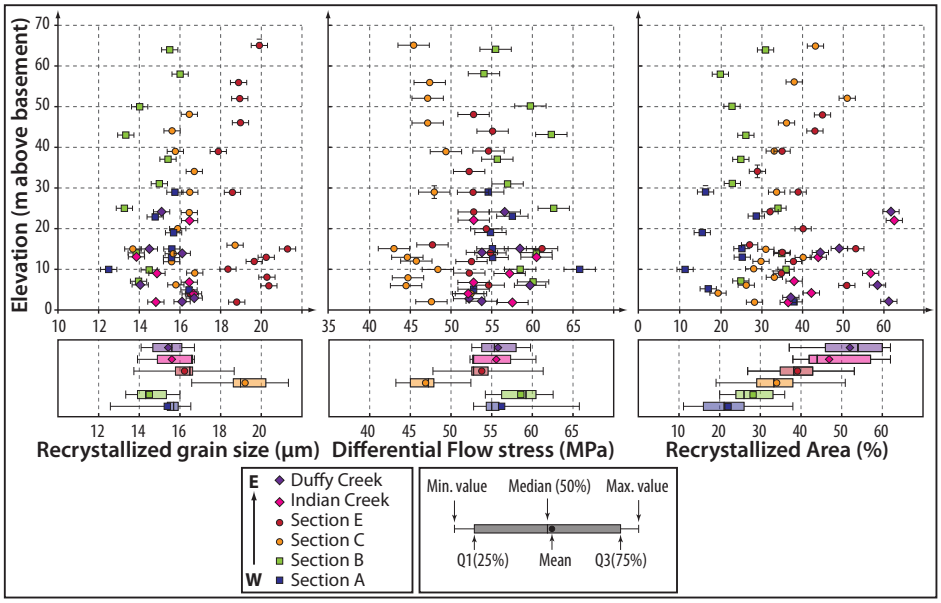

Figure 3.9: **Microstructural results.**

images are treated using Channel 5 software.

In order to investigate the CPO of a large population of grains and cover a large area of a thin section, the step size was set at 50 μm and the results were plotted by one measure per grain, over at least 800 grains, using a 15° misorientation to define grain boundaries. Quartz [c] and a axes (lower hemisphere) pole figures were generated using *PFch5* software (Mainprice, 2005).

3.5.1 CPO data

Quartz c-axis fabrics show a typical Type-I cross-girdle (Fig. 3.10) (Lister, 1977). The two samples located in the westernmost section (RR09-152 and RR09-157) display a wide girdle with equal components of basal, prism and rhomb $\langle a \rangle$ slip. Moving to the east, the maximum of the pole figures is centered, corresponding to prism $\langle a \rangle$ slip. Finally, the two pole figures of the easternmost samples (RR10-32

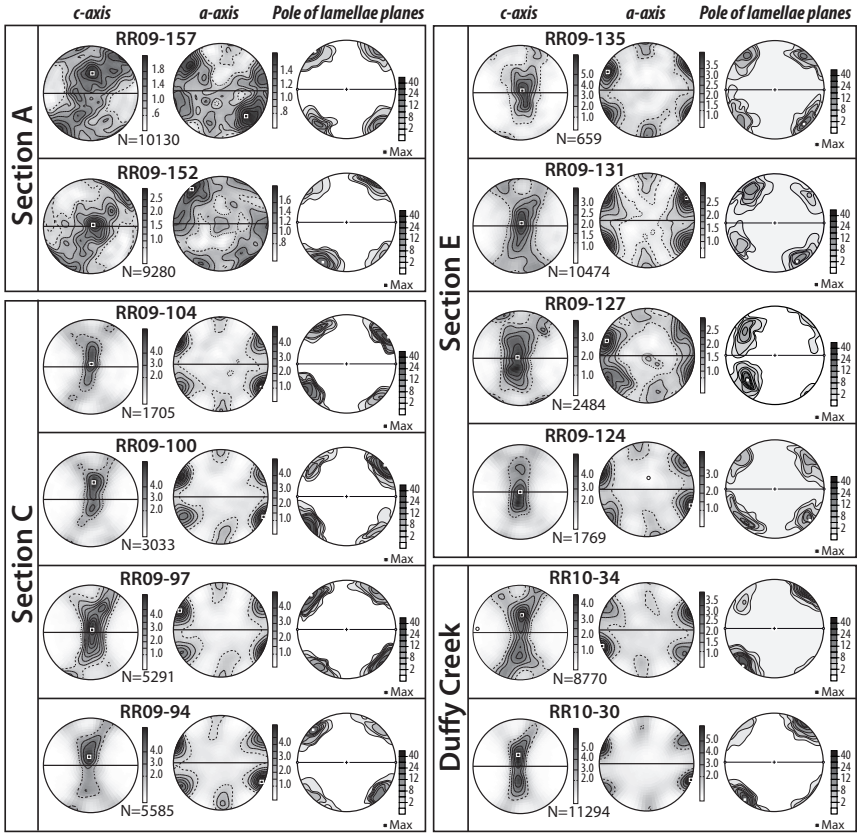

Figure 3.10: **EBSD results including c- and a-axis polefigures, and pole to lamellae plane polefigures.**

and RR10-34) show a girdle with two maxima located toward the rhomb $\langle a \rangle$ slip maximum. However, all a-axis pole figures except RR09-152 and RR09-157 show 2 point-maxima at the periphery of the stereonet that correlate best with dominant prism $\langle a \rangle$ slip.

The Type-I cross-girdle reveals that basal $\langle a \rangle$, prism $\langle a \rangle$, and rhomb $\langle a \rangle$ were the slip systems active during recrystallization. Overall, the c-axis maximum is usually located in the central segment of the girdle, suggesting that prism and

rhomb $\langle a \rangle$ were the dominant slip systems (Fig. 3.10). The a-axis pole figures show that prism $\langle a \rangle$ slip was probably the main active slip system. Type-I cross-girdles usually form in plane strain, and their symmetry indicates that the fabric developed under coaxial dominated deformation.

3.5.2 CPO strength

The strength of the CPO was investigated using the *J* index (Bunge, 1977) for the c- and a-axis, as well as the *P*, *G* and *R* indices of the c-axis distribution (Woodcock, 1977; Vollmer, 1990; Ulrich and Mainprice, 2005, see Barth et al., 2010 for review), using *PFch5* (Mainprice, 2005). The magnitude of those indices defines whether the CPO defines a point (*P*), a girdle (*G*) or a random (*R*) distribution (*R* = 1 indicates the absence of a preferred orientation). These values can be plotted in a ternary *PGR* "Vollmer" diagram (Abalos, 1997). To remove the *R* component from the determination of strain geometry, normalized point (P_n) and girdle (G_n) values can be calculated: P_n = P/(P+G) and G_n = G/(P+G) (Barth et al., 2010). Barth et al. (2010) investigated the systematic relationships between quartz slip systems and strain mode. In the case of prism $\langle a \rangle$ slip, Barth et al. (2010) showed that a high P_n-value indicates plane strain whereas low P_n-value is compatible with constriction or flattening.

On the Vollmer diagram (Fig. 3.11), our data plot in the *G* (girdle) half of the diagram (right hand side), and deviate progressively from *R* (random distribution) in samples from west to east: the two samples from Section A, with a developed c-axis girdle, show high *R* values (0.68-0.70, low CPO strength) whereas samples RR10-32 and RR10-34, with a strong c-axis central girdle, show low *R* value (0.33 - 0.17, high CPO strength). The change in c-axis pole figures is reflected in the P_n values ranging from 0.04 to 0.45 as well as the *J* index values (both $[c]$ and

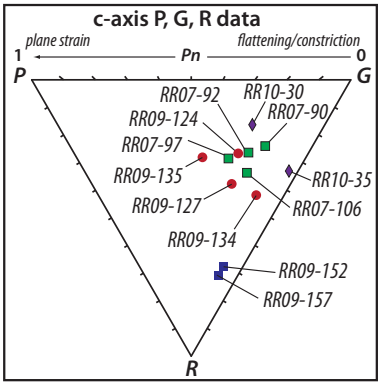

Figure 3.11: **Vollmer diagram based on the quartz CPO data, showing a transition of the rock fabrics from a random distribution (RR09-152 and RR09-157) to the constrictional field (RR10-30 and RR10-35 for example).**

$\langle a \rangle$), that also increase from west to east (Table 3.2). The distribution of *PGR* data combined with symmetrical Type-I c-axis cross-girdle in the in the Y-Z plane indicates that the deformation that produced the CPO was strongly coaxial.

3.6 Strain analysis

3.6.1 Previous work

The Elba quartzite contains useful strain markers that have been used in several studies to quantify the strain experienced by the detachment shear zone (Compton, 1980; Sabisky, 1985; Malavieille, 1987a; Wells, 2001; Sullivan, 2008). In the Clear Creek area Wells (2001) and Sullivan (2008) have reported a large west-to-east strain gradient along the transport direction, with a transition from flattening to constrictional strain attributed by Sullivan (2008) to necking of the shear zone. Strain analyses of the basal quartz-pebble conglomerate by Malavieille (1987a), Wells (2001) and Sullivan (2008) show an increase in the cobble aspect ratios from

R_{xz} = 2.6 up to 35 from west to east.

3.6.2 Results

Strain analysis was carried out using the *EllipseFit* software (Vollmer, 2011) and the results are summarized in Table 3.3 and Fig. 3.12. Three categories of grains have been analyzed: (1) the recrystallized grains (diameter smaller than 60 μm), (2) the non-recrystallized grains (diameter larger than 60 μm), and (3) the largest grains with a diameter larger than 100 μm. The recrystallized grains (< 60 μm) have a small strain ratio that slightly increases from R_s = 1.16 to R_s = 1.59, from west to east, and oriented between 11.5° and 3.2°, respectively, with respect to the foliation plane, defined by mica alignment. The less strained grains have a slightly higher angular deviation. The non-recrystallized grains (> 60 μm) show the same west to east trend in both strain ratio R_s and misorientation φ: the westernmost section has a R_s value of 1.87 oriented at φ = 10.2° while the easternmost section has a R_s of 3.60 oriented at φ = 4.0°. Finally, the largest grains show the same pattern, only more accentuated: the strain ratio becomes quite large, from R_s = 1.99 at φ = 9.3° for Section A to R_s = 4.53 at φ = 3.7 for the Indian Creek section. The increase in strain correlates with a decrease in misorientation with respect to the foliation plane. As noted by Wells (2001) and Sullivan (2008), the finite strain significantly increases from west to east and correlates with a significant thinning of the detachment shear zone: the Elba quartzite is about 80 m thick in the western section and only ~15 m thick in the eastern sections.

3.7 Vorticity analysis

Vorticity analyses are classically used to estimate the relative contributions of pure and simple shear during ductile deformation, and in this case to evaluate the mode

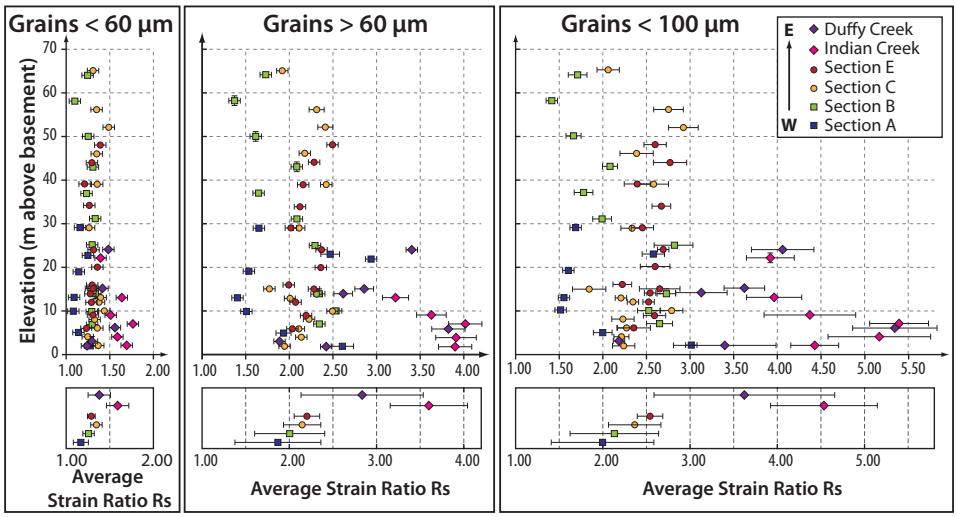

Figure 3.12: **Strain analysis results, mean strain ratio (R_s) and orientation of the strain ellipse (ϕ), for three different grain sizes, the recrystallized grains (< 60 μm), the non-recrystallized grains (> 60 μm) and larger grains (> 100 μm).**

of flow during the development and exhumation of the Raft River shear zone. The kinematic vorticity number (W_k) is a measure of the relative contribution of pure shear (W_k = 0) versus simple (W_k = 1) shear assuming steady-state instantaneous deformation. Equal components of pure and simple shear are achieved when W_k = 0.71 (Fig. 3.13, Tikoff and Fossen, 1995). Natural systems likely evolve in non-steady-state fashion, and in this case, vorticity may vary spatially and temporally. Fossen and Tikoff (1997, 1998) have shown that vorticity of the flow can be integrated in space and time by taking the mean kinematic voritcity number (W_m).

3.7.1 Previous work

Sullivan (2008) conducted a vorticity analysis of the Raft River shear zone employing three classical methods: (1) the rigid grain (prophyroclasts) orientation

method of Wallis et al. (1993); (2) the oblique recrystallized grain/quartz c-axis fabric method of Wallis (1992, 1995); and (3) the R_{xz} strain ratio/quartz c-axis fabric method of Wallis (1992, 1995). Results show that the average W_k value ranges from 0.74 to 0.81, corresponding to 50-60% of non-coaxial deformation.

3.7.2 Quartz grain shape foliation method (2)

The method based on the obliquity of both the recrystallized grains and the quartz c-axis fabric, described by Wallis (1992, 1995; see also Law, 2010) is employed here. This method is based on finding the angle between the flow plane and instantaneous stretching axes, combined with the asymmetry of Type-I cross-girdle. Depending on the flow type, the long axis of dynamically recrystallizing grains develops at an angle (θ_{max}) from the foliation plane (Fig. 3.13). Then, the orientation of the flow plane is determined by drawing a perpendicular line to the central segment of the Type-I cross-girdle c-axis fabric obtained on the XZ fabric diagram. The difference in orientation between the lineation and the flow plane defines the angle β. Finally, the mean vorticity number (W_m) is defined by: $W_m = sin\,[2 \times (\beta + \theta_{max})]$ (Fig. 14).

The orientation of recrystallized grains was captured during the analysis of grain boundary maps. In our case, all Type-I cross-girdle are very symmetrical, and β values are approximately 0°, within error of measurement, indicating that the strain that formed the CPO was almost purely coaxial. Nonetheless, the recrystallized grains show an obliquity with respect top the foliation: the mean vector orientation M varies between 7.3 and 23.8° (Table 5 and paragraph below), therefore our vorticity estimate is based on the obliquity of recrystallized grains (M angle, Table 3.4, Fig. 3.13): $W_m = \sin(2\,M)$.

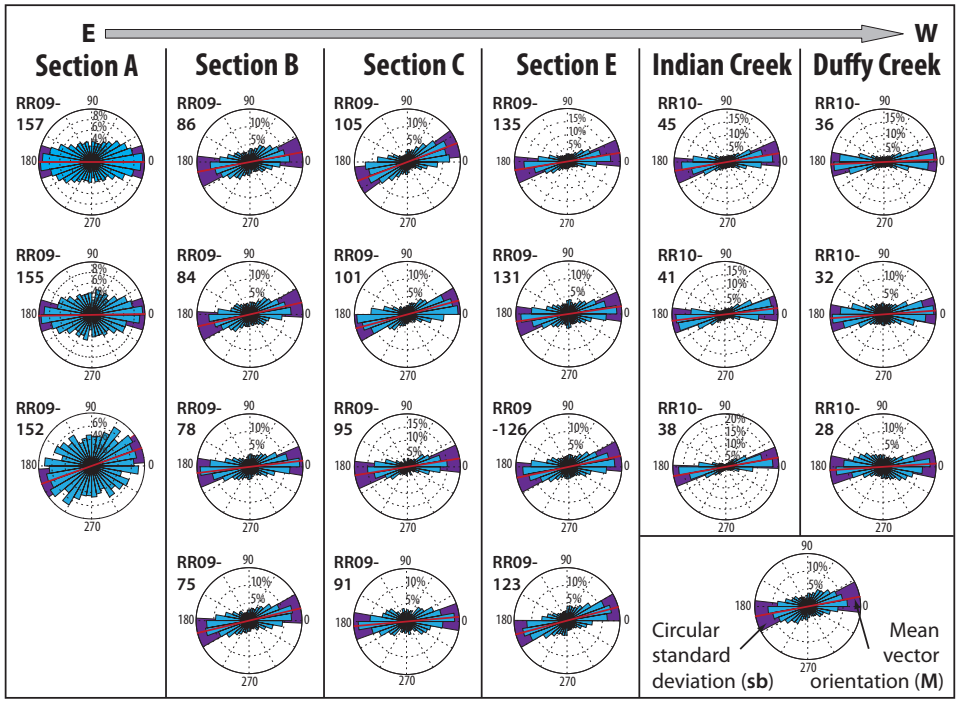

Figure 3.13: **Rose diagram showing the orientation of recrystallized grains versus foliation with the mean vector orientation (*M*, thick red line) and its associated circular standard deviation (s_b, blue cone).**

3.7.3 Recrystallized grains orientation results

The orientation of recrystallized grains (< 60 μm) was semi-quantitatively investigated using the statistical treatment of two dimensional vectorial data of Baas (2000), transcribed into a Matlab® code. The orientation of recrystallized grains is plotted in an equal area, relative frequency scale rose diagram (Fig. 3.14). The Matlab® code calculates several parameters describing the repartition of the data (see Bass, 2000 for review). The mean vector orientation (M) represents the mean orientation of the recrystallized grains. The circular standard deviation (s_b) is the two-dimensional equivalent of the standard deviation. The magnitude (length) of

the vector mean (R), is representative of the scattering of the data: a low R value correlates with scattered data, while high R values correlate with preferentially oriented data. The strength of the mean vector (K) is a representation of the vectorial concentration of the data: scattered data produce low K, while preferentially oriented data produce high K values. All the samples were analyzed and the average value of each parameter for each section is reported in Table 3.4. Both the magnitude (R) and concentration (F) of the data increase from west to east. This trend also correlates with the percent of area recrystallized.

This statistical analysis shows that, in the Clear Creek area, the obliquity of recrystallized grains with respect to the foliation is consistent with the previous work of Sullivan (2008). Over all samples the orientation of recrystallized grains ranges from 37.8° to 4.8° (Table 3.4). The average values are 23.8 $\pm$ 8.7° for Section A, 20.7 $\pm$ 7.6° for Section B, 18.6 $\pm$ 6.2° for Section C, 23.2 $\pm$ 8.3° for Section E, 15.6 $\pm$ 4.1° for Indian Creek and 7.3 $\pm$ 3.2° for Duffy Creek, respectively. Although the error associated with these measurement is quite large, the Clear Creek sections shows a larger angular deviation (~23°) than the two easternmost sections (Indian and Duffy Creek), with smaller angular deviation values (~12°).

In summary, from west to east, the obliquity of grains slightly decreases, the quartzite becomes more recrystallized, and the secondary foliation becomes stronger, as shown by the increase in R and K values. This strengthening of the recrystallized grain populations produces a secondary foliation that becomes closer in orientation to the main foliation, as shown by the decrease in the orientation of recrystallized grains.

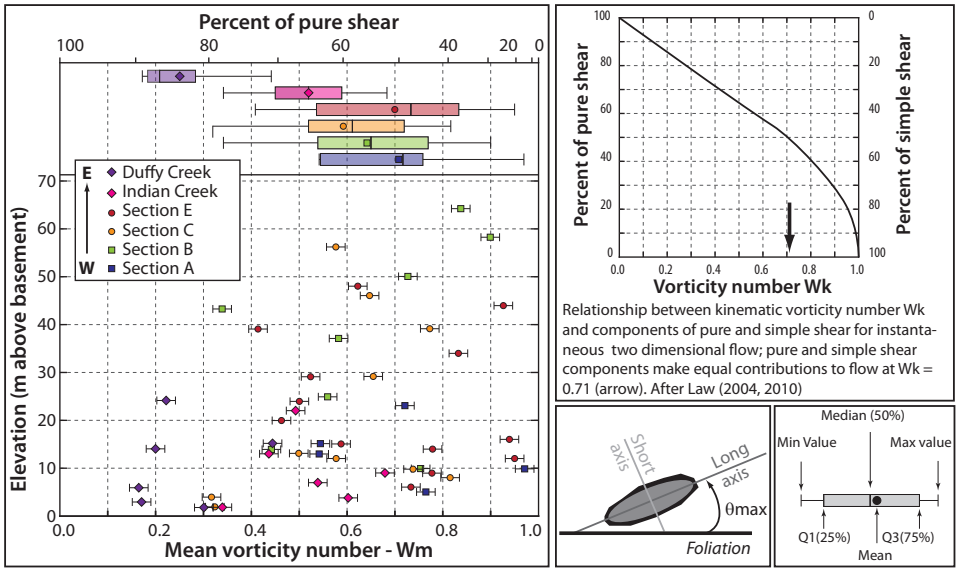

Figure 3.14: **Vorticity analysis results.**

3.7.4 Vorticity results

In the Clear Creek area, the vorticity number estimates are very close to the data of Sullivan (2008): 0.78 $\pm$ 0.18 for Section A, 0.64 $\pm$ 0.20 for Section B, 0.59 $\pm$ 0.17 for Section C, 0.70 $\pm$ 0.19 for Section E (Table 3.4). The two sections in the eastern localities show lower Wm estimates: 0.52 $\pm$ 0.12 for Indian Creek, and 0.25 $\pm$ 0.11 for Duffy Creek (Table 3.4). These vorticity estimates show that, in the Clear Creek area, the Elba Quartzite records between 50 and 60% pure shear, and this component of deformation increases to the east, with about 70% and 85% pure shear recorded in Indian Creek and Duffy Creek, respectively. The vorticity results also show a relative change in the style of deformation that correlates with the degree of recrystallization and the strength of the quartz CPO (Fig. 3.10). From west to east (along the transport direction), microstructural analysis shows a strengthening of rock fabric that positively correlates with both degree of recrystal-

lization of the quartzite and change in deformation kinematics toward a more pure shear dominated deformation.

3.8 Paleopiezometry results

3.8.1 Recrystallized grain-size paleo-piezometry

Recrystallized grain size paleopiezometers were developed based on the observation that, during experimental deformation of quartz rocks, the size of dynamically recrystallized grains deforming in the dislocation creep regime is a function of the applied differential stress (Twiss, 1977; Ross et al., 1980; Hirth and Tullis, 1992; Gleason and Tullis, 1995; Stipp and Tullis, 2003). Indeed, after a certain strain, dynamically recrystallized materials maintain a steady state microstructure (Means, 1981), with a grain size that is primarily controlled by the applied stress and only weakly dependent on temperature, pressure and water fugacity (e.g., Karato et al., 1980; van der Wal, 1993). Based on laboratory experiments, several empirical relationships between dynamically recrystallized grain size and flow stress have been calibrated for various materials, including quartz (Twiss, 1977; Post, 1977; Ross et al., 1980; Michibayashi, 1993; Stipp and Tullis, 2003).

Stipp and Tullis (2003) recently refined a new calibration of the quartz paleopiezometer for mid-crustal conditions that is used here. This piezometer does not include stereological correction; therefore, our grainsize estimates were not corrected for consistency (Table 3.1). The Stipp and Tullis (2003) piezometer was corrected based on calibration of Grigg's deformation apparatus to gas apparatus by Holyoke-III and Kronenberg (2010). Using the recrystallized grain size, we obtain in the Clear Creek area a narrow range of flow stress, from ~47 to 59 MPa: 56 MPa for Section A, 59 MPa for Section B, 47 MPa for Section C, 54 MPa for

Section E, 56 MPa Indian Creek and 56 MPa for Duffy Creek (all estimates are ± 12 MPa, Table 3.1 and Fig. 3.9).

3.8.2 Deformation lamellae paleo-piezometry

Based on observations by McCormick (1977), Koch and Christie (1981) established a relationship between the apparent spacing of deformation lamellae and stress magnitude. Using wet and dry deformation experiments (800 - 1000°C, constant strain rate 10^{-7} - 10^{-4} s^{-1}) on Simpson quartzites samples (Simpson orthoquartzite from the Sunray Cullen well, Oklahoma), they calibrated the spacing between lamellae and the differential stress and raised the possibility of using lamellae spacing as a paleopiezometer:

$\Delta\sigma = c \times s^{-\ell}$

where $\Delta\sigma$ is the differential flow stress in GPa, c a constant (3.65 μm^{ℓ}.GPa), s the average spacing between lamellae (in μm) and ℓ = -2.18 (Koch and Christie, 1981).

Using the universal stage, the lamellae planes were tilted into parallelism with the microscope axis and the lamellar spacing was determined by the intercept method on at least 16 grains per sample; the geometric mean was calculated. Results are shown in Fig. 3.15 and Table 3.5. A slight trend stands out; the spacing between lamellae planes is smaller at the top (~6.5 - 8.5 μm) compared to the base (~9 - 15 μm) of the studied sections. Using the paleopiezometer of Koch and Christie (1981), we obtain flow stress values increasing from the base to the top of the quartzite section from ~10 MPa up to 63 MPa (Fig. 3.15 and Table 3.5). The magnitude of flow stress estimates based on lamellae piezometry is in good agreement with the flow stress estimates based on the recrystallized grain size.

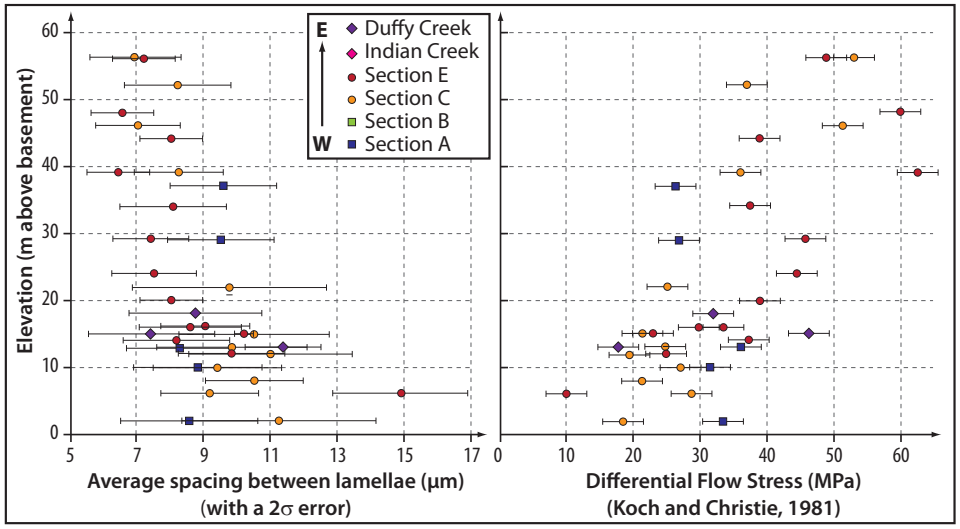

Figure 3.15: **Lamellae spacing and lamellae-based piezometry results.**

3.9 Discussion

The kinematic and rheology of low-angle detachment zones associated with MCC exhumation that accommodate most of the extension of the continental lithosphere have been debated (Davis and Lister, 1988; Lister and Davis, 1989; Axen et al., 1990; Planke and Smith, 1991; Axen, 1992; Wernicke, 1992; Manning and Bartley, 1994; Collettini and Barchi, 2002; Healy, 2009), but it appears that motion on the low-angle normal fault is primarily controlled by excess pore fluid pressure (Axen, 1992; Collettini and Barchi, 2002), weakening of the fault rock through reaction softening (Taylor and Huchon, 2002), stress increase (Axen, 1992), or the development of a high transient geotherm across the detachment zone (Gottardi et al., 2011). In the following, we will first discuss the results of detailed microstructural analysis (quartz crystallographic preferred orientation, microstructural, strain and vorticity analysis), then we will estimate the differential flow stress experienced by the detachment shear zone, by combining two paleopiezometers:

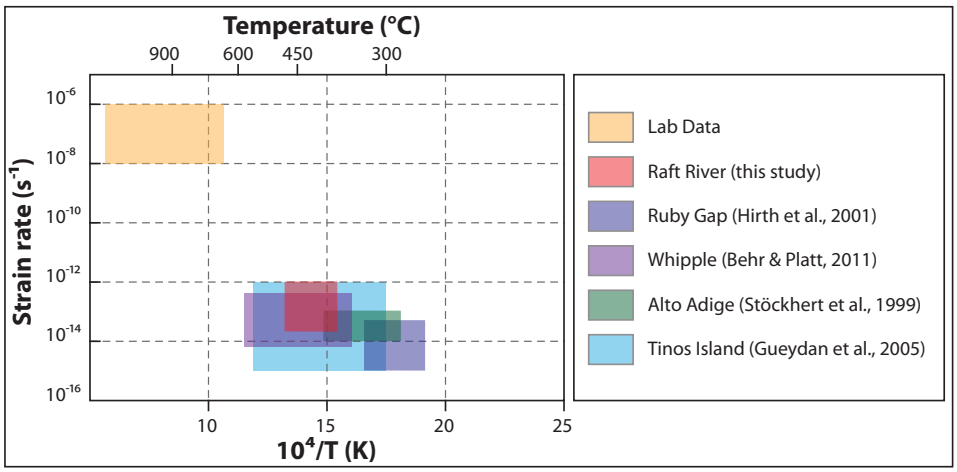

Figure 3.16: **Strain rate / Temperature space diagram, showing the experimental field and natural datasets, including the results of this study.**

the quartz recrystallized grain size piezometer of Stipp and Tullis (2003) and the deformation lamellae spacing piezometer of Kock and Christie (1981), and use the quartzite dislocation creep flow law of Hirth et al. (2001) to evaluate the strain rate and see how these results compare to independent thermochronological and finite strain data. Finally, we will explore how mechanical and thermal instabilities at the brittle-ductile transition can affect the stress/strain rate state of extensional shear zones and enhance the exhumation of MCC.

3.9.1 Strain variation along the Raft River detachement shear zone

The very symmetrical Type-I cross-girdles of the quartz CPO data (Fig. 3.10) suggest that the quartzite fabric developed under strong coaxial component of deformation. The RPG (Fig. 3.11 and Table 3.2) data show that the rock fabric strengthens from west to east, along the transport direction, as shown by the shift from relatively high R (random) values to high G (girdle) values, and the increase

in J index from west to east. These rock fabric observations correlate with some characteristics of the microstructures. From west to east, the degree of recrystallization increases, from ~20% in the Clear Creek area to 52% in Duffy Creek, while the recrystallized grain size remains the same (Table 3.1). This pattern is accompanied by a decrease in the obliquity of the recrystallized grains: in the Clear Creek area the recrystallized grains are oriented at high angle to the foliation (~25°) while this angle closes down to ~10° in the eastern sections (Table 3.4). By using the oblique grain fabric to evaluate the vorticity, we find that the quartzite fabrics in the Clear Creek area developed under 50 - 60% of pure shear, while the eastern localities where dominated by > 85% pure shear (Table 3.4). The finite strain recorded by the non-recrystallized grains also increases along the transport direction. While recrystallized grains conserve a small strain ratio (1.16 to 1.59), the non-recrystallized grains display a strain gradient from west (R_s = 1.87) to east (R_s = 3.60). This complete microstructural analysis shows an increase in intensity of the quartzite mylonite fabrics along the transport direction, from west to east. These findings corroborate the results of Compton (1980), Wells (2001), and Sullivan (2008) reporting a large finite strain gradient in the Clear Creek area, along the transport direction, compatible with a necking of the detachment shear zone (Wells, 2001; Sullivan, 2008).

3.9.2 Deformation mechanisms

The observation of quartz microstructures under the microscope reveals a lack of recovery and evidence for crystal plastic deformation of quartz grains. Undulose extinction and deformation bands are ubiquitous, indicating that recovery processes had little time to dissipate the internal energy stored in the quartz grains. The abundance of fluid inclusion trails suggests that fluids were present during deformation.

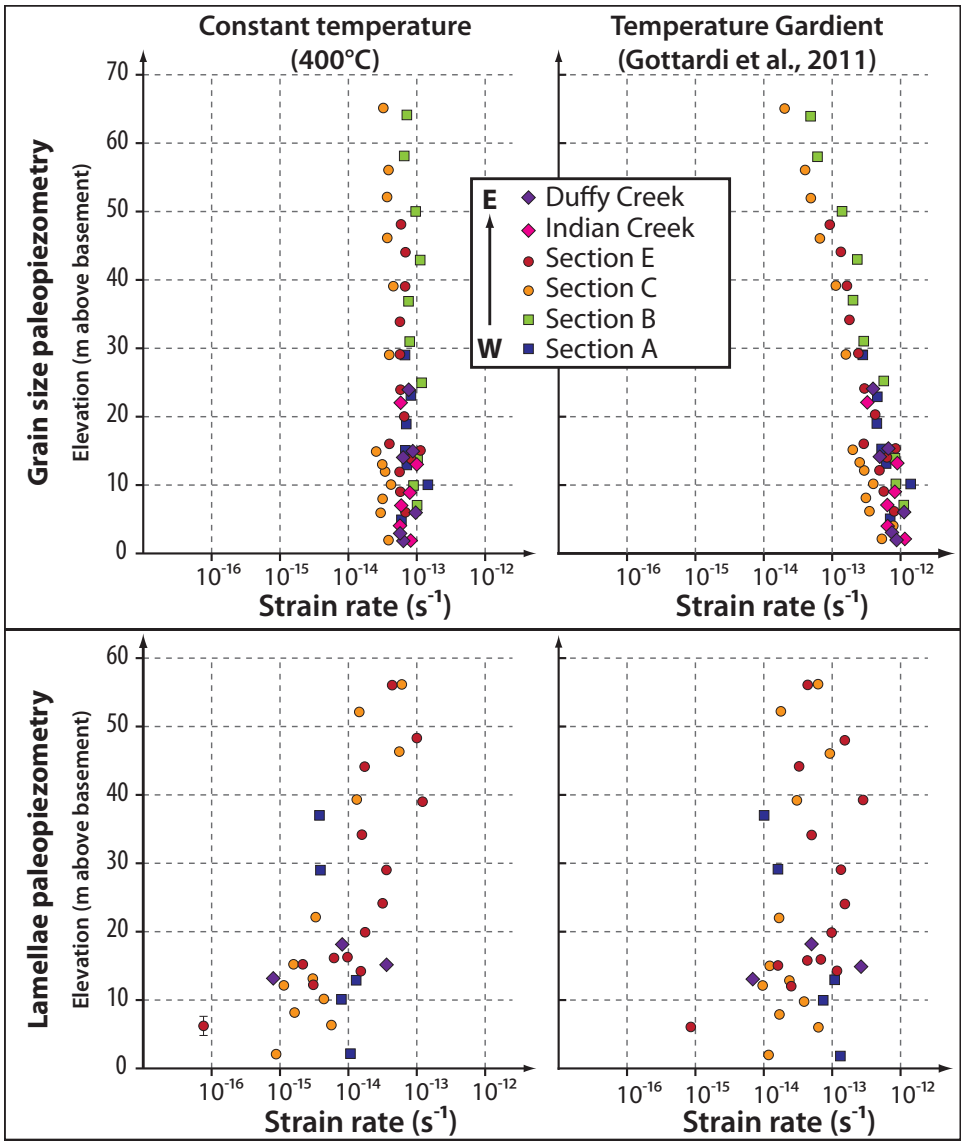

Figure 3.17: **Strain rate calculation results, based on the two estimates of the flow stress (recrystallized grain size and lamellae spacing) at constant temperature (400°C) or with the temperature gradient of Gottardi et al. (2011), using the Hirth et al. (2001) quartzite dislocation creep flow law.**

TEM analyses of deformation lamellae in quartz are not conclusive regarding their origin (e.g. McLaren et al., 1970; McLaren and Hobbs, 1972; White, 1973, 1975; Christie and Ardell, 1974; Drury, 1993). Similar deformation lamellae have also been produced experimentally in alloys, metals, and other ionic materials (see Drury, 1993 for review) where they are characteristic microstructures of exponential creep and cold working, indicative of glide-controlled deformation in the low-temperature plasticity field. Drury (1993) pointed out that the formation of deformation lamellae could possibly indicate a power-law breakdown. TEM work by McLaren and Hobbs (1972) and Trepmann and Stöckhert (2003) attributed deformation lamellae submicrostructures to non-steady state creep with strain hardening. Accepting Drury's (1993) hypothesis that deformation lamellae are indicative of plastic high-stress deformation, Trepmann and Stöckhert (2003) deduced from their observations that deformation lamellae formed during short-term plastic, and eventually brittle, deformation related to coseismic loading, and were subsequently modified by recovery, which was effective at the prevailing temperatures of 300-350°C (Trepmann and Stöckhert, 2003).

In the Raft River Mountains, deformation lamellae are abundant and affect up to 50% of the grains in some samples. Deformation lamellae are decorated with fluid inclusions in some cases (Fig. 3.4h,i), suggesting that they might have served as preferential pathways for fluids during plastic deformation, allowing the fluids to enter the crystal lattice and weakening the grains during dislocation creep. Deformation lamellae crosscut subgrain boundaries but not grain boundaries. They are well preserved owing to the lack of recovery of the quartzite. These lines of evidence indicate that the rate of recovery in the quartzite mylonite was not sufficiently rapid to keep up with strain rate and offset strain hardening. Therefore, the detachment system probably evolved close to the brittle-ductile transition, switching back and forth between dislocation creep and glide controlled exponen-

tial creep, depending on the temperature/strain rate/fluid conditions.

The presence of fluids during recrystallization has been revealed by hydrogen stable isotope (Gottardi et al., 2011), suggesting that meteoric fluids permeated the detachment zone during deformation, where their presence is recorded in synkinematic muscovite. In addition, based on oxygen isotope geochemistry of quartz-muscovite pairs, Gottardi et al. (2011) showed that the Raft River detachment shear zone recorded an extreme transient geothermal gradient (~125°C / 100 m) with temperature of ~485°C at the base of the detachment zone to 350°C at the top. This strong thermal structure was exhumed and cooled rapidly in the Miocene (Wells et al., 2000).

In summary, the quartzite mylonite in Raft River detachment shear zone at Clear Creek shows evidence of both ductile dislocation creep (subgrain rotation recrystallization of the quartzite mylonite) and plastic exponential creep (deformation lamellae), and preserved an extreme thermal gradient (125°C / 100 m, Gottardi et al., 2011) and abundance of meteoric fluids during deformation (Gottardi et al., 2011).

Mulch et al. (2006) suggested that one possible response of the mylonite to strain hardening is relocation and migration of the deformation front. Ubiquitous evidence of high stress plastic deformation in the Raft River Mountains at Clear Creek suggests another scenario in which the response to stress hardening is seismic failure. In this scenario, when the detachment is still at depth, owing to relatively high temperature (~500°C) the deformation is controlled by dislocation creep: the Elba quartzite develops its mylonitic fabric by subgrain rotation recrystallization (Fig. 3.19a). As the system exhumes, hydrogen stable isotope analyses from syn-kinematic micas and fluid inclusions (Gottardi et al., 2011) show that meteoric fluids percolate through the brittle upper crust down to the detachment zone. Owing to the coupling of fast strain rates and enhanced cooling by surface-

derived fluids (e. g. Morrison and Anderson, 1994; Gottardi et al., 2011), the system enters a strain hardening regime and the stress builds up, leading to high stress plasticity features such as undulose extinction and deformation lamellae or even brittle fracturing (Fig. 3.19b). Prior to failure, as the stress reaches critical level, dilatancy increases, allowing more fluids to be pumped into the shear zone, where they might find new fast pathways in the crystals, thereby acting as a weakening and cooling agent (Sibson, 1977; McCaig, 1988; Lister and Davis, 1989; Axen, 1992). At this point, the "continental stress guide" (Lister and Davis, 1989) reaches its maximum strength, and the thermal and mechanical contrast between the stress build-up and cooling/weakening in the detachment zone leads to seismic rupture. In the period of post seismic relaxation, the stress decays and the detachment zone re-enters the dislocation creep regime. Recovery processes obliterates the brittle/plastic microstructures (sealed fluid inclusions trails and microcracks, formation of new grains/subgrains, precipitation of hydrous phases such as white micas) and possible fluid pathways (microcracks) (Fig. 3.19c), until the cycle begins again (Lister and Davis, 1989; Küster and Stöckhert, 1999; Trepmann and Stöckhert, 2003).

3.9.3 Flow stress evolution of the detachement shear zone

Numerous experimental studies on various materials have shown that at a given shear stress, dynamic recrystallization leads to a particular grain size distribution that can be characterized by a mean value and a standard deviation. This relationship between recrystallized grain size and shear stress has been empirically calibrated into paleopiezometer equations. As recrystallization proceeds, experimental studies show that the dispersion of the grain population diameter is expected to decrease with increasing strain (Te Heege, 2002), leading eventually to a homoge-

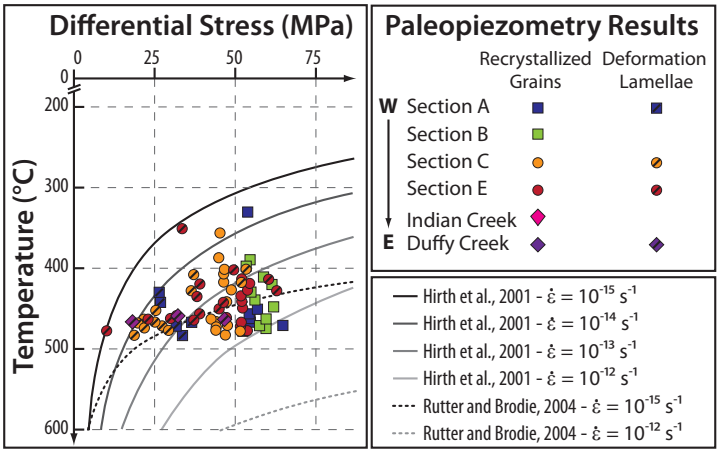

Figure 3.18: **Differential stress / temperature space diagram, with the constant strain rate curve of Hirth et al. (2001) and Rutter and Brodie (2004).**

neous population of grains. In the eastern part of the Raft River Mountains, our data show that the grain size distribution and its dispersion are fairly constant, and only the amount of material recrystallized changes along the transport direction, from ~20% up to 50% of material recrystallized. Using the recrystallized grain size paleopiezometry equation, the constant value of the recrystallized diameter suggests that the quartzite recorded the same stress everywhere, between ~45 and 55 MPa.

The study of the spacing between deformation lamellae allows us to have another estimate of the flow stress. The Koch and Christie (1981) deformation lamellae piezometer predicts an inverse power relationship between the spacing of the lamellae and the differential flow stress. Throughout the study area, the spacing between lamellae decreases from the bottom to the top of the section, leading to an increase in flow stress (~20 MPa at the base to ~60 MPa at the top).

Although both piezometers are experimentally calibrated, and are using two completely different microstructural parameters, they both give flow stress esti-

mates in surprisingly good agreement. Such estimates are comparable in magnitude to other areas like the Whipple Mountains detachment shear zone (Behr et al., 2011), the Tinos Island extensional shear zone (Gueydan et al., 2005), the Alto Adige strike-slip shear zone (Stöckhert et al., 1999) or the Ruby Gap duplex (Dunlap et al., 1997; Hirth et al., 2001) (Fig. 3.16).

Our data show that the differential flow stress estimates based on recrystallized grain size are quite uniform, while the spacing of the deformation lamellae show a flow stress decay with depth, with a maximum value at the top of the section, where the flow stress values are the same for both methods. Assuming that the lamellae do form at dislocation creep/exponential creep breakdown, our data suggest that the mylonite recrystallized during the loading cycle, at a stress getting close to the peak strength at the base of the seismogenic zone (Sibson, 1977; Brace and Kohlstedt, 1980; White, 1996; Küster and Stöckhert, 1999; Trepmann and Stöckhert (2003), in a normal overprinting sequence at the ductile-brittle transition (Passchier, 1982; Koch and Masch, 1992).

3.9.4 Strain rate of detachment tectonics

More interestingly, the paleopiezometry results show that all the microstructural features (quartz fabrics and lamellae) developed under about the same stress. Therefore, if the strength of the quartzite detachment shear zone can be described by a dislocation creep flow law (like the quartzite dislocation creep flow law of Hirth et al., 2001), then the physical parameters that control in the flow law must balance one another in order for the differential flow stress to remain spatially and temporally constant (as suggested by Mulch et al., 2006, for example). In other word, temperature, strain rate and fluid activity must balance each other for the differential flow stress to remain constant.

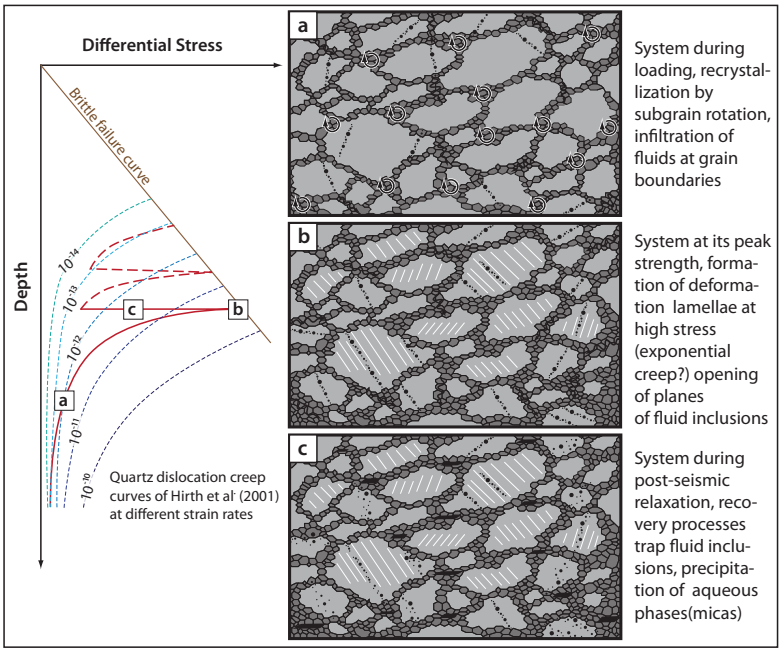

Figure 3.19: **Crustal strength profile of the continental crust, using Byerlee's law (Sibson, 1974) for the brittle upper crust and the Hirth et al. (2001) quartzite dislocation creep flow law for the lower crust. (a), (b) and (c) show possible differential stress pathway for the microstructures observed in the Raft River Mountains at Clear Creek.**

Based on oxygen stable isotope geochemistry, Gottardi et al. (2011) reported the preservation of an extreme geothermal gradient across the Raft River detachment zone, with temperature of 485 $\pm$ 50°C to 350 $\pm$ 50°C from bottom to top of the quartzite mylonite section. Hydrogen stable isotope analyses of syn-kinematic white micas and fluid inclusions show ubiquitous presence of meteoric fluid during deformation. Therefore, temperature and fluid activity were probably two major parameters that controlled the evolution of the detachment shear zone.

Based on the quartzite dislocation creep flow law of Hirth et al. (2001) for

which the stress exponent n is 4 and the activation energy Q is 135 kJ/mol, we estimated the strain rate using both a constant temperature (400°C) and the temperature gradient of Gottardi et al. (2011), assigning a temperature as a function of elevation (T = 485 - 1.5 z, z is the elevation in m above the basement) (Fig. 3.17 and 3.18).

At constant temperature, the recrystallized grain size flow stress yields strain rate estimates between 10^{-14} and 10^{-13} s^{-1}, while the variation in lamellae flow stress gives fast strain rate at the top (10^{-13} s^{-1}) decaying to slow strain rate at the bottom (10^{-15} s^{-1}) of the section. Using the thermal gradient of Gottardi et al. (2011), the recrystallized flow stress results show faster strain rate at the bottom (10^{-12} s^{-1}), where the temperatures are higher, than at the top of the section (5 $\times$ 10^{-14} s^{-1}), where the temperature is cooler. The vertical increase in lamellae flow stress combined with vertical decrease in temperature produces a narrower range of strain rates, between 10^{-14} and 10^{-13} s^{-1}. These results compare well with strain rate estimates from extensional settings such as the Basin and Range (10^{-12} to 10^{-15} s^{-1}, Campbell-Stone and John, 2002; Gans and Bohrson, 1998), the Whipple Mountains (10^{-12} to 10^{-15} s^{-1}, Behr et al., 2011), the Tinos Island (10^{-12} s^{-1}, Gueydan et al., 2005), or the Alto Adige (10^{-13} to 10^{-14} s^{-1}, Stöckhert et al., 1999). On a temperature/flow stress diagram (Fig. 3.18), the data cluster between the 10^{-14} and 10^{-12} s^{-1} constant strain rate curves of Hirth et al. (2001). The Rutter and Brodie (2004) flow law overestimates the strength of the shear zone.

Independent constraints on the strain rate can be estimated based on the finite strain analysis (Compton, 1980; Wells, 2001, Sullivan, 2008, this study) and available thermochronological data (Wells et al., 2000). Wells et al. (2000) showed that the Raft River detachment shear zone was active during Early Miocene (~25/20 Ma) and was exhumed by Late Miocene (7.5 Ma). Apatite fission track yields an estimate of the slip rate for the Raft River detachment shear zone of 7 mm/yr be-

tween 13.5 to 7.4 Ma. If we use this slip rate (7 mm/yr) and assume the width of the shear zone to be the thickness of the quartzite mylonite (100 to 10 m thick), we obtain a strain rate estimate ranging from 2.2×10^{-12} to 2.2×10^{-11} s^{-1}. This value corresponds to the fastest strain rates obtained from the flow law using both lamellae and recrystallized grain size. On the other hand, based on the argon ages from Wells et al (2000), if we assume that the shear zone was active for 10 Ma and use the final strain ratios of 1 to 10, we obtain strain rate estimates of 3.2×10^{-15} s^{-1} to 3.2×10^{-14} s^{-1} respectively. These values are in agreement with the slowest strain rates calculated using the quartzite dislocation creep flow law, based on both lamellae and recrystallized grain size flow stress estimates.

3.9.5 Thermomechanical instabilities at the brittle-ductile transition

The previous calculations show how the strain rate, calculated based on quartzite dislocation creep flow law, is sensitive to the temperature, hence, by extrapolation, the strength of the continental crust is very sensitive to its geotherm. In this section, we investigate how thermal instabilities affect the rheology of the continental crust. In the Raft River Mountains, the extreme geothermal gradient reported by Gottardi et al. (2011) is the result of (1) the dipping shear zone, advecting and juxtaposing hot rocks from the footwall and cold rocks from the hanging wall, such that a steep transient geotherm is established, (2) thinning of the footwall shear zone may also lead to heat advection (3) the influx of cool surface fluids down to the detachment can maintain a steep transient geotherm over the timescale of shearing/exhumation. Therefore, reporting the data on a strength profile (differential stress versus depth), assuming a geothermal gradient, sheds new light on flow stress and strain rate variation.

On Fig. 3.20, the strength of the continental crust is represented using Byer-

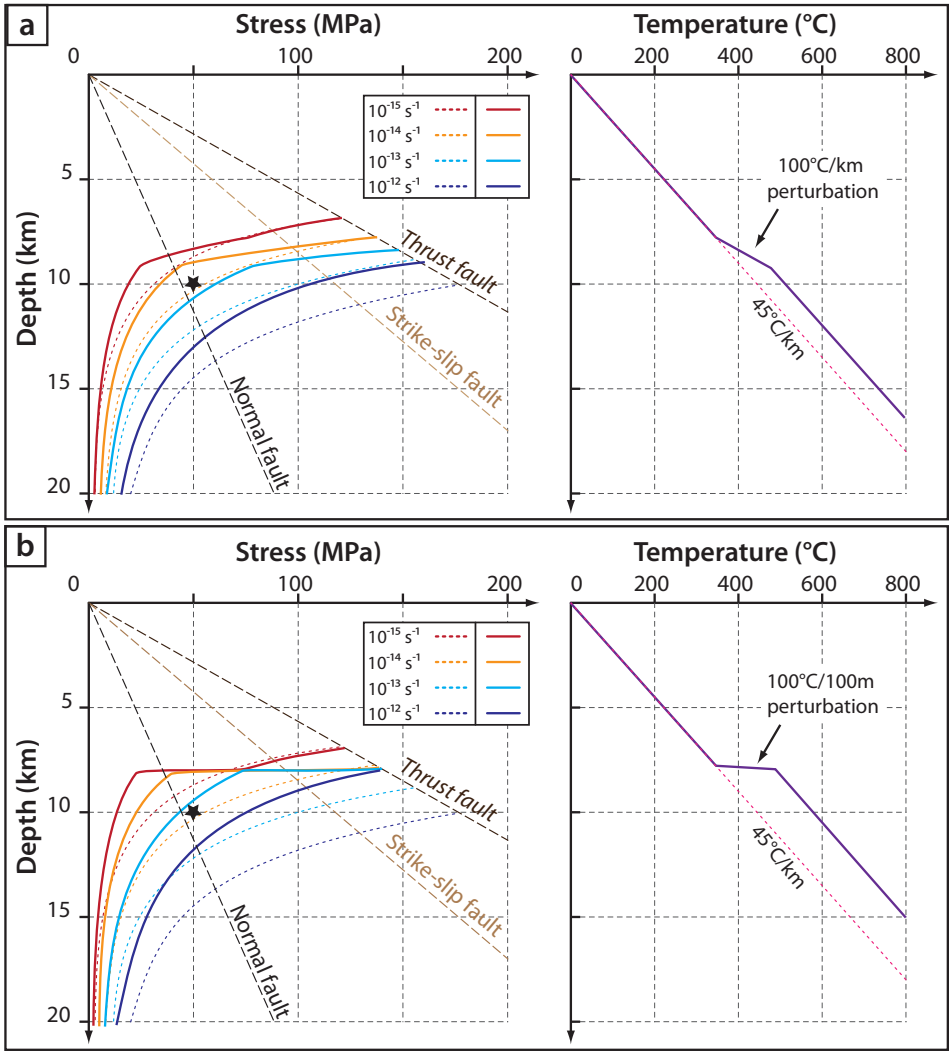

Figure 3.20: **Strength profile using Byerlee's law (Sibson, 1974) for the brittle upper crust and the Hirth et al. (2001) quartzite dislocation creep flow law for the lower crust. Different geotherm are used to calculate the strength profile: (a) 45 ℃/km geotherm (dashed lines) and compressed geotherm (100 ℃ / km, between 350 ℃ and 485 ℃) (solid line); (b) 45 ℃/km geotherm (dashed lines) and compressed geotherm (100 ℃ / 100 m, between 350 ℃ and 485 ℃) (solid line).**

lee's law for the brittle upper crust (for different tectonic regimes) (Sibson, 1974, Kohlstedt et al., 1995) and the Hirth et al. (2001) quartzite dislocation creep flow law for ductile lower crust, at different strain rates (Fig. 3.20). The dashed lines represent dislocation creep curves at constant strain rates, using a hot geotherm of 45°C/km, and form a typical crustal strength profile. However, we also plot a compressed geotherm (solid lines) based on the work by Gottardi et al. (2011): in Fig. 3.20a, the geotherm is compressed by 100°C / km between 350 and 485°C, and in Fig. 3.20b, the geotherm is compressed by 100°C / 100 m between the same temperatures.

Our piezometry results show that most of the quartzite records a differential flow stress of ~50 MPa and a strain rate of ~10^{-14} to 10^{-12} s^{-1}. Significant variations in strain rate can be achieved depending on the geotherm: for example, a rock sitting at 10 km and under a flow stress of 50 MPa (star on Fig. 21) would record a strain rate of ~10^{-14} s^{-1} with the 45°C/km geotherm, while by using a compressed geotherm, the strain rate will increase by one or more orders of magnitude: ~8×10^{-14} s^{-1} (Fig. 3.20a) up to ~8×10^{-13} s^{-1} (Fig. 3.20b). Such variations in strain rate are sufficiently large to affect the rheological behavior of the mylonite, which will respond to strain rate increase by strain hardening, embrittlement, and ultimately seismic failure. Those observations show that thermal instabilities, produced by a combination of ductile shearing, heat advection and enhanced cooling by meteoric fluids, can trigger significant mechanical instabilities, without changing the stress state or depth of the detachment shear zone.

3.10 Conclusion

Our study shows that detailed microstructural analysis of the very well exposed Raft River detachment shear zone and careful comparison of its quartzite mylonite

with laboratory results can allow us to understand the kinematics of a shear a zone and constrain the stress/strain rate conditions of its evolution. Our analysis offers the following results:

1) A strengthening of the rock fabrics from west to east, along the transport direction, compatible with observed finite strain markers (Compton, 1980; Wells, 2001; Sullivan 2008), that fits in a model of "necking" of the shear zone proposed by Wells (2001) and Sullivan (2008).

2) Flow stress estimates based on two different empirically calibrated piezometers yield similar results 40-60 MPa. These estimates correlate with other extensional settings where deformation is interpreted to occur at similar temperatures, such as the extensional Whipple Mountains (10-136 MPa, 310-550°C, Behr et al., 2011) and the Tinos Island (10-100 MPa, 400°C, Gueydan et al., 2003), strike-slip shear zone (The Alto Adige, 60-160 MPa, 280-350°C, Stöckhert et al., 1999), or compressional settings such as the Ruby Gap duplex (60-100 MPa, 250-330°C, Dunlap et al., 1997; Hirth et al, 2001).

3) Using a quartzite dislocation creep flow law (Hirth et al., 2001) we estimate that the detachment shear zone quartzite mylonite developed at a strain rate between 10^{-12} and 10^{-14} s^{-1}. This range of strain rate is also in agreement with previous published studies: 10^{-12} to 10^{-15} s^{-1} for the Whipple Mountains (Behr et al., 2011), 10^{-12} to 10^{-15} s^{-1} for the Tinos Island (Gueydan et al., 2003), 10^{-13} to 10^{-14} s^{-1} for the the Alto Adige strike-slip fault (Stöckhert et al., 1999), and 10^{-13} to 10^{-15} s^{-1} for the Ruby Gap duplex (Dunlap et al., 1997; Hirth et al, 2001).

4) Microstructural evidence (quartz microstructures and deformation lamellae) suggest that the detachment shear zone evolved at its peak strength, close to the dislocation creep/exponential creep transition, where meteoric fluids played an important role on strain hardening, embrittlement, and eventually seismic failure.

5) Compressed geothermal gradient, produced by a combination of ductile

shearing, heat advection and enhanced cooling by meteoric fluids, can trigger significant mechanical instabilities and strongly influences the rheology of the detachment shear zone.

[0]**Acknowledgments:** We gratefully acknowledge research support from the Swiss Science Foundation (FNS-117694) and the US-National Science Foundation (EAR-0838541). Parts of this work were carried out in the Characterization Facility, University of Minnesota, which receives partial support from NSF through the MRSEC program.

Section	D (μm) (non corrected)	D (μm) (corrected)	Flow stress (MPa)	Recrystallized area (%)
A	15.3 ± 2.4	23.0 ± 1.9	56.2 ± 12	22 ± 9
B	14.5 ± 1.8	21.8 ± 1.4	58.6 ± 12	28 ± 6
C	19.2 ± 2.4	28.8 ± 1.8	46.9 ± 12	34 ± 8
E	16.2 ± 2.2	24.3 ± 1.6	53.7 ± 12	39 ± 8
Indian Creek	15.6 ± 2.4	23.3 ± 1.9	55.5 ± 12	47 ± 10
Duffy Creek	15.4 ± 2.0	23.2 ± 1.5	55.8 ± 12	52 ± 10

Table 3.1: **Microstructural analysis results including the recrystallized grain size D, flow stress estimate (based on the Stipp and Tullis, 2001 paleopiezometer), and the percent of recrystallized area.**

Section	Sample	P	G	R	P_n	J $[c]$	J $\langle a \rangle$
Section 00	RR09-152	0.06	0.26	0.68	0.18	1.21	1.06
	RR09-157	0.06	0.26	0.70	0.20	1.16	1.05
Section 0	RR07-90	0.15	0.61	0.24	0.19	2.36	1.6
	RR07-92	0.19	0.54	0.27	0.26	2.27	1.49
	RR07-97	0.23	0.48	0.28	0.32	2.36	1.56
	RR07-106	0.16	0.50	0.34	0.24	2.13	1.46
Section 6	RR09-124	0.21	0.52	0.27	0.29	2.3	1.43
	RR09-127	0.18	0.44	0.38	0.29	1.84	1.23
	RR09-134	0.09	0.49	0.42	0.15	1.62	1.22
	RR09-135	0.32	0.39	0.28	0.45	2.6	1.55
Duffy Creek	RR10-35	0.03	0.64	0.33	0.04	1.89	1.33
	RR10-30	0.23	0.61	0.17	0.27	3.1	1.85

Table 3.2: **EBSD data. *P* (Point), *G* (Girdle), *R* (Random) and normalized P_n values, and *J* index calculated for the c- and a-axis polefigures.**

	Grains < 60 μm		Grains > 60 μm		Grains >100 μm	
Section	R_s	ϕ	R_s	ϕ	R_s	ϕ
A	1.2 ± 0.1	9.2 ± 7	1.9 ± 0.5	10 ± 8	2.0 ± 0.6	8 ± 7
B	1.3 ± 0.1	9.2 ± 4	2.0 ± 0.4	7.3 ± 4	2.1 ± 0.5	6 ± 4
C	1.4 ± 0.1	9.3 ± 4	2.2 ± 0.2	7.1 ± 4	2.4 ± 0.3	7 ± 4
E	1.3 ± 0.1	12 ± 4	2.2 ± 0.2	10 ± 5	2.5 ± 0.2	9 ± 4
Indian Creek	1.6 ± 0.1	7.4 ± 2	3.6 ± 0.4	5.1 ± 2	4.5 ± 0.6	6 ± 2
Duffy Creek	1.4 ± 0.1	3.2 ± 1	2.8 ± 0.7	4 ± 2	3.6 ± 1.1	4 ± 2

Table 3.3: **Strain analysis results, mean strain ratio (R_s) and orientation of the strain ellipse (ϕ), for three different grain sizes, the recrystallized grains (< 60 μm), the non-recrystallized grains (> 60 μm) and larger grains (> 100 μm).**

Section	M	s_b	R	K	W_m
A	23.8	36.1	0.20	0.42	0.71 ± 0.18
B	20.7	33.6	0.31	0.66	0.64 ± 0.20
C	18.6	31.5	0.40	0.87	0.59 ± 0.17
E	23.2	32.9	0.34	0.70	0.70 ± 0.19
Indian Creek	15.6	30.2	0.44	0.99	0.52 ± 0.12
Duffy Creek	7.3	26.4	0.57	1.39	0.25 ± 0.11

Table 3.4: **Vorticity analysis results, mean vector orientation (M), circular standard deviation (s_b), magnitude of the vector mean (R), strength of the vector mean (vectorial data concentration K) and mean vorticity number (W_m) with a 2 σ standard deviation error.**

Section	Elevation (m)	Sample	Average Spacing (μm)	Error (2σ)	Flow Stress (MPa)
A	37	RR09-158	9.6	1.7	26.5
	29	RR09-157	9.5	1.4	27.0
	13	RR09-153	8.3	1.7	36.4
	10	RR09-152	8.8	1.9	31.7
	2	RR09-151	8.6	2.1	33.8
C	56	RR09-104	6.9	1.4	53.1
	52	RR09-103	8.2	1.6	37.1
	46	RR09-102	7.0	1.4	51.9
	39	RR09-100	8.3	1.4	36.4
	22	RR09-98	9.8	2.9	25.3
	15	RR09-97	10.5	3.8	21.7
	13	RR09-96	9.8	2.2	25.0
	12	RR09-95	10.9	2.5	19.6
	10	RR09-94	9.6	1.9	27.3
	8	RR09-93	10.5	1.5	21.7
	6	RR09-92	9.2	1.4	29.1
	2	RR09-90	11.3	3.1	18.6
E	56	RR09-137	7.2	0.9	49.3
	48	RR09-135	6.6	1.0	60.5
	44	RR09-134	8.0	0.9	39.1
	39	RR09-133	6.4	1.1	63.1
	34	RR09-132	8.1	1.6	38.1
	29	RR09-131	7.4	1.2	46.4
	24	RR09-130	7.5	1.3	44.8
	20	RR09-129	8	1.2	39.1
	18	RR09-128	8.8	2	32.1
	16	RR09-127	8.6	1.5	33.5
	16	RR09-126	9.1	2.5	30.0
	15	RR09-125	10.2	1.6	23.0
	14	RR09-124	8.2	2.0	37.4
	12	RR09-123	9.9	1.3	24.9
	6	RR09-121	14.9	2.1	10.0
Duffy Creek	18	RR10-35	8.8	1.1	32.2
	15	RR10-34	7.4	1.9	46.5
	13	RR10-32	11.4	2.1	18.1

Table 3.5: **Deformation lamellae spacing (μm) with a 2 σ error and flow stress estimates (MPa) based on the Koch and Christie (1981) calibration.**

Chapter 4

EFFECT OF PERMEABILITY VARIATIONS ON FLUID FLOW AND FLUID-ROCK EXCHANGE DURING EXTENSIONAL TECTONICS, RAFT RIVER DETACHMENT SHEAR ZONE, UTAH

Combined geochronological and stable isotope data of quartzite mylonite from the footwall of the Raft River detachment shear zone (NW Utah, USA) reveal that ductile deformation, and infiltration of meteoric fluids in the detachment shear zone,

occurred between 26 and 20 Ma. $^{40}Ar/^{39}Ar$ release spectra are complex, but plateau ages decrease systematically from 31.1 $\pm$ 0.8 Ma at the top to 20.2 $\pm$ 0.6 Ma at the bottom of quartzite mylonite. Throughout the studied area, hydrogen stable isotope values of syn-kinematic muscovite are low, ranging from -123 ‰ to -88 ‰ suggesting that meteoric fluids were infiltrating the detachment shear zone over the time scale of mylonite formation. Hydrogen stable isotope analyses from both muscovite and fluid inclusions show that the fluid infiltrating the detachment shear zone was meteoric in origin, with a low D/H and low $^{18}O/^{16}O$ composition. Quartz and muscovite oxygen isotope analyses show different degree of oxygen isotope depletion, suggesting different time-integrated interaction of the minerals with meteoric fluid; these fluids would be channelized in preferential layers or shear zones within the deforming system. The variability in oxygen stable isotope of both quartz and muscovite can be explained by variations in permeability in the basement units (confined versus diffuse flow), and strain variations along the transport direction of detachment shear zone (from flattening to constriction), resulting in different fluid-rock exchange patterns.

4.1 Introduction

The presence of fluids during active deformation has a profound impact on the rheology of the crust (e. g. Kohlstedt et al., 1995; Ranalli, 1997; Bürgman and Dresen, 2008). Actively migrating fluids influence heat and mass transport, facilitate melting and mechanical deformation, and are hence an important control on the thermomechanical evolution of the crust. Therefore, constraining the hydrology and the permeability structure of tectonically active areas is critical to understand the rheology of deformational processes.

During extension that accompanies orogenic collapse, the cool brittle upper

crust is separated from the hot lower crust by a detachment zone, that localizes deformation, fluid flow, and thermal exchange, eventually leading to the formation of metamorphic core complexes (MCC) (Brun et al., 1994; Rey et al., 2001; Huismans et al., 2005; Teyssier et al., 2005, Tirel et al., 2004, 2008; Gessner et al., 2007; Rey et al., 2009, 2010; Huet et al., 2011, Wijns et al., 2005). Extensive brittle faulting in the upper crust leads to significant increase in permeability and porosity, thus enhancing the circulation of fluids at the crustal scale. Based on oxygen and hydrogen stable isotope analyses, the presence of surface-derived fluids during mylonitization has been revealed from different MCC's and extensional detachments including the Thor-Odin dome (Holk et al., 1997, 2000; Mulch et al., 2004, 2006), Kettle dome (Mulch et al. 2007), the Bitterroot MCC (Kerrish et al., 1986; Quilichini, 2012), the Raft River Mountains (Gottardi et al., 2011), the Ruby Mountains (Fricke et al, 1992), the Snake Range (Gébelin et al., 2011), the Whipple Mountains (Morrison and Anderson, 1998; Gébelin et al. 2012), and the Simplon detachment in the Central European Alps (Campani et al. 2012).

Here, we combine $^{40}Ar/^{39}Ar$ geochronology, and oxygen and hydrogen isotope geochemistry from a quartzite mylonite of the Miocene Raft River detachment shear zone (Utah) to evaluate the permeability of the shear zone and constrain the extent and duration of fluid flow during extensional tectonics. The combined data show that an extensive hydrological system draining low D/H and low $^{18}O/^{16}O$ meteoric fluids was active during the evolution of the shear zone in Miocene times. Muscovite $^{40}Ar/^{39}Ar$ ages decreasing systematically with depth in the detachment, combined with hydrogen stable isotope ratios suggest that meteoric fluids were infiltrating the detachment shear zone over the time scale of mylonite formation. Quartz and muscovite oxygen isotope analyses show different degrees of ^{18}O depletion, that we explain by different time-integrated interaction of synkinematic minerals with meteoric fluid, variation in permeability in the basement units (con-

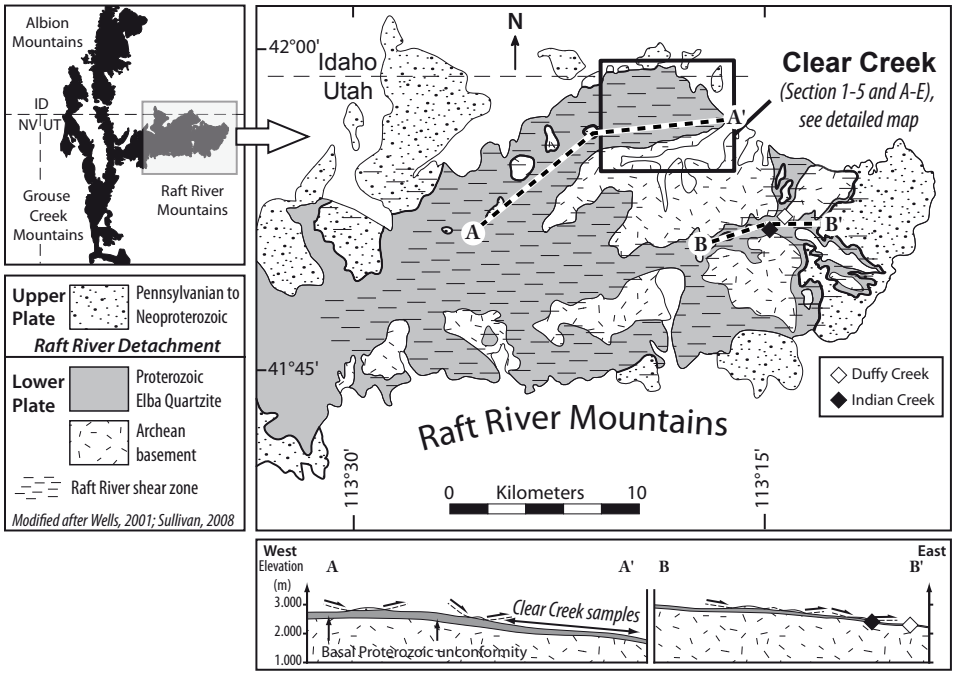

Figure 4.1: **Map of the Raft River metamorphic core complex.**

fined versus diffuse flow), and strain variations from flattening (planes) to constriction (pipes) along the transport direction of the detachment shear zone.

4.2 Geologic setting

The Raft River Mountains form the eastern limb of the Albion-Raft River-Grouse Creek metamorphic core complex in NW Utah and expose amphibolite- to greenschist-facies Archean to Permian rocks (Fig. 4.1). These rocks experienced alternating crustal thickening and thinning during the Sevier orogeny (Wells, 1997; Wells et al., 1998; Hoisch et al., 2002; Harris et al., 2007), followed by episodes of extension on the west-rooted Eocene to early Oligocene Middle Mountain shear zone (Compton, 1983; Saltzer and Hodges, 1988; Wells, 1997; Wells et al. 2000), that

was accompanied by a long-lived period of magmatism, attested by the intrusion of the 32 Ma Middle Mountain gneiss (Strickland et al, 2011), 30 Ma Almo pluton (Strickland et al, 2011), 29 to 28 Ma Vipont pluton (Strickland et al, 2011), 25 Ma Red Butte pluton (Compton et al., 1977; Egger et al., 2003).

The east-rooted Raft River detachment (Malavieille, 1987; Wells et al., 2000; Wells, 2001) studied here shows muscovite $^{40}Ar/^{39}Ar$ ages as young as 15 Ma. Apatite fission-track ages record an episode of protracted, progressive east-directed unroofing along the detachment fault between 13.6 and 7.4 Ma (Wells et al., 2000). This study focuses on the Miocene detachment zone exposed at Clear Creek (Fig. 4.1 and 4.2), which has incised a continuous section through the detachment (Compton, 1975; Wells, 2001; Sullivan, 2008).

The Green Creek Complex (Armstrong and Hills, 1967; Armstrong, 1968) is the lowest unit in the detachment zone and consists of ca. 2.55 Ga gneissic monzogranite (metamorphosed adamellite of Compton, 1972) that intrudes metatrondhjemite, metagabbro, and hornblende-biotite schist (Armstrong, 1968; Compton et al., 1977; Todd, 1980; Miller, 1980). The Clear Creek canyon cuts across the transition between relatively undeformed Archean adamellite, that underlies most of the Raft River shear zone in the central part of the Raft River Mountains, and the more intensely deformed schist units (hornblend schist and biotite schist) intruded by trondhjemite and gabbros (Compton, 1980, Sullivan, 2008) that underlies the Eastern part of the Raft River shear zone (Fig. 4.2). These basement units are separated from the overlying Elba Quartzite by a conspicuous schist unit that has been interpreted as a metamorphosed paleosol/regolith (Armstrong, 1968) or a metamorphosed basement-derived arkose (Compton, 1975). The overlying Elba quartzite and schist (Wells et al., 1998; Sullivan, 2008) display a distinct stratigraphy that includes, from bottom to top, a basal quartzite-cobble metaconglomerate, an alternating sequence of white quartzite and muscovite-quartzite schist, a very dis-

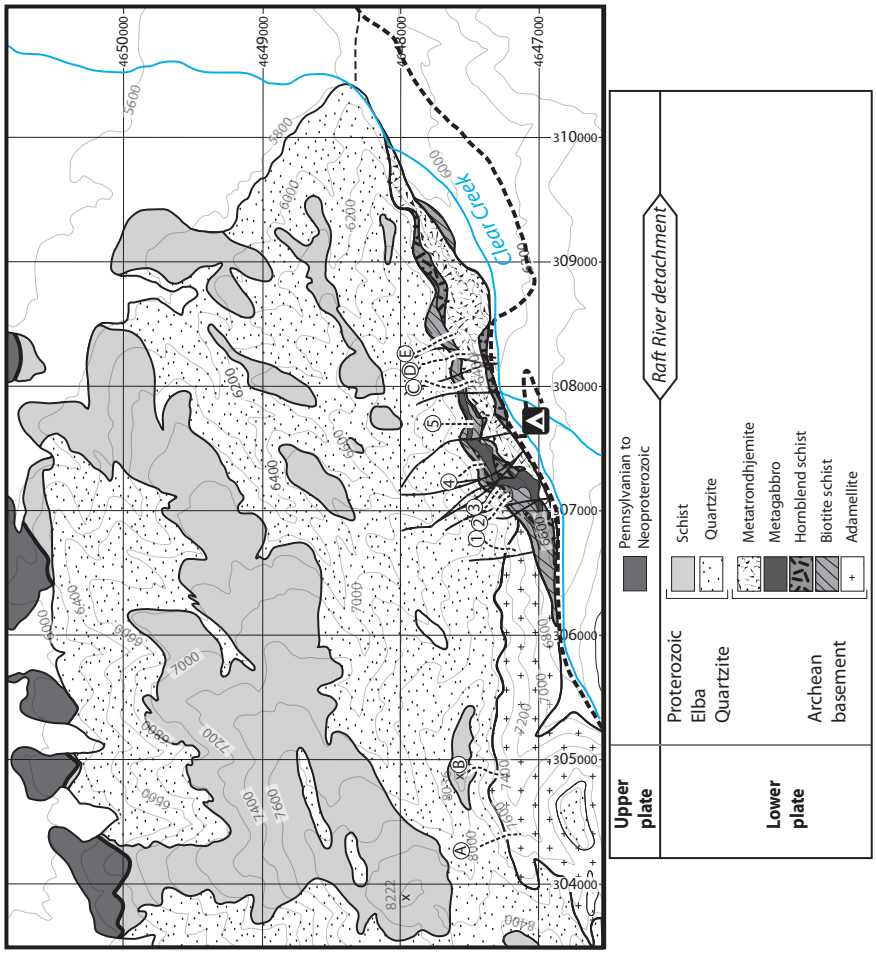

Figure 4.2: **Detailed map of the study area, the Clear Creek canyon.**

tinctive layer of red quartzite, and a sequence of alternating feldspar-rich quartzite, quartzite, and pebble-gravel metaconglomerate, which we refer to as microconglomerate. In the first 15 m above the contact between the basement and the Elba quartzite, the quartzite is interlayered with centimeter- to meter-thick muscovite-rich schist that makes a distinctive "notch" in the quartzite cliff, approximately 15 m above the contact. The base of this physiographic notch is characterized by an abrupt transition from typical cliff-forming Elba quartzite to a zone where muscovite makes up 80-100% of the friable rock. Paleozoic metasedimentary rocks are preserved as a few scattered klippen above the quartzite and schist and define the hanging wall of the Miocene Raft River detachment (Compton, 1975, Wells, 1997, 2001, 2009; Wells et al., 1998).

4.3 Microstructures

4.3.1 Quartz microfabrics

Throughout the Clear Creek area foliation and lineation are strongly developed and constant in orientation and are defined by flattened and elongated quartz and muscovite grains (Compton, 1980; Wells, 1997; Sullivan 2008). We sampled 11 profiles across the sub-horizontal foliation and along the East-West Clear Creek canyon that parallels the lineation from West to East, from the Archean basement to the uppermost quartzite and microconglomerate.

The Elba quartzite is strongly deformed and shows two populations of quartz grains (Fig. 4.3). The first population of coarse elongated (>500 μm long) grains defines the macroscopic fabric and exhibits strong undulose extinction, deformation bands, and deformation lamellae, indicating that quartz deformed under high flow stress conditions (Hirth and Tullis, 1992). The second population consists

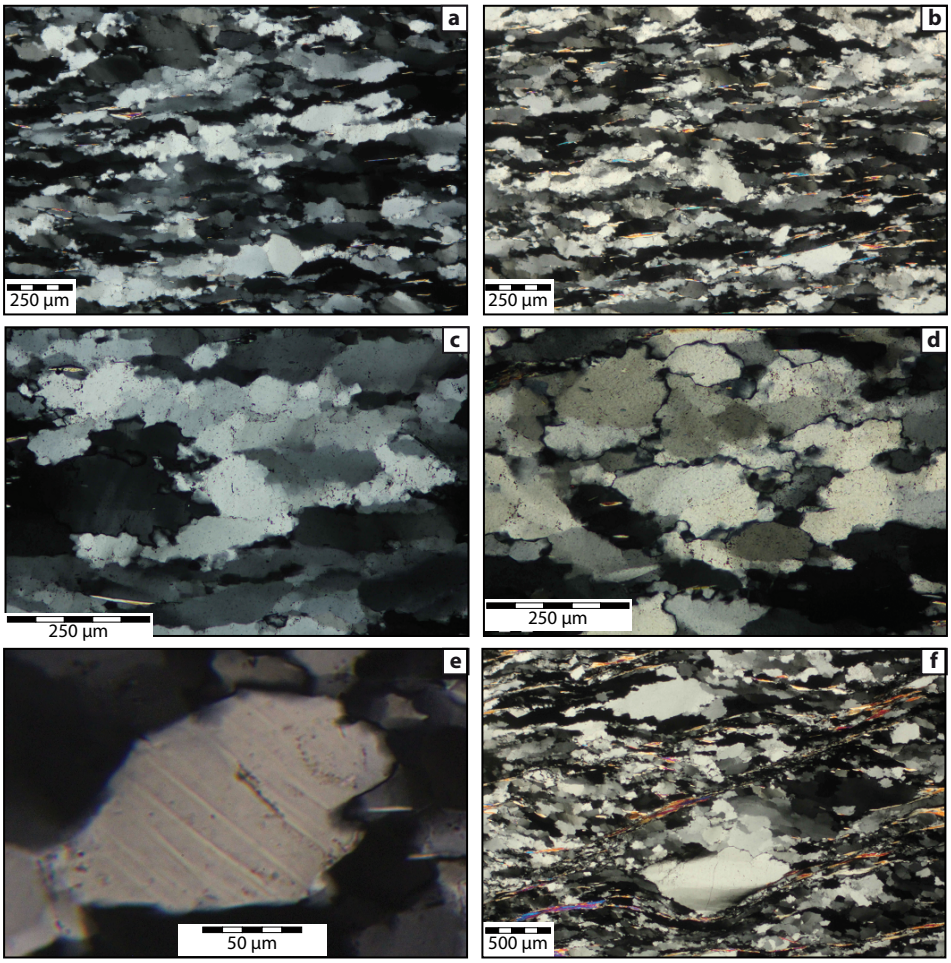

Figure 4.3: **Quartz microstructures. (a) and (b), typical quartz microstructures from the Raft River shear zone; (c) and (d) close-up of the microstructures, showing that the main recrystallization process is subgrain rotation; (e) deformation lamellae are quite common; (f) shear bands are locally present. All pictures are oriented top-to-the East.**

of finer recrystallized grains (20 - 100 μm) that occupy the boundaries of coarser grains. Recrystallized grains are commonly equant to slightly elongate and have a direct relation to subgrains present in large grains, suggesting that the dominant process of recrystallization was subgrain rotation, where recovery is accommodated by dislocation climb (Regime II of Hirth and Tullis, 1992). Recrystallized grains locally form a low angle oblique secondary foliation at 30-35° to the macroscopic foliation, indicating top-to-east sense of shear. This sense of shear deduced microscopically is consistent with macroscopic kinematic criteria such as extensional shear bands, drag folds, S-C fabrics, and the sigmoidal shapes of pebble-size grains, indicating a top-to-east sense of shear irrespective of position within the Miocene Raft River detachment shear zone.

In the easternmost sampled localities (Indian and Duffy Creek), where the quartzite mylonite is strongly attenuated (about 15 m thick), there is a sharper contrast between the two grain size populations, and a larger area (up to ~50%) of the thin section is occupied by recrystallized grains (Fig. 4.3). The large relic grains are very elongate (>2000 μm) with high aspect ratios (X/Z), forming single grain ribbons that are typically asymmetric and indicate top-to-east sense of shear. These large grains have their basal planes nearly parallel to the foliation. The recrystallized grains are more equant than in the western transects, and triple junctions are observed at the grain boundaries.

The quartz crystallographic preferred orientation has been analyzed by electron backscattered diffraction analysis (EBSD) on six samples from Section 1 and nine samples from Section 5. All analyzed samples display a strong crystallographic fabric indicating that the rocks deformed in the dislocation creep regime. Quartz c-axis fabrics display a Type-I cross-girdle (Lister, 1977), with maxima indicating dominant prism-a, rhomb-a, and basal-a slip systems. The c-axis cross-girdle is highly symmetrical, suggesting a strong coaxial component of deformation during

fabric development, which was also documented by Compton (1980), Wells (2001) and Sullivan (2008). These observations are consistent with Sullivan's (2008) who also noted an increase in the coaxial component of flow downward through the quartzite layer.

4.3.2 Fluid inclusions

Fluid inclusions are very common throughout the detachment shear zone in quartz of the Elba quartzite, They either form fluid inclusion planes in larger relict grains (Fig. 4.4a, b) or are distributed along grain and subgrain boundaries (Fig. 4.4c). Fluid inclusion planes are interpreted to have been fluid-filled microfractures that subsequently healed (cf. Roeders, 1984; Samson et al., 2003). The samples close to the "notch" level show large amounts of fluid inclusion planes (Fig. 4.4a, b) that are closely spaced (~25 μm) and spatially related to zones of microveining. In some cases, fluid inclusion planes cross several adjacent relict grains (Fig. 4.4a, b, d), and most inclusion planes within individual quartz grains are not obviously aligned. Fluid inclusion planes usually do not cross subgrain boundaries within recrystallized grains. Intergranular fluid inclusions are very common at the boundary between adjacent quartz grains (Fig. 4.4c). Deformation lamellae are also commonly decorated with fluid inclusions (Fig. 4.4e, f)

4.3.3 Muscovite microstructure

Mylonitic Elba Quartzite contains, in general, ~5 to 10 % muscovite. Muscovite grains are typically 50 to 200 μm long and a few tens of microns thick, and occur as grains along quartz grain boundaries (Fig. 4.5a, b). Muscovite grains rarely form fish and are instead concentrated in bundles or layers that are 10 to 50 μm thick and up to 1 cm long and define the foliation. Depending on bulk mica content

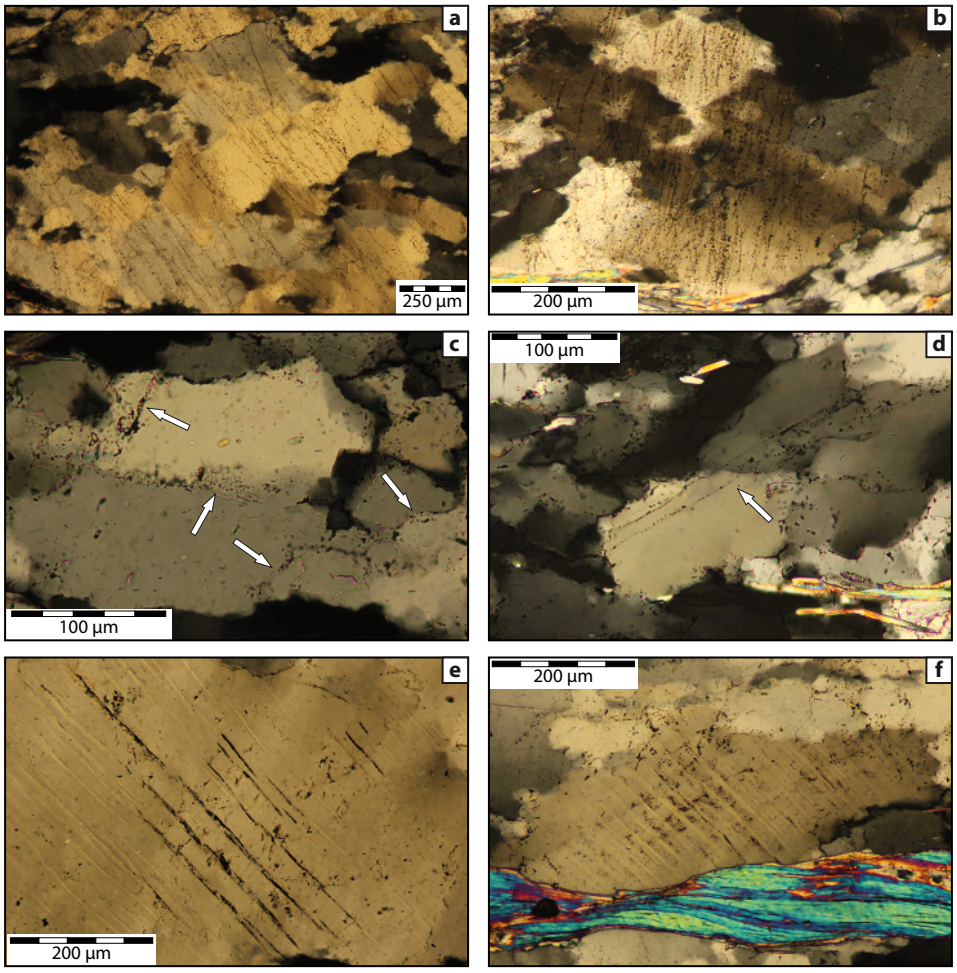

Figure 4.4: **Fluid inclusions microstructures. (a) and (b), quartzite rich in fluid inclusions that form subparallel planes, from a sample very close to the "notch" area; (c) intergranular fluids inclusions, located at grain and subgrains boundaries; (d) fluid inclusion trail cross-cutting several grains; (e) and (f) fluid inclusions associated with deformation lamellae. All pictures are oriented top-to-the East. All pictures are oriented top-to-the East.**

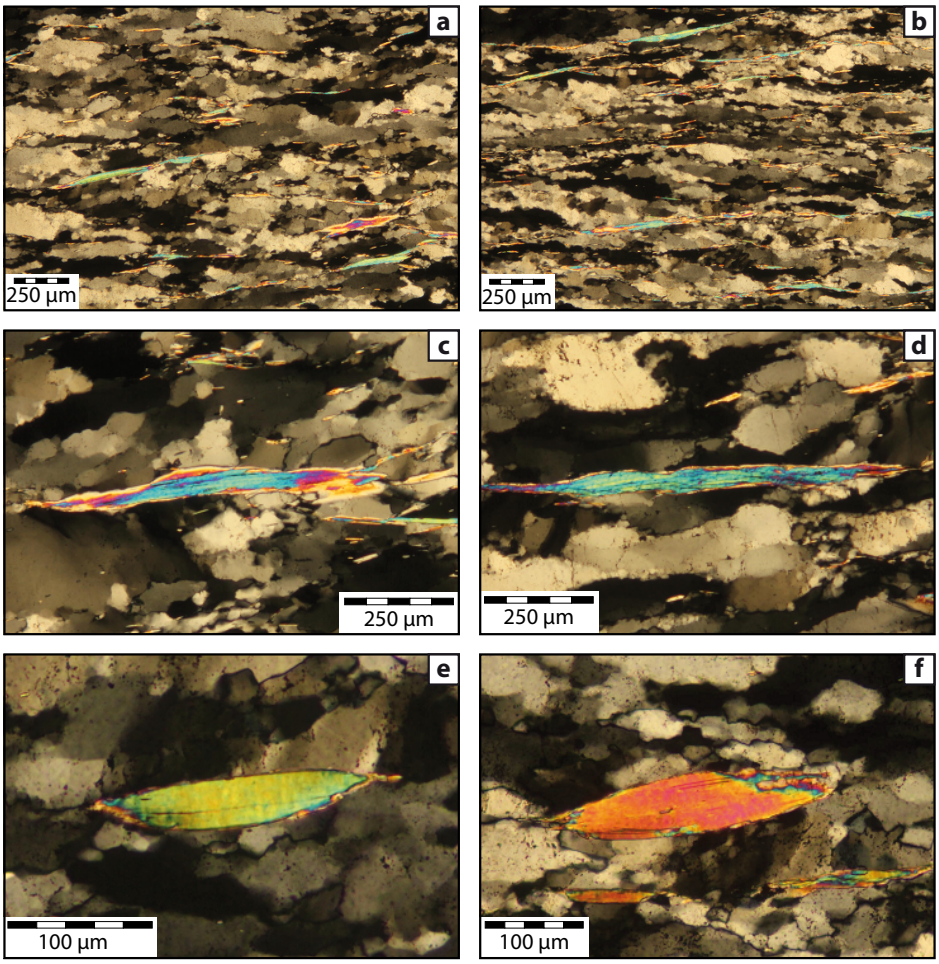

Figure 4.5: **Mica microstructures. (a) and (b) the Elba quartzite contains ~5 to 10 % of muscovite; (c) and (d) mica with high aspect ratio and inverted stair stepping; (e) and (f) rare mica fish. All pictures are oriented top-to-the East.**

these layers are more or less continuous and are, on average, 500 μm to 1 mm apart. According to the morphological grouping of mica fish mica grains in the Raft River shear zone belong to Group 6 (ten Grotenhuis et al., 2003) with high aspect ratio and inverted stair stepping (Fig. 4.5c, d); the rare mica fish that are present are commonly small (30 to 75 μm long, 25 μm thick, Fig. 4.5e, f) and would belong to Group 2 of that same classification.

Muscovite grains define the mylonitic fabric in the detachment, and microstructural evidence suggests that mica recrystallized during deformation. The preferred recrystallization process for mica is dissolution-reprecipitation (e.g. Elliott, 1973; Rutter, 1983), which is likely to reset argon content and equilibrate the oxygen and hydrogen isotopes of mica with that of the fluid at elevated temperature (e.g., Mulch et al., 2005, 2006). Therefore, during dynamic recrystallization of quartz and muscovite in the Miocene Raft River detachment, muscovite likely recorded the isotopic composition of the fluid from which it grew and exchanged isotopically (oxygen and hydrogen) with quartz (Mulch et al., 2006, 2007; Wells et al., 2000) during deformation.

4.4 ^{40}Ar/^{39}Ar geochronology

We analyzed four muscovite separates from Section C (Fig. 4.2), distributed over the ~100 m thick quartzite mylonite by furnace step heating ^{40}Ar/^{39}Ar geochronology (analytical procedures in Appendix 1; Table 1). The four muscovite separates (> 125 μm) show complex age spectra (Fig. 4.6), with a decrease in apparent age during the first gas release steps (0 to 5%) followed by a monotonous rise and a "saddle" shaped release spectrum at higher temperatures. Plateau ages for these samples were calculated for the flattest part of multiple contiguous steps including > 50% of total ^{39}Ar released in at least five successive steps. From bottom to top,

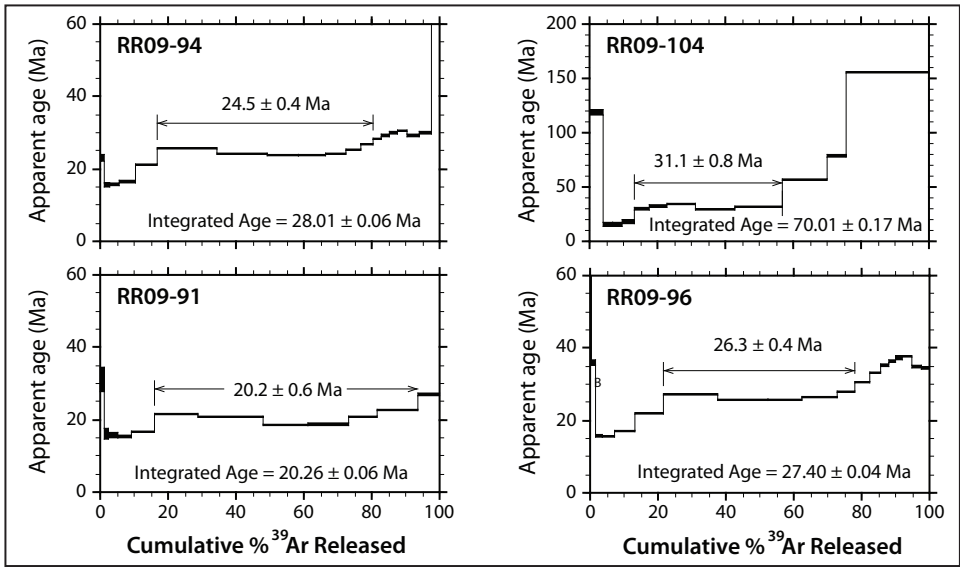

Figure 4.6: **^{40}Ar/^{39}Ar spectra.**

the apparent ^{40}Ar/^{39}Ar ages of muscovite grains are: 20.2 $\pm$ 0.6 Ma (RR09-91; at 8 m above the basement), 24.5 $\pm$ 0.4 Ma (RR09-94; 15 m), 26.3 $\pm$ 0.4 Ma (RR09-96; 22 m), and 31.1 $\pm$ 0.8 Ma (RR09-104; 70 m). These plateau ages correspond to total integrated ages of 20.26 $\pm$ 0.06 Ma, 28.01 $\pm$ 0.06 Ma, 27.40 $\pm$ 0.04 Ma, and 70.01 $\pm$ 0.17 Ma, respectively. The ^{40}Ar/^{39}Ar spectra from the three lowest samples, collected below the "notch" become progressively flat toward the contact with the basement.

4.5 Stable isotope geochemistry

Oxygen isotope ratios (δ^{18}O) of mineral separates from Sections 1, 3, 4, 5 and C were analyzed at the University of Lausanne (Switzerland) and mineral separates from Section E were analyzed at the University of Wisconsin, Madison. The hydrogen (δD) isotopic ratios were determined at the University of Lausanne

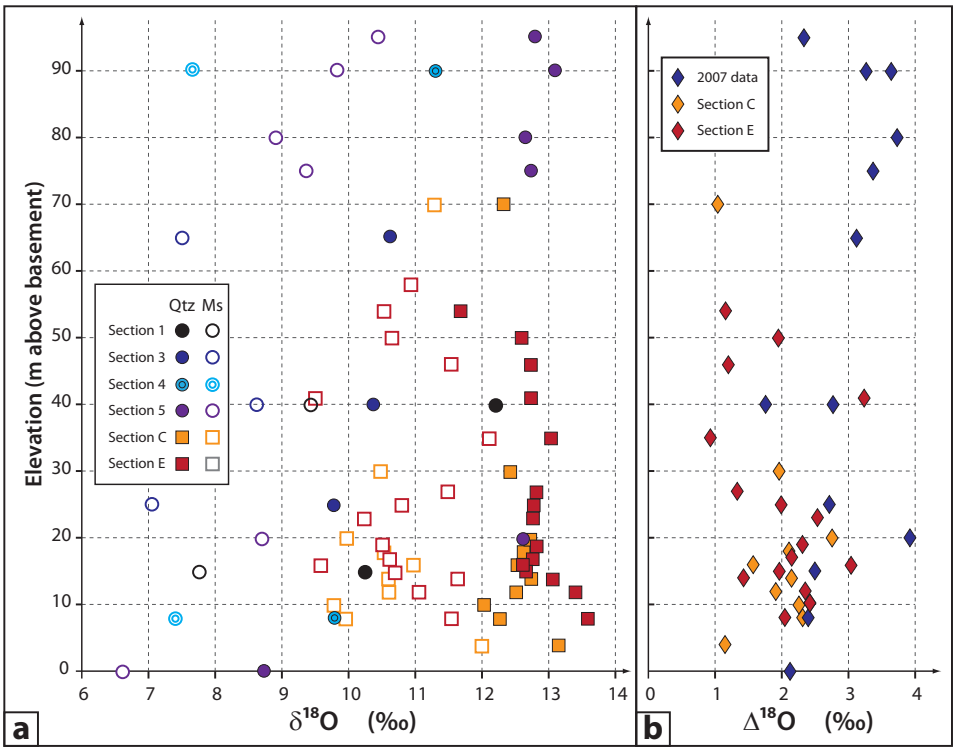

Figure 4.7: **(a) oxygen stable isotope data of quartz ($\delta^{18}O_{qtz}$) and muscovite ($\delta^{18}O_{ms}$) and (b) fractionation coefficient ($\Delta^{18}O_{qtz-ms}$) reported as a function of elevation (m above basement).**

(Switzerland) and the University of Hannover (Germany). Analytical facilities and procedures are described in Appendix 2; this section focuses on the analytical results.

4.5.1 Oxygen stable isotopes

New oxygen stable isotope analyses (Table 4.6, Fig. 4.7) are complementing the data of Gottardi et al. (2011), which are also included and integrated here. Quartz $\delta^{18}O$ values from Sections 1 to 5 are variable, from 9.8 ‰ at the base of Section 4 (RR07-57) to 13.1 ‰ at the top of Section 5 (RR07-98) (Fig. 4.7a). The muscovite

$\delta^{18}O$ values range from 7.1 ‰ (RR07-71, base of section 3) to 10.5 ‰ (RR07-99, top of Section 5) (Fig. 4.7a). The lowest $\delta^{18}O$ value for both quartz (8.7 ‰) and muscovite (6.6 ‰) are obtained from a quartz vein that lies at the base of the section, at the contact between the basement and the Elba quartzite (RR07-87, base of Section 5). Sections C and E, collected east of Sections 1 to 5, display a much more uniform oxygen stable isotope composition, with values ranging from 11.7 ‰ to 13.6 ‰ for quartz, and 9.5 ‰ to 12.2 ‰ for muscovite (Table 4.6, Fig. 4.7).

On average, in the eastern Sections C and E, quartz $\delta^{18}O$ values are higher (average $\delta^{18}O$ = 12.2 ‰) and fall within a narrow range (11.7 ‰ < $\delta^{18}O$ < 13.6 ‰), whereas $\delta^{18}O$ data from the western Sections 1 to 5 display considerably more scatter (average $\delta^{18}O$ = 11.4 ‰, 8.7 ‰ < $\delta^{18}O$ < 13.1 ‰) and are systematically shifted to lower $\delta^{18}O$ values (Table 4.6, Fig. 4.7). The increase in $\delta^{18}O$ eastward occurs along the same quartzite layers and is unlikely reflecting on original variation in lithologic isotopic compositions.

$\delta^{18}O$ values of the basal metaconglomerate were investigated at a millimeter scale. The metaconglomerate is composed of a quartz matrix, relatively rich in muscovite (~20%) and typically pure quartzite clasts. The microstructures of the matrix and the pebbles are similar and dominated by subgrain rotation recrystallization. 1 mm thick sections of two samples collected at the bottom of Section 1 were cut into, ~1 mm^3 cubes, allowing micro-sampling of both the quartz matrix and the quartz pebbles (Fig. 4.8). Forty-four micro-samples were selected for oxygen stable isotope analysis. $\delta^{18}O$ values fall within a very narrow range of 11.0 to 11.2 ‰ (Fig. 4.8) within the pebbles and 10.8 to 11.2 ‰ in the matrix demonstrating complete oxygen isotope homogenization within the basal metaconglomerate.

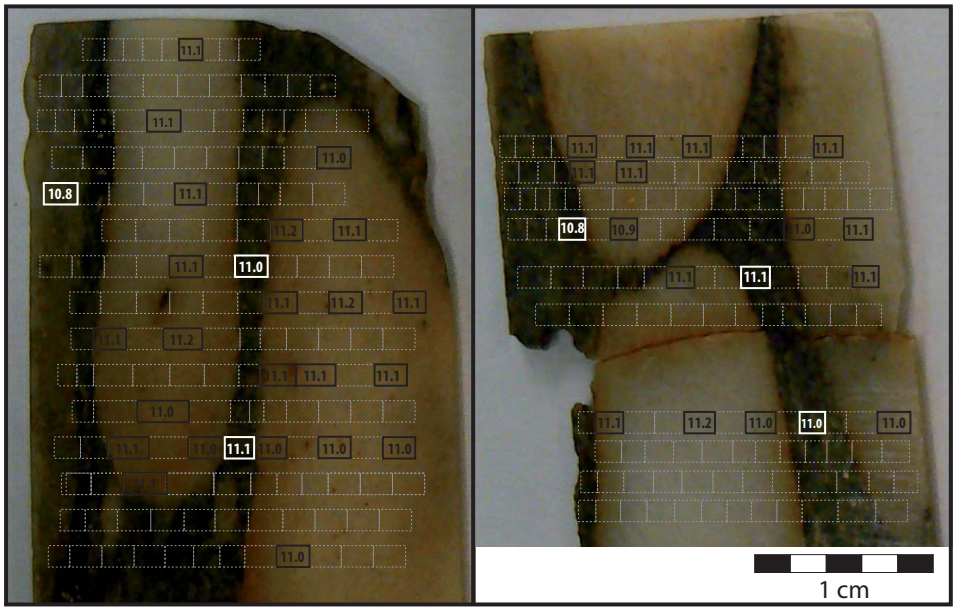

Figure 4.8: **Oxygen stable isotope data from the basal metaconglomerate. Two samples were cut into 1 mm^3 cubes and analyzed; results are shown according to their position on the sample. White and black fonts are used for the δ^{18}O of the matrix and the pebbles respectively.**

4.5.2 Hydrogen stable isotopes

We present two different sets of hydrogen isotope measurements: (a) δD values of muscovite (δD_{ms}) (Table 4.7, Fig. 4.9), and (b) δD values of fluid inclusions in quartz (δD_{FI}) from 6 different quartz veins and 4 different mylonitic quartzite samples distributed from the basement/cover contact to the top of the shear zone section (Table 4.7, Fig. 4.9).

Muscovite hydrogen isotope compositions were analyzed in 64 samples of mylonitic Elba quartzite collected from 7 different vertical profiles, spreading from West to East (Fig. 4.2 and 4.9) over ~100 m of Raft River detachment shear zone. Muscovite shows δD values ranging from -123 ‰ to -88 ‰ (± 4 ‰; all values with

respect to SMOW) (Table 4.7, Fig. 4.9). The same range of δD values is observed within single profiles, with no particular vertical trend. However, the spread in δD values seems to be larger in the first 15 m above the contact between the basement and the Elba quartzite where both the lowest and highest δD values are reached (-124 ‰ to -88 ‰). Higher in the quartzite mylonite section (top 50m), the δD values are less variable and average around ~-110 ‰(Table 4.7, Fig. 4.9).

Using the calibration of Suzuoki and Epstein (1976), we can calculate the hydrogen isotopic composition of the fluid (δD_w) during recrystallization and hydrogen isotope exchange, based on an equilibrium temperature and the hydrogen isotopic composition for muscovite. Using a temperature of 450°C as representative for deformation at the base of the section (Gottardi et al., 2011), a mica composition of δD_{ms} = -120 ‰ yields a fluid composition δD_w = -99 ‰ that is typical of meteoric fluids, while for the same temperature, a mica with δD_{ms} = -95 ‰ yields a δD_w = -74 ‰.

δD values of quartz fluid inclusions (δD_{FI}) analyzed in four quartzite samples over the entire section display a narrow range between -84 ‰ and -94 ‰, and do not show any systematic variation with respect to vertical position in the section (Table 4.7, Fig. 4.9). Analyses of fluid inclusions from six foliation-parallel quartz veins yield δD values ranging from -83 ‰ to -104 ‰, with two low-δD samples (RR07-67 at δD_{FI} = -103 ‰; and RR07-42 at δD_{FI} = -104 ‰). Fluid inclusions in both quartz veins and quartzite mylonite have similar δD values. Assuming that the measured values are representative of δD_w present during deformation and recrystallization, these values are in good agreement with those calculated from the most negative δD_{ms} values.

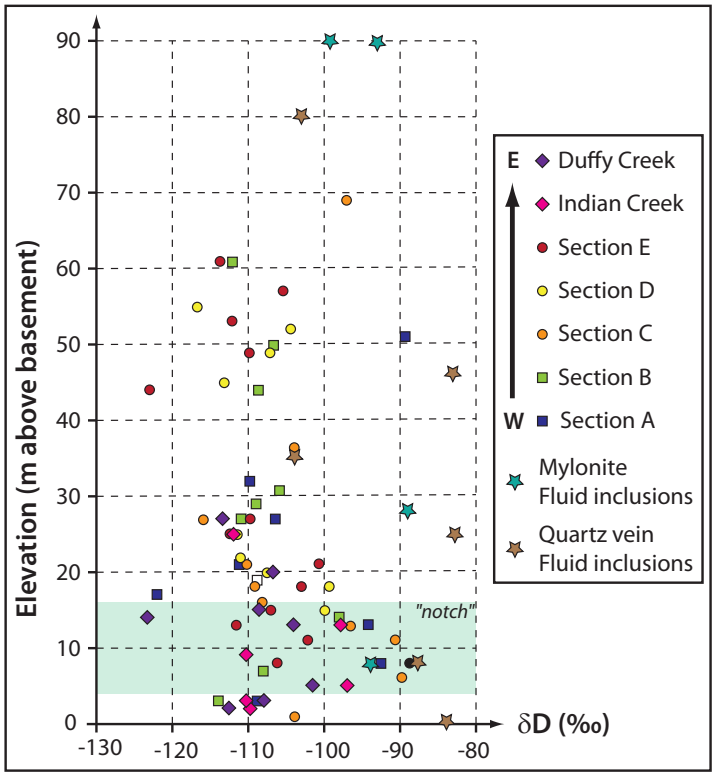

Figure 4.9: **δD vs. elevation, from both muscovite and fluid inclusions. Very variable δD values are obtained from the "notch" area.**

4.6 Discussion

The partitioning of oxygen and hydrogen stable isotopes in minerals and waters has been used for decades to elucidate fluid-rock interaction (e.g. Valley, 1986) at various timescales and different geological settings including intrusions and fault zones, thrust faults (Burkhard and Kerrish, 1988, Rye and Bradbury, 1988; Banks et al., 1991; Moore and Vrolijk, 1992; Sibson, 1994, 1998; Crespo-Blanc et al., 1995; Goddard and Evans, 1995, McCaig et al., 1995; Ghisetti et al., 2001; Kirschner and Kennedy, 2001), strike-slip faults (O'Neil and Hanks, 1980; Unruh

et al., 1992, Chester et al., 1993; Barton et al., 1995; Sibson, 1998, Kharaka et al., 1999; Pili et al., 2002), and extensional detachment systems (e.g. Bowman and Willett, 1991; Bowman et al., 1994; Gerdes et al., 1998; Cook et al., 1997; Mulch et al., 2004, 2007; Gébelin et al., 2011, 2012; Campani et al. 2012). However, the mechanisms of fluid transport and mineral-water isotope exchange at the transition between brittle and ductile deformation regimes in the crust are still poorly understood, because the critical conditions under which oxygen isotope exchange occurs between a mineral and an intragranular fluid is controlled by a number of factors including oxygen diffusivity, temperature, grain size, and deformation. Several stable isotope studies have shown that meteoric water can circulate to significant depths (down to the ductile crust) in normal fault systems (e.g. Wickham and Taylor, 1987; Fricke et al., 1992; Morrison, 1994; Morrison and Anderson, 1998; Bebout et al., 2001; Mulch et al., 2004, 2006, 2007; Person et al., 2007; Gébelin et al., 2011; Gottardi et al., 2011). In the following we will use the geochronological and geochemical results presented here to assess the extent and duration of fluid rock exchange, investigate the permeability and hydrology of the Raft River detachment shear zone at Clear Creek, and evaluate the role of crustal scale fluid flow during large-scale extensional tectonics.

4.6.1 Interpretation of $^{40}Ar/^{39}Ar$ data

Using a cooling rate of 10°C/Ma for the Raft River shear zone (Wells et al. 2000) closure to argon diffusion in muscovite at grain sizes similar to the ones considered here occurs at temperatures of 420°C or higher (Harrison et al. 2009). Such temperatures are within the range of temperatures of mylonitization estimated for the Raft River shear zone (Gottardi et al., 2011).

The argon release spectra show different asymptotes and limits, with a general

saddle shape. Such saddle shapes obtained from step heating experiments may be due to excess argon (McDougall and Harrison, 1999) and the older ages at the ends of the spectra might be due to the presence of more retentive domains (Baldwin and Lister, 1998). Forster and Lister (2004) also pointed out that during deformation and metamorphism of white micas, new microstructures can separate distinct classes of argon gas reservoirs that can be released separately during step-heating analyses, and can result in "mixing" of such reservoirs (Forster and Lister, 2004).

Even though all $^{40}Ar/^{39}Ar$ spectra are complex, they share very similar characteristics: they have a general saddle shape, the age released during the first heating step tend to be older than the plateau part of the spectrum, and the spectra tend to flatten into a plateau shape closer to the contact with the basement. In addition, plateau ages become younger with depth below the hanging wall. Similar observations have been made on white micas from the Snake Range by Lee and Sutter (1991) and Gébelin et al. (2011). Such systematic decrease in age with structural depth in the $^{40}Ar/^{39}Ar$ spectra may be the result of ductile deformation and increased mica recrystallization within the detachment shear zone (Gébelin et al. 2011) or reflect the response of the mylonite to strain hardening by progressive relocation and migration of the deformation front toward deeper levels of the shear zone (Mulch et al., 2006). However, in the latter case, all release spectra were perfect plateaus indicative of grain-scale $^{40}Ar/^{39}Ar$ homogeneity.

Throughout the Raft River detachment shear zone at Clear Creek, (1) muscovite is recrystallized and quartz - muscovite microstructures define the very strong Miocene lineation and foliation; (2) $^{40}Ar/^{39}Ar$ geochronology yields Miocene muscovite ages that decrease systematically with depth in the detachment; (3) Muscovite hydrogen stable isotope ratios as low as -123 ‰ require the presence of meteoric fluids during deformation in the detachment shear zone; and (4) quartz

and muscovite oxygen isotope analyses show different degree of ^{18}O depletion, suggesting that quartz and muscovite interacted with low D/H and low $^{18}O/^{16}O$ meteoric fluids. Based on those microstructural and isotopic evidences, we interpret the $^{40}Ar/^{39}Ar$ ages from muscovite grains from the Raft River detachment zone to reflect the timing of muscovite recrystallization. Therefore, the hydrogen and argon data are likely recording the fluid composition, the timing, and duration of fluid-rock isotopic exchange during exhumation of the Raft River detachment shear zone.

4.6.2 Eocene or Miocene signal?

Geochronological work by Wells et al. (2000) show that significant Eocene tectonics affected the area prior to Miocene. Extension along the top-to-the-west/northwest Middle Mountain shear zone initiated in middle Eocene time, followed in late Oligocene to early Miocene by motion along the top-to-the-east Raft River detachment (Wells et al., 2000). Although the timing of deformation along these oppositely rooted shear zones may have overlapped late in the movement history of the Middle Mountain shear zone and early in the movement history of the Raft River detachment, much of the extensional exhumation along these shear zones was temporally distinct (Wells et al., 2000). North of the Snake River plain, several metamorphic core complexes show the presence of meteoric fluid and ubiquitous fluid rock interaction already during the Eocene , such as the Thor-Odin dome (Holk et al., 1997, 2000; Mulch et al., 2004, 2006), Kettle dome (Mulch et al. 2007; Quilichini et al., in rev.) and the Bitterroot (Kerrish et al., 1986). It is therefore legitimate to question the age of the isotopic signature observed in the east Raft River Mountains: Is it a Miocene fluid signature or an older Eocene signature that was partially reset during Miocene detachment tectonics?

Throughout the Raft River detachment at Clear Creek, the relation of muscovite grains to recrystallized quartz grains suggests that muscovite grew during recrystallization of quartz. The $^{40}Ar/^{39}Ar$ ages record this (latest Oligocene to) Miocene deformation and recrystallization event, and if intragrain argon concentration gradients were affected during mylonitic deformation and mica recrystallization, it is unlikely that the more thoroughly bound D/H and $^{18}O/^{16}O$ systematics remained unaffected and preserved their Eocene composition. In addition, pristine fluid inclusions in quartz grains form planes at high angle to the foliation, and fluid inclusion trails frequently cross-cut grain and subgrain boundaries. This suggests that the fluid was trapped late during the Miocene deformation event. If fluid inclusions were of Eocene age, we would expect them to occur isolated and be preserved in the center of the quartz grains, in areas unaffected by recrystallization processes. Collectively these observations suggest that the measured fluid compositions reflect Miocene fluid-rock exchange preserved in the Raft River shear zone at Cleat Creek.

4.6.3 Open system stable isotope exchange

Prior to its deformation and rapid exhumation in the Raft River detachment, the Elba quartzite likely resided at amphibolite-facies conditions, which favored a high degree of isotopic exchange and homogenization (Valley, 2001). Therefore, the relatively large variations (3 ‰) in $\delta^{18}O_{Qtz}$ values in the Raft River detachment are probably not related to a primary sedimentary signal; such variations would have been largely erased during high-grade metamorphism (Valley, 2001). Furthermore, in other detachments in which quartzite underwent a similar thermal evolution, quartz $\delta^{18}O$ values tend to be higher, around ~+12 to +13 ‰ (Mulch et al., 2006, 2007). Even during intense quartz deformation and recrystallization in detachment

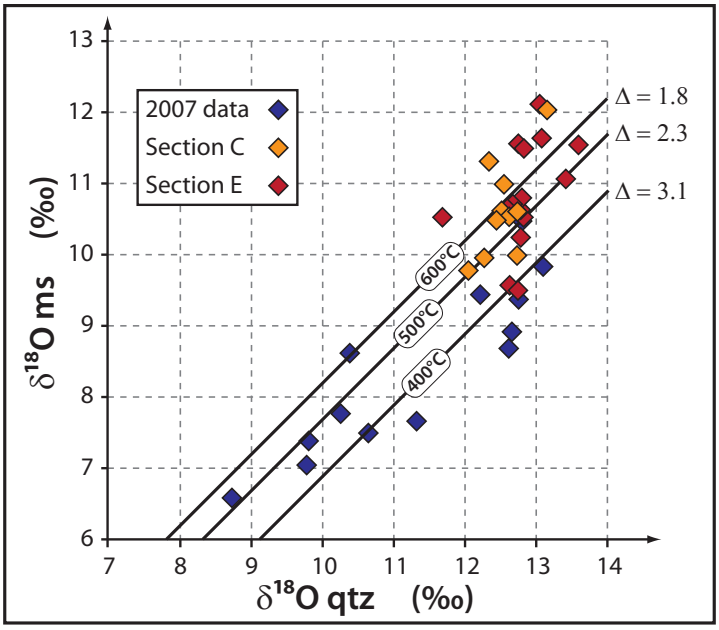

Figure 4.10: $\delta^{18}O_{qtz}$ vs. $\delta^{18}O_{ms}$.

mylonites, these values change significantly only as a result of very high time-integrated water-rock ratios. Although detachments are, in general, rock-buffered systems with respect to oxygen, the congruent $\delta^{18}O$ variations in muscovite and quartz in the Raft River detachment likely indicate variable degrees of fluid-rock interaction during deformation rather than protolith inheritance (Gottardi et al., 2011). In addition, quartz $\delta^{18}O$ varies along the same quartzite layer, from lower values in the west to higher values in the east, which is also inconsistent with a sedimentary record. Furthermore, in other detachments in which quartzite underwent a similar thermal evolution, quartz $\delta^{18}O$ values tend to be higher, around ~+12 to +13 ‰ (Mulch et al., 2006, 2007).

The oxygen isotope fractionation between quartz and muscovite is quite variable, ranging from ~1 ‰ to ~4 ‰, with 18 out of 38 samples comprised between

2 ‰ and 3 ‰ (Table 4.6 and Fig. 4.7b). However, we observe that some samples with very similar fractionation coefficient can have drastically different absolute $\delta^{18}O$ values. For example, RR07-57 has much more depleted $\delta^{18}O$ values ($\delta^{18}O_{Qtz}$ = 9.8 ‰, $\delta^{18}O_{ms}$ = 7.4 ‰) than sample RR09-123 ($\delta^{18}O_{Qtz}$ = 13.4 ‰, $\delta^{18}O_{ms}$ = 11.1 ‰), while they share about the same fractionation coefficient (~2.4). These results can only be explained by variable degrees of fluid-rock interaction during deformation.

The extent of fluid-rock interaction can be examined on a $\delta^{18}O_{Qtz}$ / $\delta^{18}O_{ms}$ diagram (Fig. 4.10): the data splits into two groups: a low $\delta^{18}O_{Qtz}$ / $\delta^{18}O_{ms}$ group that plots on the low left side of the diagram and a high $\delta^{18}O_{Qtz}$ on the right side. Most of the data have quartz $\delta^{18}O$ values ranging from 12 to 13 ‰ (all samples but one from Sections C and E, Table 4.6), but display a wider range of muscovite $\delta^{18}O$ (9 to 12 ‰), hence the vertical trend on the right side of the diagram (Fig. 4.10). This pattern suggests that, even though muscovite formed by dissolution-precipitation during recrystallization of quartz, the muscovite didn't fully equilibrate with the fluid, and rather reflects time-integrated interaction with the fluid. Moreover, the relatively constant value of quartz $\delta^{18}O$ in the right side of the diagram suggests that quartz did not exchange significantly with the fluid.

Nevertheless, several points stand out of this trend and plot on the low left side of the diagram, with low $\delta^{18}O_{Qtz}$ / $\delta^{18}O_{ms}$ (8.7 ‰ < $\delta^{18}O_{Qtz}$ < 11.3 ‰, and 6.6 ‰ < $\delta^{18}O_{ms}$ < 8.6 ‰, most of those samples com from the western sections 1 to 5) (Table 4.6 and Fig. 4.10). Those $\delta^{18}O_{Qtz}$ variations can be interpreted to reflect the time-integrated interaction of quartz with a meteoric fluid that lowered the initial protolith $\delta^{18}O_{Qtz}$ value by 2 or 3 ‰. Such a shift over the scale of meters to tens of meters may be related to fluids buffering the isotopic compositions of the minerals; these fluids would be channelized in preferential layers or shear zones within the deforming system.

4.6.4 Meteoric fluid infiltration during mylonitization

Both the oxygen and hydrogen isotope compositions of muscovite show that muscovite recrystallized and equilibrated to some degree with meteoric fluids in the Raft River detachment shear zone during ductile deformation. Over the entire thickness of the shear zone and across the studied area, the hydrogen isotope composition of synkinematic muscovite shows systematically low δD values (Table 4.7 and Fig. 4.9) that can only be explained by interaction with fluids of meteoric origin during deformation (Fricke et al., 1992; Morrison, 1992; Holk and Taylor, 1997, 2000). Using the temperature data of Gottardi et al. (2011) and the calibration of Suzuoki and Epstein (1976), based on the muscovite δD values ranging from -89 ‰ to -123 ‰, we can evaluate the composition of the fluid (δD_w) that permeated the detachment during recrystallization between -60 ‰ and -106 ‰ (δD_{ms} = -89 ‰ at 350°C and δD_{ms} = -123 ‰ at 485°C, respectively). In addition, muscovite oxygen isotope values shifted toward lower $\delta^{18}O$ values necessitate an interaction with a low $\delta^{18}O$ and low δD meteoric fluid.

Even though, as discussed in the previous section, using the oxygen isotope shifts recorded by the quartz to evaluate the composition of the fluid may be unsound because we don't know if the rock fully equilibrated with the infiltrating fluid, or if the fluid partly back-exchanged with other rocks during its infiltration (Fricke et al., 1992), more constraints on the composition of the fluid can be added based on the oxygen stable isotope data. Sample RR07-87 has the most depleted $\delta^{18}O$ values for quartz (8.7 ‰) and we also have a measure of the δD of fluid inclusions for this sample. These data can be used to calculate the oxygen isotopic composition of the fluid. Depending on temperature, the quartz grains in this sample would have been in equilibrium with a water of $\delta^{18}O$ ~3.4 - 2.2 ‰ at 350°C or $\delta^{18}O$ ~4.6 - 3.5 ‰ at 450°C (using the calibration of Clayton et al., 1972 and Sharp

and Kirschner, 1993, respectively). The quartzite must have been in equilibrium with water of $\delta^{18}O < \sim+4$ ‰ over the range of probable temperatures of fluid-rock interaction. Meteoric water is the only major terrestrial source of oxygen with the appropriate isotopic composition to explain such values (Sheppard 1986, Fricke et al., 1992).

Additional constraints on the composition of the meteoric water can be added on the basis of hydrogen isotope D/H ratios, which are much more sensitive to water infiltration than the $^{18}O/^{16}O$. The δD_{FI} composition of fluid inclusions of both quartzite mylonite and syn-mylonitic quartz vein is low, ranging from -83 to -104 ‰. Using the $\delta D/\delta^{18}O$ relation of Craig (1961) and the measured δD_{FI} values, we obtain a range of oxygen isotope $\delta^{18}O$ composition for the meteoric fluid between -14.5 ‰ and -11.5 ‰. These values encompass the range of meteoric water during the Tertiary (Fig. 4.11). Altogether, oxygen and hydrogen stable isotope data show that the Raft River detachment shear zone was extensively permeated by meteoric fluid at the time of deformation and recrystallization of the mylonite.

4.6.5 Permeability of the detachement shear zone

Changes in permeability of the different rock types might be a valuable explanation for the variations in stable isotope data observed at Clear Creek. The basement consists in the western part of the study area of Adamellite basement, hardly deformed, while the eastern part is underplated by schistic units. Those two rock unit have probably very different permeabilities: the Adamellite is likely to be less permeable than the schistose units of the *xy* formation. Therefore, when the fluid flow descends through the quartzite section and reaches the Adamellite, the basement probably acts as a bottom boundary for the flow (Fig. 4.12). Therefore, the overlying quartzite column is likely to be in equilibrium with a focused

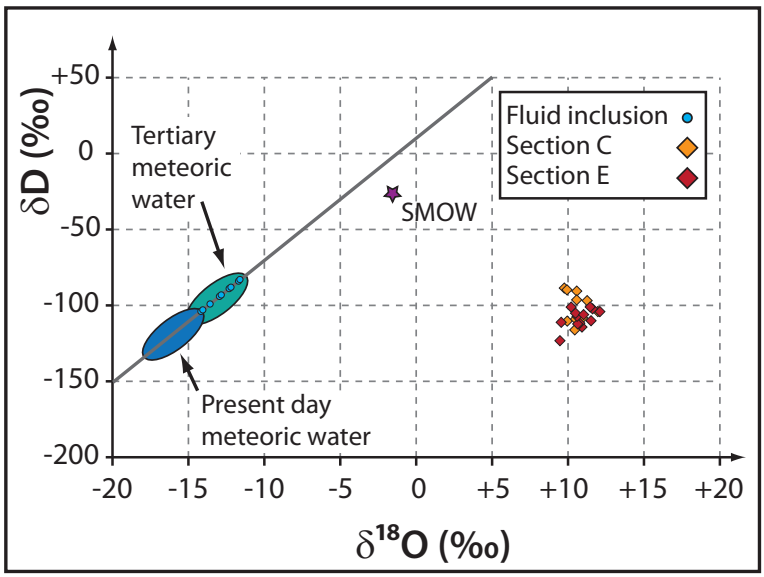

Figure 4.11: **δD vs. δ^{18}O values of muscovite. The meteoric water line and field of NE Nevada waters during Tertiary and at present are presented after Sheppard et al. (1969), Sheppard (1986), O'Neil and Silberman (1974) and Fricke et al (1992). The composition of fluid inclusions are also plotted based on their δD and calculated δ^{18}O, using the δD/δ^{18}O relation of Craig (1961).**

fluid in a confined aquifer; hence resulting in more achieved equilibrium between quartz, muscovite and fluid (low transport/exchange ratio). On the other hand, in the east (Fig. 4.12), the more permeable basement will generate a more diffuse flow, where the fluid is likely to flow through the quartzite column down to high permeability schist; hence, the mineral phases are less likely to equilibrate their isotope composition owing to a too high transport/exchange ratio. This is observed in section C and E by the broad range of fractionation coefficients. Owing to its heterogeneous and more permeable structure, the metaconglomerate at the interface quartzite/basement might act as a conduit and connect the two aquifers, focusing

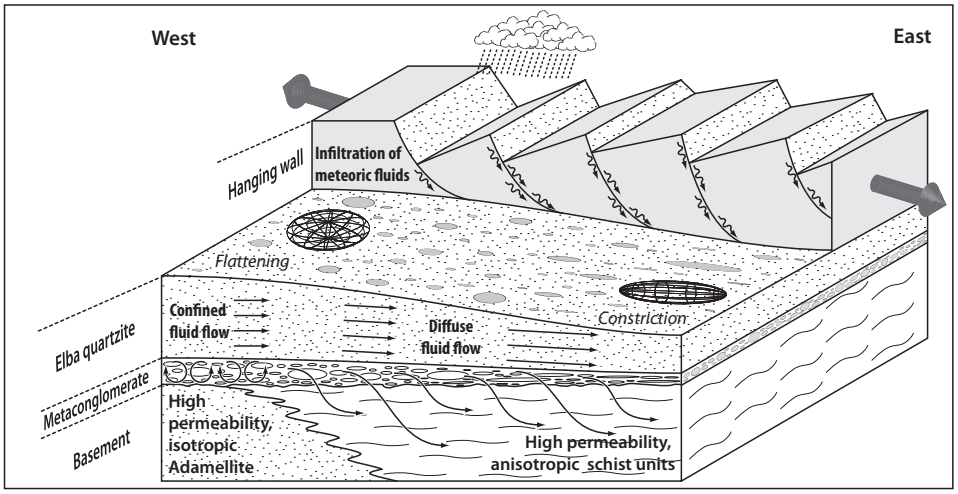

Figure 4.12: **Conceptual model to explain the isotopic variability observed in the Raft River detachment shear zone. In the West, flattening fabrics (planes) and low permeability basement (Adamellite) lead to a focused flow in a confined aquifer, enhancing fluid-rock exchange. In the East, constrictional fabrics (pipes) and high permeability basement (schists) lead to a more diffuse flow.**

the fluid flow and fluid-rock exchange, hence recording more ^{18}O isotope depletion than the overlying quartzite ($\delta^{18}O = 11$ ‰).

4.6.6 Relation between strain and isotopes

Structural and microstructural analyses of the Raft River shear zone at Clear Creek by Compton (1980), Wells (1997) and detailed mapping and structural work by Sullivan (2008) shows that the Raft River shear zone records an extreme gradient, west-to-east, along transport, in finite-strain intensity associated with a shift in the shape of the finite-ellipsoid from the flattening field into the constrictional field (Sullivan, 2008). This strain gradient represents the necking of the shear zone (Wells, 1997; Sullivan, 2008), in a mechanism similar to that observed in

the Snake Range metamorphic core complex (Miller, 1983; Lee et al., 1987). The detailed three-dimensional finite-strain and strain intensity analysis of the basal metaconglomerate by Sullivan (2008) shows that there is a transition from flattening strain in the western part to constrictional strain in the Eastern part, associated with an increase in deformation intensity (Sullivan, 2008). Sullivan (2008) relates this transition to the difference in rheology of the basement units. The western part of the shear zone is developed above the Archean Adamellite, rheologically strong, whereas the eastern part of the shear zone, characterized by a more intense deformation and representing the necking of the shear zone, is localized above the biotite and hornblende schist, rock that are rheologically weaker (Fig. 4.2, Sullivan, 2008).

This contrast in strain and rheology may also have controlled the hydrological framework at the time of mylonitization. In a deforming material, the porosity and permeability tensors that control groundwater flow are sensitive to stress that can induce anisotropy (Morgan, 1987; Sibson, 1996; Zhu, 1997; Zang et al., 1999). A material deformed under flattening strain, will develop permeability anisotropy in the direction perpendicular to the maximum shortening direction, namely horizontal planes if the maximum shortening direction is vertical. On the other hand, a material deformed in constriction will develop a linear anisotropy in the direction of maximum elongation. Therefore the flow in the flattening field will be two-dimensional (planes perpendicular to the main shortening direction), whereas it will be unidimensional in the constrictional field (lines parallel to the stretching direction).

Also, stable isotope exchange between the fluid and the solid results from three processes, solution-precipitation, fluid-assisted chemical reaction, and diffusion (Giletti, 1985; Cole and Ohmoto, 1986; Valley, 2001), all strongly dependent on the mineral surface areas between two phases relative to the volume of solid, which

in turns depends on the shape and size of individual particles and packing arrangement of the particles in the aggregate. In general, small spherical grains have a higher surface to volume ratios and will exchange faster with interstitial fluids than larger elliptic grains with low surface to volume ratio (Kirschner, 1992). Therefore the change in particle shape due to deformation and recrystallization (e.g. from spherical to ellipsoidal) must be considered when considering stable isotope data owing to the effect particle size and shape has on the total surface area to volume ratio of the entire aggregate (Kirschner, 1992).

Based on those considerations, it is plausible that the groundwater flow during development of the shear zone may have followed permeability anisotropies on the deforming material: in the western region of the studied Raft River shear zone, above the rheologically strong adamellite basement, where the strain is mostly in the flattening field, groundwater flow would be distributed on subhorizontal planes, whereas in the eastern region, where the strain is in the constrictional field, the groundwater flow would follow subhorizontal lines, parallel to the lineation (Fig. 4.12). This difference in flow pattern could explain the degree of fluid-rock isotope exchange. In orogenic systems, groundwater flow is driven either by the tectonic compression (Oliver, 1986; Ge and Garven, 1994; McPherson and Garven, 1999) or by topography, due to rock and surface uplift (Garven and Freeze, 1984b; Woodbury and Smith, 1988; Person et al. 2007). When a constant volume of fluid circulates in the system, if the flow is distributed in two-dimensions (planes), the flux of fluids will be slower than that of a one-dimensional flow (pipes). Since the fluid-rock exchange depends on the ratio between transport and exchange (Bowman et al., 1994), if the flux of fluid is too rapid, then the exchange is limited; whereas if the flux is slow, the exchange is more likely to reach equilibrium.

4.7 Conclusions

Combined microstructural, geochronological and stable isotope analyses of the Raft River detachment shear zone at Clear Creek show that an extensive hydrological system was active during the evolution of the shear zone at Miocene time. The most important results are as follow.

1) Muscovite $^{40}Ar/^{39}Ar$ ages ranging from 26 to 20 Ma and decreasing systematically with depth in the detachment, combined with hydrogen stable isotope composition suggest that meteoric fluids were infiltrating the detachment shear zone over the time scale of mylonite formation.

2) Hydrogen stable isotope analyses from both muscovite and fluid inclusions show that the fluid infiltrating the detachment shear zone was meteoric in origin, with a low D/H and low $^{18}O/^{16}O$ composition.

3) Quartz and muscovite oxygen isotope analyses show different degrees of oxygen isotope depletion, suggesting different time-integrated interaction of the minerals with meteoric fluids; these fluids would be channelized in preferential layers or shear zones within the deforming system.

4) Variation in permeability in the basement units might affect the flow pattern: confined versus diffuse flow may be responsible for the different degrees of isotopic depletion.

5) Strain variations from flattening (planes) to constriction (pipes) along the transport direction might affect fluid pathways resulting in different fluid-rock exchange patterns.

ID	T	$^{40}Ar/^{39}Ar$	$^{37}Ar/^{39}Ar$	$^{36}Ar/^{39}Ar$	^{39}ArK	K/Ca	$^{40}Ar^{*}$	^{39}Ar	Age	$\pm 1\ \sigma$
	(℃)			$(\times 10^{-3})$	$(\times 10^{-15}$ mol)		(%)	(%)	(Ma)	(Ma)
RR09-91, Muscovite, 2.43 mg, J=0.0016011 ± 0.06 %, D=1.005 ± 0.001, NM-233K, Lab 59589-01										
A	600	61.29	0.2905	170.9	1.01	1.8	17.7	1.4	31.0	1.7
B	650	9.097	0.0613	11.96	1.00	8.3	61.2	2.7	15.99	0.68
C	700	7.027	0.0219	5.604	1.90	23.2	76.4	5.3	15.43	0.35
D	750	6.439	0.0111	3.710	3.16	45.9	83.0	9.5	15.34	0.19
E	800	6.790	0.0125	3.508	4.92	40.7	84.7	16.1	16.52	0.14
F	840	8.534	0.0089	3.767	9.60	57.4	86.9	29.1	21.28	0.12
G	880	7.693	0.0061	1.662	14.3	83.2	93.6	48.3	20.655	0.064
H	920	7.021	0.0075	1.862	9.81	68.4	92.2	61.5	18.567	0.081
I	980	7.297	0.0045	2.785	8.77	113.8	88.7	73.4	18.58	0.11
J	1050	8.262	0.0048	3.778	6.35	105.8	86.5	81.9	20.49	0.12
K	1110	8.818	0.0026	3.230	8.85	199.1	89.2	93.8	22.55	0.11
L	1170	10.18	0.0045	2.604	4.60	114.3	92.4	100.0	26.96	0.17
Integrated age $\pm 1\sigma$			n=12		74.3	44.4		K_2O=7.34%	20.263	0.058
Plateau $\pm$ 1 σ	steps F-K		n=6	MSWD=247.64	57.709	101.324 ± 51.007		77.7	20.23	0.593

Table 4.1: **Furnace step heating $^{40}Ar/^{39}Ar$ data of muscovite from the Raft River detachment shear zone, NW Utah.**

ID	T (℃)	$^{40}Ar/^{39}Ar$	$^{37}Ar/^{39}Ar$	$^{36}Ar/^{39}Ar$ ($\times 10^{-3}$)	^{39}ArK ($\times 10^{-15}$ mol)	K/Ca	$^{40}Ar^{*}$ (%)	^{39}Ar (%)	Age (Ma)	$\pm 1\ \sigma$ (Ma)
RR09-94, Muscovite, 9.07 mg, J=0.0015948 $\pm$ 0.06 %, D=1.005 $\pm$ 0.001, NM-233K, Lab 59588-01										
A	550	154.6	0.1761	432.6	2.12	2.9	17.3	0.8	75.5	2.0
B	600	15.24	0.2067	24.45	2.31	2.5	52.7	1.6	22.94	0.50
C	650	9.372	0.0791	13.71	4.25	6.4	56.8	3.1	15.24	0.26
D	700	7.219	0.0206	6.055	8.07	24.8	75.2	6.0	15.53	0.14
E	750	6.903	0.0128	4.076	12.9	39.8	82.5	10.5	16.30	0.11
F	800	8.356	0.0123	3.324	18.4	41.6	88.2	17.0	21.065	0.078
G	850	9.933	0.0073	3.068	49.6	70.2	90.9	34.7	25.758	0.052
H	880	8.791	0.0069	1.245	41.2	73.8	95.8	49.3	24.046	0.054
I	900	8.616	0.0066	1.125	26.2	77.3	96.1	58.7	23.649	0.066
J	930	8.747	0.0068	1.615	21.9	75.1	94.5	66.5	23.612	0.073
K	960	8.874	0.0054	1.770	16.7	94.0	94.1	72.4	23.841	0.083
L	990	9.455	0.0041	2.291	12.8	124.9	92.8	76.9	25.05	0.10
M	1020	10.06	0.0031	2.374	9.79	167.0	93.0	80.4	26.70	0.12
N	1040	10.45	0.0035	1.899	7.52	147.0	94.6	83.1	28.21	0.14
O	1060	10.65	0.0026	1.674	6.53	200.1	95.4	85.4	28.96	0.18
P	1080	10.84	0.0025	1.409	6.27	207.5	96.2	87.6	29.71	0.17
Q	1110	11.52	0.0024	3.004	8.22	212.8	92.3	90.6	30.32	0.15
R	1140	10.86	0.0019	2.200	9.80	273.7	94.0	94.0	29.11	0.12
S	1170	10.91	0.0012	1.514	10.6	424.4	95.9	97.8	29.84	0.12
T	1650	96.59	0.0071	121.6	6.11	71.5	62.8	100.0	166.55	0.82
Integrated age $\pm 1\sigma$			n=20		281.3	47.3		K2O=7.47%	28.009	0.064
Plateau $\pm$ 1 σ	steps G-L		n=6	MSWD=210.44	168.484	79.313 $\pm$ 20.829		59.9	24.43	0.393

Table 4.2: **Furnace step heating $^{40}Ar/^{39}Ar$ data of muscovite from the Raft River detachment shear zone, NW Utah.**

ID	T	$^{40}Ar/^{39}Ar$	$^{37}Ar/^{39}Ar$	$^{36}Ar/^{39}Ar$	^{39}ArK	K/Ca	$^{40}Ar^{*}$	^{39}Ar	Age	$\pm 1\ \sigma$
	(℃)			($\times 10^{-3}$)	($\times 10^{-15}$ mol)		(%)	(%)	(Ma)	(Ma)
RR09-96, Muscovite, 8.79 mg, J=0.0015921 $\pm$ 0.07 %, D=1.005 $\pm$ 0.001, NM-233K, Lab 59587-01										
A	550	70.60	0.0205	68.48	1.69	24.9	71.3	0.7	139.13	0.89
B	600	18.74	0.0450	20.81	2.52	11.3	67.2	1.8	35.80	0.41
C	650	8.006	0.0092	8.801	4.82	55.3	67.5	3.8	15.43	0.18
D	700	6.713	0.0025	4.323	9.01	207.7	80.9	7.6	15.518	0.095
E	750	6.737	0.0022	2.815	14.1	232.1	87.6	13.5	16.854	0.082
F	800	8.217	0.0016	2.139	19.7	313.7	92.3	21.7	21.627	0.063
G	850	10.02	0.0009	1.922	38.3	566.3	94.3	37.8	26.932	0.056
H	880	9.306	0.0007	1.013	35.7	780.5	96.8	52.7	25.657	0.049
I	900	9.302	0.0006	1.134	23.9	834.3	96.4	62.7	25.547	0.071
J	930	9.603	0.0003	1.351	24.4	1766.0	95.8	72.9	26.216	0.064
K	960	10.33	0.0003	1.819	13.0	1494.4	94.8	78.4	27.891	0.090
L	990	11.33	0.0006	2.327	9.67	843.9	93.9	82.4	30.29	0.12
M	1020	12.43	0.0002	2.810	7.82	2270.6	93.3	85.7	32.99	0.13
N	1040	13.28	-0.0003	3.323	5.94	-	92.6	88.2	34.95	0.17
O	1060	13.85	0.0008	3.785	4.99	616.9	91.9	90.3	36.16	0.19
P	1080	14.22	-0.0005	3.893	4.80	-	91.9	92.3	37.14	0.20
Q	1110	14.32	0.0013	3.779	6.74	393.6	92.2	95.1	37.51	0.15
R	1140	13.32	0.0007	3.922	6.25	701.1	91.3	97.7	34.57	0.17
S	1170	13.41	0.0008	4.692	5.38	644.4	89.7	100.0	34.17	0.19
Integrated age $\pm 1\sigma$			n=19		238.7	314.8		K2O=6.55%	27.403	0.046
Plateau $\pm$ 1 σ		steps G-K	n=5	MSWD=180.90	135.244	975.670 $\pm$ 513.815		56.7	26.27	0.373

Table 4.3: **Furnace step heating $^{40}Ar/^{39}Ar$ data of muscovite from the Raft River detachment shear zone, NW Utah.**

ID	T	$^{40}Ar/^{39}Ar$	$^{37}Ar/^{39}Ar$	$^{36}Ar/^{39}Ar$	^{39}ArK	K/Ca	$^{40}Ar^*$	^{39}Ar	Age	$\pm 1\ \sigma$
	(℃)			($\times 10^{-3}$)	($\times 10^{-15}$ mol)		(%)	(%)	(Ma)	(Ma)
RR09-104, Muscovite, 1.63 mg, J=0.0016051 $\pm$ 0.06 %, D=1.005 $\pm$ 0.001, NM-233K, Lab 59590-01										
A	600	55.28	0.1806	44.14	1.34	2.8	76.4	4.1	118.4	1.1
B	650	8.345	0.1201	10.39	0.880	4.2	63.3	6.8	15.21	0.95
C	700	7.069	0.0158	6.453	0.948	32.2	73.0	9.7	14.86	0.93
D	750	7.474	0.0044	4.891	1.22	114.8	80.6	13.5	17.35	0.70
E	800	11.86	0.0060	5.350	1.46	84.4	86.7	17.9	29.48	0.58
F	840	12.28	0.0035	3.648	1.69	144.2	91.2	23.1	32.12	0.49
G	880	13.25	0.0033	4.526	2.76	156.2	89.9	31.5	34.15	0.33
H	920	11.13	0.0001	2.875	3.77	7267.9	92.4	43.1	29.49	0.23
I	980	11.87	0.0002	3.158	4.57	2170.2	92.1	57.1	31.36	0.21
J	1050	20.80	-0.0005	3.764	4.29	-	94.7	70.2	56.10	0.25
K	1050	28.77	-0.0007	3.785	1.80	-	96.1	75.8	78.33	0.52
L	1650	65.38	0.0019	32.33	7.91	271.7	85.4	100.0	154.80	0.42
Integrated age $\pm 1\sigma$			n=12		32.6	41.1		K2O=4.79%	70.01	0.17
Plateau $\pm$ 1 σ	steps E-I		n=5	MSWD=36.17	14.247	2674.117 $\pm$ 3093.798		43.6	31.15	0.801

Table 4.4: **Furnace step heating $^{40}Ar/^{39}Ar$ data of muscovite from the Raft River detachment shear zone, NW Utah.**

Elevation (m above basement)	Sample	$\delta^{18}O_{qtz}$ (‰)	$\delta^{18}O_{ms}$ (‰)	$\Delta^{18}O_{qtz-ms}$ (‰)	δD_{ms} (‰) vs. SMOW	δD_{FI} (‰) vs. SMOW
Section 1						
46	RR07-46 (qtz vein)					-83
40	RR07-43	12.2	9.4	2.8		
35	RR07-42 (qtz vein)					-104
28	RR07-41					-89
15	RR07-40					
Section 3						
65	RR07-77	10.6	7.5	2.7		
40	RR07-73	10.4	8.6	1.8		
25	RR07-71	9.8	7.1	3.1		
Section 4						
90	RR07-68	11.3	7.7	3.7		-93
80	RR07-67 (qtz vein)					-103
25	RR07-59 (qtz vein)					-83
8	RR07-57 (qtz vein)					-88
8	RR07-57	9.8	7.4	2.4		-94
Section 5						
95	RR07-99	12.8	10.5	2.3		
90	RR07-98	13.1	9.8	3.3		-99
80	RR07-94	12.7	8.9	3.7		
75	RR07-92	12.7	9.4	3.4		
20	RR07-91	12.6	8.7	3.9		
0	RR07-87	8.7	6.6	2.1		-84

Table 4.5: **Oxygen isotope data of quartz ($\delta^{18}O_{qtz}$) and muscovite ($\delta^{18}O_{ms}$), fractionation coefficient ($\Delta^{18}O_{qtz-ms}$), hydrogen isotope composition of muscovite (δD_{ms}), and hydrogen isotope composition of fluid inclusion (δD_{FI}).**

Elevation (m above basement)	Sample	$\delta^{18}O_{qtz}$ (‰)	$\delta^{18}O_{ms}$ (‰)	$\Delta^{18}O_{qtz-ms}$ (‰)	δD_{ms} (‰) vs. SMOW	δD_{FI} (‰) vs. SMOW
Section C						
70	RR09-103	12.3	11.3	1	-97	
30	RR09-098	12.4	10.5	1.9	-116	
20	RR09-097	12.7	9.9	2.8	-110	
18	RR09-096	12.6	10.5	2.1	-109	
16	RR09-095	12.5	11	1.6	-108	
14	RR09-094	12.7	10.6	2.2	-96	
12	RR09-093	12.5	10.6	1.9	-91	
10	RR09-092	12	9.8	2.3	-89	
8	RR09-091	12.3	9.9	2.3	-90	
4	RR09-090	13.2	12	1.2	-104	
Section E						
58	RR09-137		10.9		-114	
54	RR09-136	11.7	10.5	1.2	-105	
50	RR09-135	12.6	10.6	2	-112	
46	RR09-134	12.7	11.5	1.2	-110	
41	RR09-133	12.7	9.5	3.3	-123	
35	RR09-132	13	12.1	0.9	-104	
27	RR09-131	12.8	11.5	1.3	-101	
25	RR09-130	12.8	10.8	2	-112	
23	RR09-129	12.8	10.2	2.6	-101	
19	RR09-128	12.8	10.5	2.3		
17	RR09-127	12.8	10.6	2.2	-107	
16	RR09-126	12.6	9.6	3.1	-111	
15	RR09-125	12.7	10.7	2		
14	RR09-124	13.1	11.6	1.4	-102	
12	RR09-123	13.4	11.1	2.3	-106	
8	RR09-122	13.6	11.5	2.1		

Table 4.6: **Oxygen isotope data of quartz ($\delta^{18}O_{qtz}$) and muscovite ($\delta^{18}O_{ms}$), fractionation coefficient ($\Delta^{18}O_{qtz-ms}$), hydrogen isotope composition of muscovite (δD_{ms}), and hydrogen isotope composition of fluid inclusion (δD_{FI}) (continued).**

Elevation (m above basement)	Sample	δD (‰)
Section A		
51	RR09-158	-89
32	RR09-156	-110
27	RR09-155	-106
21	RR09-154	-111
17	RR09-153	-122
13	RR09-152	-94
8	RR09-151	-93
3	RR09-150	-109
Section B		
61	RR09-86	-112
43	RR09-83	-107
38	RR09-82	-109
30	RR09-80	-106
29	RR09-79	-109
27	RR09-78	-111
19	RR09-77	-109
15	RR09-76	-98
6	RR09-74	-108
2	RR09-73	-114

Table 4.7: **Muscovite hydrogen stable isotope data (δD).**

Elevation (m above basement)	Sample	δD (‰)
Section C		
69	RR09-103	-97
27	RR09-98	-116
21	RR09-97	-110
18	RR09-96	-109
16	RR09-95	-108
13	RR09-94	-96
11	RR09-93	-91
8	RR09-92	-88
6	RR09-91	-90
1	RR09-90	-104
Section D		
55	RR09-119	-117
52	RR09-118	-104
49	RR09-117	-107
45	RR09-115	-113
25	RR09-113	-112
22	RR09-112	-111
20	RR09-111	-107
18	RR09-110	-99
15	RR09-109	-100

Table 4.8: **Muscovite hydrogen stable isotope data (δD) (continued).**

Elevation (m above basement)	Sample	δD (‰)
Section E		
61	RR09-137	-114
57	RR09-136	-105
53	RR09-135	-112
49	RR09-134	-110
44	RR09-133	-123
36	RR09-132	-104
27	RR09-131	-110
25	RR09-130	-112
21	RR09-129	-101
18	RR09-128	-103
15	RR09-127	-107
13	RR09-126	-111
11	RR09-124	-102
8	RR09-123	-106
5	RR10-28	-112
Indian Creek		
25	RR10-45	-112
13	RR10-42	-98
9	RR10-41	-110
5	RR10-39	-97
3	RR10-38	-110
2	RR10-37	-110
Duffy Creek		
22	RR10-36	-113
19	RR10-35	-107
17	RR10-33	-109
15	RR10-32	-123
11	RR10-31	-104
9	RR10-30	-101
7	RR10-29	-108
5	RR10-28	-112

Table 4.9: **Muscovite hydrogen stable isotope data (δD) (continued).**

Chapter 5

EFFECTS OF PERMEABILITY FIELDS ON FLUID, HEAT, AND OXYGEN ISOTOPE TRANSPORT IN EXTENSIONAL DETACHMENT SYSTEMS

Several field studies of cordilleran metamorphic core complexes indicate that meteoric fluids permeated the upper crust down to the detachment shear zone and interacted with recrystallized rocks. The presence of fluids in the brittle/ductile transition zone is recorded in the oxygen and hydrogen stable isotope composition of the recrystallized rocks, and may play an important role in the thermomechanical evolution of the detachment shear zone. Geochemical data show that fluid flow in the brittle upper crust is primarily controlled by the large-scale fault-zone

architecture.

We conduct continuum-scale (i.e., large-scale, partial-bounceback) lattice-Boltzman fluid, heat, and oxygen isotope transport simulations of an idealized cross-section of a metamorphic core complex. The simulations investigate the effects of crustal and fault permeability and buoyancy driven flow on two-way coupled fluid and heat transfer and resultant exchange of oxygen isotopes between the meteoric fluid and rock. Our results show that fluid migration to mid- to lower-crustal levels has to be fault controlled and depends primarily on the permeability contrast between the fault zone and the crustal rock. High fault/crust permeability ratios lead to channelized flow in the fault and shear zones while lower ratios allow leakage of the fluids from the fault into the crust. Buoyancy affects mainly flow patterns (more upward directed) and, to a lesser extent, temperature distributions (disturbance of the geothermal field by ~25°C). Channelized fluid flow in the shear zone leads to strong vertical and horizontal thermal gradients, comparable to field observations. The oxygen isotope results show profound oxygen depletion (starting value of $\delta^{18}O = +13$ ‰ down to 4 ‰) concentrated along the faults and shear zone, similar to field data.

Introduction

A growing body of studies shows that water plays a major role in the thermal, mechanical, and geochemical evolution of the Earth, from crust to mantle (Austrheim, 1987; Nesbitt and Muehlenbachs, 1989; Marquer and Burkhard, 1992; Hirth and Kohlstedt, 1996; Oliver, 1996; Koons et al., 1998; Manning and Ingebritsen, 1999; Iio et al., 2002; Saar and Manga, 2003; Hirschmann et al., 2005; Bürgmann and Dresen, 2008; Ingebritsen and Manning, 2010). In active tectonic areas faults cross-cutting lower to upper crust are heterogeneous and anisotropic

structures that can serve as conduits or barriers or combined conduit-barrier systems for groundwater flow, with ramifications for heat transport and ore formation (Smith et al., 1990; Antonellini and Aydin, 1994; Forster et al., 1994; Newman and Mitra, 1994; Lopez and Smith, 1995; Caine et al., 1996, Sibson and Scott, 1998, Saar and Manga, 2004; Saar et al., 2005; Bense and Person, 2006, Person et al., 2007; Saar, 2011). Therefore, understanding the geometry and permeability structure of such flow zones has important implications for the thermomechanics of lithospheric deformation.

Faults in crustal rocks are complex structures that are composed of a fault core that consist of gouge, cataclasite, and mylonite, where most of the displacement is accommodated (Caine et al., 1996). This core is mechanically associated with an outer damage zone consisting of small faults, fractures, veins, and folds. Beyond these first-order observations, fault geometry and permeability are not well understood, although there appears to be consensus that fault zones represent hydrologic units (Haneberg, 1995; Bense and Person, 2006) as they typically direct fluid flow either within their high-permeability zones or outside, along their low-permeability zones. In this paper, we address crustal-scale fluid flow in regions of crustal extension, where normal and detachment faults provide a relatively simple flow system. Following Person et al. (2007), we are particularly interested in the thermal implications of fluid flow in this tectonic regime and in the resulting oxygen isotope interaction between fluid and rock at elevated temperatures. Our approach is based on two-dimensional modeling, which is necessarily restrictive but offers first-order insights into the relationship between fluid flow, the thermal structure of the crust, and associated oxygen isotope exchange, so that the sensitivity of fluid-rock interaction to crustal and fault permeability fields can be evaluated.

At elevated temperature, fluid-rock interaction is quantified most effectively by stable isotope exchange (e.g., Valley, 1986). The distribution of oxygen and

hydrogen isotopes in fluids and minerals has become an important fingerprint to elucidate the origin and fluxes of fluids over a wide range of timescales and geological settings such as intrusions and fault zones, including thrust faults (Burkhard and Kerrish, 1988, Rye and Bradbury, 1988; Banks et al., 1991; Moore and Vrolijk, 1992; Sibson, 1994, 1998; Crespo-Blanc et al., 1995; Goddard and Evans, 1995, McCaig et al., 1995; Ghisetti et al., 2001; Kirschner and Kennedy, 2001), strike-slip faults (O'Neil and Hanks, 1980; Unruh et al., 1992, Chester et al., 1993; Barton et al., 1995; Sibson, 1998, Kharaka et al., 1999; Pili et al., 2002), and extensional detachment systems (Bowman and Willett, 1991; Bowman et al., 1994; Gerdes et al., 1998; Cook et al., 1997; Mulch, 2007; Gébelin et al., 2011). Although the details of fluid transport and exchange with rock in the transition between brittle and ductile deformation regimes are still poorly understood, several stable isotope, and other, studies have shown that meteoric water can circulate to significant depths (down to the ductile crust) in normal fault systems (e.g. Wickham and Taylor, 1987; Fricke et al., 1992; Morrison, 1994; Morrison and Anderson, 1998; Bebout et al., 2001; Mulch et al., 2004, 2006, 2007; Person et al., 2007; Ingebritsen and Manning, 2010; Gébelin et al., 2011; Gottardi et al., 2011).

The focus of this paper is to study the effects of permeability fields on groundwater flow, heat distribution, and isotope composition in a fault-controlled system associated with uplift and exhumation of metamorphic rocks at a detachment zone. The model is intended to idealize the geometry of an extension system affecting hot and thick crust, such as found in Cordilleran metamorphic core complexes (Vanderhaeghe and Teyssier, 2001). The geometry of the extensional domain is inspired by a model that was proposed by Person et al. (2007), but the method to compute the fluid, heat, and isotope transport follows a macroscale lattice-Boltzmann approach. In the first part of the paper, we summarize the field evidence for fluid circulation and fluid-rock isotope exchange that have been reported from the North American

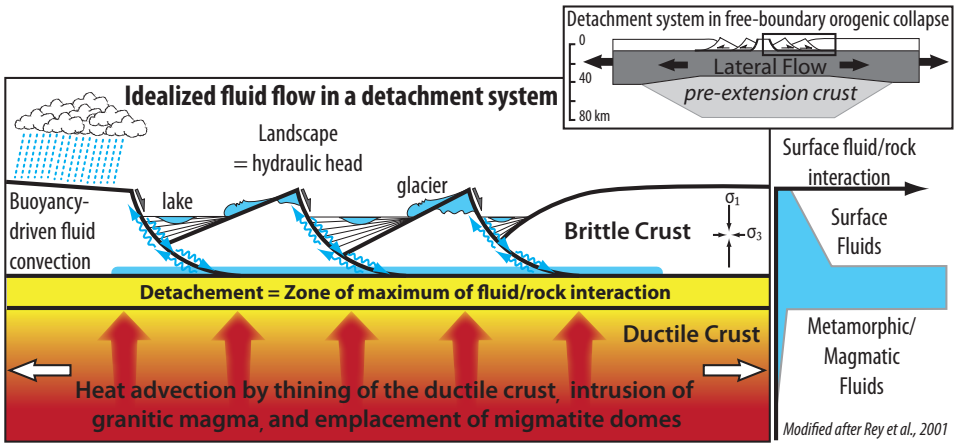

Figure 5.1: **Idealized fluid flow in a detachment system.**

Cordilleran metamorphic core complexes. We then set up the model domain based on generalized field observations and introduce the numerical method. Model results are presented in terms of the thermal and isotope records for various cases of permeability fields and fault zone connectivities. Finally, modeling results are compared to temperature and isotope ratios measured in rocks pegged to the field setting and provide insight into the permeability conditions that must be fulfilled to explain observed temperature and isotope values.

5.1 Geologic evidence for crustal-scale fluid flow

Our study aims at modeling crustal-scale fluid circulation in the context of continental extension that accompanies orogenic collapse. On a first order, the continental crust accommodates extension in two layers (brittle and ductile) with contrasting thermal and mechanical behavior (Kuznir and Park, 1987). The brittle upper crust thins by normal faulting and is separated from the ductilely flowing lower crust by a detachment zone. In this framework, localized extension leads

to the formation of metamorphic core complexes (Brun et al., 1994; Rey et al., 2001; Teyssier et al., 2005). Stable isotope studies have shown that at the time of extension, surface-derived fluids can permeate the brittle upper crust down to the detachment footwall (Fig. 5.1), where meteoric fluid signatures are preserved in metamorphic minerals (Fricke, 1992; Morrison and Anderson, 1994; Holk et al., 1997, 2000; Mulch et al., 2004, 2006; Gébelin et al., 2011; Gottardi et al., 2011). In extensional systems, arrays of normal faults crosscut the upper crust, are rooted in the detachment surface, and provide natural pathways for fluid flow. The high geothermal gradient that characterizes extension zones enhances buoyancy-driven convective circulation of surface fluids from the surface to the detachment at the base of the brittle crust (Fig. 5.1) (Mulch et al., 2004; 2007).

Following a Mesozoic protracted tectonic history of compression, accretion, and crustal thickening that built the North American Cordillera, extensional detachments evolved rapidly during Paleocene-Eocene time along crustal scale low-angle shear zones (Armstrong, 1992; Coney and Harms, 1984; Brown et al., 1986; Price, 1986; Parrish et al., 1988; Carr, 1992; Vanderhaeghe and Teyssier, 1997; Crowley et al., 2001, Bird, 2002). Thermochronological and geochemical studies of core complexes show two groups (Fig. 5.2): North of the Snake River plain, from British Columbia to Washington State, the Omineca belt comprises the largest region of Cordilleran metamorphic core complexes (Armstrong, 1985; Coney et al., 1987; Brown et al., 1986). In this belt, the $^{40}Ar/^{39}Ar$ ages of fabric-forming, synkinematic white mica concentrate narrowly between 49 and 46 Ma (Fig. 5.3). These metamorphic core complexes are characterized, below the detachment zone, by significant partial melting, granite intrusion, and flow of the lower crust synchronous with extensional activity (Fig. 5.3 and 5.4) (Parrish et al., 1988; Vanderhaeghe and Teyssier, 1997; Vanderhaeghe et al., 1999; Vanderhaeghe and Teyssier, 2001; Foster et al., 2001; Foster and Raza, 2002; Teyssier

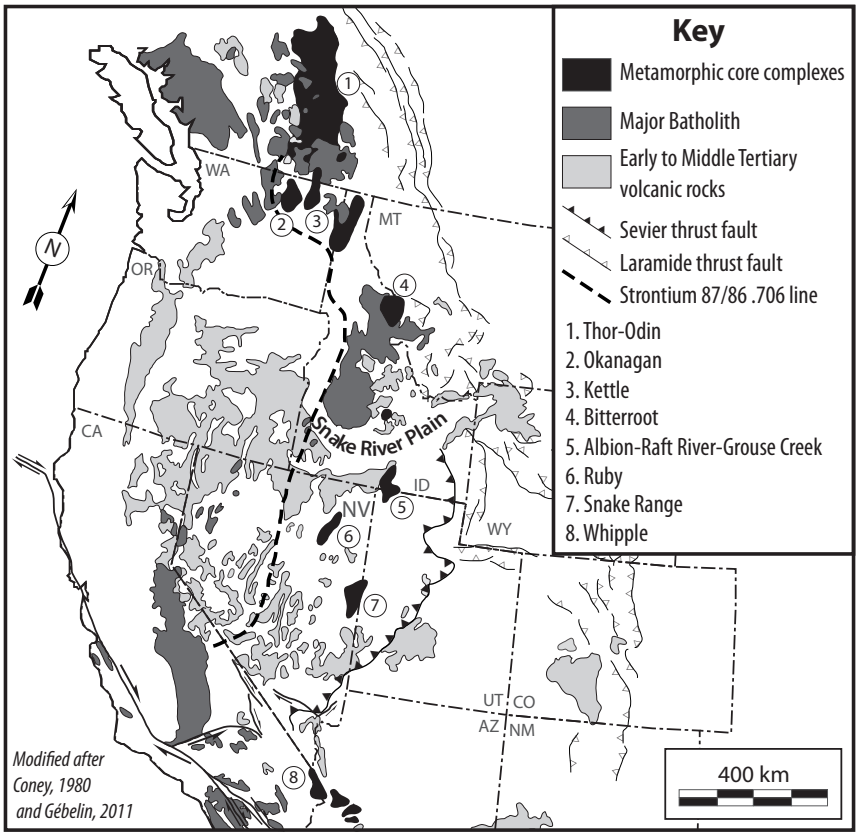

Figure 5.2: **Map of the North American metamorphic core complexes.**

et al., 2005). In contrast, south of the Snake River plain (Fig. 5.2), the southern core complexes of the Raft River-Grouse Creek-Albion Mountains, Ruby-East Humboldt Range, Snake Range, and Whipple Mountain show a more prolonged extension history from Eocene to recent Basin-and-Range extension, with a pulse of mylonite development in Oligo-Miocene time (Fig. 5.3).

Detailed stable isotope work on the Thor-Odin dome (Holk et al., 1997, 2000; Mulch et al., 2004, 2006) and Kettle dome (Mulch et al. 2007) documents fluid-rock exchange (Fig. 5.3). Along the Thor-Odin detachment, the δD values of

	Detachment	Detachment Ar age (Ma)	Lithologies	Thickness (m)	Structure defining detachment	Temperature of mylonitization (°C)	Quartz $\delta^{18}O$ (‰)	Water δD (‰)
1	Thor Odin	49-47.9[(1)]	Feslic gneiss	500-1000	Mylonite, ultramylonite, pseudotacholite	420 ± 40[(1)]	10.0-13.5[(2)]	-110/-135[(2)]
2	Kettle	49.1[(3)]	Quartzite, amphibolite, felsic gneiss	100-300	Mylonite, (ultra)mylonite	400 ± 40[(3)]	5.0-12.8[(3)]	-110/-125[(3)]
3	Bitterroot	46-47[(4)]	Granite, Gneiss	500-1000	Progressive from magmatic fabric to (ultra) mylonite and cataclasite	550[(5)]	9.8-12.2[(5)]	-120/-140[(6)]
4	Raft River	47-45/22-10[(7)]	Quartzite	50-100	Mylonite, veined fracture zones, cataclasite	345-485[(8)]	9.8-12.7[(8)]	-83/-98[(8)]
5	Ruby	36-29/27-21[(9)]	Quartzite, breccia, leucogranite	100-200	Mylonite, cataclasite, breccia	580-620[(10,11,12)]	2.8-11.6[(13)]	-80/-146[(13)]
6	Snake Range	48-41/30-26/17[(14)]	Quartzite	200-600	Mylonite, cataclasite, breccia	400 ± 50[(15)]	11.4-13.8[(15)]	-120/-130[(15)]
7	Whipple	26-16[(16)]	Gneiss	50-300	Mylonite, cataclasite, breccia	460-535[(17)]	7.90-10[(17)]	NA

Table 5.1: **Summary of available data on metamorphic core complexes.** [(1)]**Mulch et al., 2006;** [(2)]**Mulch et al., 2004;** [(3)]**Mulch et al., 2007;** [(4)]**Foster et al., 2000;** [(5)]**Kerrich et al., 1986;** [(6)]**Quilichini, pers. com.;** [(7)]**Wells et al., 2000;** [(8)]**Gottardi et al., 2011;** [(9)]**Mueller and Snoke, 1993;** [(10)]**McGrew and Snee, 1994;** [(11)]**Mueller and Snoke, 1993;** [(12)]**Hurlow et al., 1991;** [(13)]**Fricke et al., 1992;** [(14)]**Lee, 1995; Miller et al. 1999;** [(15)]**Gébellin et al., 2011;** [(16)]**Davis, 1988;** [(17)]**Morrison and Anderson, 1994.**

syntectonic muscovite fish are extremely low (between -140 and -160 ‰) and relatively constant in the top few hundred meters of the detachment. The quartzite protolith in the detachment footwall has muscovite with -80 < δD < -40 ‰, consistent with metamorphic muscovite (Fig. 5.3) (Mulch et al., 2004, 2006; Quilichini, personal comm.). Quartz-muscovite oxygen stable isotope thermometry estimates the temperature of mylonitization at 420 ± 40°C for the Thor Odin mylonite, and, therefore, the isotopic composition of the water that interacted with the mica was -140 < δD < -120 ‰ (Fig. 5.3). Surface water is the only reasonable candidate for such very low deuterium values (Taylor, 1977). Similarly, synkinematic muscovite displays δD values as low as -135 ‰ for the Kettle detachment (Mulch et al. 2007, Quilichini, 2012) (Fig. 5.3). The Kettle dome quartzite mylonite shows little variation in $\delta^{18}O$ and displays oxygen isotope equilibrium with deformation temperatures of 400 ± 40°C (Mulch et al., 2007) and 365 ± 45°C (Quilichini, 2012) (Fig. 5.3). Based on the hydrogen isotope composition of muscovite, muscovite at this temperature exchanged isotopically with meteoric water with maximum δD_{water} = -115 ± 5 ‰ in the Kettle dome. In the Bitterroot, Kerrish et al. (1986) estimated the temperature of mylonitization at 550°C based on quartz-muscovite oxygen stable isotope thermometry (Fig. 5.3), but Quilichini (2012) proposes a temperature of mylonitization with a range from 500 to 300°C.

On the other hand, south of the Snake River plain (Fig. 5.2) the Raft River-Grouse Creek-Albion Mountains, Ruby-East Humboldt Range, Snake Range and Whipple Mountain $^{40}Ar/^{39}Ar$ ages of mylonitization are more complicated, showing a protracted history. However, all were finally exhumed in Oligo-Miocene time: 22-10 Ma for the Raft River (Wells et al., 2000), 27-21 Ma for the Ruby - East Humboldt Range (Mueller and Snoke, 1993; McGrew and Snee, 1994), 27-17 Ma for the Snake Range (Lee, 1995, Miller, 1999, Gébelin et al., 2011) and 26-16 Ma for the Whipple Mountains (Davis, 1988) (Fig. 5.3). The peak temper-

atures for this latest metamorphism, based on oxygen stable isotope thermometry are estimated at 345 - 485°C for the Raft River Mountains (Wells, 2000, Gottardi et al., 2011), 400 $\pm$ 50°C for the Snake Range: (Gébelin et al., 2011), and 460°C - 535°C for the Whipple Mountains (Anderson, 1985, Davis et al., 1982) (Fig. 5.3). In the Ruby Range, petrological constraints put the temperature of Miocene metamorphism around 550°C (Mueller and Snoke, 1993; McGrew and Snee, 1994) (Fig. 5.3), and mylonite development likely occurred down to 480°C (Fricke et al., 1992).

Stable isotope data are also available for these metamorphic core complexes. In the Raft River detachment, Gottardi et al. (2011) revealed a sharp thermal gradient (~140°C / 100 m) based on quartz/muscovite stable isotope thermometry. $\delta^{18}O$ values of quartz and muscovite are variable, with values ranging from 9.8 to 12.7 ‰ for quartz and 7.1 to 9.4 ‰ for muscovite (Fig. 5.3). Hydrogen isotope composition of muscovite varies from -120 to -90 ‰, in agreement with a fluid composition of -100 to -70 ‰ (Suzuoki and Epstein, 1976) (Fig. 5.3). In addition, quartz fluid inclusions analyzed in five samples over the entire section have a narrow range between -94 ‰ and -82 ‰; these values are in agreement with those calculated from the hydrogen isotope composition of muscovite, and are also consistent with meteoric fluids.

In the Ruby Mountains, Fricke et al (1992) report very low quartz $\delta^{18}O$ values (as low as 2.8 ‰) from the mylonite zone compared to the unmylonitized quartz from adjacent basins (values around 10.0 to 12.0 ‰)(Fig. 5.3), and fluid inclusions δD yield a composition of -119 ‰ (Fig. 5.3). Mylonitized leucogranite also shows large oxygen isotope disequilibrium. Fricke et al. (1992) conclude that their measurements can only be explained by a fluid composition depleted in $\delta^{18}O$ and δD from interaction with a meteoric fluid. Very low muscovite hydrogen isotope compositions are also reported in the uppermost part of the detachment in the

Snake Range by Gébelin et al. (2011) (-150 to -145 ‰) (Fig. 5.3). In the Whipple Mountains, Morrison and Anderson (1998) report an extreme thermal gradient below the detachment fault (82°C over 38 m). Indeed, oxygen isotope compositions of epidote and quartz from chloritic breccias that underlie the detachment fault yield quartz-epidote fractionations that range from 4.1 to 6.4 ‰(Fig. 5.3) and increase systematically toward the fault, giving mean temperatures that decrease from 432°C at 50m below the fault to ~350°C at 12m below the fault (82°C over 38 m) (Fig. 5.3). Morrison and Anderson (1998) pioneered the concept of fluid-induced fault-zone refrigeration. In general, it has been recognized that groundwater recharge typically leads to subsurface cooling (e.g., Saar, 2011).

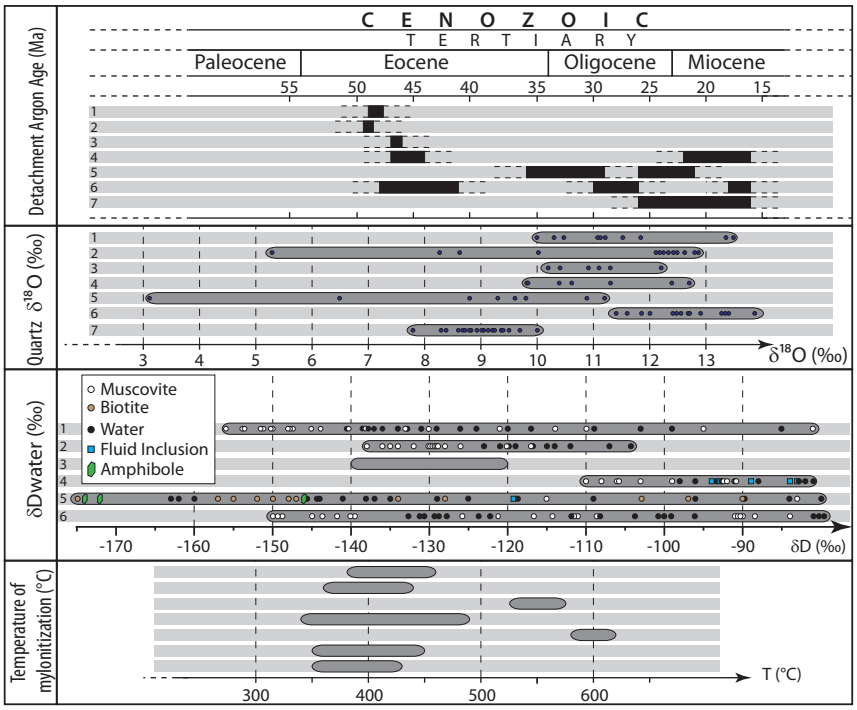

Figure 5.3: **Summary of available data on metamorphic core complexes.**

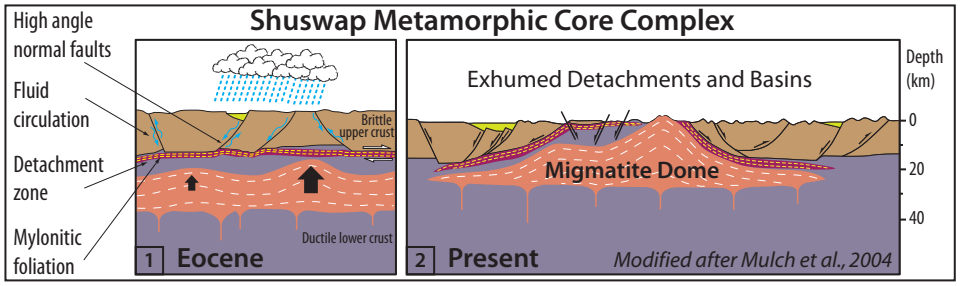

Figure 5.4: **Present day and restored cross-sections of a cordilleran metamorphic core complex, the Columbia River detachment.**

5.2 Idealized geometry of the model

The previous summary on isotope studies on metamorphic core complexes shows that significant oxygen isotope depletion is observed in detachment zones, caused by the infiltration and interaction of meteoric fluids with the recrystallizing rocks. During orogenic collapse, the brittle faulting and subsequent domino-style evolution of the upper crust opens numerous faults that create pathways for surface fluids to percolate deep into the crust (Fig. 5.1 and 5.4). The geometry of the model represents such a generalized Cordilleran metamorphic core complex during the onset of extension, prior to exhumation of the detachment zone (Fig. 5.5). The upper crust is divided into ~10 km blocks (6, 6.75 and 7 km thick), separated by two 750 m thick high angle faults that take root in the shear zone (one for groundwater recharge and one for discharge). Several metamorphic core complexes have preserved a syndeformational basin that developed by domino-style faulting during the evolution of the detachment (Trinity Hills and Endery basins in the Columbia River detachment and Sacramento Pass basin in the Snake Range, Fig. 5.4). Therefore our model geometry also includes two 2-km-thick near-surface basins in close association with the faults. There is a 1500 m elevation difference over 22.5 km

between the lowest and highest block, which corresponds to a 6.6 % topography gradient, a relatively common slope in mountainous areas (Woodbury and Smith, 1988), which induces some topography-driven flow even though the majority of groundwater flow is caused by buoyancy as a result of basal heating. The base of the model includes a 4.5 km thick crust below the detachment zone that is represented by a 1500 m thick shear zone.

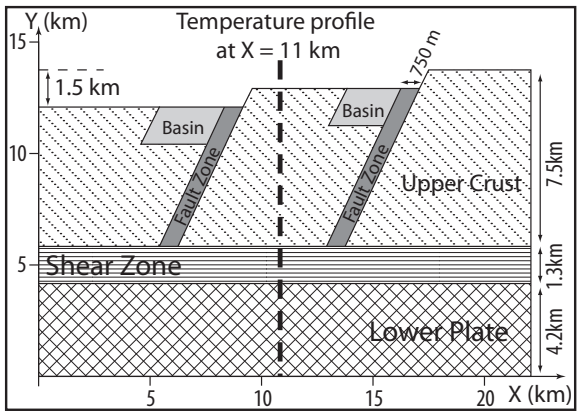

Figure 5.5: **Model set up.**

5.3 Numerical modeling method

In the last two decades, lattice-Boltzmann (LB) methods have been developed as promising numerical techniques for modeling fluid flow, solute or heat transport, reactive flow, and multicomponent and multiphase flow inside heterogeneous porous media over both microscopic and macroscopic spatial scales (Chen and Dolen, 1998; Wolf-Gladrow, 2000; Succi, 2001; Guo and Zhao, 2005; Walsh and Saar, 2010, Myre et al., 2010). These methods are different from conventional computational fluid dynamics (CFD) approaches that are based on discretized forms of continuum-based macroscopic equations. In contrast, LB methods employ a

mesoscopic version of the classic Boltzmann equations to solve complex flow and transport behavior. LB methods include two steps: 1) a streaming step in which the physical properties (represented by fluid, heat, or solute "packages") are propagated between two neighboring nodes; and 2) a collision step which re-distributes the fluid momentum, thermal energy, or solute concentration based on kinetic theory. These features of LB methods provide the advantage of modeling non-equilibrium dynamics with relative simple algorithms, and simulating porous media flows with interfacial dynamics and complex boundaries (Chen and Dolen, 1998). In the present study, we develop a simple, reliable, and highly efficient computational tool for simulating large-scale fluid flow and heat transport with fluid-rock isotope exchange, based on LB algorithms (Myre et al., 2011; Walsh et al. 2009; Kao and Saar, submitted); and Kao and Saar, in prep).

5.3.1 Groundwater flow

In standard LB algorithms, streaming and collision steps are implemented as described above, to simulate fluid flow through explicitly described small-scale pore-space geometries, as opposed to providing permeability tensor fields of discretized, large-scale continuum space. The latter is done in standard macroscopic groundwater flow modeling.

A relative simple way to introduce the capability of simulating macro-scale porous medium fluid flow in LB methods is to add a partial-bounce-back step into the standard two-step LB scheme (Dardis and McCloskey, 1998a,b; Sukop and Thorne, 2006; Walsh et al, 2009). Here, the degree of bounce-back is analytically determined according to local permeability via a solid fraction, as described in Walsh et al. (2009). This partial-bounce-back scheme exactly satisfies Darcy's Law in the incompressible limit (Walsh et al., 2009).

A standard two-dimensional (2D) version of the groundwater flow equation under incompressible and isotropic conditions can be given as (Garven and Freeze, 1984):

$$\frac{\partial}{\partial x}\left[\frac{k}{\nu\cdot\rho_f}\left(\frac{\partial P}{\partial x}+\frac{\partial P}{\partial y}\right)\right]+\frac{\partial}{\partial y}\left[\frac{k}{\nu\cdot\rho_f}\left(\frac{\partial P}{\partial x}+\frac{\partial P}{\partial y}\right)\right]= -\frac{k\cdot g}{\nu}\cdot\frac{\left(\rho_f-\rho_f^{ref}\right)}{\rho_f^{ref}}\cdot\frac{1}{L_f^{ref}} \tag{5.1}$$

where k is the local, here isotropic, permeability of the heterogeneous medium, ν is the local kinematic fluid viscosity, ρ_f is the local fluid density, which is a function of local temperature, g is Earth's gravitational acceleration, P is the fluid pressure given as $P=\rho_f\cdot g\cdot h$, where h is the hydraulic head, i.e., the sum of pressure head and elevation head), ρ_f^{ref} is a reference fluid density at a reference temperature of 25°C and specified at the ground surface (i.e., upper boundary), and L_y^{ref} is the vertical characteristic length along the gravitational direction, y, which is evaluated at a depth of interest, measured from the surface elevation (with ρ_f^{ref}) to the local crust elevation (with ρ_f).

The left-hand side in Equation (5.1) is the flow momentum term, which can be solved employing the partial-bounce-back LB scheme as it reaches steady state. The buoyant momentum on the right-hand side of Equation (5.1) is treated as a body-force term in the LB algorithm, as proposed by Kao and Yang (2007). Note that a porous medium buoyant characteristic velocity (q_{Buoy}) is defined as

$$q_{bouy}=-\frac{k\cdot g}{\nu}\cdot\frac{\rho_f-\rho_f^{ref}}{\rho_f^{ref}} \tag{5.2}$$

and, thus, the buoyant momentum, $\frac{q_{bouy}}{L_f^{ref}}$ satisfies the dimensions of $\nabla\cdot q$ as applied in the flow momentum equation as shown in Garven and Freeze (1984).

This buoyant source term was also used in Person et al. (2007), but in that study the buoyant momentum term does not satisfy the dimensioàns of $\nabla \cdot q$ which causes an over-evaluation of the buoyant momentum that results from the basal heat flux. For this reason, we test the actual significance of the geothermal buoyancy effect on fluid flow in our sensitivity study of crust permeabilities.

The LB formulation uses a dimensionless unit system with some numerical limitations. In order to implement geofluids simulations, we perform a scaling analysis to establish the relationship between numerical and physical unit systems (Appendix).

5.3.2 Coupled groundwater and heat transfer

As shown in Table 5.1, the thermal diffusivities of water (1.4×10^{-7} m^2/s) and rock (1.3×10^{-6} m^2/s) result in a linearly wheighted (e.g., Saar and Manga, 2004; Walsh and Saar, 2010) local mixed fluid-solid diffusivity range of 1.2×10^{-6} m^2/s $< D_m < 1.3 \times 10^{-6}$ m^2/s for the relatively low porosities of 0.08 to 0.03. These thermal diffusivity values are much larger than diffusivities of a solute (isotope) in water (10^{-10} m^2/s). Note that, the solid-phase solute diffusion can typically be ignored for computing the isotope transport and exchange (Bowman et al., 1994). As a result, the timescale differences between diffusive heat and isotope transport are significant, i.e., diffusive isotope transport is much slower than diffusive (i.e., conductive) heat transport. Hence, the coupled fluid flow and heat transport equations can be modeled until steady-state conditions are reached. In the present study, the macroscopic hydrothermal behavior is formulated by an advective-diffusive thermal transport equation under so-called “local-transport-equilibrium” (LTE) conditions, given as

$$\frac{\partial\left(\rho_m\, Cp_m\, T_m\right)}{\partial t} + q_x\, \rho_f\, Cp_f \frac{\partial T_m}{\partial x} + q_y\, \rho_f\, Cp_f \frac{\partial T_m}{\partial y} = \frac{\partial}{\partial x}\left(K_m \frac{\partial T_m}{\partial x} + K_m \frac{\partial T_m}{\partial y}\right) + \frac{\partial}{\partial y}\left(K_m \frac{\partial T_m}{\partial x} + K_m \frac{\partial T_m}{\partial y}\right) \tag{5.3}$$

where T_m is the local mixed fluid-solid temperature that is based on the LTE condition, q_x and q_y are Darcy velocities for the horizontal, x, and vertical, y, dimensions, respectively, $\rho_f Cp_f$ is the volumetric heat capacity of the fluid, $\rho_m Cp_m$ is the local mixed fluid-solid volumetric heat capacity inside the medium, which is determined by a linear-weighting, $\rho_m Cp_m = \phi \cdot \rho_f Cp_f + (1-\phi) \cdot \rho_s Cp_s$, where ϕ is the local porosity, and $\rho_s Cp_s$ is the rock volumetric heat capacity, and $K_m = \phi \cdot K_f + (1-\phi) \cdot K_s$ is the mixed thermal conductivity, where K_f and K_s are the thermal conductivities in the fluid and in the solid, respectively.

Note that in order to evaluate the buoyant momentum properly, the time-accurate term $\frac{\partial\left(\rho_m\, Cp_m\, T_m\right)}{\partial t}$ in Equation (5.3) is preserved when coupling the thermal computation with the fluid flow algorithm to evaluate the buoyancy effect at each numerical time-step. To solve Equation (5.3), we apply the macroscopic local-transport-equilibrium lattice-Boltzmann (LTE-LB) model proposed by Kao and Saar (in preparation). The numerical-physical scaling analysis is described in the Appendix.

5.3.3 Isotope transport and fluid solid exchange

As stated above, the solute (isotope) diffusivity is sapproximately four orders of magnitude smaller than the thermal diffusivities in the solid phase, in the fluid phases, or in the mixed fluid-solid complex phase. This implies that the diffusive isotope transport and fluid-solid isotope exchange is much slower than the diffusive (i.e., conductive) heat transfer. Hence, a time-dependent advective-diffusive solute

transport equation with a kinetic reaction term for fluid-solid isotope exchange must be considered (Bowman et al., 1994), such as

$$\frac{\partial R_f}{\partial t} + u_x \frac{\partial R_f}{\partial x} + u_y \frac{\partial R_f}{\partial y} = D_k \left(\frac{\partial^2 R_f}{\partial x^2} + \frac{\partial^2 R_f}{\partial y^2} \right) + \left. \frac{\partial R_f}{\partial t} \right|_{Reaction} \tag{5.4}$$

where R_f is the oxygen isotope in the fluid phase, D_h is the mixed solute diffusivity and is evaluated by linear weighting of $D_h = \phi \cdot D_f + (1-\phi) D_s$, where D_f and D_s are the solute diffusivities in the fluid and solid phase respectively, and $u_x = q_x/\phi$ and $u_y = q_y/\phi$ are the seepage velocities in the x and y directions, respectively. Other weighting functions could be employed instead, such as a geometric mean (e.g., Sass et al., 1971; Walsh and Saar, 2010), however, for low porosities, linear weighting is typically a good approximation (e.g., Saar and Manga, 2004).

The reaction term in Equation (5.4) employs a kinetic interfacial reaction and satisfies the conservation principle of solute exchange,

$$\left. \frac{dR_f}{dt} \right|_{Reaction} = - \left. \frac{dR_s}{dt} \right|_{Reaction} = -Da \cdot (\alpha_r \cdot R_f - R_s) \tag{5.5}$$

where R_s is the oxygen isotope in the solid phase, α_r is the equilibrium solute exchange factor, $Da = \dfrac{\bar{A} \cdot r_k \bar{L}}{u_f}$ is the local Damköhler number, where $\bar{A}$ is the bulk solid surface area, r_k is the local reaction rate, $\bar{L}$ is the characteristic length of interfacial reaction, and the characteristic seepage speed of the fluid is given as $u_f = \sqrt{u_x^2 + u_y^2}$, where ux and uy are seepage velocity components, obtained from dividing Darcy velocity components by the local porosity. In Equation (5.5) both α_r and r_k are determined as a function of the local temperature and the mineral components of the crustal unit (Person et al, 2007).

Based on the formulations of Equations 5.4 and 5.5, we implement a macroscopic lattice-Boltzmann fluid, heat, and isotopic transport as well as isotope reaction model, the latter employing an implicit reaction algorithm as described in

Kao and Saar (in prep). The numerical-physical scaling analysis is described in Appendix.

5.3.4 Computational domain and simulating conditions

The spatial dimensions of the computational domain, illustrated in Fig. 5.5 are 22.5 km horizontally and 12.5 km vertically. The upper plate is up to 7.5 km thick, the horizontal shear zone that simulates the brittle-ductile transition is 1.3 km thick, and the underlying lower plate is 4.2 km thick. We also study two different fault structures within the horizontal shear zone. In Case 1 ("connected"), there exists a 100 m thick hotizontal sub-fault (with the same permeability as the sub-vertical fault zones) that connects the two sub-vertical fault zones in the upper-plate crust. In Case 2 ("non-connected"), the sub-vertical upper-plate fault zones are not connected.

The lattice-Boltzmann (LB) numerical simulations employ the D2Q9 model, i.e., a squared two-dimensional (D2), nine-velocity (Q9) lattice system. The computational domain is divided into = 13,500 grid blocks for the horizontal, x, and vertical, y, dimensions, respectively. Applying our scaling analysis (Appendix), this grid number of 13,500 is sufficient to obtain accurate results using our LB models. Hence, special grid treatments employing complex computational techniques, are not required. In comparison to previous crustal fluid-flow models (Person et al., 2007), the simulation algorithms implemented here are simpler and result in higher computational efficiency, allowing more efficient exploration of larger parameter space. In addition, and as mentioned in Section 3.1, the buoyancy effect employed by Person et al. (2007) has been corrected here.

Therefore, in this paper, we investigate cases in which 1) the buoyancy effect due to heat transfer is turned on or off, 2) the sensitivity of fluid and heat transport

as well as isotope exchange dependence is investigated for various combinations of crust and fault permeability structures, 3) the two steep fault zones in the upper plate are connected by a high-permeability, horizontal fault within the shear zone, or not.

In our simulations, we apply no-fluid-flow boundary conditions on the two sides and at the bottom of the computational domain. A constant-pressure hydraulic head boundary condition is implemented at the upper land-surface boundary, i.e., the elevation of the high-, middle-, and low-elevation upper walls, shown in Fig. 5.5, determine the hydraulic head. For heat transfer computations, the two side walls are specified as no-heat-flux boundary conditions $\left(\frac{\partial T}{\partial x}\right)_{Sides} = 0$. The upper boundary is set by a constant temperature T_{upper} = 25°C at the ground surface. As mentioned before, we test both constant heat-flux and constant temperature boundary conditions at the bottom boundary of the model. For simulating fluid-rock oxygen isotope exchange, the equilibrium initial condition, $R_{s\cdot LB}^{initial} = \alpha_{rk} \cdot R_{f\cdot LB}^{initial}$, is implemented throughout the computational domain, where $R_{f\cdot LB}^{initial} = 1.0$ denotes $\delta^{18}O_{f\cdot phy}^{initial} = +8$ ‰. The boundary value of $R_{f\cdot LB} = 0$ (for $\delta^{18}O_{f\cdot phy} = -18$ ‰) is used at upper boundaries for representing the fresh fluid-phase oxygen isotope injected to the groundwater, and an extrapolating scheme is applied for the condition of $\left(\frac{\partial R_{f\cdot LB}}{\partial y}\right)_{bottom} = 0$.

In our numerical studies, computations of groundwater flow and advective-diffusive heat transfer are coupled by the buoyancy source term during each numerical time-step until steady-state conditions are reached. The steady state fluid and heat transfer solution is then used to simulate oxygen isotope transport and its fluid-rock exchange. Parameters used are listed in Table 1.

Property	Value
Thermal diffusivity of water (D_f)	1.4×10^{-7} m^2
Thermal diffusivity of rock (D_s)	1.3×10^{-6} m^2
Solute (isotope) diffusivity (D_h)	10^{-10} m^2
Fluid kinematic viscosity (ν)	9.8×10^{-7} m^2
Porosity (ϕ)	0.03 - 0.08
Geothermal gradient	45°C/km

Table 5.2: **Physical properties.**

5.4 Numerical modeling results

We conduct a numerical modeling sensitivity study to investigate the effects of permeability fields on groundwater flow patterns, heat transfer, as well as oxygen stable isotope transport and fluid-rock exchange. Different combinations of permeabilities are used for the upper crust, the steep fault zones, and the horizontal shear zone; six of the most significant cases are detailed in this paper (Table 5.2). For simplicity reasons and to keep the number of variable parameters to a minimum, all rock units in the model are isotropic with respect to permeability, i.e., the otherwise second-rank permeability tensor is reduced to a single, local permeability value that is applicable to both the horizontal and vertical directions. The basin and the lower crust have constant permeabilities of k = 10^{-14} m^2 and 10^{-19} m^2, respectively. The permeability of the fault zones and the shear zone are varied from 10^{-15} m^2 to 10^{-14} m^2 and 10^{-19} m^2 to 10^{-15} m^2, respectively. The upper crust permeability ranges from 10^{-19} m^2 to 10^{-17} m^2 (Table 5.2).

Our numerical modeling technique also offers the possibility of turning buoyancy driven convection on and off to assess the effects of buoyancy on flow pat-

	Log of Permeability (m^2)		
	Fault zone	Shear zone	Upper plate
Case 1	-15	-18	-19
Case 2	-15	-16	-19
Case 3	-14	-18	-19
Case 4	-15	-17	-17
Case 5	-14	-17	-17
Case 6	-19	-16	-17

Table 5.3: **Different permeability cases presented in this study.**

terns, temperature redistributions, and resultant oxygen isotope distributions.

Finally, the model is run with two different fault zone domains. In order to induce significant fluid flow through the sub-vertical fault zones, the fault zones need to be connected by a high-permeability horizontal channel within the shear zone, for example exhibiting the same permeability as the fault zone. This configuration is referred to as "fault-connected", whereas in the other case the faults are referred to as "unconnected".

5.4.1 Fluid flow pattern

In our simulation, Case 1 is the base model (Table 5.2). In this case, the upper and lower crust have the same, low permeability (10^{-19} m^2) and the permeability contrast between the fault zones (10^{-15} m^2) and the upper crust (10^{-19} m^2) is high (four orders of magnitude), thus forcing the fluid flow into the fault zones. When the fault zones are connected by a high-permeability, horizontal channel within the shear zone, the fluid flux increases along the path from the recharge fault zone (~1.5 m/yr) to the shear zone channel (~1.8 m/yr) and up the discharge fault zone

(~3.2 m/yr). When the faults are disconnected, because of the high permeability contrast between the fault and the shear zones (3 orders of magnitude), fluid flow is partly inhibited between the recharge and the discharge fault zones, leading to low fluid flow values of 0.6 m/yr in the recharge fault zone and 1.2 m/yr in the discharge fault zone.

In Case 2, the permeabilities of the upper crust and the fault zones remain the same as in Case 1, but the shear zone permeability is now 10^{-16} m^2, only one order of magnitude lower than that of the fault zones. Consequently, the higher permeability contrast between the upper crust and the shear zone enhances fluid flow through the shear zone, leading to higher fluid fluxes in the discharging fault. When, in addition, the fault zones are connected by a high permeability channel, the flow pattern is similar to Case 1: the fluid flux increases along the fault zone, from lower values (~2 m/yr) in the recharge fault zone to ~3 m/yr in the shear zone channel, to the highest values as the discharge fault zone connects to the near-surface basin (~3.8 m/yr). When the fault zone connection is no further enhanced by a high-permeability channel whithin the shear zone, in Case 2, the elevated permeability of the shear zone concentrates the fluid flow from the recharge to the discharge fault zone leading to slightly lower fluid flux values than those obtained in the "connected" scenario (~1.8 m/yr in the recharge fault zone, ~3.4 m/yr in the discharge fault zone).

Case 3 has higher-permeability fault zones (Table 5.2) than the base model (Case 1). The permeability contrast between the fault zones and the upper crust is five orders of magnitudes (10^{-14} m^2 and 10^{-19} m^2, respectively), one order of magnitude higher than the permeability contrast in the base model. Consequently, when the faults are connected by a high-permeability channel within the shear zone, fluid flow is even more restrained to the fault zones and the fluid flux values increase along the flow path from ~3.6 m/yr in the recharging fault zone to ~4.0

m/yr in the shear zone channel and up to ~4.6 m/yr in the discharge fault zone close to the near-surface basin. When the fault zones are not connected, the values are ~1.2 m/yr in the recharge fault zone and ~2.8 m/yr in the discharge fault zone. Increasing the permeability contrast by one order of magnitude between Cases 1 and 3 leads to a significant increase of the fluid fluxes in the fault zone (about 2 to 4 times higher in the disconnected and connected scenarios, respectively).

A higher permeability of the upper crust is investigated in Cases 4 through 6. In Case 4, the upper crust and shear zone both have the same (lower) permeability (10^{-17} m^2), whereas the fault zones remain at a permeability of 10^{-15} m^2. Lower permeabilities of the upper crust and shear zone lead to a higher fluid flux (~2 m/yr). Because the fault/upper crust permeability contrast is reduced to two orders of magnitudes, the fluid flow is less restricted to the fault zones and fluid leaks into the shear zone. When the fault zones are disconnected, the fluid flux reaches high values in the recharging and discharging areas (top of the fault zones), but decreases rapidly along these steep fault zones.

Case 5 has the same configuration as Case 4, except that the permeability of the fault zone is one order of magnitude higher (10^{-14} m^2). A higher fault/upper crust permeability contrast again enhances flow in the fault zones and the shear zone channel. Therefore, the fluid fluxes double between Case 4 (~12 m/yr) and Case 5 (~24 m/yr)

In the barrier configuration (Case 6), the permeability of the fault zone is set to 10^{-19} m^2, two orders of magnitude smaller than the upper crust (10^{-17} m^2), leading to a very small fluid flux across and within the fault zone. The permeability of the crust and shear zone is identical to Cases 4 and 5 leading to the same fluid flux (~2 m/yr).

5.4.2 Temperature distribution

In the base model (Case 1), when the sub-vertical fault zones are connected by the horizontal, high-permeability channel within the shear zone, the flow along the recharge fault zone carries cool fluids downwards, deflecting the isotherms (Fig. 5.6). The temperature at the bottom of the recharge fault zone is thus only about 175°C. Within the horizontal, high-permeability shear zone channel, the fluids are heated up by ~100°C, resulting in a temperature of ~275°C at the bottom of the discharge fault zone. The rapid flow of initially, relatively cool fluid in the shear zone channel produces a concave deflection and tightening of the isotherms in the lower crust. The discharge fault zone brings the heated fluid up to the near-surface basin, displacing the isotherms upward and heating the basin in the vicinity of the discharge fault zone by ~25°C (Fig. 5.6. When the faults are not connected by the horizontal high-permeability channel (Fig. 5.7), the temperature field around the recharge fault zone is slightly reduced by ~25°C. However, in this case, the isotherms are also pinned and compressed at the bottom of the discharge fault zone, leading to a ~100°C vertical gradient over ~2 km across the shear zone.

In Case 2, the permeability of the shear zone (without a high-permeability channel) is 10^{-16} m^2, higher than in the base case so that the permeability contrast between the shear zone and the crust is also higher (by three orders of magnitude). This leads to a strong channeling of the fluids within the shear zone, with minor leakage into the lower crust (Fig. 5.6). The temperature distribution is similar to the base model (Case 1). The shear zone channelizes the influx of cool fluids that are then slowly heated within the shear zone, leading to a temperature inversion close to the bottom of the discharge fault zone. When the faults are disconnected (Fig. 5.7), the same temperature pattern is observed as Case 1, with a more pronounced pinning effect at the bottom of the discharge fault zone (~125°C of vertical

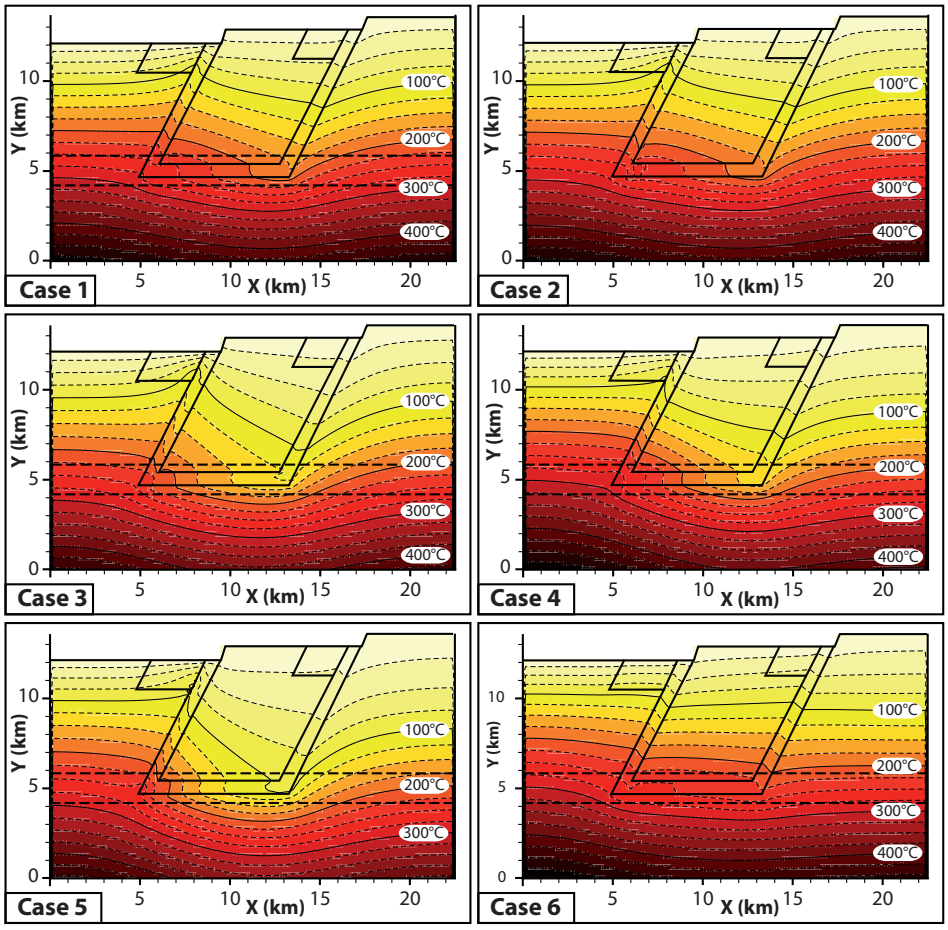

Figure 5.6: **Temperature results, faults connected.**

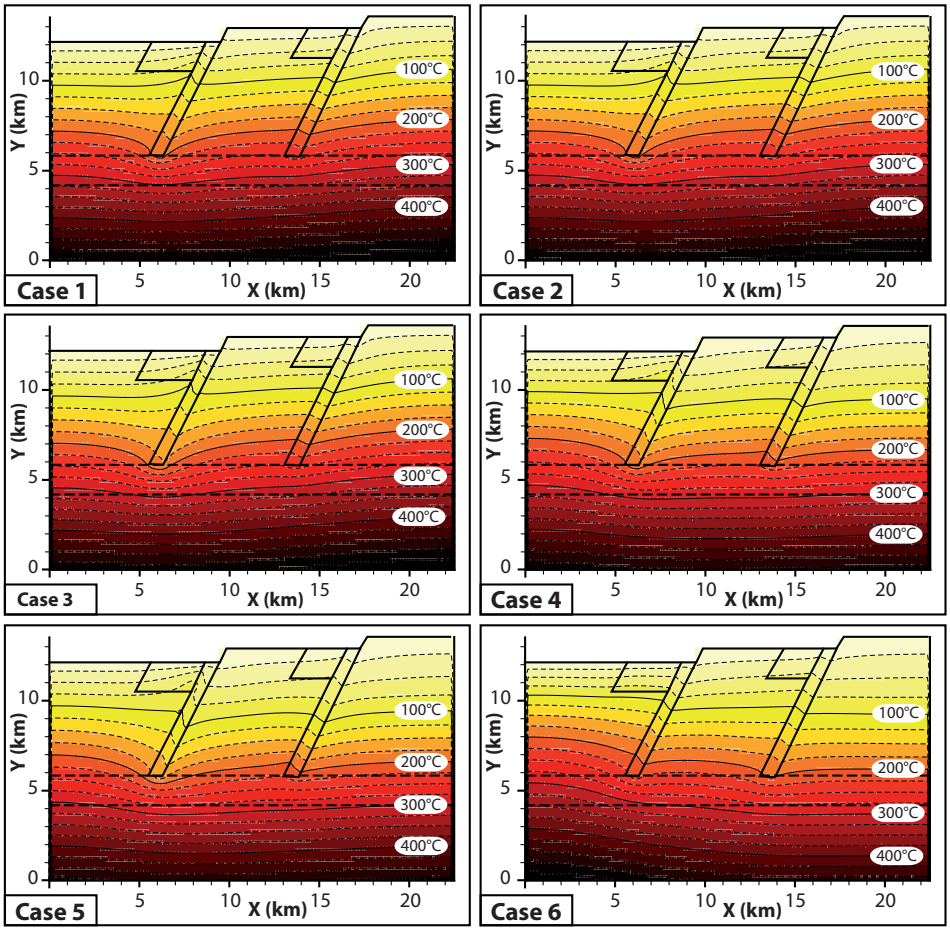

Figure 5.7: **Temperature results, faults unconnected.**

gradient over the 2km thick across the shear zone). This pinning of the isotherms produces a reduced thermal gradient along the discharge fault zone.

In Case 3, the fault zone has a high permeability (10^{-14} m^2) so that the permeability contrast with the shear zone and upper crust is significant (4 and 5 orders of magnitude, respectively) and is responsible for concentrating the flow in the shear zone channel. Consequently, the upper crust experiences significant cooling with temperatures as low as ~125°C at the bottom of the recharge fault zone at a depth of ~6 km (Fig. 5.6). The isotherms in the upper crust to the right of the recharge fault zone become significantly more bent downwards in the vicinity of the fault zone, creating temperature perturbations of ~-50°C. The block between the two fault zones is also significantly cooled. Under the shear zone the leakage of cool fluids produces a strong downward deflection and a tightening of the isotherms in the lower crust. As the fluids find their way upward in the discharge fault zone, they heat the discharge area, with temperature perturbations >+50°C in the basin. The disconnected vertical faults scenario is similar to Case 2 (Fig. 5.7).

In Case 4, because the permeability contrast between the fault zones and the crust is lower, flow is more distributed within the crust and cooling is less localized than in Case 3 (Fig. 5.6). However, the same concave deflection and tightening of the isotherms under the shear zone and sharper vertical thermal gradients across the shear zone channel (150°C / 2 km) are observed. The more distributed flow in the crust leads to strong upward flow in the discharge area and resultant heating of the discharge basin. The disconnected scenario is similar to Case 3 (Fig. 5.7).

In Case 5, the permeability of the fault zones is decreased by one order of magnitude (10^{-14} m^2) and the patterns observed are similar to Case 4, but are more pronounced (Fig. 5.6). The high permeability of the recharge fault zone concentrates fluid flow down into the shear zone, leading to a dramatic cooling of the recharge fault zone (~-65°C temperature perturbations), with temperatures < 100°C as the

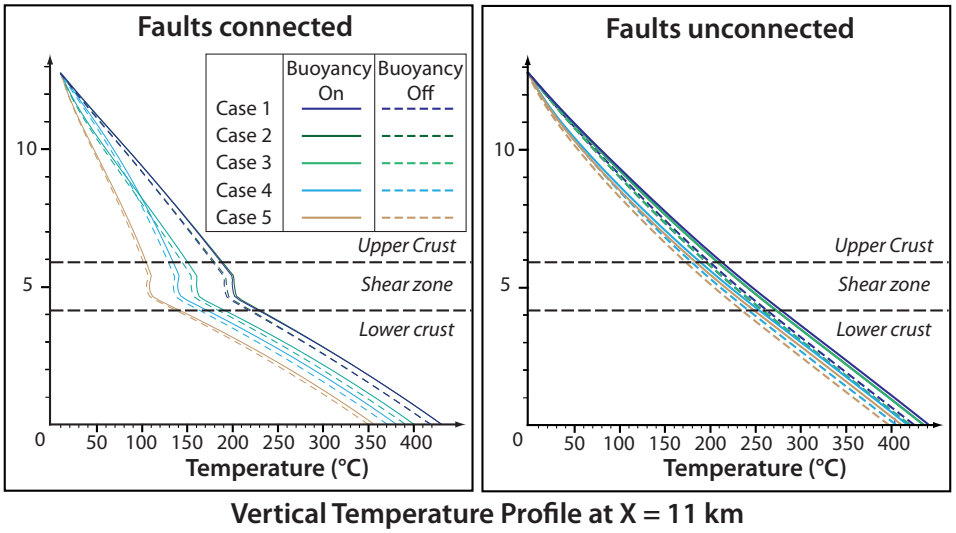

Figure 5.8: **Effect of buoyancy.**

flow reaches the shear zone at ~6 km depth. The block between the two fault zones is profoundly cooled, and the same strong bending of the isotherms to the right of the recharge fault zone is observed. The fluids are heated along the shear zone producing a strong thermal gradient from the recharge fault zone (~100°C) to the discharge fault zone (~250°C). Hot fluids are brought up to the surface along the discharge fault zone, heating the discharge basin resulting in temperature perturbations of >+25°C. The same downward deflection and tightening of the isotherms generated by the flow of cool fluids in the shear zone is observed in the lower crust. The disconnected steep fault zone scenario is similar to Case 3 (Fig. 5.7).

5.4.3 Oxygen isotope distribution

A review of oxygen and hydrogen stable isotope data available for metamorphic core complexes allows us to constrain the oxygen isotopic composition of the fluid and the starting value of the rock. Typical hydrogen stable isotope values esti-

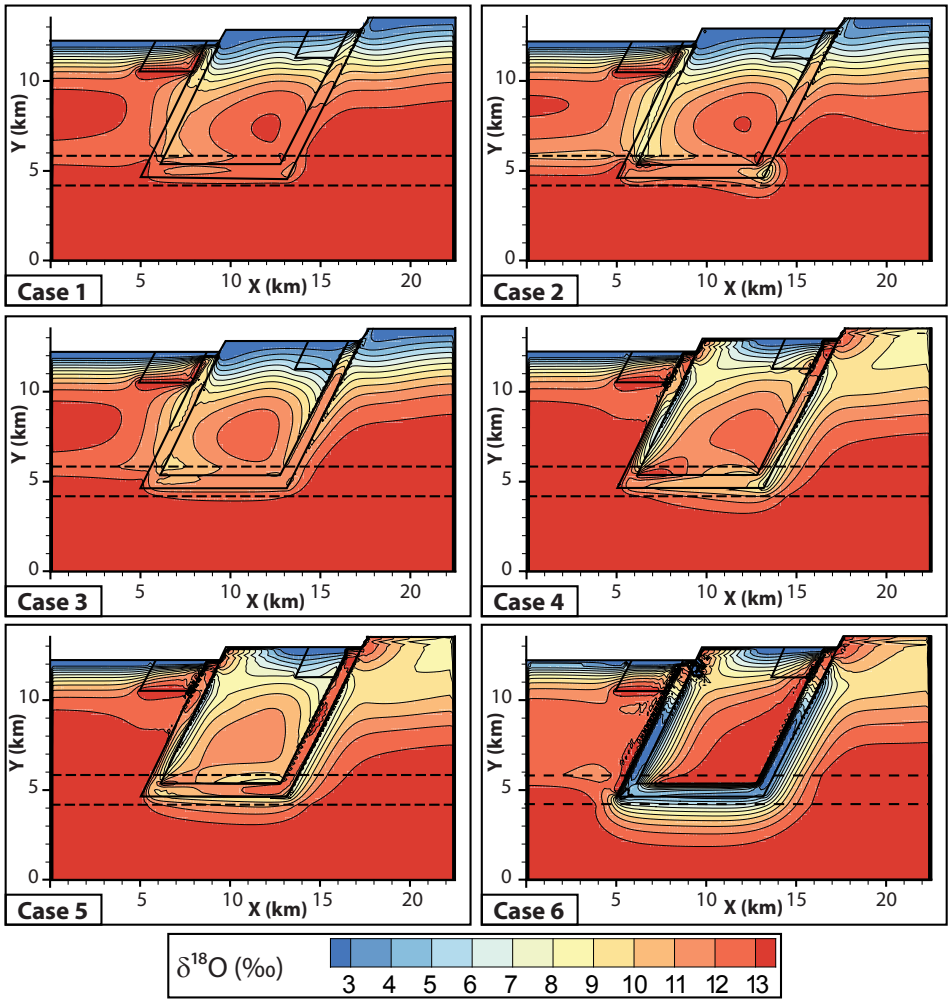

Figure 5.9: **Oxygen stable isotope results, faults connected.**

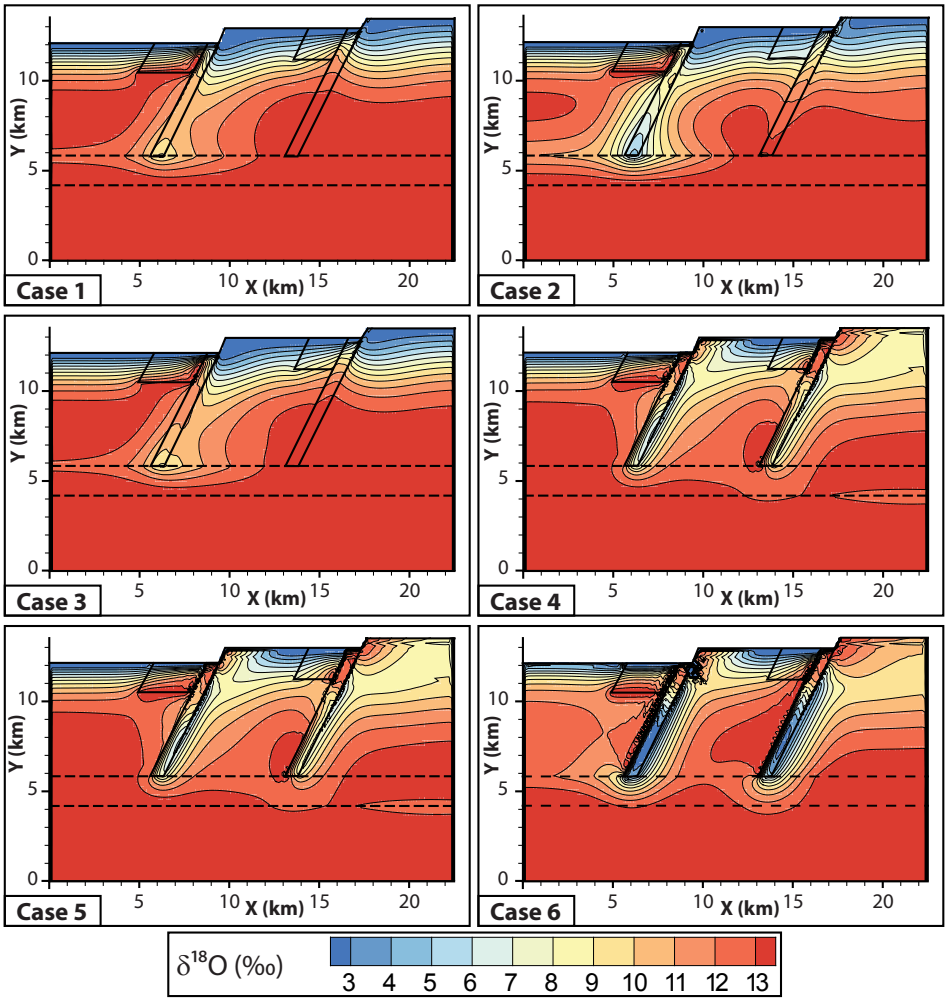

Figure 5.10: **Oxygen stable isotope results, faults unconnected.**

mated for fluids percolating in a detachment system during mylonitization range from -80 to -120 ‰ (see Fig. 5.3 and reference therein). Using the calibration of Suzuoki and Epstein (1976) and assuming a temperature of mylonitization of 450°C, a fluid with a δD of -120 ‰yields a $\delta^{18}O$ of ~-18 ‰. Therefore, the fluid composition is set to $\delta^{18}O$ = -18 ‰ in our model. Typical $\delta^{18}O$ of quartz from the protolithe of mylonitic zones are about 13 ‰. Therefore, the starting oxygen isotope composition of the rock in our model is set to $\delta^{18}O$ = +13 ‰.

In the base model, Case 1, when the steep fault zones are connected, the infiltration of $\delta^{18}O$ depleted water is recorded at shallow depth (upper 1 km) where the oxygen isotope composition of the rock is gradually less depleted with depth, from ~3 ‰ at the surface to normal values of 13 ‰ at ~4 km below the surface (Fig. 5.9). The oxygen depletion is more pronounced on the right side of the model where the hydraulic head gradient is the highest. The rock oxygen isotope composition is only slightly modified (~12 ‰) along the recharge fault zone and the shear zone channel. However, the combination of compressed isotherms and high fluid flux on the discharging limb of the fault system yields more depleted (~10 ‰) rocks along the discharging fault zone. Hot fluids discharging in the basin maintain the initial composition of the rock in the discharging area at the connection between fault and basin. When the fault zones are not connected (Fig. 5.10), the pinning effect of compressed isotherms under the discharging fault zone leads to strong oxygen isotope depletion down to ~7 ‰. The only major depletion occurs along the discharging path, with values ~10 ‰ in the fault zone.

In Case 2, the higher permeability shear zone concentrates the flow leading to a stronger depletion of the rock oxygen isotope composition. When the fault zones are connected, relatively depleted values (~8 ‰) are reached at the base of the recharge fault zone, where cool fluids reach the shear zone (Fig. 5.9). Then fluids are progressively heated along the shear zone, and the composition is less

affected (~12 ‰). In the discharging fault zone, the same pattern as in Case 1 is observed, only more pronounced, with values down to ~7 ‰ in the discharging fault zone. In the disconnected scenario (Fig. 5.10), the isotopic pattern observed is similar to Case 1, but the depletion at the bottom of the discharging fault zone is more pronounced (~4 ‰). The depletion spreads outward from the discharging fault zone.

In Case 3, the isotope results for the both connected and the disconnected scenarios show a pattern intermediate to Cases 1 and 2, except for the block between the two fault zones is more depleted because of the more pronounced channelized fluid flow induced by the faults (Fig. 5.9 and 5.10).

Case 4 has a more permeable crust (10^{-17} m^2) and fluid flow through the system is faster. In addition, a lower permeability contrast between the crust and the fault zones (only two orders of magnitude) allows leakage of fluids through the crust. Therefore, when the faults are connected (Fig. 5.9), a strong depletion in oxygen isotope values is observed in areas of high hydraulic head gradients. At the beginning of the recharge fault zone, the fluid flux is too strong, compared to the rate of fluid-rock oxygen isotope exchange, to affect the rock composition, which, thus, maintains a value of ~12 ‰. However, the rock in the upper crust, close to the fault, shows oxygen isotope values as low as 6 ‰, gradually less depleted as the temperature increases along the shear zone channel, indicating strong fluid-rock oxygen isotope interaction. On the right side of the model, the isocomposition curves show the same deflection as the isotherms. Along the discharging fault zone, high fluid flux values strongly deplete the fault zone rocks in oxygen isotope values (down to ~4 ‰). In contrast, discharge fluid flux on the left side of the model is sufficiently vigorous to maintain the starting oxygen isotope composition. A similar depletion pattern is observed for the disconnected fault zone scenario (Fig. 5.10), with oxygen isotope values as low as ~4 ‰ along the fault zones. The

shear zone, however, almost preserves its original oxygen isotope composition of ~12 ‰.

In both the disconnected and the connected fault zone scenarios, Case 5 is very similar to Case 4, except that the block between the two faults is more depleted in oxygen isotopes, with upper values of ~12 ‰.

5.5 Discussion

Here we discuss the effects that buoyancy-driven flow has on fluid flow, temperature, and oxygen isotope fields (Section 5.1). Numerical modeling results are discussed in Section 5.2 that provide fluid flow patterns and rates and resultant temperature and oxygen isotope distributions as a function of permeability fields. Section 5.3 compares our results with field observations.

5.5.1 Effect of buoyancy

Buoyancy affects fluid flow patterns, and, therefore, controls temperature and oxygen isotope transfer as well as fluid-rock isotope exchange. When buoyancy is turned off (Fig. 5.8), fluid flow is driven only by the hydraulic head gradient from the high-elevation block on the right to the low-elevation block on the left. When buoyancy is turned on (Fig. 5.8), a significant upward component is added to the fluid flow, which in turn causes significant downward flow. Upward flow in the lower crust and topography-driven flow in the upper crust meet in the model, such that flow lines converge to the left side of the model. Even though there is a significant difference in the flow direction, the magnitude of fluid flow, which is largely controlled by permeability (Manning and Ingebritsen, 1999), shows little to no variation. Upward flow in the lower crust, when buoyancy is on, transfers significant heat, which leads to a different temperature distribution compared to the

buoyancy-off case (Fig. 5.8). When buoyancy is on, the temperature field shows positive deviations of about ~25°C compared to the case when buoyancy is off, although the model isotherms have essentially the same shape and distribution. This temperature increase is not sufficient to affect oxygen isotope fluid-rock exchange, and, therefore, isotope values remain the same whether buoyancy is turned on or off.

5.5.2 Effect of high permeability connection between the fault zones on the temperature and oxygen isotope distributions

Our motivation to connect the fault zones by a high-permeability channel within the shear zone is to strongly enhance fluid flow through the system and, in particular, along the detachment shear zone. Detachment zones usually develop at the brittle ductile transition and the deforming rock develops a strong foliation (Lister and Williams, 1979; Davis and Coney, 1979; Bell, 1981). This foliation is usually subhorizontal and thus constitutes a major anisotropy for fluid flow (Sibson, 1996; Zharikov et al., 2003). Therefore, connecting the fault zones is a way to take into account such anisotropy without introducing anisotropic permeability tensors into the system. Without connection, fluid flow is controlled by the permeability contrast between the shear zone and the upper/lower crust. If this permeability contrast is small (one order of magnitude), the flow is not significant enough to produce major thermal and/or oxygen isotope perturbations.

When the fault zones are not connected, the isotherms are relatively flat around the shear zone, with a temperature of about 250°C. In contrast, when the fault zones are connected, cool fluids from the high-elevation block are focused into the shear zone, strongly deflecting the isotherms downward by more than 50°C. At the same time, the isotherms become vertical in the shear zone, leading to a

temperature gradient along the flow path of about +75°C from the right to the left of the shear zone. This effect becomes stronger as the permeability contrast between the crust and the shear zone increases. In addition, since the fault zones are connected to the shear zone and serve as conduit for fluids, if the fault zones have a high permeability, they bring more fluids into the shear zone, which has the effect of cooling the recharge fault zone and the shear zone.

These results on the flow and temperature field are also expressed in the oxygen isotope distribution. When the fault zones are not connected, enhanced flow in the upper part of the recharge fault zone produces strong isotopic depletion of the rock (down to $\delta^{18}O$ = ~5 ‰). But as the fluid migrates toward the bottom tip of the fault zone, flow slows down and isotopic exchange is limited resulting in $\delta^{18}O$ values of ~7 ‰ in the crustal rocks. When the fault zones are connected, we observe progressively lower $\delta^{18}O$ values along the path of the fluids through the recharge fault and shear zone where $\delta^{18}O$ values reach ~10 ‰. An interesting observation is that, in the fault-connected scenario, the rocks that form the core of the fault zones usually remain at a higher oxygen isotope value than the surrounding rocks outside the fault zones. This could be explained by the "leakage" of fluids away from the fault zones and into rocks that are at higher temperature, leading to a stronger depletion of the isotopes in the vicinity of the fault. At the same time, transport within the fault is too fast, compared to the rate of fluid-rock oxygen isotope exchange, for significant oxygen isotope depletion to occur in the fault itself. This effect is more pronounced as the fault/crust permeability contrast increases (very strong in Case 5).

The case that best documents these relations is Case 5, where the fault/crust permeability contrast is two orders of magnitude. The low-permeability recharge fault zone brings the cool fluids down to the shear zone. When the fault zones are not connected, no heat deflection effect is observed because the fluids do not flow

efficiently past the tip of the fault zone, and, therefore, the temperature field is not affected. If the fault zones are connected, the fluids have an outlet and the recharge fault zone experiences significant cooling (T = 100°C at only 5 km depth). In this case, the fluid flows in the shear zone, where it is heated along its path, yielding a strong temperature gradient along the shear zone of ~150°C. The temperature at the base of the shear zone is in this case ~200°C, while it is about 300°C when the faults are not connected. Hence, fault connection has a very strong influence on both temperature and oxygen isotope distribution around the fault and shear zones.

Another important result comes from the shape of the isotherms in the vicinity of the recharge fault zone. When the fault zones are not connected, the isotherms are deflected downward at the bottom of the recharge fault zone. The discharge fault zone drains the cooler fluid that flows upward in the higher-permeability conduit. At the bottom of the fault zone, transport is more efficient than heating, which results in a general cooling. As the fluid moves up, it eventually heats up, leading to an upward deflection of the isotherms. When the fault zones are connected, no such feature is observed and the isotherms are always deflected upward in the discharging fault zone, since the fault zone drains the hot fluids out of the shear zone. This observation is not reflected in the isotope distribution. Along the discharging fault zone, the isotopes tend to show a gradient from higher $\delta^{18}O$ at the bottom tip of the fault zone to lower values near the surface, the intensity of this gradient depending on the fault/crust permeability contrast; when the contrast is higher, the gradient is stronger.

Finally, it is important to note that significant heat perturbations are typically observed in the basin. The temperature boundary is fixed and cannot change at the surface. The high permeability of the basin attracts and deviates the fluid coming out of the fault zone, leading to heating of ~50°C of basin material in the vicinity of the fault zone. When faults are connected, the substantial discharge of hot fluid

produces an even stronger perturbation in the basin (nearly 100°C). Although this strong thermal perturbation is observed, the flow of hot fluid is too fast, compared to the isotopic exchange rate, leading to little perturbation of the $\delta^{18}O$ composition.

5.5.3 Comparison with field observations

Extensional tectonics driven by orogenic collapse and leading to the development of metamorphic core complexes generates high amplitude relief, for example through domino-style tilting of upper crustal blocks as observed in the present topography of the Basin-and-Range province. Hot ductile lower crust is brought in contact with the brittle upper crust that thins by normal faulting and locally opens major crustal-scale conduits for upward or downward fluid flow, which enhances heat transfer. In such a system, fluid circulation is driven by the high-amplitude topography and typically more importantly the fluid buoyancy that is generated by the high heat flux in the lower crust.

Our numerical lattice-Boltzmann (LB) fluid flow model attempts to reproduce this scenario and shows that significant heat and oxygen isotope perturbations result from such meteoric fluid flow of originally meteoric water, the magnitude of these changes depending on the permeability contrast between the different hydrologic units. Results show that significant heat transfer and isotopic depletion of crustal rocks is achieved when the permeability contrast between the fault and the crust is at least two orders of magnitudes (10^{-15} m^2 to 10^{-14} m^2 for the fault zones, 10^{-19} m^2 to 10^{-17} m^2 for the crustal units). Heat transfer and oxygen isotope depletion is even more pronounced when the steep fault zones are connected by a horizontal zone of similar permeability within the shear zone. In our model, this connecting “channel” is 750 m thick (like the fault zones) and is comparable in

nature to the development of strongly foliated mylonitic or cataclastic shear zones of similar thicknesses (Fig. 5.5).

In nature, preserved transient thermal gradients have been reported based on oxygen stable isotope thermometry studies, ranging from 82°C / 38 m to 140°C / 100 m (Whipple Mountains, Morrisson and Anderson, 1994; Raft River Mountains, Gottardi et al., 2011, respectively). Such sharp transient thermal gradients are the results from crust thinning and heat advection. Most detachment shear zones that develop during the exhumation of metamorphic core complexes probably evolved at a shallow dip angle (for example in the Raft River Mountains, Wells et al., 2000; in the Snake Range, Miller et al., 1999), a process that can lead to a high metamorphic gradient only if the shear zone accommodates large displacement. In addition, thinning of the lower crust also leads to heat advection. Even though our model does not include any deformation, it produces instantaneous thermal gradients across the shear zone of up to ~75°C/km. Coupling extensional deformation to the model would lead to major compression of the isotherms and higher thermal gradients, as observed in large-scale deformation models (Rey at al., 2009a, 2009b).

Another outcome of the numerical models is the static horizontal temperature gradient along the shear zone that is significant (~25°C/km) and should be kept in mind when observing temperature gradients from rocks sampled along the transport direction. Finally, thermal results also show that, depending on the permeability of the upper crust, significant cooling of recharge fault zone and the recharge basin as well as heating of the discharge fault zone and discharge basin can be produced. The magnitude of these perturbations (up to 50°C) is sufficiently large to affect low-temperature thermochronometers.

The model as constructed in this paper yields temperatures in the upper crust and the shear zone that are below the temperature of mylonitization estimated from

field studies: the highest temperatures are produced in Cases 1 and 2, where the temperature at the top of the shear zone (~7 km deep) is ~200°C (160°C, 140°C and 110°C for Cases 3, 4, and 5 respectively). The natural data (Table 5.1 and Fig. 5.3) show that the midcrustal shear zone of a metamorphic core complex develops at ~5 to 8 km depth, at temperatures ranging from 300°C to 500°C, substantially higher than our modeling results. This discrepancy between our modeling results and the measurements has several implications. First, if the results are taken at face value, midcrustal shear zones develop much deeper in the crust, probably around 12 km. Second, we used a 45°C/km geothermal gradient in our calculation, so if we want to reproduce the natural measurement (~400°C shear zone at ~7 km depth), we would need to use a much higher geothermal gradient value. This implies that natural detachment system may develop under higher geothermal gradients than usually estimated. Unfortunately our model couldn't support geothermal gradients higher than 55°C/km, so we couldn't test the effect of higher geotherms. Finally, if the temperatures in natural systems are higher, then, more fluid-rock isotope exchange is expected since temperature enhances the fluid-rock exchange.

Our model also shows oxygen isotope depletion patterns that are very similar to natural cases. Typical quartz $\delta^{18}O$ compositions from the unmylonitized core of Cordilleran metamorphic core complexes is ~13 ‰ (Kettle Dome, Mulch et al., 2004, 2006; Bitterroot, Foster et al., 1997, 2002) and the lowest quartz $\delta^{18}O$ values range from 7.90 ‰ (Whipple, Morrisson and Anderson, 1994), 9.8 ‰ (Bitterroot, Foster et al., 1997, 2002; Raft River, Gottardi et al., 2011), 10 ‰ (Thor-Odin, Mulch et al., 2004, 2006) to 11.4 ‰ (Snake Range, Gébellin et al., 2011). However, the extreme depletion observed in the Ruby Mountains ($\delta^{18}O_{quartz}$ = 2.8 ‰, Fricke et al., 1992, and 5.0 ‰ in the Kettle dome, Mulch et al., 2007) are not predicted. In addition, several studies show that in general, surface fluids do not penetrate into the lower crust below the detachment fault zone (Fricke et al., 1992;

Holk and Taylor, 2007) but do penetrate to the detachment shear zones and the ductile layer in the footwall of the detachment fault (Mulch et al., 2004, 2006, 2007). This is observed in our model: the oxygen isotope depletion is restricted to the fault zones and along the detachment zone at the interface between upper and lower crust, with oxygen isotope ratios lowered from 13 ‰ (starting value) down to ~6 ‰. There are few studies of stable isotopes from supra-detachment basins available in the metamorphic core complex literature. A very detailed study (Wickham et al., 1993; Bickle et al., 1995) of the Lizzies Basin, which developed during the exhumation of the Ruby Mountains shows preservation of high $\delta^{18}O$ values in rocks of the basin (~12 to 13 ‰). Similar oxygen isotope distribution patterns are produced in our model. Fluids approaching the ground surface within a discharging fault zone spread into the high-permeability basin, where the temperature is not high enough and the flow rate is too large, compared to fluid-rock oxygen isotope exchange rates, to alter oxygen isotope composition, thereby preserving the original oxygen isotope composition of the rocks.

Conclusion

Several oxygen and hydrogen isotopic studies of North-American core complexes show that circulation of meteoric fluids during the development of the detachment shear zone is ubiquitous. The fluid-rock oxygen isotope exchange is a result of the interplay between rock type, temperature, fluid flow, duration of exchange, permeability, and fluid pathways. The results of our numerical model suggest that the characteristics of the permeability field is primarily controls the flow of meteoric fluids and the resultant distribution of temperature and oxygen isotopes. Strong thermal gradients (vertical and lateral) as well as significant oxygen isotope depletion are produced by our model when the fault zones are connected, i.e., when

fluid flow is channelized into the horizontal shear zone, corresponding, in nature, to the development of planar anisotropy in the shear zone due to foliation-enhancing horizontal flow.

Conclusions

This multidisciplinary project on the Raft River metamorphic core complex provides insight on the hydrology and the thermal and mechanical evolution of the continental crust during extension and orogenic collapse. Detailed microstructural analysis combined with oxygen stable isotope thermometry provide critical information on the thermomechanical evolution of detachment shear zones, and oxygen and hydrogen stable isotopes analyses pooled with 2D heat and fluid flow modeling demonstrate that fluids play a major role in deformational processes.

During orogenic collapse the thickened continental crust is divided into two layers with contrasting thermal and rheological behaviors. The cold and brittle upper crust is separated from the hot and ductile lower crust by a mylonitic detachment zone. Detachment zones are therefore critical interfaces for studying the interplay between the parameters that govern the rheology of the crust (temperature, stress, strain rate, fluids).

The east-rooted, Oligo-Miocene Raft River shear zone is localized in the Proterozoic Elba Quartzite that rests unconformably on an Archean basement complex. This study focuses on the eastern part of the Oligo-Miocene shear zone, in the Clear Creek area, where the detachment is localized in a 100 m thick quartzite-dominated shear zone. Quartzite is an excellent material to study because the mechanisms of quartz deformation are relatively well-known from both

natural and experimental investigations. The main conclusions of this study are as follows:

1) $^{40}Ar/^{39}Ar$ geochronology of 4 samples spread vertically over the detachment shear zone display complex release spectra, but plateau ages decrease systematically from 31.1 $\pm$ 0.8 Ma at the top to 20.2 $\pm$ 0.6 Ma at the bottom of quartzite mylonite.

2) Hydrogen stable isotope values of synkinematic muscovite and fluid inclusions are low (-123 ‰ < $\delta D_{muscovite}$ < 88 ‰, and -104 ‰ < $\delta D_{fluidinclusions}$ < -83 ‰, respectively) suggesting that meteoric fluids with low D/H and $^{18}O/^{16}O$ ratios were infiltrating the detachment shear zone over the time scale of mylonite formation.

3) Oxygen isotope thermometry using recrystallized quartz-muscovite pairs indicates a sharp thermal gradient (140°C/100 m) across the detachment shear zone, from 350°C at the top to 485°C at the bottom of the shear zone.

4) Detailed microstructural, electron backscattered diffraction, strain, and vorticity analyses of the very well exposed quartzite mylonite show a strengthening of the rock fabrics from west to east, along the transport direction, compatible with observed finite strain markers, that fits a model of necking of the shear zone.

5) Both quartz recrystallized grain size paleopiezometry and paleopiezometry based on the spacing of deformation lamellae reveal very similar results, indicating that the shear zone developed under stress ranging from 40 MPa to 60 MPa. Combining stress and temperature estimates in a quartzite dislocation creep flow law constrains the strain rate experienced by the detachment shear zone between 10^{-12} and 10^{-14} s^{-1}.

6) Microstructural evidence (quartz microstructures and deformation lamellae) suggests that the detachment shear zone evolved at its peak strength, close to the dislocation creep/exponential creep transition. Quasi-constant flow stress over the entire study area suggests that strain rate, temperature, and fluid activity

must balance one another in response to the evolving strength of the shear zone. The abrupt thermal gradient (140°C/100 m) revealed by oxygen isotope thermometry was likely produced by a combination of ductile shearing and thinning (deformed isograds), heat advection, and enhanced cooling by meteoric fluids. The interplay of these thermal, mechanical, and hydrological processes can trigger significant shear instabilities and strongly influence the rheology of the detachment shear zone.

7) Detailed oxygen stable isotope analyses of quartz/muscovite pairs show different degree of oxygen isotope depletion, suggesting different time-integrated interaction of the minerals with meteoric fluid. Variations in permeability of the basement units and in finite strain along the transport direction (from flattening to constriction) can affect the flow pattern (confined vs. diffuse flow, plane vs. pipe flow) and therefore the various degrees of fluid-rock interaction revealed by the stable isotopic record.

8) Continuum-scale (i.e., large-scale, partial-bounceback) lattice-Boltzman simulations of fluid, heat, and oxygen isotope transport in an idealized cross-section of a metamorphic core complex reveal that fluid migration to mid- to lower-crustal levels has to be fault controlled and depends primarily on the permeability contrast between the fault zone and the crustal rock. Channelized fluid flow in the shear zone leads to strong vertical and horizontal thermal gradients.

References

Abalos, B., 1997, Omphacite fabric variation in the Cabo Ortegal Eclogite (NW Spain); relationship with strain symmetry during high pressure deformation. *Journal of Structural Geology*, v. 19, p. 621-637.

Afonso, J. C., and Ranalli, G., 2004, Crustal and mantle strengths in continental lithosphere: is the jelly sandwich model obsolete?, *Tectonophysics*, v. 394, no. 3-4, p. 221-232.

Anderson, J. L., 1985, Contrasting depths of core complex mylonitization. Abstract with programs, *Geological Society of America*, v. 17, p. 337.

Antonellini, M., and Aydin, A., 1994, Effect of faulting on fluid flow in porous sandstones: Petrophysicial properties, *American Association of Petroleum Geologists Bulletin*, v. 78, p. 355-377.

Armstrong, R.L., 1968, Mantled gneiss domes in the Albion Mountains, southern Idaho. *Geological Society of America Bulletin*, v. 79, p. 1295-1314.

Armstrong, R. J., 1982, Cordilleran metamorphic core complexes-from Arizona to southern Canada, *Annual Reviews of Earth and Planetary Sciences*, v. 10, p. 129-154.

Armstrong, R.L., and Hills, F.A., 1967, Rb-Sr and K-Ar geochronologic studies of mantled gneiss domes, Albion range, southern Idaho, USA, *Earth and Planetary Science Letters*, v. 3, p. 114-124.

Austrheim, H., 1987, Eclogitization of lower crustal granulites by fluid migration through shear zones, *Earth and Planetary Science Letters*, v. 81, no. 2-3, p. 221-232.

Axen, G.J., Wernicke, B. P., Skelly, M. F., and Taylor, W. J., 1990, Mesozoic and Cenozoic tectonics of the Sevier thrust belt in the Virgin River Valley area, southern Nevada: in Wernicke, B.P. (ed.), Basin and Range extensional tectonics near the latitude of Las Vegas, Nevada, *Geological Society of America Memoir 176*, p. 123-153.

Axen, G.J., 1992, Pore pressure, stress increase, and fault weakening in low-angle normal faulting, *Journal of Geophysical Research*, v. 97, no. 6, p. 8979-8992.

Axen, G.J., and Selverstone, J., 1994, Stress state and fluid pressure level on the Whipple detachment fault, California, *Geology*, v. 22, p. 835-838.

Baas, J. H., 2000, EZ-ROSE: a computer program for equal area circular histograms and statistical analysis of two dimensional vectorial data, *Computers and Geosciences*, v. 26, p. 153-166.

Baldwin, S. L., and Lister, G. S., 1998, Thermochronology of the South Cyclades Shear Zone, Ios, Greece: Effects of ductile shear in the argon partial retention zone, *Journal of Geophysical Research*, v. 103, no. 4-7, p. 315-7336.

Banks, D.A , Da Vies, G.R, Yardley, B. W. D, McCaig, A. M., and Grant, N. T., 1991, The chemistry of brines from an Alpine thrust system in the Central Pyrenees: An application of fluid inclusion analysis to the study of fluid behaviour in orogenesis, *Geochimica et Cosmochimica Acta*, v. 55, no. 4, p. 1021-1030.

Barrett, S. D., 2008, Image SXM, *http://www.ImageSXM.org.uk.*

Barth, N. C., Hacker, B. R., Seward, G. G. E., Walsh, E. O., Young, D., and Johnston, S., 2010, Strain within the ultrahigh-pressure Western Gneiss region of Norway recorded by quartz CPOs, *Geological Society of London, Special*

Publications, v. 335, p. 663-685.

Barton, C. A., Zoback, M. D., and Moos, D., 1995, Fluid flow along potentially active faults in crystalline rock, *Geology*, v. 23, p. 683-686.

Bebout, G. E., Anastasio, D. J., and Holl, J. E., 2001, Synorogenic crustal fluid infiltration in the Idaho-Montana Thrust Belt, *Geophysical Research Letters*, v. 28, no. 22, p. 4295-4298.

Behr, W. M., and Platt, J. P., 2011, A naturally constrained stress profile through the middle crust in an extensional terrane, *Earth and Planetary Science Letters*, v. 303, no. 3-4, p. 181-192.

Bell, T. H., 1981, Foliation development - The contribution, geometry and significance of progressive, bulk, inhomogeneous shortening, *Tectonophysics*, v. 75, no. 3-4, p. 273-296.

Bense, V. F., and Person, M., 2006, Faults as conduit-barrier systems to fluid flow in siliciclastic sedimentary aquifers, *Water Resources Research*, v. 42.

Berger, B. C., and Snee, L. W., 1992, Thermochronologic constraints on mylonite and detachment fault development, Kettle Highlands, northeastern Washington and southern British Columbia, *Geological society of America, Abstr. Program*, v. 24, p. 65.

Bickle, M. J., Chapman, H. J., Wickham, S. M., and Peters, M. T., 1995, Strontium and oxygen isotope profiles across marble-silicate contacts, Lizzies Basin, East Humboldt Range, Nevada: constraints on metamorphic permeability contrasts and fluid flow, *Contributions to mineralogy and petrology*, v. 121, no. 4, p. 400-413.

Bird, P., 2002, Stress direction history of the western United States and Mexico since 85 Ma, *Tectonics*, v. 21, no. 3, p. 1014.

Blenkinsop, T. G., and Drury, M. R., 1988, Stress estimate and fault history from quartz microstructures, *Journal of Structural Geology*, v. 10, p. 673-684.

Böhm, A., 1883, Uber die Gesteine des Wechsels, *Tschermak min. u. petrog. Mitt.*, v. 5, p. 197-214.

Bowman, J. R., and Willett, S. D., 1991, Spatial patterns of oxygen isotope exchange during one-dimensional fluid infiltration, *Geophysical Research Letters*, v. 18, no. 5, p. 971-974.

Bowman, J. R., Willett, S. D., and Cook, S. J., 1994, Oxygen isotopic transport and exchange during fluid flow; one-dimensional models and applications, *American Journal of Science*, v. 294, p. 1-55.

Brown, R. L., Journeay, J. M., Lane, L. S., Murphy, D. C., and Rees, C. J., 1986, Obduction, backfolding and piggyback thrusting in the metamorphic hinterland of the southeastern Canadian Cordillera, *Journal of Structural Geology*, v. 8, p. 255 - 268.

Brun, J.-P., Sokoutis, D., Van Den Driessche, J., 1994, Analogue modeling of detachment fault systems and core complexes, *Geology*, v. 22, p. 319-322.

Bunge, H.-J., 1982, Texture analysis in Material science, Butterworths, London.

Bürgmann, R. and Dresen, G., 2008, Rheology of the Lower Crust and Upper Mantle: Evidence from Rock Mechanics, Geodesy, and Field Observations, *Annual Review of Earth and Planetary Sciences*, v. 36, p. 531-567.

Burkhard, M., and Kerrich, R., 1988, Fluid regimes in the deformation of the Helvetic nappes, Switzerland, as inferred from stable isotope data, *Contributions to Mineralogy and Petrology*, v. 99, no. 4, p. 416-429.

Caine, J., Evans, J. P., and Craig, F., 1996, Fault zone architecture and permeability structure, *Geology*, v. 24, n. 11, p. 1025-1028.

Campbell-Stone, E., and John, B., 2002, Temporal changes in deformation mode: from failure to flow in the Colorado River extensional corridor, *International Geological Reviews*, v. 44, p. 512-527.

Carter, N. L., and Friedman, M., 1965, Dynamic analyses of deformed quartz and calcite from the Dry Creek Ridge anticline, Montana, *American Journal of Science*, v. 263, p. 747-785.

Carter, N. L., and Raleigh, C. B., 1969, Principal Stress Directions from Plastic Flow in Crystals, *Geological Society of America Bulletin*, v. 80, no. 7, p. 1231-1264.

Chacko, T., Hu, X., Mayeda, T. K., Clayton, R. N., and Goldsmith, J. R., 1996, Oxygen isotope fractionations in muscovite, phlogopite, and rutile, *Geochimica et Cosmochimica Acta*, v. 60, p. 2595 - 2608.

Chen, S., Doolen, G. D., 1998, Lattice Boltzmann method for fluid flows, *Annual Reviews in Fluid Mechanics*, v. 30, p. 329-364.

Chester, F. M., Evans, J. P., and Biegel, R. L., 1993, Internal Structure and Weakening Mechanisms of the San Andreas Fault, *Journal of Geophysical Research*, v. 98, no. B1, p. 771-786.

Christie, J. M., and Raleigh, C. B., 1959, The origin of deformation lamellae in quartz, *American Journal of Science*, v. 257, p. 385-407.

Christie, J. M., and Ardell, A. J., 1974, Substructures of deformation lamellae in quartz, *Geology*, v. 2, p. 405-408.

Clayton, R. N., O'Neil, J. R., and Mayeda, T. K., 1972, Oxygen isotope exchange between quartz and water, *Journal of Geophysical Research*, v. 77, p. 3057-3067.

Cole, D. R, Ohmoto, H, and Lasaga, A. C., 1983, Isotopic exchange in mineral-fluid systems. I Theoretical evaluations of oxygen isotopic exchange accompanying surface reactions and diffusion, *Geochimica et Cosmochimica Acta*, v. 47, p. 1681-1693.

Collettini, C., and Barchi, M. R., 2002, A low-angle normal fault in the Umbria region (Central Italy): a mechanical model for the related microseismicity,

Tectonophysics, v. 359, no. 1-2, p. 97-115.

Compton, R.R., 1972, Geologic map of the Yost quadrangle, Box Elder County, Utah and Cassia County, Idaho, *US Geologic Survey Miscellaneous Investigation Map I-873*, scale 1:31,680, 1972.

Compton, R.R., 1975, Geological map of the Park Valley quadrangle, Box Elder County, Utah and Cassia County, Idaho, *US Geologic Survey Miscellaneous Investigation Map I-873*, scale 1:31,680.

Compton, R.R, 1983, Displaced Miocene rocks on the west flank of the Raft River-Grouse Creek core complex, Utah. In V.R.; Howard K.A. Miller, D.M.; Todd, editor, Tectonic and Stratigraphic Studies in the Eastern Great Basin, *Geological Society of America Memoir 157*, p. 271-279.

Compton, R. R., 1980, Fabrics and strain in quartzites of a metamorphic core complex, Raft River Mountains, Utah, *Geological Society of America Memoir 153*, p. 385-398.

Compton, R.R., Todd, V.R., Zartman, R.E., and Naeser, C.W., 1977, Oligocene and Miocene metamorphism, folding, and low angle faulting in northwest Utah. *Geological Society of America Bulletin*, v. 88, p. 1237-1250.

Coney, P., Harms, J., and Tekla, A., 1984, Cordilleran metamorphic core complexes; Cenozoic extensional relics of Mesozoic compression, *Geology*, v. 12, n. 9, p. 550-554.

Cook, S. J., Bowman, J. R., and Forster, C. B., 1997, Contact metamorphism surrounding the Alta Stock; finite element model simulation of heat- and 18O/ 16O mass-transport during prograde metamorphism, *American Journal of Science*, v. 297, no. 1, p. 1-55.

Craig H., 1961, Isotopic variations in meteoric water, *Science*, v. 133, p. 1702-1703.

Crespo-Blanc, A., 1995, Interference pattern of extensional fault systems: a

case study of the Miocene rifting of the Alboran basement (North of Sierra Nevada, Betic Chain), *Journal of Structural Geology*, v. 17, no. 11, p. 1559-1563.

Crowley, J. L., Brown, R. L., and Parrish, R. R., 2001, Diachronous deformation and a strain gradient beneath the Selkirk allochthon, northern Monashee complex, southeastern Canadian Cordillera, *Journal of Structural Geology*, v. 23, p. 1103-1121.

Dardis, O., and McCloskey, J., 1998a, Lattice Boltzmann scheme with real numbered solid density for the simulation of flow in porous media, *Phys. Rev. E 57*, pp. 4834-4837.

Dardis, O., and McCloskey, J., 1998b, Permeability porosity relationships from numerical simulations of fluid flow, *Geophysical Research Letters*, v.25, p. 1471-1474.

Davis, G., 1988, Rapid upward transport of mid-crustal mylonitic gneisses in the footwall of a Miocene detachment fault, Whipple Mountains, southeastern California, *Geologische Rundschau*, v. 77, no. 1, p. 191-209.

Davis, G. H., and Coney, P. J., 1979, Geologic development of the Cordilleran metamorphic core complexes, *Geology*, v. 7, p. 120-124.

Drury, M. R., 1993, Deformation lamellae in materials and minerals, in: Defects and Processes in the Solid State: Geosciences Applictions, The McLaren Volume edited by J. N. Noland and J. D. Fitz Gerald, Elsevier Science Publishers.

Egger, A. E., Dumitru, T. A., Miller, E. L., Savage, C. F. I., and Wooden, J. L., 2003, Timing and Nature of Tertiary Plutonism and Extension in the Grouse Creek Mountains, Utah, *International Geological Review*, v. 45, no. 6.

Elliott, D., 1973, Diffusion flow laws in metamorphic rocks. *Geological Society of America Bulletin*, v. 84, p. 2645-2664.

Fairbairn, H. W., 1941, Deformation lamellae in quartz from the Ajibik formation, Michigan, *Geological Society of America Bulletin*, v. 52, p. 1265-1277.

Forster, C. B., Goddard, J. V., and Evans, J. P., 1994, Permeability structure of a thrust fault, in The mechanical involvement of fluids in faulting, *U.S. Geological Survey Open-File Report 94-228*, p. 216-223.

Foster, D. A., and Fanning, C. M., 1997, Geochronology of the Idaho-Bitterroot batholith and Bitterrot metamorphic core complex: Magmatism preceding and contemporaneous with extension, *Geological society of America Bulletin*, v. 109, p. 370 - 394.

Foster, D. A., Schafer, C., Fanning, C. M., and Hyndman, D. W., 2001, Relationships between crustal partial melting, plutonism, orogeny, and exhumation: Idaho-Bitterroot batholith, *Tectonophysics*, v. 342, p. 313-350.

Foster, D. A., and Raza, A., 2002, Low-temperature thermochronological record of exhumation of the Bitterroot metamorphic core complex, northern Cordilleran Orogen, *Tectonophysics*, v. 349, p. 23-36.

Forster, M. A., and Lister, G. S., 2004, The interpretation of 40Ar/39Ar apparent age spectra produced by mixing: Application of the method of asymptotes and limits, *Journal of Structural Geology*, v. 26, p. 287-305.

Foster, D. A., Doughty, P. T., Kalakay, T. J., Fanning, C. M., Coyner, S., Grice, W. C., and Vogl, J., 2007, Kinematics and Timing of Exhumation of Metamorphic Core Complexes Along the Lewis and Clark Fault Zone, Northern Rocky Mountains, USA, *in: Till A., Roeske S., Sample J., Foster D.A., eds., Exhumation along Major Continental Strike-Slip Systems: Geological Society of America Special Paper 434*, p. 205-229.

Fossen, H., and Tikoff, B., 1997, Forward modeling of nonsteady-state deformations and the 'minimum strainpath', *Journal of Structural Geology*, v. 19, p. 987-996.

Fossen, H., and Tikoff, B., 1998, Forward modeling of non-steady-state deformations and the 'minimum strain path': Reply. *Journal of Structural Geology*,

v. 20, p. 979-981.

Fricke, H. C., Wickham, S. M., and O'Neil, J. R., 1992, Oxygen and hydrogen isotope evidence for meteoric water infiltration during mylonitization and uplift in the Ruby Mountains-East Humboldt Range core complex, Nevada, *Contributions to Mineralogy and Petrology*, v. 111, no. 2, p. 203-221.

Fricke, H. C., 2003, Investigation of early Eocene water-vapor transport and paleoelevation using oxygen isotope data from geographically widespread mammal remains, *Geological Society of America Bulletin*, v. 115, p. 1088-1096.

Gans, P., and Bohrson, W., 1998, Suppression of volcanism during rapid extension in the Basin and Range Province, United states. *Science*, v. 279, p. 66-68.

Garven, G., Freeze, R. A., 1984, Theoretical analysis of the role of groundwater flow in the genesis of stratabound ore deposits: 1 Mathematical and numerical model, *American Journal of Science*, v. 284, p. 1085-1124.

Gébelin, A., Mulch, A., Teyssier, C., Heizler, M., Vennemann, T., Seaton , N. C. A., 2011, Oligo-Miocene extensional tectonics and fluid flow across the Northern Snake Range detachment system, Nevada, *Tectonics*, v. 30.

Gerdes, M., Baumgarnter, L. P., and Person, M., 1998, Convective flow through heterogeneous country rocks during contact metamorphism, *Journal of Geophysical Research*, v. 103, p. 23,983-24,003.

Gessner, K., Wijns, C., and Moresi, L., 2007, Significance of strain localization in the lower crust for structural evolution and thermal history of metamorphic core complexes, *Tectonics*, v. 26.

Ghisetti, A., Kirschner, D., Vezzani, L., and Agosta, F., 2001, Stable isotope evidence for contrasting paleofluid circulation in thrust faults and normal faults of the central Apennines, Italy, *Journal of Geophysical Research*, v. 106, p. 8811-8825.

Goddard, J. V., and Evans, J.P. , 1995, Fluid-rock interactions in faults of crystalline thrust sheets, northwestern Wyoming U.S.A. Inferences from geochemistry of fault-related rocks, *Journal of Structural Geology*, v. 17, p. 533-549.

Gottardi, R., Teyssier, C., Mulch, A., Vennemann, T.W., and Wells, M.L., 2011, Preservation of an extreme transient geotherm in the Raft River detachment shear zone, *Geology*, v. 39, p. 759-762.

Götze, J., Plötze, M., and Habermann, D., 2001, Origin, spectral characteristics and practical applications of the cathodoluminescence (CL) of quartz - a review, *Mineralogy and Petrology*, v. 71, no. 3, p. 225-250.

Gleason, G. C., and Tullis, J., 1995, A flow law for dislocation creep of quartz aggregates determined with the molten salt cell, *Tectonophysics*, v. 247, no. 1-4, p. 1-23.

Gueydan, F., Mehl, C., and Parra, T., 2005, Stress-strain rate history of a midcrustal shear zone and the onset of brittle deformation inferred from quartz recrystallized grain size, *Geological Society of London, Special Publications*, v. 243, p. 127-142.

Guo, Z., and Zhao, T. S., 2005, A lattice Boltzmann model for convection heat transfer in porous media, *Num. Heat Transf. Part B 47*, p.157-177.

Haneberg, W. C., 1995, Steady state groundwater flow across idealized faults, *Water Resources Research*, v. 31, n. 7, p. 1815-1820.

Harris, C. R., Hoisch, T. D., and Wells, M. L., 2007, Construction of a composite pressure-temperature path: revealing the synorogenic burial and exhumation history of the Sevier hinterland, USA, *Journal of Metamorphic Geology*, v. 25, no. 8, p. 915-934.

Harrison, M., Célérier, J., Aikman, A. B., Hermann, J., and Heizler, M. T., 2009, Diffusion of ^{40}Ar in muscovite, *Geochimica et Cosmochimica Acta*, v. 73, no. 4, p. 1039-1051.

Heard, H. C., and Carter, N. L., 1968, Experimentally induced natural intragranular flow in quartz and quartzite, *American Journal of Science*, n. 266, p. 1-42.

Healy, D., 2009, Anisotropy, pore fluid pressure and low angle normal faults, *Journal of Structural Geology*, v. 31, no. 6, p. 561-574.

Hirschmann, M. M., Aubaud, C., Withers, A. C., 2005, Storage capacity of H_2O in nominally anhydrous minerals in the upper mantle, *Earth and Planetary Science Letters*, v. 236, no. 1-2, p.167-181.

Hirth, G., and Kohlstedt, D. L., 1996, Water in the oceanic upper mantle: implications for rheology, melt extraction and the evolution of the lithosphere, *Earth and Planetary Science Letter*, v. 144, no. 1-2, p. 93-108.

Hirth, G., and Tullis, J. A., 1992, Dislocation creep regimes in quartz aggregates, *Journal of Structural Geology*, v. 14, p. 145-159.

Hirth, G., Teyssier, C., and Dunlap, J., 2001, An evaluation of quartzite flow laws based on comparisons between experimentally and naturally deformed rocks, *International Journal of Earth Sciences*, v. 90, no. 1, p. 77-87.

Hodges, K. V., Snoke, A. W., and Hurlow, H. A., 1992, Thermal evolution of a portion of the Sevier hinterland: The northern Ruby Mountains-East Humboldt Range and Wood Hills, northeastern Nevada, *Tectonics*, v. 11 p. 154-164.

Hoisch, T. D., Wells, M. L., and Hanson, L. M., 2002, Pressure-temperature paths from garnet-zoning: Evidence for multiple episodes of thrust burial in the hinterland of the Sevier orogenic belt, *American Mineralogist*, v. 87, p. 115-131.

Holk, G. J., 1997, The role of water in the magmatic and tectonic evolution of metamorphic core complexes: A stable isotope study of the southern Omineca Crystalline Belt, British Columbia, Canada: Pasadena, California, California Institute of Technology, Ph. D. thesis, 444 p.

Holk, G. J., and H. P. Taylor, 2000, Water as a petrologic catalyst driving

$^{18}O/^{16}O$ homogenization and anatexis of the middle crust in the metamorphic core complexes of British Columbia, *International Geological Reviews*, v. 42, p. 97-130.

Holyoke III, C. W., and Kronenberg, A. K., 2010, Accurate differential stress measurement using the molten salt cell and solid salt assemblies in the Griggs apparatus with applications to strength, piezometers and rheology, *Tectonophysics*, v. 494, no. 1-2, p. 17-31.

House, M. A., Hodges, K. V., and Bowring, S. A., 1997, Petrological and geochronological constraints on regional metamorphism along the northern border of the Bitterroot batholith, *Journal of Metamorphic Geology*, v. 15, n. 6, p. 753-764.

Huet, B., Le Pourhiet, L., Labrousse, L., Burov, E., and Jolivet, L., 2011, Post-Orogenic Extension and Metamorphic Core Complexes in a Heterogeneous Crust: The Role of Crustal Layering Inherited from Collision. Application to the Cyclades (Aegean Domain). *Geophys J Int*, v. 184, p. 611-625.

Huismans, R. S., Buiter, S. J. H., and Beaumont, C., 2005, Effect of plastic-viscous layering and strain softening on mode selection during lithospheric extension, *Journal of Geophysical Research*, v. 110.

Hurlow, H. A., Snoke, A. W., and Hodges, K. V., 1991, Temperature and pressure of mylonitization in a Tertiary extensional shear zone, Ruby Mountains-East Humboldt Range, Nevada: Tectonic implications, *Geology*, v. 19, p. 82-86.

Hyndman, D. W., 1980, Bitterroot dome-Sapphire tectonic block, an example of a plutonic core-gneiss-dome complex with its detached suprastructure, *in: Crittenden, M. D., Coney, P. J., and Davis, G. H., eds., Cordilleran metamorphic core complexes: Geological Society of America Memoir 153*, p. 427-443.

Iio, Y., Sagiya, T., Kobayashi, Y., Shiozaki, I., 2002, Water-weakened lower crust and its role in the concentrated deformation in the Japanese Islands, *Earth*

and Planetary Science Letters, v. 203, no. 1, p. 245-253.

Ingerson, E., and Tuttle, O. F., 1945, Relations of lamellae and crystallography of quartz and fabric directions in some deformed rocks, *AGU Trans.*, v. 26, p. 95-105.

Kao, P.-H., Yang, R.-J., 2007, Simulating oscillatory flows in Rayleigh-Bénard convection using the lattice Boltzmann method, *Int. J. Heat Mass Trans.*, v. 50, p. 3315-3328.

Kao, P.-H., Saar, M. O., Lattice Boltzmann models for local transports equilibrium (LTE) and non-equilibrium (LTNE) advective-diffusive equations, *Int. J. Heat Mass Trans.* (to be submitted).

Kao, P.-H., Saar, M. O., Macroscale lattice-Boltzmann model for the equilibrium and kinetic reactions in porous media, (In preparation).

Karato, S., Toriumi, M., and Fujii, T., 1980, Dynamic recrystallization of olivine single crystals during high temperature creep, *Geophysical Research Letters*, v. 7, no. 9, p. 649-652.

Kerrich, R., 1986, Fluid infiltration into fault zones: Chemical, isotopic, and mechanical effects, *Pure and Applied Geophysics*, v. 124, no. 1, p. 225-268.

Kharaka, Y. K., Thordsen, J. J., and Evans, W. C., Geochemistry and hydromechanical interactions of fluids associated with the San Andreas fault system, California.

Kirschner, D. L., 1992, Structural and stable isotope analyses of the Heavitree Quartzite deformed in the Arltunga nappe complex, central Australia, PhD Thesis, University of Minnesota.

Kirschner, D. L., and Kennedy, L. A., 2001, Limited syntectonic fluid flow in carbonate-hosted thrust faults of the Front Ranges, Canadian Rockies, inferred from stable isotope data and structures, *Journal of Geophysical Research*, v. 106, p. 8827-8840.

Koch, P. S., and Christie, J. M., 1981, Spacing of deformation lamellae as a paleopiezometer, *EOS Trans Am Geophys Un*, v. 62, p. 1030.

Koch, P. S., and Masch, L., 1992, Formation of Alpine mylonites and pseudotachylytes at the base of the silvretta nappe, Eastern Alps, *Tectonophysics*, v. 204, p. 289-306.

Koons, P. O., Craw, D., Cox, S. C., Upton, P., Templeton, A. S., and Chamberlain, C. P., 1998, Fluid flow during active oblique convergence: A Southern Alps model from mechanical and geochemical observations, *Geology*, v. 26, p. 159-162.

Küster, M., and Stöckhert, B., 1999, High differential stress and sublithostatic pore fluid pressure in the ductile regime - microstructural evidence for short-term post-seismic creep in the Sesia Zone, Western Alps, *Tectonophysics*, v. 303, no. 1-4, p. 263-277.

Kusznir, N. J. and Park, R. G., 1987, The extensional strength of the continental lithosphere; its dependence on geothermal gradient, and crustal composition and thickness (in Continental extensional tectonics), *Geological Society Special Publications*, v. 28, p. 35-52.

Law, R.D., 1990, Crystallographic fabrics: a selective review of their applications to research in structural geology, *Geological Society of London, Special Publications*, v. 54, p. 335-352.

Law, R. D., 2010, Moine Thrust zone mylonites at the Stack of Glencoul: II - results of vorticity analyses and their tectonic significance, *Geological Society of London, Special Publications*, v. 335, p. 579-602.

Lee, J., Miller, E. L., and Sutter, J. F., 1987, Ductile strain and metamorphism in an extensional tectonic setting: a case study from the northern Snake Range, Nevada, USA, *Geological Society of London, Special Publications*, v. 28, p. 267-298.

Lee, J., and Sutter, J. F., 1991, Incremental $^{40}Ar/^{39}Ar$ thermochronology of mylonitic rocks from the Northern Snake Range, Nevada, *Tectonics*, v. 10, no. 1, p. 77-100.

Lee, J., 1995, Rapid uplift and rotation of mylonitic rocks from beneath a detachment fault: Insights from potassium feldspar $^{40}Ar/^{39}Ar$ thermochronology, northern Snake Range, Nevada, *Tectonics*, v. 14, p. 54-77.

Lister, G.S., 1977, Discussion: Crossed-girdle c-axis fabrics in quartzites plastically deformedby plane strain and progressive simple shear, *Tectonophysics*, v. 39, no. 1-3, p.51-54.

Lister, G. S., and Davis, G. A, 1989, The origin of metamorphic core complexes and detachment faults formed during Tertiary continental extension in the northern Colorado River region, U.S.A., *Journal of Structural Geology*, v. 11, no. 1-2, p. 65-94.

Lister, G.S, and Hobbs, B.E, 1980, The simulation of fabric development during plastic deformation and its application to quartzite: the influence of deformation history. *Journal of Structural Geology*, v. 2, no. 3, p. 355-370.

Lopez, D. L., and Smith, L., 1995, Fluid flow in fault zones: Analysis of the interplay of convective circulation and topographically driven groundwater flow, *Water Resources Research*, v. 31, no. 6, p. 1489-1503.

Mainprice, D., 2005, Pfch5 (computer software) edited by
$ftp://www.gm.univ-montp2.fr/mainprice//CareWare_Unicef_Programs/$.

Malavieille, J., 1987, Extensional shearing deformation and kilometer-scale "a"-type folds in a cordilleran metamorphic core complex (Raft River Mountains, northwest Utah), *Tectonics*, v. 6, p. 423-448.

Manning, A. H., and Bartley, J. M., 1994, Postmylonitic deformation in the Raft River metamorphic core complex, northwestern Utah: Evidence of a rolling hinge, *Tectonics*, v. 13, no. 3, p. 596-612.

Manning, C. E., and Ingebritsen, S. E., 1999, Permeability of the continental crust: Implications of geothermal data and metamorphic systems, *Rev. Geophys.*, v. 37, no. 1, p. 127-150.

Marquer, D., Burkhard, M., 1992, Fluid circulation, progressive deformation and mass-transfer processes in the upper crust: the example of basement-cover relationships in the External Crystalline Massifs, Switzerland, *Journal of Structural Geology*, v. 4, no. 8-9, p. 1047-1057.

McCaig, A. M., 1988, Deep fluid circulation in fault zones, *Geology*, v. 16, p. 867-870.

McCaig, A. M., Wayne, D. M., Marshall, J. D., Banks, D., and Henderson, I., 1995, Isotopic and fluid inclusion studies of fluid movement along the Gavarnie Thrust, central Pyrenees; reaction fronts in carbonate mylonites, *American Journal of Science*, v. 295, p.309-343.

McCormick, J. W., 1977, Transmission electron microscopy of experimentally deformed synthetic quartz, Ph.D. thesis, University of California, Los Angeles, California.

McDougall, I., and Harrison, T. M., 1999, Geochronology and Thermochronology by the $^{40}Ar/^{39}Ar$ Method, 2nd ed., 269 pp., Oxford Univ. Press, New York, 1999.

McGrew, A. J., and Snee, L. W., 1994, $^{40}Ar/^{39}Ar$ thermochronologic constraints on the tectonothermal evolution of the northern East Humboldt Range metamorphic core complex, Nevada, *Tectonophysics*, v. 238, p. 425-450.

McLaren, A. C., 1991, Transmission electron microscopy of minerals and rocks, Cambridge University press, New York, 387 pp.

McLaren, A. C., and Hobbs, B. E., 1972, Transmission electron microscopy investigation of some naturally deformed quartzites. In: Flow and Fractures of Rocks, *Geophys. Monograph, AGU*, v. 16, p. 55-66.

McPherson B., and Garven G., 1999, Compressional tectonics, hydrodynamics and overpressure mechanisms in the Sacramento basin, California, *American Journal of Science*, v. 299, p. 429-466.

Means, W.D., 1981, The concept of steady-state foliation, *Tectonophysics*, v. 78, no. 1-4, p. 179-199.

Michibayashi, K., 1993, Syntectonic development of a strain-independent steady-state grain size during mylonitization, *Tectonophysics*, v. 222, no. 2, p. 151-164.

Miller, D.M., 1980, Structural geology of the northern Albion Mountains, south-central Idaho. In P.J. Coney, Crittenden, M. D. and G. H. Davis, editors, Cordilleran metamorphic core complexes, *Geological Society of America Memoir 153*, p. 399-423.

Miller, E. L., Gans, P. B., and Garing, J., 1983, The Snake Range Décollement: an exhumed mid-Tertiary ductile-brittle transition, *Tectonics*, v. 2, p. 239-263.

Miller, E. L., Dumitru, T. A., Brown, R. W., and Gans, P. B., 1999, Rapid Miocene slip on the Snake Range-Deep Creek Range fault system, east-central Nevada, *Geological Society of America Bulletin*, v. 111, p. 886-905.

Moore, J. C., and Vrolijk, P., 1992, Fluids in accretionary prisms, *Reviews in Geophysics*, v. 30, no. 2, p. 113-135.

Morgan, J. P., 1987, Melt migration beneath mid-ocean spreading centers, *Geophysical Research Letters*, v. 14, no. 12, p. 1238-1241.

Morrison, J., 1994, Meteoric water-rock interaction in the lower plate of the Whipple Mountain metamorphic core complex, California, Journal of Metamorphic Geology, v. 12, p. 827-840.

Morrison, J., and Anderson, J. L., 1998, Footwall refrigeration along a detachment fault: implications for thermal evolution of core complexes, *Science*, v.

279, p. 63-66.

Mueller, K. J., and Snoke, A. W., 1993, Progressive overprinting of normal fault systems and their role in Tertiary exhumation of the East Humboldt Range-Wood Hills metamorphic core complex northeast Nevada, *Tectonics*, v. 12, p. 361-373.

Mulch, A., Teyssier, C., Cosca, M. A., Vanderhaeghe, O., and Vennemann, T. W., 2004, Reconstructing paleoelevation in eroded orogens, *Geology*, v. 32, p. 525-528.

Mulch, A., Cosca, M. A., Fiebig, J., and Andresen, A., 2005, Time scales of mylonitic deformation and meteoric fluid infiltration during extensional detachment faulting: an integrated in situ $^{40}Ar/^{39}Ar$ geochronology and stable isotope study of the Porsgrunn-Kristiansand Shear Zone (Southern Norway), *Earth and Planetary Science Letters*, v. 233, p. 375-390.

Mulch, A., Teyssier, C., Cosca, M. A., and Vennemann, T. W., 2006, Thermomechanical analysis of strain localization in a detachment zone, *Jounral of Geophysical Research*, v. 111, no. B12405.

Mulch, A., Teyssier, C., Cosca, M. A., and Chamberlain, C. P., 2007, Stable isotope paleoaltimetry of Eocene core complexes in the North American Cordillera, *Tectonics*, v. 26.

Myre, J., Walsh, S. D. C., Lilja, D., Saar, M. O., 2011, Performance analysis of single-phase, multiphase, and multicomponent lattice-Boltzmann fluid flow simulations on GPU clusters, *Concurrency and Computation: Practice and Experience*, v. 23, no. 4, p. 332-350.

Nesbitt, B. E., and Muehlenbachs, V, 1989, Origins and Movement of Fluids During Deformation and Metamorphism in the Canadian Cordillera, *Science*, v. 245, p. 733-736.

Newman, J., and Mitra, G., 1994, Fluid-influenced deformation and recrys-

tallization of dolomite at low temperatures along a natural fault zone, Mountain City window, Tennessee, *Geological Society of America Bulletin*, v. 106, p. 1267-1280.

Oliver, J., 1986, Fluids expelled tectonically from orogenic belts: Their role in hydrocarbon migration and other geological phenomena, *Geology*, v. 14, p. 99-102.

O'Neil, J. R., and Hanks, T. C., 1980, Geochemical Evidence for Water-Rock Interaction Along the San Andreas and Garlock Faults of California, *Journal of Geophysical Research*, v. 85, no. B11, p. 6286-6292.

Parrish, R. R., Carr, S. D., and Parkinson, D. L., 1988, Eocene extensional tectonics and geochronology of the southern Omineca Belt, British Columbia and Washington, *Tectonics*, v. 7, p. 181-212.

Passchier, C. W., 1982, Pseudotachylyte and the development of ultra-mylonite bands in the Saint-Barthélemy Massif, French Pyrenees, *Journal of structural Geology*, v. 4, p. 60-79.

Pavlis, T. M., Bruhn, R. L., 1988, Stress history during propagation of a lateral fold-tip and implications for the mechanics of fold-thrust belts, *Tectonophysics*, v. 145, no. 1-2, p. 113-127.

Person, M. P., Mulch, A., Teyssier, C., Gao, Y., 2007, Isotope Transport and Exchange During Detachment Tectonics, Shuswap Metamorphic Core Complex, British Columbia, *American Journal of Science*, v. 307, p. 555-589.

Pili, E., Poitrasson, F., and Gratier, J.-P., 2002, Carbon-oxygen isotope and trace element constraints on how fluids percolate faulted limestones from the San Andreas Fault system: partitioning of fluid sources and pathways, *Chemical Geology*, v. 190, no. 1-4, p. 231-250.

Planke, S., and Smith, R. B., 1991, Cenozoic extension and evolution of the Sevier Desert Basin, Utah, from seismic reflection, gravity, and well log data,

Tectonics, v. 10, no. 2, p. 345-365.

Post, R.L., 1977, High-temperature creep of Mt. Burnet dunite, *Tectonophysics*, v. 42, p. 75-102.

Price, R. A., 1986, The Canadian Cordillera: Thrust faulting, tectonic wedging and delamination of the lithosphere, *Journal of Structural Geology*, v. 8, p. 238-254.

Quilichini, A., 2012, Fluid-rock-strain feedbacks in extensional shear zones. Doctoral thesis, University of Lausanne.

Rey, P., Vanderhaeghe, O., and Teyssier, C., 2001, Gravitational collapse of the continental crust: definition, regimes and modes. *Tectonophysics*, v. 342, no. 3-4, p. 435-449.

Rey, P. F., Teyssier, C., and Whitney, D. L., 2009a, Extension rates, crustal melting, and core complex dynamics, *Geology,* v. 37, p. 391-394.

Rey, P. F., Teyssier, C., Whitney, D. L., 2009b, The role of partial melting and extensional strain rates in the development of metamorphic core complexes, *Tectonophysics*, v. 477, no. 3-4, p. 135-144.

Rey, P. F., Teyssier, C., and Whitney, D. L., 2010, Limit of channel flow in orogenic plateaux, *Lithosphere*, v. 2, p. 328-332.

Reynolds, S.J., and Lister, G.S., 1990, Folding of mylonitic zones in Cordilleran metamorphic core complexes: Evidence from near the mylonitic front, *Geology*, v. 18, p. 216-219.

Roedder, E., 1984, Fluid Inclusions. Reviews in Mineralogy, 12, *Mineralogical Society of America*, 644 pp.

Ross, J. V., Ave Lallemant, H. G., and Carter, N. L., 1980, Stress dependence of recrystallized-grain and subgrain size in olivine, *Tectonophysics*, v. 70, no. 1-2, p. 39-61.

Rutter, E.H., 1983. Pressure solution in nature, theory and experiment. *Jour-*

nal of the Geological Society of London, v. 140, p. 725-740.

Rutter, E.H., Brodie, K.H., 2004, Experimental grain size-sensitive flow of hot-pressed Brazilian quartz aggregates, *Journal of Structural Geology*, v. 26, no. 11, p. 2011-2023.

Rye, D. M, and Bradbury, H. J, 1988, Fluid flow in the crust: An example from a Pyrenean thrust ramp, *American Journal of Science*, v. 288, p. 197-235.

Sabisky, M., 1985, Ductile flow and folding in the Raft River Mountains, Northwestern Utah, *Eos*, v. 66, p. 1089.

Saltzer, S. D. and Hodges, K. V., 1988, The Middle Mountain shear zone, southern Idaho: Kinematic analysis of an early Tertiary high-temperature detachment, *Geological Society of America Bulletin*, v. 100, p. 96-103.

Samson, A., and Marshall, D., 2003, Fluid inclusions: analysis and interpretation Short Course, v. 32, *Mineralogical Association of Canada,* 374 pp.

Schmid, S. M., and Casey, M., 1986, Complete fabric analysis of some commonly observed quartz c-axis patterns, in: Honns, B. E. and Heard, H. C. (eds) Mineral and Rock deformation laboratory studies: the Patterson volume. *AGU, Geophysical Monograph*, v. 36, p. 263-286.

Sharp, Z. D, and Kirschner, D. L, 1994, Quartz-calcite oxygen isotope thermometry: A calibration based on natural isotopic variations, *Geochimica et Cosmochimica Acta*, v. 58, no. 20, p. 4491-4501.

Sheppard, D. S., 1986, Ngawha geothermal field, *Monogr. Ser. Miner. Depos.,* v. 26, p. 185-192.

Sibson, R. H., 1977, Fault rocks and fault mechanisms, *Journal of the Geological Society of London*, v. 133, p. 192-214.

Sibson, R., 1983, Continental fault structure and the shallow earthquake source, *Journal of the Geological Society of London*, v. 140, p. 741-767.

Sibson, R. H., 1994, Crustal stress, faulting and fluid flow, *Geological Society*

of London, Special Publications, v. 78, p. 69-84.

Sibson, R. H., 1996, Structural permeability of fluid-driven fault-fracture meshes, *Journal of Structural Geology*, v. 18, no. 8, p. 1031-1042.

Sibson, R.H., 1998. Brittle failure mode plots for compressional and extensional tectonic regimes, *Journal of Structural Geology*, v. 20, p. 655-660.

Smith, L., Forster, C. B., and Evans, J. P., 1990, Interaction of fault zones, fluid flow, and heat transfer at the basin scale, in Hydrogeology of permeability environments, *International Association of Hydrogeologists*, v. 2, p. 41-67.

Stipp, M., and Tullis, J., 2003, The recrystallized grain size piezometer for quartz, *Geophysical Research Letters*, v. 30, p. 2088.

Strickland, A., Miller, E. L., and Wooden, J. L., 2011, The Timing of Tertiary Metamorphism and Deformation in the Albion-Raft River-Grouse Creek Metamorphic Core Complex, Utah and Idaho, *The Journal of Geology*, v. 119, no. 2, p. 185-206.

Succi, S., 2001, The lattice Boltzmann equation for fluid dynamics and beyond, Clarendon Press, Oxford.

Sukop, M. C., and Thorne, D. T., 2006, Lattice Boltzmann Modeling: An introduction for geoscientists and engineers, Springer-Verlag, Berlin Heidelberg.

Sullivan, W. A., 2008, Significance of transport-parallel strain variations in part of the Raft River shear zone, Raft River Mountains, Utah, USA, *Journal of Structural Geology*, v. 30, no. 2, p. 138-158.

Suzuoki, T., and Epstein, S., 1976, Hydrogen isotope fractionation between OH-bearing minerals and water, *Geochimica et Cosmochimica Acta*, v. 40, p. 1229-1240.

Taylor, B., and Huchon, P., 2002, Active continental extension in the western Woodlark Basin: A synthesis of Leg 180 results, *Proc. Ocean Drill. Program Sci. Results*, v. 180, p. 1-36.

ten Grotenhuis, S.M. , Trouw, R. A. J., and Passchier, C.W., 2003, Evolution of mica fish in mylonitic rocks, *Tectonophysics*, v. 372, no. 1-2, p. 1-21.

Ter Heege, J., H., 2002, Relationship between dynamic recrystallization, grain size distribution, and rheology, PhD Thesis, Universiteit Utrecht.

Teyssier, C., Ferré, E., Whitney, D. L., Norlander, B., Vanderhaeghe, O., and Parkinson , D., 2005, Flow of partially molten crust and origin of detachments during collapse of the Cordilleran orogen, *Geological Society of London, Special Publication*, v. 245, p. 39-64.

Tikoff, B., and Fossen, H., 1995, The limitations of three-dimensional kinematic vorticity analysis, *Journal of Structural Geology*, v. 17, p. 1771-1784.

Tirel, C., Gueydan, F., Tiberi, C., and Brun, J.-P., 2004, Aegean crustal thickness inferred from gravity inversion. Geodynamical implications, *Earth and Planetary Science Letters*, v. 228, no. 3-4, p. 267-280.

Tirel, C., Brun, J.-P., and Burov, E., 2008, Dynamics and structural development of metamorphic core complexes, *Journal of Geophysical Research*, v. 113.

Todd, V.R., 1980, Structure and petrology of a Tertiary gneiss dome in northwestern Utah, in: M.D. Crittenden Jr., P.J. Coney, G.H. Davis (Eds.), Cordilleran Metamorphic Core Complexes, *Geological society of America Memoir 153*, p. 349-383.

Trepmann, C.A., and Stöckhert, B., 2001, Mechanical twinning of jadeite-an indication of synseismic loading beneath the brittle-ductile transition, *International Journal of Earth Science*, v. 90, p. 4-13.

Trepmann, C.A., and Stöckhert, B., 2002, Cataclastic deformation of garnet: a record of synseismic loading and postseismic creep, *Journal of Structural Geology*, v. 24, p. 1845-1856.

Trepmann, C. A., and Stöckhert, B., 2003, Quartz microstructures developed during non-steady state plastic flow at rapidly decaying stress and strain rate,

Journal of Structural Geology, v. 25, no. 12, p. 2035-2051.

Twiss, R. J., 1977, Theory and applicability of a recrystallized grain size paleopiezometer, *Pure and Applied Geophysics*, v. 115, no. 1, p. 227-244.

Twiss, R.J., and Moores, E.M., 1992, Structural Geology, W.H. Freeman, San Francisco.

Ulrich, S., and Mainprice, D., 2005, Does cation ordering in omphacite influence development of lattice preferred orientation? *Journal of structural Geology*, v. 27, p. 419-431.

Unruh, J. R., Davisson, M. L., Criss, R. E., and Moores, E. M., 1992, Implications of perennial saline springs for abnormally high fluid pressures and active thrusting in western California, *Geology*, v. 20, p. 431-434.

Valley, J. W., 1986, Stable isotope geochemistry of metamorphic rocks, *Reviews in Mineralogy and Geochemistry*, v. 16, p. 445-489.

Valley, J. W., 2001, Stable Isotope Thermometry at High Temperatures, *Reviews in Mineralogy and Geochemistry*, v. 43, p. 365-413.

Vanderhaeghe, O., and Teyssier, C., 1997, Formation of the Shuswap metamorphic core complex during late-orogenic collapse of the Canadian Cordillera: Role of ductile thinning and partial melting of the mid- to lower crust, *Geodinamica Acta*, v. 10, p. 41-58.

Vanderhaeghe, O., and Teyssier, C., 2001, Partial melting and flow of orogens, *Tectonophysics*, v. 342, p. 451-472.

Vanderhaeghe, O., Teyssier, C., and Wysoczanski, R., 1999, Structural and geochronological constraints on the role of partial melting during the formation of the Shuswap metamorphic core complex at the latitude of the Thor-Odin Dome, British Columbia, *Canadian Journal of Earth Sciences*, v. 36, p .917-943.

Van der Wal, D., Chopra, P., Drury, M., and Gerald, J. F., 1993, Relationships between dynamically recrystallized grain size and deformation conditions in

experimentally deformed olivine rocks, *Geophysical Research Letters*, v. 20, no. 14, p. 1479-1482.

Vernon, R. H., 2004, A practical guide to microstructure, Cambridge University Press, New York, 594 pp.

Vollmer, F., 1990, An application of eigenvalue methods to structural domain analysis, *Geological Society of America Bulletin*, v. 102, p. 786-791.

Vollmer, F.W., 2011, EllipseFit 2.0., *http://www.frederickvollmer.com/ellipsefit/*.

Walsh, S. D. C., Burwinkle, H., and Saar, M. O., 2009, A new partial-bounceback lattice- Boltzmann method for fluid flow through heterogeneous media, *Computers and Geosciences*, v. 35, p. 1186-1193.

Walsh, S. D. C., Saar, M. O., 2010, Marcoscale lattice-Boltzmann methods for low Peclet- number solute and heat transport in heterogeneous porous media, *Water Resource Research*, v. 46.

Wallis, S. R., 1992, Vorticity analysis in a metachert from the Sanbagawa Belt, SW Japan, *Journal of Structural Geology*, v. 14, p. 271-280.

Wallis, S. R., 1995, Vorticity analysis and recognition of ductile extension in the Sanbagawa belt, SW Japan, *Journal of Structural Geology*, v. 17, p. 1077-1093.

Wegner, M. W., and Christie, J. M., 1983, Chemical etching of deformation sub-structures in quartz, *Physics and Chemistry of Minerals*, v. 9, p. 67-78.

Wells, M.L., 1997, Alternating contraction and extension in the hinterlands of orogenic belts: An example from the Raft River Mountains, Utah, *Geological Society of America Bulletin*, v. 109, no. 1, p. 107-126.

Wells, M. L., 2001, Rheological control on the initial geometry of the Raft River detachment fault and shear zone, western United States, *Tectonics*, v. 20, p. 435-457.

Wells, M. L., Hoisch, T. D., Peters, M. T., Miller, D. M., Wolff, E. D., and

Hanson , L. M., 1998, The Mahogany peaks fault, a late Cretaceous-Paleocene(?) normal fault in the hinterland of the Sevier orogen, *The Journal of Geology*, v. 106, no. 5, p. 623-634.

Wells, M.L., Snee, L.W., and Blythe, A.E., 2000, Dating major normal fault systems using thermochronology: an example from the Raft River detachment, Basin and Range, western United States, *Journal of Geophysical Research*, v. 105.

Wernicke, B. P., 1992, Cenozoic extensional tectonics of the U.S. Cordillera, in The Geology of North America, vol. G-3, The Cordilleran Orogen: Conterminous U.S., edited by B. C. Burchfiel, P. W. Lipman, and M. L. Zoback, p. 553-583, *Geological Society of America*, Boulder, Colo.

White, S. H., 1973, Deformation lamellae in naturally deformed quartz, *Nature Physical Sciences*, v. 245, p. 26-28.

White, S. H., 1996, Transient discontinuities revisited: pseudotachylyte, plastic instability and the influence of low pore fluid pressure on deformation processes in the mid-crust, *Journal of Structural Geology*, v. 18, no. 12, p. 1471-1486.

Wickham, S. M., and Taylor, H. P., 1987, Stable isotope constraints on the origin and depth of penetration of hydrothermal fluids associated with Hercynian regional metamorphism and crustal anatexis in the Pyrenees, *Contributions to Mineralogy and Petrology*, v. 95, no. 3, p. 255-268.

Wickham, S. M., Taylor, H. P., Snoke, A. W., and O'Neil, J. R., 1991, An oxygen and hydrogen isotope study of high-grade metamorphism and anatexis in the Ruby Mountains-East Humboldt Range core complex, Nevada, *in: Stable Isotope Geochemistry; A Tribute To Samuel Epstein, edited by H. P. Taylor.*

Wickham, S. M., Peters, M. T., Fricke, H. C., and O'Neil, J. R., 1993, Identification of magmatic and meteoric fluid sources and upward- and downward-moving infiltration fronts in a metamorphic core complex, *Geology*, v. 21, p. 81-84.

Wijns, C., Weinberg, R., Gessner, K., and Moresi, L., 2005, Mode of crustal extension determined by rheological layering, *Earth and Planetary Science Letters*, v. 236, no. 1-2, p. 120-134.

Wolf-Gladrow, D. A., 2000, Lattice-gas cellular automata and lattice Boltzmann models - An introduction, Springer-Verlag, Berlin Heidelberg.

Woodbury, A. D. and Smith, L., 1988, Simultaneous inversion of hydrogeologic and thermal data: 2. Incorporation of thermal data, *Water Resources Research*, v. 24, no. 3, p. 356-372.

Woodcock, N. H., 1977, Specification of fabric shapes using an eigenvalue method, *Geological Society of America Bulletin*, v. 88, no. 9, p. 1231-1236.

Zhang, S., Tullis, T. E., and Scruggs, V. J., 1999, Permeability anisotropy and pressure dependency of permeability in experimentally sheared gouge materials, *Journal of Structural Geology*, v. 21, no. 7, p. 795-806.

Zharikov, A. V., Vitovtova, V. M., Shmonov, V. M., Grafchikov, A. A., 2003, Permeability of the rocks from the Kola superdeep borehole at high temperature and pressure: implication to fluid dynamics in the continental crust, *Tectonophysics*, v. 370, no. 1-4, p. 177-191.

Zhu, W., Montesi, L. G.J., and Wong, T.-F., 1997, Shear-enhanced compaction and permeability reduction: Triaxial extension tests on porous sandstone, *Mechanics of Materials*, v., no. 3, p. 199-214.

Appendix 1 - Additional Microstructural data

MICROSTRUCTURAL DATA

Elevation (m above basement)	Sample	Recrystallized Diameter (μm)	Recrystallized Area (%)	Corrected Diameter (μm)	Flow Stress (MPa)
		Section A			
29	RR09-157	15.8	16	15.8	55
23	RR09-156	14.8	29	14.8	58
19	RR09-155	15.7	16	15.7	55
15	RR09-154	15.6	25	15.6	55
13	RR09-153	15.6	25	15.6	55
10	RR09-152	12.5	11	12.5	66
5	RR09-151	16.5	17	16.5	53
2	RR09-150	16.1	38	16.1	54
Mean			22	15.3	56
Harmonic Mean			19	15.2	56
Std Dev.			9	1.2	4.1
Minimum			11	12.5	53
1st quart (25%)			16	15.4	54
Median (50%)			21	15.7	55
2nd quart (75%)			26	15.9	56
Maximum			38	16.5	66

Table 5.4: **Microstructural data - Section A.**

Elevation (m above basement)	Sample	Recrystallized Diameter (μm)	Recrystallized Area (%)	Corrected Diameter (μm)	Flow Stress (MPa)
		Section B			
64	RR09-86	15.5	31	16.5	55
58	RR09-85	16.0	20	16.0	54
50	RR09-84	14.1	23	14.1	60
43	RR09-83	13.4	26	13.4	62
37	RR09-82	15.4	25	15.4	56
31	RR09-81	15.0	23	15.0	57
25	RR09-78	13.3	34	13.3	63
14	RR09-76	13.9	35	13.9	60
10	RR09-75	14.5	36	14.5	58
7	RR09-74	14.0	25	14.0	60
Mean			28	14.5	59
Harmonic Mean			27	14.5	59
Std Dev.			6	0.93	3.0
Minimum			20	13.3	54
1st quart (25%)			24	13.9	56
Median (50%)			26	14.3	59
2nd quart (75%)			33	15.3	60
Maximum			36	16.0	63

Table 5.5: **Microstructural data - Section B.**

Elevation (m above basement)	Sample	Recrystallized Diameter (μm)	Recrystallized Area (%)	Corrected Diameter (μm)	Flow Stress (MPa)
		Section C			
65	RR09-105	19.9	43	19.9	45
56	RR09-104	18.9	38	18.9	47
52	RR09-103	19	51	19.0	47
46	RR09-102	19	36	19.0	47
39	RR09-101	17.9	33	17.9	49
29	RR09-100	18.6	34	18.6	48
22	RR09-99				
22	RR09-98				
15	RR09-97	21.3	31	21.3	43
13	RR09-96	20.3	40	20.3	45
12	RR09-95	19.7	30	19.7	46
10	RR09-94	18.4	28	18.4	48
8	RR09-93	20.3	33	20.3	45
6	RR09-92	20.4	26	20.4	45
4	RR09-91	16.6	19	16.6	53
2	RR09-90	18.8	28	18.8	48
Mean			34	19.2	47
Hamonic Mean			32	19.1	47
Std Dev.			8	1.2	2
Minimum			19	16.6	43
1st quart (25%)			29	18.7	45
Median (50%)			33	19.0	47
2nd quart (75%)			38	20.2	48
Maximum			51	21.3	53

Table 5.6: **Microstructural data - Section C.**

Elevation (m above basement)	Sample	Recrystallized Diameter (μm)	Recrystallized Area (%)	Corrected Diameter (μm)	Flow Stress (MPa)
		Section E			
48	RR09-135	16.5	45	16.5	53
44	RR09-134	15.6	43	15.6	55
39	RR09-133	15.8	35	15.8	55
34	RR09-132	16.7	29	16.7	52
29	RR09-131	16.5	39	16.5	53
24	RR09-130	16.5	32	16.5	53
20	RR09-129	15.9	40	15.9	54
16	RR09-127	18.7	27	18.7	48
15	RR09-126	13.7	53	13.7	61
14	RR09-125	15.7	35	15.7	55
12	RR09-123	16.6	38	16.6	53
9	RR09-122	16.7	35	16.7	52
6	RR09-121	15.8	51	15.8	55
Mean			39	16.2	54
Harmonic Mean			37	16.1	54
Std Dev.			8	1.1	3.0
Minimum			27	13.7	48
1st quart (25%)			35	15.8	53
Median (50%)			38	16.5	53
2nd quart (75%)			43	16.6	55
Maximum			53	18.7	61

Table 5.7: **Microstructural data - Section E.**

Elevation (m above basement)	Sample	Recrystallized Diameter (μm)	Recrystallized Area (%)	Corrected Diameter (μm)	Flow Stress (MPa)
		Indian Creek			
22	RR10-45	16.5	62	16.5	53
13	RR10-43	13.9	44	13.9	60
9	RR10-41	14.9	57	14.9	57
7	RR10-40	16.5	38	16.5	53
4	RR10-38	16.7	42	16.7	52
2	RR10-37	14.8	37	14.8	58
Mean			47	15.6	56
Harmonic Mean			47	15.6	55
Std Dev.			10	1.2	4
Minimum			38	13.9	52
1st quart (25%)			42	14.9	53
Median (50%)			44	16.5	53
2nd quart (75%)			57	16.5	57
Maximum			62	16.7	60

Table 5.8: **Microstructural data - Indian Creek Section.**

Elevation (m above basement)	Sample	Recrystallized Diameter (μm)	Recrystallized Area (%)	Corrected Diameter (μm)	Flow Stress (MPa)
		Duffy Creek			
24	RR10-36	15.1	62	15.1	57
15	RR10-34	14.5	49	14.5	58
14	RR10-32	16.1	44	16.1	54
6	RR10-30	14.1	59	14.1	60
3	RR10-29	16.7	37	16.7	52
2	RR10-28	16.1	61	16.1	54
Mean			52	15.4	56
Harmonic Mean			50	15.4	56
Std Dev.			10	1.0	3.0
Minimum			37	14.1	52
1st quart (25%)			46	14.7	54
Median (50%)			54	15.6	55
2nd quart (75%)			60	16.1	58
Maximum			62	16.7	60

Table 5.9: **Microstructural data - Duffy Creek Section.**

STRAIN DATA

		Grains < 60 μm			Grains > 60 μm			Grains > 100 μm		
Elevation	Sample	N	R_s	φ	N	R_s	φ	N	R_s	φ
					Section A					
29	RR09-157	1657	1.16 ± 0.01	177.1 ± 2.3	157	1.65 ± 0.06	175.0 ± 2.5	81	1.69 ± 0.07	175.3 ± 3.2
23	RR09-156	1837	1.24 ± 0.01	169.4 ± 1.4	82	2.46 ± 0.10	171.7 ± 1.8	41	2.58 ± 0.14	171.1 ± 2.2
19	RR09-155	881	1.14 ± 0.02	177.6 ± 4.0	86	1.53 ± 0.06	177.8 ± 3.3	41	1.60 ± 0.08	178.2 ± 4.6
13	RR09-153	1421	1.09 ± 0.01	173.6 ± 4.4	89	1.40 ± 0.05	159.8 ± 4.5	41	1.55 ± 0.08	161.4 ± 4.7
10	RR09-152	999	1.08 ± 0.01	159.9 ± 6.5	71	1.50 ± 0.06	160.5 ± 4.4	44	1.52 ± 0.07	163.5 ± 4.6
5	RR09-151	937	1.14 ± 0.02	166.1 ± 4.1	93	1.93 ± 0.08	172.9 ± 2.2	48	1.99 ± 0.10	173.8 ± 2.8
2	RR09-150	2162	1.27 ± 0.01	179.0 ± 1.2	81	2.60 ± 0.12	172.7 ± 2.0	31	3.01 ± 0.22	178.5 ± 2.4
Mean			1.16	171.8		1.87	169.6		1.99	171.7
Std Dev.			0.07	7.0		0.48	7.6		0.58	6.8

Table 5.10: **Strain results - Section A.**

		Grains < 60 μm			Grains > 60 μm			Grains > 100 μm		
Elevation	Sample	N	R_s	φ	N	R_s	φ	N	R_s	φ
					Section B					
70	RR09-86	2198	1.25 ± 0.01	167.7 ± 1.4	134	1.72 ± 0.06	167.8 ± 2.3	52	1.70 ± 0.10	168.2 ± 3.4
58	RR09-85	1473	1.10 ± 0.01	166.1 ± 4.3	177	1.37 ± 0.03	169.3 ± 3.7	63	1.41 ± 0.06	171.9 ± 5.1
50	RR09-84	2160	1.25 ± 0.01	168.8 ± 1.6	131	1.61 ± 0.05	166.5 ± 3.1	65	1.65 ± 0.08	168.6 ± 3.5
43	RR09-83	2723	1.30 ± 0.01	173.8 ± 1.0	152	2.08 ± 0.07	175.2 ± 1.6	66	2.08 ± 0.09	176.1 ± 2.5
37	RR09-82	2032	1.23 ± 0.01	171.4 ± 1.5	152	1.64 ± 0.06	173.5 ± 2.3	56	1.78 ± 0.12	175.3 ± 3.0
31	RR09-81	1823	1.33 ± 0.01	178.0 ± 1.2	127	2.08 ± 0.09	178.2 ± 1.7	59	1.99 ± 0.11	179.5 ± 2.6
25	RR09-78	3518	1.29 ± 0.01	172.1 ± 0.9	130	2.28 ± 0.11	173.9 ± 1.2	47	2.82 ± 0.22	174.5 ± 1.6
14	RR09-76	3760	1.34 ± 0.01	173.2 ± 0.7	165	2.33 ± 0.07	171.7 ± 1.1	50	2.72 ± 0.13	172.0 ± 1.4
10	RR09-75	3447	1.29 ± 0.01	168.3 ± 1.0	56	2.53 ± 0.12	171.0 ± 1.6	56	2.53 ± 0.12	171.0 ± 1.7
7	RR09-74	2260	1.30 ± 0.01	178.5 ± 1.1	147	2.34 ± 0.09	179.9 ± 1.5	63	2.65 ± 0.16	179.3 ± 2.2
Mean			1.27	171.8		2.00	172.7		2.13	173.6
Std Dev.			0.07	4.2		0.39	4.3		0.51	4.0

Table 5.11: **Strain results - Section B.**

		Grains < 60 μm			Grains > 60 μm			Grains > 100 μm		
Elevation	Sample	N	R_s	φ	N	R_s	φ	N	R_s	φ
					Section C					
65	RR09-105	1751	1.31 ± 0.02	162.3 ± 1.2	122	1.92 ± 0.06	164.3 ± 1.9	37	2.05 ± 0.12	162.9 ± 3.2
56	RR09-104	1722	1.34 ± 0.01	171.8 ± 1.1	109	2.31 ± 0.10	175.4 ± 1.6	43	2.75 ± 0.17	173.8 ± 1.9
52	RR09-103	2339	1.48 ± 0.01	178.3 ± 0.7	98	2.41 ± 0.08	177.2 ± 1.5	29	2.92 ± 0.18	177.5 ± 2.0
46	RR09-102	1525	1.34 ± 0.01	170.3 ± 1.1	121	2.17 ± 0.07	173.0 ± 1.7	41	2.38 ± 0.15	176.4 ± 2.6
39	RR09-101	1726	1.35 ± 0.01	168.9 ± 1.1	114	2.42 ± 0.07	170.0 ± 1.1	40	2.58 ± 0.15	169.2 ± 1.9
29	RR09-100	1640	1.26 ± 0.01	171.5 ± 1.5	115	2.11 ± 0.06	175.5 ± 1.5	39	2.33 ± 0.11	175.1 ± 2.1
15	RR09-97	1037	1.28 ± 0.02	171.5 ± 1.8	132	1.77 ± 0.05	171.6 ± 1.7	47	1.84 ± 0.19	171.8 ± 2.8
13	RR09-96	1545	1.39 ± 0.02	172.8 ± 1.1	115	2.00 ± 0.07	174.2 ± 1.6	40	2.20 ± 0.11	174.0 ± 2.3
12	RR09-95	1233	1.38 ± 0.02	172.4 ± 1.2	128	2.05 ± 0.06	172.9 ± 1.5	40	2.35 ± 0.13	172.6 ± 2.1
10	RR09-94	1278	1.43 ± 0.02	169.1 ± 1.0	126	2.50 ± 0.09	170.6 ± 1.1	45	2.78 ± 0.17	171.6 ± 1.8
8	RR09-93	1287	1.33 ± 0.02	167.3 ± 1.4	116	2.22 ± 0.08	170.3 ± 1.4	44	2.23 ± 0.14	169.5 ± 2.0
6	RR09-92	949	1.36 ± 0.02	178.0 ± 1.4	119	2.10 ± 0.07	177.5 ± 1.5	52	2.26 ± 0.10	179.5 ± 2.1
4	RR09-91	959	1.25 ± 0.02	174.2 ± 2.0	112	2.14 ± 0.07	172.6 ± 1.5	57	2.21 ± 0.09	173.5 ± 2.1
2	RR09-90	1205	1.37 ± 0.02	175.1 ± 1.3	127	1.94 ± 0.06	176.3 ± 1.7	42	2.23 ± 0.12	177.3 ± 0.1
Mean			1.35	171.7		2.15	172.9		2.37	173.2
Std Dev.			0.06	4.2		0.21	3.5		0.30	4.2

Table 5.12: **Strain results - Section C.**

		Grains < 60 μm			Grains > 60 μm			Grains > 100 μm		
Elevation	Sample	N	R_s	φ	N	R_s	φ	N	R_s	φ
					Section E					
48	RR09-135	2949	1.39 ± 0.01	171.7 ± 0.7	122	2.49 ± 0.08	173.6 ± 1.6	37	2.60 ± 0.14	173.4 ± 2.5
44	RR09-134	3657	1.29 ± 0.01	163.7 ± 0.9	132	2.28 ± 0.08	165.8 ± 1.4	44	2.76 ± 0.16	166.9 ± 2.0
39	RR09-133	2718	1.21 ± 0.01	174.1 ± 1.4	154	2.15 ± 0.07	179.4 ± 1.4	53	2.40 ± 0.15	179.4 ± 1.9
34	RR09-132	2085	1.27 ± 0.01	165.5 ± 1.4	153	2.12 ± 0.07	165.2 ± 1.5	52	2.67 ± 0.13	166.7 ± 1.9
29	RR09-131	2950	1.27 ± 0.01	172.2 ± 1.1	165	2.01 ± 0.06	173.3 ± 1.4	54	2.45 ± 0.13	174.2 ± 1.7
24	RR09-130	2326	1.31 ± 0.01	172.9 ± 1.2	167	2.37 ± 0.09	174.5 ± 1.2	53	2.69 ± 0.17	174.9 ± 1.6
20	RR09-129	2860	1.36 ± 0.01	167.1 ± 0.9	155	2.36 ± 0.08	168.7 ± 1.3	42	2.59 ± 0.16	170.1 ± 2.1
16	RR09-127	1589	1.30 ± 0.02	163.5 ± 1.4	177	1.99 ± 0.06	162.0 ± 1.4	60	2.23 ± 0.11	163.0 ± 2.1
15	RR09-126	4782	1.29 ± 0.01	171.1 ± 0.8	109	2.28 ± 0.10	171.1 ± 1.6	33	2.65 ± 0.21	172.1 ± 2.3
14	RR09-125	2766	1.28 ± 0.01	168.2 ± 1.0	157	2.32 ± 0.07	169.5 ± 1.3	58	2.54 ± 0.11	170.1 ± 1.9
12	RR09-123	2703	1.29 ± 0.01	163.3 ± 1.1	149	2.07 ± 0.08	165.4 ± 1.6	45	2.52 ± 0.14	166.4 ± 1.9
9	RR09-122	2442	1.31 ± 0.01	167.9 ± 1.1	129	2.19 ± 0.09	171.4 ± 1.7	58	2.59 ± 0.14	173.4 ± 1.9
6	RR09-121	3912	1.23 ± 0.01	169.1 ± 1.2	118	2.03 ± 0.07	168.0 ± 1.5	33	2.35 ± 0.16	168.3 ± 2.2
Mean			1.29	168.5		2.20	169.8		2.54	170.7
Std Dev.			0.05	3.7		0.16	4.7		0.15	4.4

Table 5.13: **Strain results - Section E.**

		Grains < 60 μm			Grains > 60 μm			Grains > 100 μm		
Elevation	Sample	N	R_s	φ	N	R_s	φ	N	R_s	φ
					Indian Creek					
22	RR10-45	3733	1.39 ± 0.01	173.0 ± 0.6	88	2.93 ± 0.12	175.5 ± 1.1	16	3.91 ± 0.31	177.3 ± 1.9
13	RR10-43	2308	1.64 ± 0.02	174.1 ± 0.7	78	3.21 ± 0.14	177.3 ± 1.3	23	3.95 ± 0.33	178.5 ± 1.7
9	RR10-41	3923	1.51 ± 0.01	170.3 ± 0.5	75	3.62 ± 0.17	172.4 ± 1.2	18	4.36 ± 0.50	174.0 ± 1.8
7	RR10-40	1290	1.75 ± 0.02	172.3 ± 0.6	77	4.02 ± 0.19	173.1 ± 1.1	20	5.39 ± 0.35	173.6 ± 1.7
4	RR10-38	1670	1.59 ± 0.02	170.7 ± 0.6	77	3.91 ± 0.22	173.9 ± 1.0	20	5.15 ± 0.58	175.0 ± 1.3
2	RR10-37	2223	1.69 ± 0.02	175.4 ± 0.6	92	3.89 ± 0.17	177.3 ± 0.9	33	4.42 ± 0.27	178.8 ± 1.3
Mean			1.59	172.6		3.60	174.9		4.53	176.2
Std Dev.			0.13	2.0		0.44	2.1		0.61	2.3

Table 5.14: **Strain results - Indian Creek.**

		Grains < 60 μm			Grains > 60 μm			Grains > 100 μm		
Elevation	Sample	N	R_s	φ	N	R_s	φ	N	R_s	φ
					Duffy Creek					
24	RR10-36	4119	1.49 ± 0.01	176.5 ± 0.5	79	3.40 ± 0.17	175.5 ± 1.1	19	4.05 ± 0.35	174.9 ± 1.9
15	RR10-34	3474	1.42 ± 0.01	174.4 ± 0.6	109	2.85 ± 0.11	174.8 ± 1.1	30	3.62 ± 0.24	176.4 ± 1.5
14	RR10-32	2563	1.29 ± 0.01	177.3 ± 0.8	100	2.61 ± 0.11	179.3 ± 1.3	32	3.13 ± 0.30	179.0 ± 2.1
6	RR10-30	3762	1.56 ± 0.01	177.2 ± 0.6	88	3.82 ± 0.19	175.0 ± 0.9	20	5.34 ± 0.48	175.3 ± 1.0
3	RR10-29	1980	1.28 ± 0.01	177.8 ± 1.1	153	1.89 ± 0.06	175.1 ± 3.2	35	2.19 ± 0.12	176.9 ± 2.3
2	RR10-28	3854	1.23 ± 0.01	177.5 ± 1.0	85	2.42 ± 0.10	176.2 ± 1.4	25	3.40 ± 0.54	175.5 ± 1.8
Mean			1.38	176.8		2.83	176.0		3.62	176.3
Std Dev.			0.13	1.2		0.69	1.7		1.05	1.5

Table 5.15: **Strain results - Duffy Creek.**

ORIENTATION AND VORTICITY

DATA

Elevation (m above basement)	Sample	**M**	$\mathbf{s}_b$	**R**	**K**	$\mathbf{W}_k$
		Section A				
29	RR09-157	23.1	35.8	0.22	0.45	0.72
19	RR09-155	16.5	36.6	0.18	0.38	0.54
15	RR09-154	16.5	37.6	0.14	0.28	0.54
13	RR09-153	37.8	37.6	0.14	0.28	0.97
10	RR09-152	24.9	38.4	0.10	0.20	0.76
Mean		23.8	37.2	0.16	0.32	0.71
Harmonic Mean		21.6	37.2	0.1	0.3	0.68
Std Dev.		8.7	1.0	0.0	0.1	0.18
Minimum		16.5	35.8	0.1	0.2	0.54
1st quart (25%)		16.5	36.6	0.1	0.3	0.54
Median (50%)		23.1	37.6	0.1	0.3	0.72
2nd quart (75%)		24.9	37.6	0.2	0.4	0.76
Maximum		37.8	38.4	0.2	0.5	0.97

Table 5.16: **Vorticity and Orientation data - Section A.**

Elevation (m above basement)	Sample	**M**	$\mathbf{s}_b$	**R**	**K**	$\mathbf{W}_k$
		Section B				
64	RR09-86	28.3	34.1	0.3	0.6	0.84
58	RR09-85	32.2	37.9	0.1	0.2	0.90
50	RR09-84	23.3	34.1	0.3	0.6	0.73
43	RR09-83	9.9	32.4	0.4	0.8	0.34
37	RR09-82	17.8	34.0	0.3	0.6	0.58
25	RR09-78	17.0	32.6	0.4	0.7	0.56
14	RR09-76	13.1	32.2	0.4	0.8	0.44
10	RR09-75	24.4	32.6	0.4	0.8	0.75
Mean		20.7	33.7	0.3	0.6	0.64
Harmonic Mean		18.1	33.7	0.3	0.6	0.58
Std Dev.		7.6	1.9	0.1	0.2	0.20
Minimum		9.9	32.2	0.1	0.2	0.34
1st quart (25%)		16.0	32.6	0.3	0.6	0.53
Median (50%)		20.5	33.3	0.3	0.7	0.65
2nd quart (75%)		25.4	34.1	0.4	0.8	0.77
Maximum		32.2	37.9	0.4	0.8	0.90

Table 5.17: **Vorticity and Orientation data - Section B.**

Elevation (m above basement)	Sample	**M**	$\mathbf{s}_b$	**R**	**K**	$\mathbf{W}_k$
		Section C				
56	RR09-104	17.7	31.6	0.4	0.8	0.58
46	RR09-102	20.2	31.1	0.4	0.9	0.65
39	RR09-101	25.3	31.1	0.4	0.9	0.77
29	RR09-100	20.4	33.0	0.3	0.7	0.65
13	RR09-96	15.0	30.0	0.5	1.0	0.50
12	RR09-95	17.6	31.1	0.4	0.9	0.58
10	RR09-94	23.9	30.2	0.4	1.0	0.74
8	RR09-93	27.4	31.6	0.4	0.8	0.82
4	RR09-91	9.3	33.8	0.3	0.6	0.32
2	RR09-90	9.4	31.9	0.4	0.8	0.32
Mean		18.6	31.6	0.4	0.9	0.59
Harmonic Mean		16.4	31.5	0.4	0.8	0.54
Std Dev.		6.2	1.1	0.0	0.1	0.17
Minimum		9.3	30.0	0.3	0.6	0.32
1st quart (25%)		15.6	31.1	0.4	0.8	0.52
Median (50%)		18.9	31.4	0.4	0.9	0.61
2nd quart (75%)		23.0	31.9	0.4	0.9	0.72
Maximum		27.4	33.8	0.5	1.0	0.82

Table 5.18: **Vorticity and Orientation data - Section C.**

Elevation (m above basement)	Sample	**M**	$\mathbf{s}_b$	**R**	**K**	$\mathbf{W}_k$
		Section E				
48	RR09-135	19.3	30.9	0.4	0.9	0.62
44	RR09-134	34.1	32.4	0.4	0.8	0.93
39	RR09-133	12.2	34.7	0.3	0.6	0.41
34	RR09-132	28.2	33.1	0.3	0.7	0.83
29	RR09-131	15.9	33.6	0.3	0.7	0.53
24	RR09-130	15.0	32.9	0.3	0.7	0.50
20	RR09-129	13.9	31.7	0.4	0.8	0.47
16	RR09-127	34.9	33.1	0.3	0.7	0.94
15	RR09-126	17.9	32.8	0.3	0.7	0.59
14	RR09-125	25.5	32.8	0.3	0.7	0.78
12	RR09-123	36.0	33.0	0.3	0.7	0.95
9	RR09-122	25.5	32.1	0.4	0.8	0.78
6	RR09-121	23.6	34.2	0.3	0.3	0.73
Mean		23.2	32.9	0.3	0.7	0.70
Harmonic Mean		20.5	32.9	0.3	0.6	0.65
Std Dev.		8.3	1.0	0.0	0.2	0.19
Minimum		12.2	30.9	0.3	0.3	0.41
1st quart (25%)		15.9	32.4	0.3	0.7	0.53
Median (50%)		23.6	32.9	0.3	0.7	0.73
2nd quart (75%)		28.2	33.1	0.4	0.8	0.83
Maximum		36.0	34.7	0.4	0.9	0.95

Table 5.19: **Vorticity and Orientation data - Section E.**

Elevation (m above basement)	Sample	**M**	$\mathbf{s}_b$	**R**	**K**	$\mathbf{W}_k$
		Indian Creek				
22	RR10-45	14.8	27.3	0.5	1.3	0.49
13	RR10-43	13.0	28.7	0.5	1.1	0.44
9	RR10-41	21.4	32.1	0.4	0.8	0.68
7	RR10-40	16.3	28.0	0.5	1.2	0.54
4	RR10-38	18.5	32.4	0.4	0.8	0.60
2	RR10-37	9.9	33.0	0.3	0.7	0.34
Mean		15.6	30.2	0.4	1.0	0.52
Harmonic Mean		14.7	30.1	0.4	0.9	0.49
Std Dev.		4.1	2.5	0.1	0.3	0.12
Minimum		9.9	27.3	0.3	0.7	0.34
1st quart (25%)		13.5	28.1	0.4	0.8	0.45
Median (50%)		15.5	30.4	0.4	1.0	0.52
2nd quart (75%)		18.0	32.3	0.5	1.2	0.59
Maximum		21.4	33.0	0.5	1.3	0.68

Table 5.20: **Vorticity and Orientation data - Indian Creek section.**

Elevation (m above basement)	Sample	**M**	$\mathbf{s}_b$	**R**	**K**	$\mathbf{W}_k$
		Duffy Creek				
24	RR10-36	6.4	29.1	0.5	1.1	0.22
15	RR10-34	13.2	26.2	0.6	1.4	0.44
14	RR10-32	5.7	27.0	0.6	1.3	0.20
6	RR10-30	4.8	24.9	0.6	1.6	0.17
3	RR10-29	5.0	25.4	0.6	1.5	0.17
2	RR10-28	8.7	25.9	0.6	1.5	0.30
Mean		7.3	26.4	0.6	1.4	0.25
Harmonic Mean		6.4	26.3	0.6	1.4	0.22
Std Dev.		3.2	1.5	0.0	0.2	0.11
Minimum		4.8	24.9	0.5	1.1	0.2
1st quart (25%)		5.1	25.5	0.6	1.3	0.2
Median (50%)		6.0	26.0	0.6	1.4	0.2
2nd quart (75%)		8.1	26.8	0.6	1.5	0.3
Maximum		13.2	29.1	0.6	1.6	0.4

Table 5.21: **Vorticity and Orientation data - Duffy Creek section.**

STRAIN RATE CALCULATIONS

Elevation (m above basement)	Sample	Strain rate (s^{-1}) at constant temperature (400℃)	Strain rate (s^{-1}) with temperature gradient of Gottardi et al. (2011)	
		Section A		
29	RR09-157	6.9×10^{-14}	442	2.8×10^{-13}
23	RR09-156	8.5×10^{-14}	451	4.6×10^{-13}
19	RR09-155	7.1×10^{-14}	457	4.6×10^{-13}
15	RR09-154	7.2×10^{-14}	463	5.6×10^{-13}
13	RR09-153	7.2×10^{-14}	466	6.1×10^{-13}
10	RR09-152	1.5×10^{-13}	470	1.4×10^{-12}
5	RR09-151	6.0×10^{-14}	478	7.3×10^{-13}
2	RR09-150	6.5×10^{-14}	482	8.9×10^{-13}

Table 5.22: **Strain rate results - Section A.**

Elevation (m above basement)	Sample	Strain rate (s^{-1}) at constant temperature (400℃)	Strain rate (s^{-1}) with temperature gradient of Gottardi et al. (2011)	
		Section B		
64	RR09-86	7.3×10^{-14}	389	4.9×10^{-14}
58	RR09-85	6.6×10^{-14}	398	6.2×10^{-14}
50	RR09-84	9.9×10^{-14}	410	1.4×10^{-13}
43	RR09-83	1.2×10^{-13}	421	2.4×10^{-13}
37	RR09-82	7.5×10^{-14}	430	2.1×10^{-13}
31	RR09-81	8.2×10^{-14}	439	3.0×10^{-13}
25	RR09-78	1.2×10^{-13}	448	5.9×10^{-13}
14	RR09-76	1.0×10^{-13}	464	8.4×10^{-13}
10	RR09-75	9.1×10^{-14}	470	8.8×10^{-13}
7	RR09-74	1.0×10^{-13}	475	1.1×10^{-12}

Table 5.23: **Strain rate results - Section B.**

Elevation (m above basement)	Sample	Strain rate (s^{-1}) at constant temperature (400°C)	Strain rate (s^{-1}) with temperature gradient of Gottardi et al. (2011)	
		Section C		
65	RR09-105	3.3×10^{-14}	388	2.1×10^{-14}
56	RR09-104	3.9×10^{-14}	401	4.1×10^{-14}
52	RR09-103	3.8×10^{-14}	407	4.9×10^{-14}
46	RR09-102	3.8×10^{-14}	416	6.7×10^{-14}
39	RR09-101	4.7×10^{-14}	427	1.2×10^{-13}
29	RR09-100	4.1×10^{-14}	442	1.7×10^{-13}
15	RR09-97	2.7×10^{-14}	463	2.1×10^{-13}
13	RR09-96	3.1×10^{-14}	466	2.7×10^{-13}
12	RR09-95	3.4×10^{-14}	467	3.0×10^{-13}
10	RR09-94	4.3×10^{-14}	470	4.1×10^{-13}
8	RR09-93	3.1×10^{-14}	473	3.3×10^{-13}
6	RR09-92	3.1×10^{-14}	476	3.6×10^{-13}
4	RR09-91	5.9×10^{-14}	479	7.5×10^{-13}
2	RR09-90	4.0×10^{-14}	482	5.5×10^{-13}

Table 5.24: **Strain rate results - Section C.**

Elevation (m above basement)	Sample	Strain rate (s^{-1}) at constant temperature (400℃)	Strain rate (s^{-1}) with temperature gradient of Gottardi et al. (2011)	
		Section E		
48	RR09-135	6.0×10^{-14}	413	9.5×10^{-14}
44	RR09-134	7.2×10^{-14}	419	1.4×10^{-13}
39	RR09-133	6.9×10^{-14}	427	1.7×10^{-13}
34	RR09-132	5.8×10^{-14}	434	1.8×10^{-13}
29	RR09-131	6.0×10^{-14}	442	2.4×10^{-13}
24	RR09-130	6.0×10^{-14}	449	3.1×10^{-13}
20	RR09-129	6.8×10^{-14}	455	4.2×10^{-13}
16	RR09-127	4.0×10^{-14}	461	3.0×10^{-13}
15	RR09-126	1.1×10^{-13}	463	8.4×10^{-13}
14	RR09-125	7.1×10^{-14}	464	5.7×10^{-13}
12	RR09-123	5.9×10^{-14}	467	5.3×10^{-13}
9	RR09-122	5.8×10^{-14}	472	5.9×10^{-13}
6	RR09-121	6.9×10^{-14}	476	8.0×10^{-13}

Table 5.25: **Strain rate results - Section E.**

Elevation (m above basement)	Sample	Strain rate (s^{-1}) at constant temperature (400℃)	Strain rate (s^{-1}) with temperature gradient of Gottardi et al. (2011)	
		Indian Creek		
22	RR10-45	6.0×10^{-14}	452	3.4×10^{-13}
13	RR10-43	1.0×10^{-13}	466	8.8×10^{-13}
9	RR10-41	8.3×10^{-14}	472	8.4×10^{-13}
7	RR10-40	6.0×10^{-14}	475	6.7×10^{-13}
4	RR10-38	5.8×10^{-14}	479	7.3×10^{-13}
2	RR10-37	8.5×10^{-14}	482	1.2×10^{-12}

Table 5.26: **Strain rate results - Indian Creek.**

Elevation (m above basement)	Sample	Strain rate (s^{-1}) at constant temperature (400℃)	Strain rate (s^{-1}) with temperature gradient of Gottardi et al. (2011)	
		Duffy Creek		
24	RR10-36	8.0×10^{-14}	449	4.1×10^{-13}
15	RR10-34	9.1×10^{-14}	463	7.1×10^{-13}
14	RR10-32	6.5×10^{-14}	464	5.3×10^{-13}
6	RR10-30	9.9×10^{-14}	476	1.1×10^{-12}
3	RR10-29	5.8×10^{-14}	481	7.6×10^{-13}
2	RR10-28	6.5×10^{-14}	482	8.9×10^{-13}

Table 5.27: **Strain rate results - Duffy Creek.**

Appendix 2 - Argon Geochronology

SAMPLE PREPARATION AND IRRADIATION:

Separates were loaded into machined Al discs and irradiated for 10 hours, USGS TRIGA Reactor, Denver.

Neutron flux monitor Fish Canyon Tuff sanidine (FC-2). Assigned age = 28.02 Ma (Renne et al., 1998)

INSTRUMENTATION:

Mass Analyzer Products 215-50 mass spectrometer on line with automated all-metal extraction system.

Samples step-heated in Mo double vacuum resistance furnace.

Reactive gases removed during a 7 minute heating with a SAES GP-50 getter operated at ~450°C.

Additional cleanup (2 minutes) following heating with 2 SAES GP-50 getters, 1 operated at ~450°C and 1 at 20°C.

Gas also exposed to cold finger -140°C during heating.

ANALYTICAL PARAMETERS:

Electron multiplier sensitivity about 1.0×10^{-16} moles/pA

Total system blank and background: 200, 1.5, 0.4, 2.0, 0.9 x 10^{-17} moles for

masses 40, 39, 38, 37, 36, respectively.

J-factors determined to a precision of ~*pm* 0.10 % by CO_2 laser-fusion of 6 single crystals from each of 6 radial positions around the irradiation tray.

NOTE:

Isotopic ratios corrected for blank, radioactive decay, and mass discrimination, not corrected for interfering reactions.

Errors quoted for individual analyses include analytical error only, without interfering reaction or J uncertainties.

Integrated age calculated by summing isotopic measurements of all steps.

Integrated age error calculated by quadratically combining errors of isotopic measurements of all steps.

Plateau age is inverse-variance-weighted mean of selected steps.

Plateau age error is inverse-variance-weighted mean error (Taylor, 1982) times root MSWD where MSWD>1.

Plateau error is weighted error of Taylor (1982).

Decay constants and isotopic abundances after Steiger and Jäger (1977).

Weight percent K_2O calculated from ^{39}Ar signal, sample weight, and instrument sensitivity.

Ages calculated relative to FC-2 Fish Canyon Tuff sanidine interlaboratory standard at 28.02 Ma.

Decay Constant (λ_K total) = 5.543×10^{-10}/a

CORRECTION FACTORS:

($^{39}Ar/^{37}Ar$)Ca = $0.0007 \pm 5 \times 10^5$

($^{36}Ar/^{37}Ar$)Ca = $0.00028 \pm 2 \times 10^5$

($^{38}Ar/^{39}Ar$)K = 0.013

($^{40}Ar/^{39}Ar$)K = 0.01 ± 0.002

Appendix 3 - Stable Isotopes Geochemistry

The δD values of hydrous silicates were determined by continuous flow mass spectrometry using a high temperature elemental analyzer (Thermo Finnigan TC/EA) coupled to a mass spectrometer (Delta V Advantage). Three internationally referenced standard materials and additional in-house working standards were run with the samples. After correction of mass bias, daily drift of the thermal combustion reactor and offset from the certified reference values, NBS30 (biotite), NBS22 (oil), CH7 (polyethylene foil) had dD = -65.8 ‰, -118.6 ‰, and -102.1 ‰, respectively. Repeated measurements of various standards and unknowns gave a precision of ± 2 ‰ for δD. All isotopic ratios are reported relative to standard mean ocean water (VSMOW).

The $\delta^{18}O$ values of quartz and muscovite pairs were measured using laser-fluorination mass spectrometry. About 1.2 to 1.5 mg of muscovite and quartz were heated using a CO_2-laser fluorination line coupled to a Finnigan MAT253 mass spectrometer in the Stable Isotope Laboratory at the University of Lausanne, Switzerland. Mineral pairs were measured within the same run together with at least two mineral standards. All samples were run in duplicate, and measurements were accepted if duplicate analyses were within ± 0.25 ‰. $\delta^{18}O$ values are nor-

malized to values of 9.6 ‰measured for NBS-28 quartz and average precision of in-house standards is $\pm$ 0.1 ‰.

Appendix 4 - Modeling

SCALING ANALYSES FOR GROUNDWATER FLOW, HEAT TRANSFER, ISOTOPE TRANSPORT, AND FLUID-SLID EXCHNAGE

In order to scale the mesoscopic dimensionless lattice-Boltzmann algorithms to physical fluid flow, and heat transport with fluid-solid isotope exchange over large spatial scales, we apply scaling analyses to establish the relationship between the numerical and physical unit systems.

Length scaling

Dimensional (physical) spatial length scale for unit grid size is chosen by $\Delta x_{phy} =$ 150 (m) for current simulations. Thus, the physical length scale (L_{phy}) can be computed by:

$$L_{phy} = N_{LB} \cdot \Delta x_{phy} \tag{5.6}$$

where N_{LB} is grid numbers used in the computational domain.

Pressure scaling

In LB algorithm, numerical pressure is determined by the equation of state: i.e. $P_{LB} = c_s^2 \rho_{LB} = \rho_{LB}/3$, where c_s is the speed of sound, and ρ_{LB} is the numerical fluid density. The numerical-physical pressure relationship can be normalized as:

$$\frac{P_{phy\cdot local} - P_{phy\cdot min}}{P_{phy\cdot max} - P_{phy\cdot min}} = \frac{P_{LB\cdot local} - P_{LB\cdot min}}{P_{LB\cdot max} - P_{LB\cdot min}} \tag{5.7}$$

where $P_{LB\cdot max/min} = \dfrac{\rho_{LB\cdot max/min}}{3}$, and P_{phy} is physical pressure, which is determined by $\rho_f gh$ (h is the hydraulic-head).

Temperature scaling

Normalization is also applied for the numerical-physical temperature relationship with the maximum $T_{LB\dot{m}ax} = 1.0$ and minimum $T_{LB\dot{m}in} = 0.0$ values, so that:

$$\frac{T_{phy\cdot local} - T_{phy\cdot min}}{T_{phy\cdot max} - T_{phy\cdot min}} = \frac{T_{LB\cdot local} - T_{LB\cdot min}}{T_{LB\cdot max} - T_{LB\cdot min}} \tag{5.8}$$

Crust permeability scaling

For simulating geofluid cases here, we implement the 2^{nd}-order partial-bounceback LB scheme, in which, the available value range of numerical permeability is restricted by $k_{LB} = 0.5833 \approx 0.0072$. However, the practical (physical) permeability range in Earth's crust is usually within the range: $10^{-14}m^2 < k_{phy} < 10^{-19}m^2$. In order to overcome this numerical limitation and difficulty, a logarithm-normalization algorithm is proposed to model the numerical-physical permeability relationship, such that,

$$\frac{log\left(k_{LB\cdot local}/k_{LB\cdot min}\right)}{log\left(k_{LB\cdot max}/T_{LB\cdot min}\right)} = \frac{log\left(k_{phy\cdot local}/k_{phy\cdot min}\right)}{log\left(k_{phy\cdot max}/T_{phy\cdot min}\right)} \tag{5.9}$$

Once physical and numerical maximum/minimum permeabilities are defined by: $k_{LB\cdot max} = 0.583333333$, $k_{LB\cdot max} = 0.007201646$, $k_{phy\cdot max} = 10^{14} m^2$, $k_{phy\cdot min} = 10^{19} m^2$ and in Eq. 5.9. Permeability scaling equations can then be obtained:

$$k^R = \frac{log\left(k_{phy\cdot max}/k_{phy\cdot min}\right)}{log\left(k_{LB\cdot max}/T_{LB\cdot min}\right)} \tag{5.10}$$

So that:

$$k_{phy\cdot local} = k_{phy\cdot min} \cdot 10^{C_{phy}} \tag{5.11}$$

where

$$C_{phy} = k^R \cdot log\left(k_{LB\cdot local}/k_{LB\cdot min}\right) \tag{5.12}$$

and

$$k_{LB\cdot local} = k_{LB\cdot min} \cdot 10^{C_{LB}} \tag{5.13}$$

where

$$C_{LB} = \frac{log\left(k_{phy\cdot local}/k_{phy\cdot min}\right)}{k^R} \tag{5.14}$$

Velocity scaling

A format for numerical-physical velocity relationship is chosen by:

$$q_{phy} = q_{LB} \cdot \frac{\Delta x_{phy}}{\Delta t_{Flow/Thermal\cdot phy}} \tag{5.15}$$

where q is Darcy's velocity in porous media, $\Delta t_{Flow/Thermal\cdot phy}$ is the physical time scale (seconds) per unit numerical time-step ($\Delta t_{LB} = 1$) for fluid flow and thermal transfer, as modeled in Appendix-C.6.

However, the grid-number mapped in faults-zones (Fig 5) shall be $N_{LB\cdot Faults} > 4$ to provide the sufficient resolution in computing accurate numerical results, where the computational fault width is larger than the real (physical) width in fault layers. Hence, we apply a velocity correcting factor (qwt), based on the flow-rate conservation principle, to obtain the reality velocity inside faults-zones:

$$(q_{phy})_{faults} = qwt \cdot (q_{LB})_{Faults} \cdot \frac{\Delta x_{phy}}{\Delta_{Flow/Thermal\cdot phy}} \tag{5.16}$$

In current simulations, the characteristic fault width is chosen by 100 m and mapped by $N_{LB\cdot Faults} = 5$, and thus, $qwt = 7.5$ shall be used. Note that, the velocity correction Eq. 5.16 is only applied to correct the physical velocity inside faults-zones. We do so for the important reason that, the computation does not need to implement complicate grid techniques or numerical schemes, e.g. the local-refinement grid treatment with special simulation algorithms. Hence, the computational algorithm can be maintained as simple as possible, and the simulation efficiency is much improved with sufficiently accurate results.

Time scaling for fluid flow and thermal transfer

For modeling the time scale of fluid flow and thermal transfer, we apply an "'effective 1D Darcy's formation"' to represent the overall heterogeneous medium flow. In the numerical unit system, the equation is considered by:

$$(\rho_{LB} \cdot q_{LB})_{overall} = \frac{\Delta P_{LB\cdot Eff}}{\nu_{LB}} \cdot \frac{k_{LB\cdot Eff}}{L_{LB\cdot Eff}} \tag{5.17}$$

where $(\rho_{LB} \cdot q_{LB})_{overall}$ is the overall characteristic flow moment inside the heterogeneous medium, which is solved by partial-bounceback LB computation,

$\Delta P_{LB\cdot Eff}$ is the effective boundary pressure-difference, which is determined by:

$\Delta P_{LB\cdot Eff} = \dfrac{2}{N_H + N_M + N_L}\left(N_H \cdot P_H + N_M \cdot P_M - N_L \cdot P_L\right)$, where P_H, P_M, P_L and N_H, N_M, N_L are the numerical boundary pressures and boundary grid numbers at higher-, middle-, and lower-elevation upper-boundaries (Fig 5), $k_{LB\cdot Eff}/L_{LB\cdot Eff}$ is a ratio of the effective permeability to the effective characteristic-flow-length, these values are need to be determined.

When $(\rho_{LB} \cdot q_{LB})_{overall}$, $\Delta P_{LB\cdot Eff}$, and ν_{LB} are specified or computed,

$k_{LB\cdot Eff}/L_{LB\cdot Eff}$ can then be obtained by 5.17. Subsequently, the $k_{LB\cdot Eff}$ and $L_{LB\cdot Eff}$ can further be computed by following procedures:

1. Using a weighting approach to evaluate the effective numerical solid-fraction ($n_{s\cdot Eff}$):

$$n_{s\cdot Eff} = \frac{N_{Faults}}{N_{Total}} n_{s\cdot Faults} + \frac{N_{Faults}}{N_{Basins}} n_{s\cdot Basins} + \frac{N_{Shear-zone}}{N_{Total}} n_{s\cdot Shear-zone} + \frac{N_{Upper-plate}}{N_{Total}} n_{s\cdot Upper-plate} + \frac{N_{Lower-plate}}{N_{Total}} n_{s\cdot Lower-plate} \tag{5.18}$$

   where N_{Total} is the total grid-number used for the computational domain, and is the sum of grid-numbers of crust-layers, n_s is the numerical solid fraction in those crust-layers

2. $k_{LB\cdot Eff}$ is obtained by the equation for 2nd-order partial-bounceback LB scheme:

$$k_{LB\cdot Eff} = \frac{\nu_{LB}\left(1 - n_{s\cdot Eff}\right)}{2 \cdot n_{s\cdot Eff}} \tag{5.19}$$

3. $L_{LB\cdot Eff}$ can be computed using the $k_{LB\cdot Eff}$ and $(k_{LB\cdot Eff}/L_{LB\cdot Eff})$ values.

   In the physical unit system, considering the logarithm relationship for the physical and numerical permeabilities, the 1D effective Darcy's formation shall be formulated as,

$$q_{phy} = 10^{k^R} \cdot \frac{\Delta P_{phy \cdot Eff}}{\nu_{phy} \cdot \rho_{phy}} \cdot \frac{k_{phy \cdot Eff}}{L_{phy \cdot Eff}} \tag{5.20}$$

In 5.20, ν_{phy} and ρ_{phy} are all given values, and k^R is computed by 5.10. $\Delta P_{phy \cdot Eff}$ can be evaluated using the approach for determining the numerical boundary pressures modeled in Eq. 5.17, where the physical boundary pressures (P_H, P_M, P_L) and physical upper boundary lengths (L_H, L_M, L_L) are used to instead of the numerical pressures and grid numbers, respectively. Furthermore, the relationship between $k_{phy \cdot Eff}$ and $k_{LB \cdot Eff}$ shall satisfy 5.12, and $L_{phy \cdot Eff}$ is obtained by $L_{LB \cdot Eff}$ using 5.6. Applying this procedure, q_{phy} can be determined using Eq. 5.20. Hence, the physical time-scale for fluid flow and thermal transport can further be obtained by:

$$\Delta t_{Flow/Thermal \cdot phy} = \frac{q_{LB \cdot overall}}{q_{phy}} \cdot \Delta x_{phy} \tag{5.21}$$

Note that the $q_{LB \cdot overall}$ value is directly obtained by partial-bounceback LB simulation.

Heat flux scaling for Crust-Bottom boundary

The physical crust-bottom heat flux satisfies the Fourier's Law, i.e.:

$$\mathbf{q}_{Btm \cdot phy} = k_{rk} \left(\frac{dT}{dy} \right)_{phy} \tag{5.22}$$

where $\mathbf{q}_{Btm \cdot phy}$ is the physical crust-bottom heat flux (with unit: W/m^2), k_{rk} is the thermal conductivity (W/°C m) at bottom-crust, $\left(\frac{dT}{dy} \right)_{phy}$ is the physical temperature gradient (°C/m) along vertical (y) direction. When the heat flux ($\mathbf{q}_{Btm \cdot phy}$) and thermal conductivity (k_{rk}) are given, the temperature gradient $\left(\frac{dT}{dy} \right)_{phy}$ can

be determined. The numerical temperature gradient per each LB-element (Δx_{LB}) can then be obtained by the length and temperature scaling relationships, such as:

$$\left(\frac{\Delta T}{\Delta x}\right)_{LB} = \left(\frac{\Delta T}{\Delta y}\right)_{phy} \cdot \frac{\Delta x_{phy}}{(T_{max} - T_{min})_{phy}} \tag{5.23}$$

Buoyancy scaling

For evaluation of the physical characteristic buoyant velocity $(q_{buoy \cdot phy}, m/s)$ within a porous medium, the logarithm permeability relationship shall be taken into account and has a format of:

$$q_{Buoy \cdot phy} = 10^{k^R} \cdot (\beta\, \Delta T)_{phy} \cdot \frac{k_{phy \cdot Eff} \cdot g_{phy}}{\nu_{phy}} \tag{5.24}$$

where $\beta = \dfrac{-1}{\rho_f^{ref}} \cdot \left(\dfrac{d\rho}{dT}\right)_P$ is the thermal expansion coefficient, and ρ_f^{ref} is the reference fluid density (kg/m^3), chosen by the temperature (25°C) specified at the ground surface (upper) boundaries, g_{phy} is the physical gravity (m/sec^2) along the vertical (y) direction, ν_{phy} is physical fluid kinematic viscosity (m^2/sec).

Note that, this format for modeling the characteristic buoyant velocity (q_{Buoy}) is actually identical with the format in Eq. 5.6, because of $\beta \cdot \Delta T = \dfrac{\left(\rho_f - \rho_f^{ref}\right)}{\rho_f^{ref}}$. In LB algorithm, the buoyant body force term is treated as:

$$q_{Buoy \cdot LB} = (\beta \cdot g) \cdot \Delta T_{LB} \cdot \Delta t_{LB} \tag{5.25}$$

where Δt_{LB} is the unity numerical time-step, i.e. $\Delta t_{LB} = 1$, ΔT_{LB} is the numerical temperature difference between ground surface (upper) boundary and local boundary, and shall satisfy the temperature relationship of 5.8.

As the numerical-physical velocity relationship shall satisfy Eq. 5.15, the appropriate value range of $(\beta g)_{LB}$ can be found within the range of $0.00034 \approx 0.00026$. For current simulations, we fix the $(\beta g)_{LB} = 0.0003$ as a constant.

Oxygen isotopes scaling

In isotope transport/exchange LB computations, we apply normalized (numerical) oxygen-isotopes, i.e. $R_{f\cdot LB}$ and $R_{s\cdot LB}$, to represent physical $\delta^{18}O$ isotope components (in $‰$unit) in the fluid-phase and solid-phase, respectively, which satisfy the following relationships:

$$\frac{\delta^{18}O_{f\cdot phy} - \delta^{18}O^{min}_{f\cdot phy}}{\delta^{18}O^{max}_{f\cdot phy} - \delta^{18}O^{min}_{f\cdot phy}} = \frac{R_{f\cdot LB} - R^{min}_{f\cdot LB}}{R^{max}_{f\cdot LB} - R^{min}_{f\cdot LB}} \tag{5.26}$$

$$\frac{\delta^{18}O_{s\cdot phy} - \delta^{18}O^{min}_{s\cdot phy}}{\delta^{18}O^{max}_{s\cdot phy} - \delta^{18}O^{min}_{s\cdot phy}} = \frac{R_{s\cdot LB} - R^{min}_{s\cdot LB}}{R^{max}_{s\cdot LB} - R^{min}_{s\cdot LB}} \tag{5.27}$$

Once the numerical ($R_{f\cdot LB}$ and $R_{s\cdot LB}$) and physical ($\delta^{18}O_{f\cdot phy}$ and $\delta^{18}O_{s\cdot phy}$) oxygen isotopes are solved by LB simulation and by Eq. 5.26 and Eq. 5.27, the physical phase oxygen-isotope-ratios ($\mathbf{R}$) can then be obtained by:

$$\mathbf{R}_{f/s\cdot phy} = \left(\frac{\delta^{18}O_{f/s\cdot phy}}{1000} + 1 \right) \cdot \mathbf{R}^{^{18}O}_{Std} \tag{5.28}$$

where $\mathbf{R}^{^{18}O}_{Std}$ is the isotopic standard for oxygen with a value of 0.0020052 based on mean sea water composition (SMOW).

Time scaling for oxygen isotope transport and exchange

Because the LB computations of fluid-flow/thermal-transfer and for isotope-exchange are performed individually in the present investigation, a scaling analysis for the

relative time-scale between those transport phenomena is essential. We model the time-scale ratio of the flow/thermal behaviors to isotope-exchange by means of the Lewis number, which is defined by $Le \equiv D_{Thermal}/D_{Isotope}$ where D are the thermal and/or solute (isotope) diffusivities. Since the length scales of unit grid size (Δx) in flow/thermal field and in isotope field are identical (grid size is fixed for a non-deformable crustal topography), the Lewis number can be regarded as the time-scale ratio of those transport phenomena, i.e.:

$$Le = \frac{\Delta t_{Isotope}}{\Delta t_{Flow/Thermal}} \tag{5.29}$$

Then, a relative time factor (C_{time}) is defined by:

$$C_{time} \equiv \frac{Le_{phy}}{Le_{LB}} \tag{5.30}$$

where the physical and numerical Lewis numbers, i.e. Le_{phy} and Le_{LB}, shall be determined by their respective thermal and solute diffusivities applied in geofluid computations. Note that, for the reason of computational stability using LB algorithms, those numerical properties can be specified with values much different from the real physical values.

Finally, the time-scale relationship between isotope-exchange and the flow/thermal transport can be determined by:

$$\Delta t_{Isotope \cdot phy} = C_{time} \cdot \Delta t_{Flow/Thermal \cdot phy} \tag{5.31}$$

where $\Delta t_{Flow/Thermal \cdot phy}$ is obtained by the model formulated in Appendix-C6.

In current investigation, we apply $Le = 6.5439248$ for LB simulations, and then get $C_{time} \approx 1.93 \times 10^3$ for physical crust porosities range: $0.03 < \phi < 0.08$.

Appendix 5 - Complementary Modeling Results

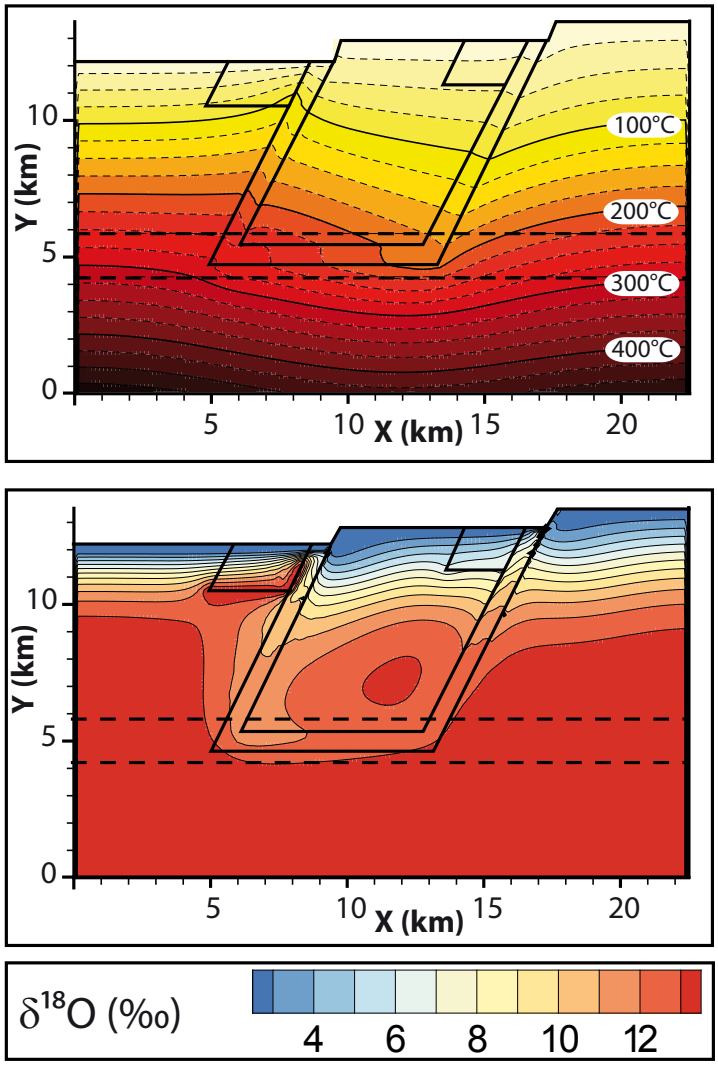

Figure 5.11: **Temperature (top) and Oxygen isotopes (bottom) results, with connected faults, using the following permeabilities: $k_{lowerplate}$ = 10^{-19} m^2, $k_{upperplate}$ = 10^{-19} m^2, $k_{shearzone}$ = 10^{-19} m^2, k_{faults} = 10^{-15} m^2, k_{basin} = 10^{-14} m^2.**

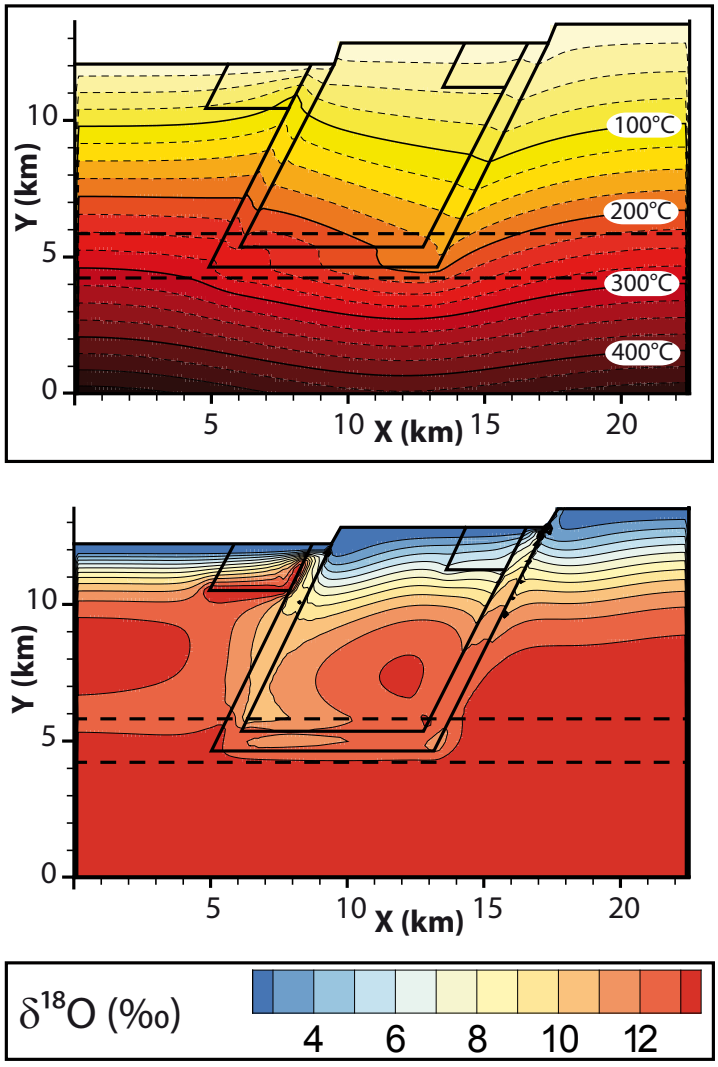

Figure 5.12: **Temperature (top) and Oxygen isotopes (bottom) results, with connected faults, using the following permeabilities: $k_{lowerplate}$ = 10^{-19} m^2, $k_{upperplate}$ = 10^{-19} m^2, $k_{shearzone}$ = 10^{-18} m^2, k_{faults} = 10^{-15} m^2, k_{basin} = 10^{-14} m^2.**

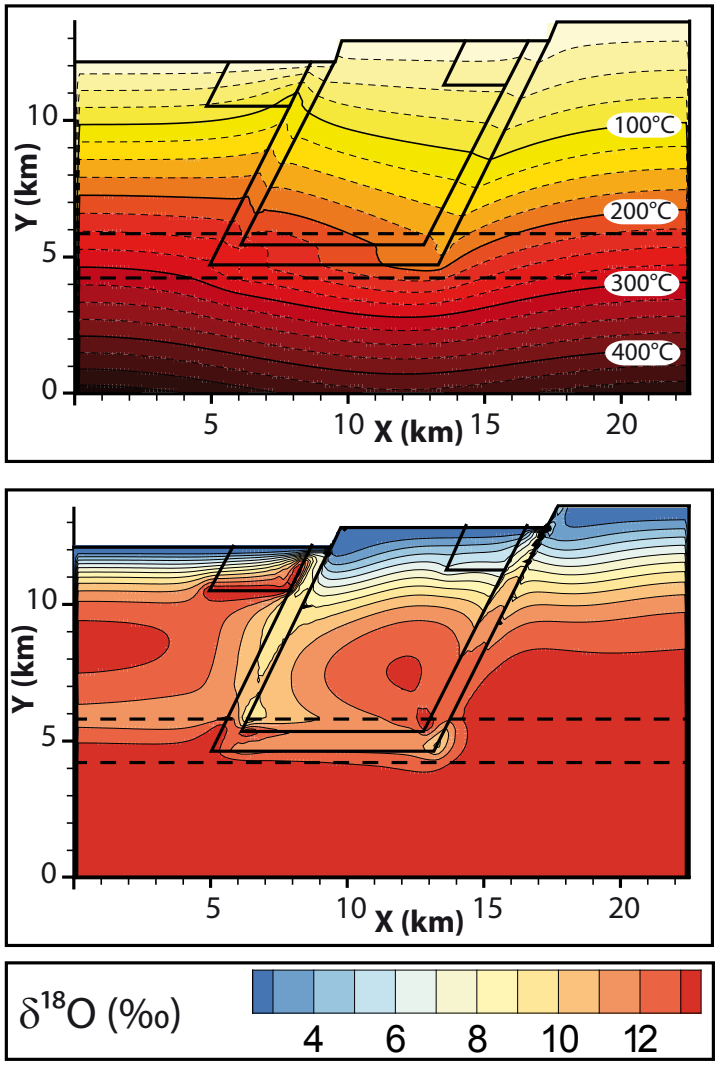

Figure 5.13: **Temperature (top) and Oxygen isotopes (bottom) results, with connected faults, using the following permeabilities: $k_{lowerplate}$ = 10^{-19} m^2, $k_{upperplate}$ = 10^{-19} m^2, $k_{shearzone}$ = 10^{-17} m^2, k_{faults} = 10^{-15} m^2, k_{basin} = 10^{-14} m^2.**

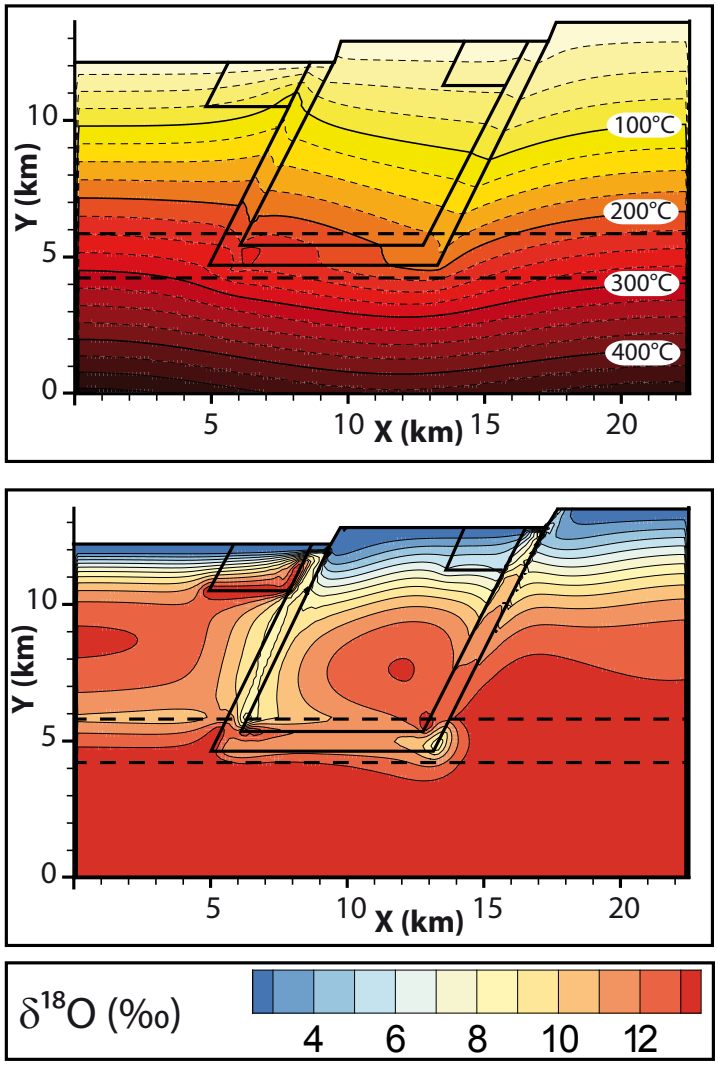

Figure 5.14: **Temperature (top) and Oxygen isotopes (bottom) results, with connected faults, using the following permeabilities: $k_{lowerplate}$ = 10^{-19} m^2, $k_{upperplate}$ = 10^{-19} m^2, $k_{shearzone}$ = 10^{-16} m^2, k_{faults} = 10^{-15} m^2, k_{basin} = 10^{-14} m^2.**

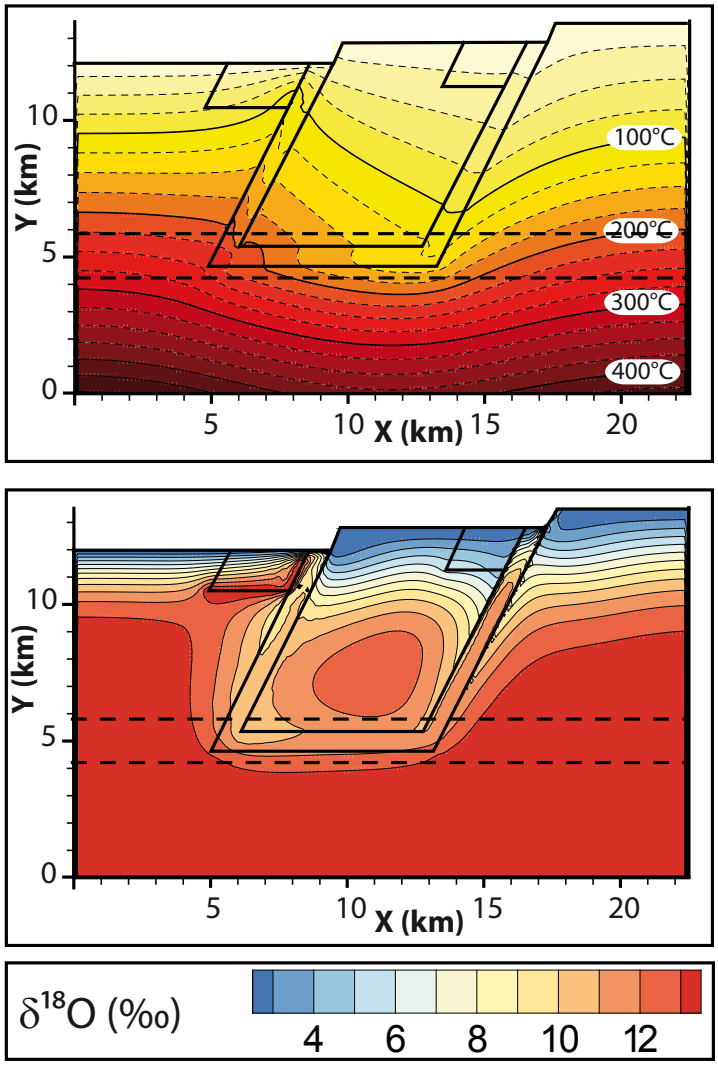

Figure 5.15: **Temperature (top) and Oxygen isotopes (bottom) results, with connected faults, using the following permeabilities: $k_{lowerplate}$ = 10^{-19} m^2, $k_{upperplate}$ = 10^{-19} m^2, $k_{shearzone}$ = 10^{-19} m^2, k_{faults} = 10^{-14} m^2, k_{basin} = 10^{-14} m^2.**

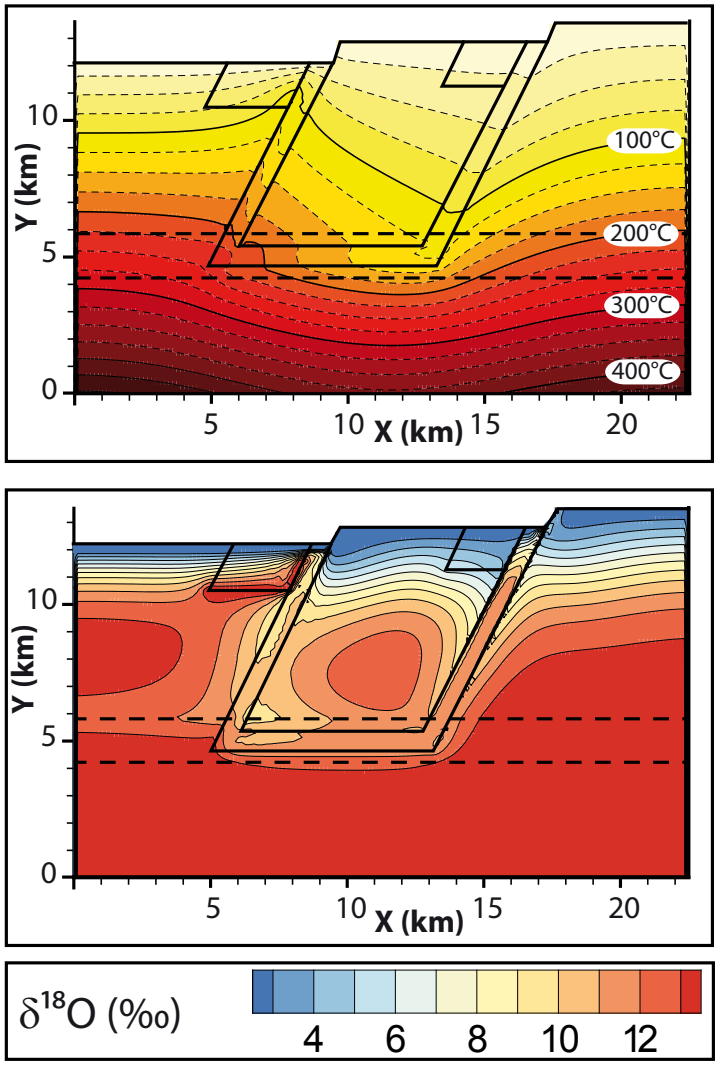

Figure 5.16: **Temperature (top) and Oxygen isotopes (bottom) results, with connected faults, using the following permeabilities: $k_{lowerplate}$ = 10^{-19} m^2, $k_{upperplate}$ = 10^{-19} m^2, $k_{shearzone}$ = 10^{-18} m^2, k_{faults} = 10^{-14} m^2, k_{basin} = 10^{-14} m^2.**

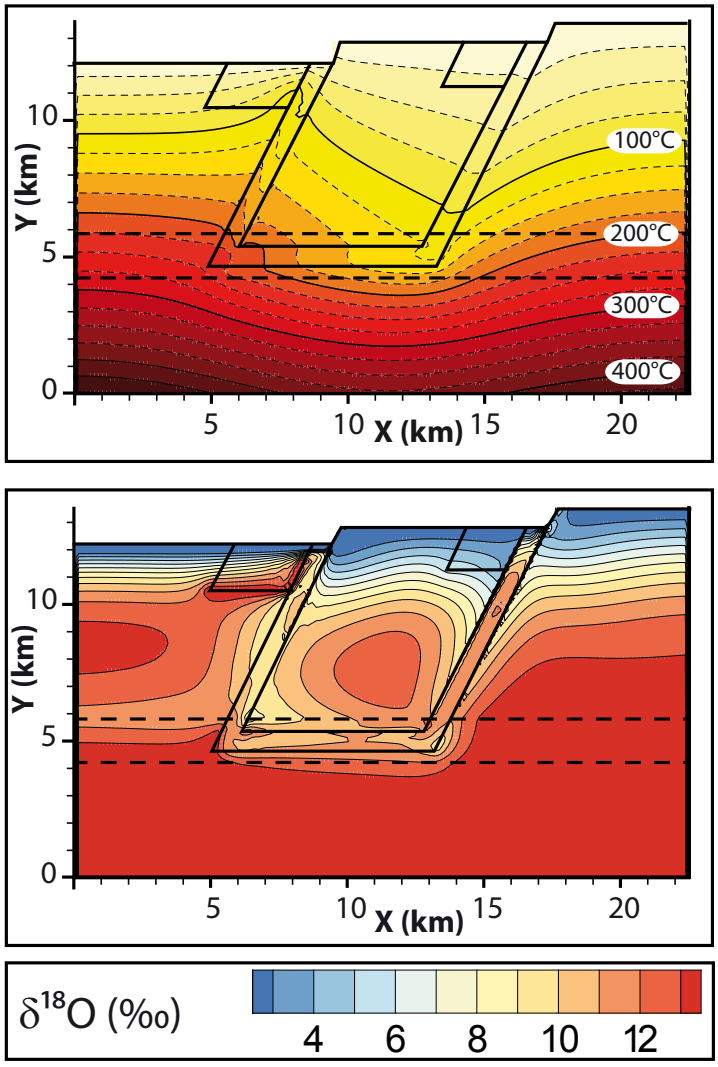

Figure 5.17: **Temperature (top) and Oxygen isotopes (bottom) results, with connected faults, using the following permeabilities: $k_{lowerplate} = 10^{-19}$ m^2, $k_{upperplate} = 10^{-19}$ m^2, $k_{shearzone} = 10^{-17}$ m^2, $k_{faults} = 10^{-14}$ m^2, $k_{basin} = 10^{-14}$ m^2.**

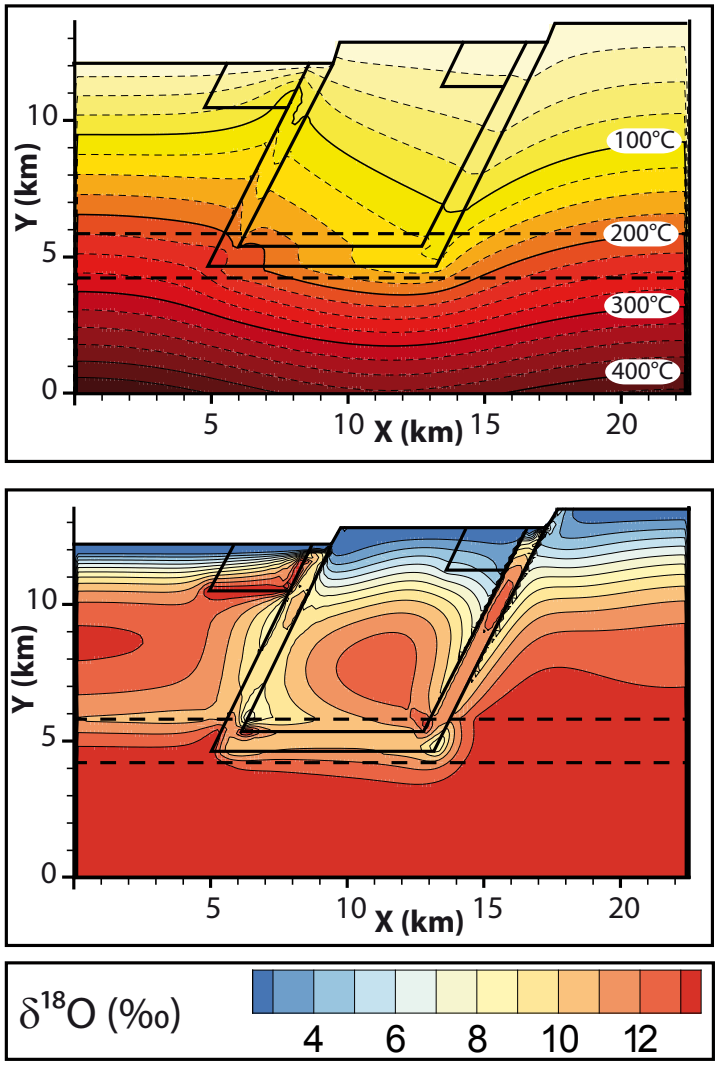

Figure 5.18: **Temperature (top) and Oxygen isotopes (bottom) results, with connected faults, using the following permeabilities: $k_{lowerplate}$ = 10^{-19} m^2, $k_{upperplate}$ = 10^{-19} m^2, $k_{shearzone}$ = 10^{-16} m^2, k_{faults} = 10^{-14} m^2, k_{basin} = 10^{-14} m^2.**

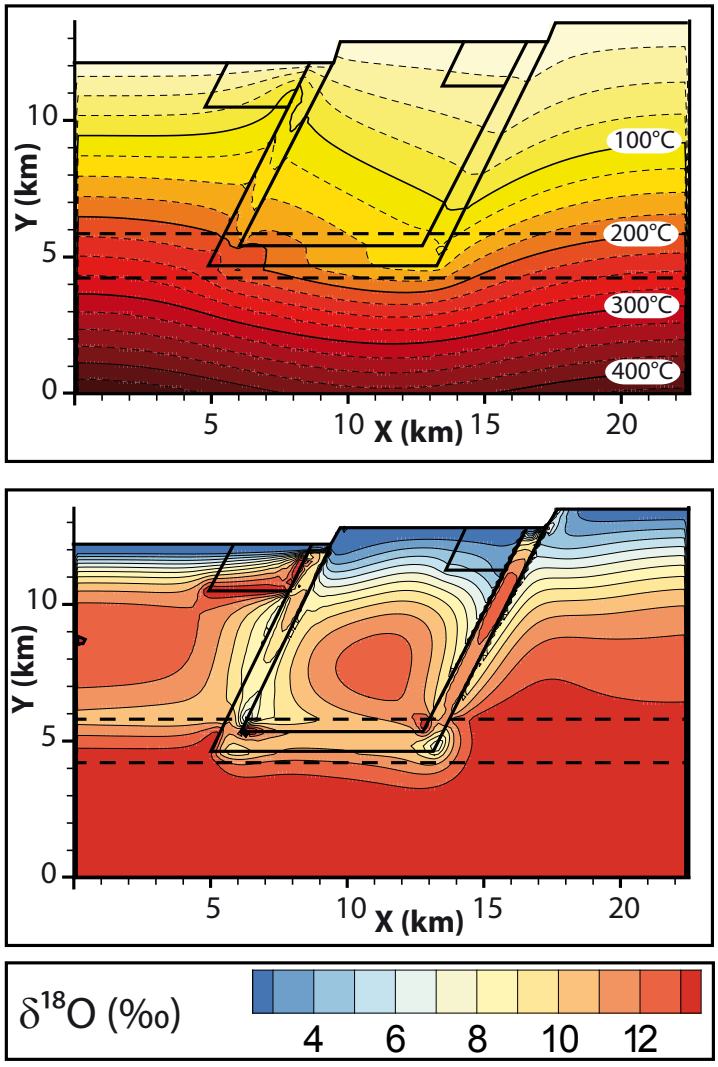

Figure 5.19: **Temperature (top) and Oxygen isotopes (bottom) results, with connected faults, using the following permeabilities: $k_{lowerplate}$ = 10^{-19} m^2, $k_{upperplate}$ = 10^{-19} m^2, $k_{shearzone}$ = 10^{-15} m^2, k_{faults} = 10^{-14} m^2, k_{basin} = 10^{-14} m^2.**

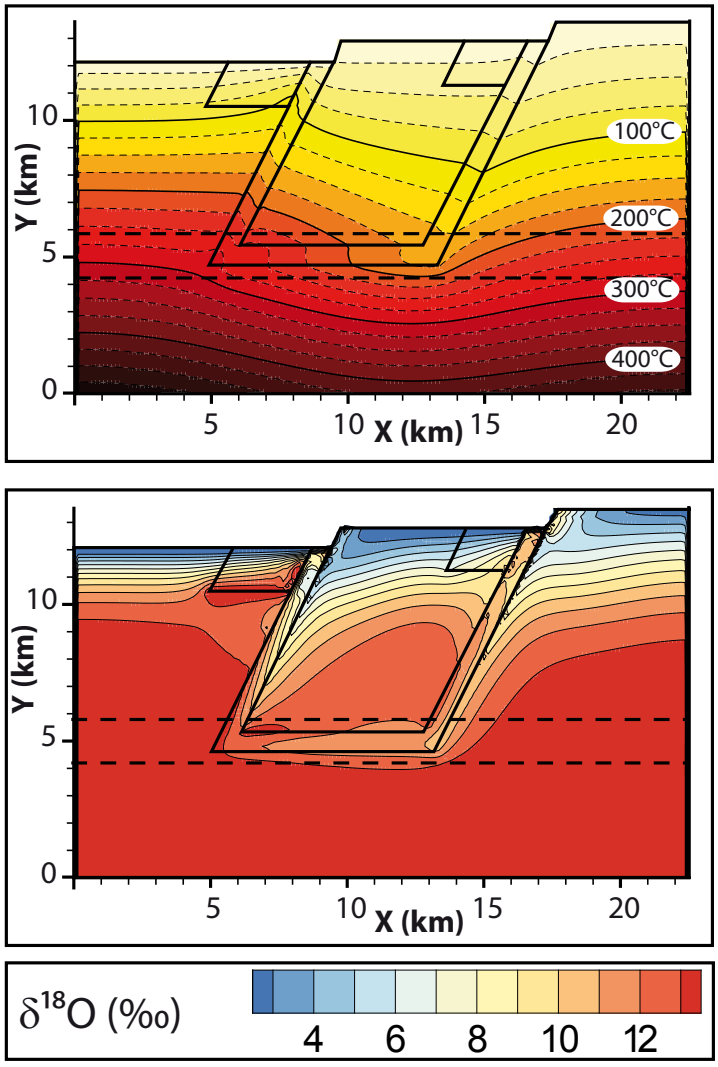

Figure 5.20: **Temperature (top) and Oxygen isotopes (bottom) results, with connected faults, using the following permeabilities: $k_{lowerplate}$ = 10^{-19} m^2, $k_{upperplate}$ = 10^{-18} m^2, $k_{shearzone}$ = 10^{-18} m^2, k_{faults} = 10^{-15} m^2, k_{basin} = 10^{-14} m^2.**

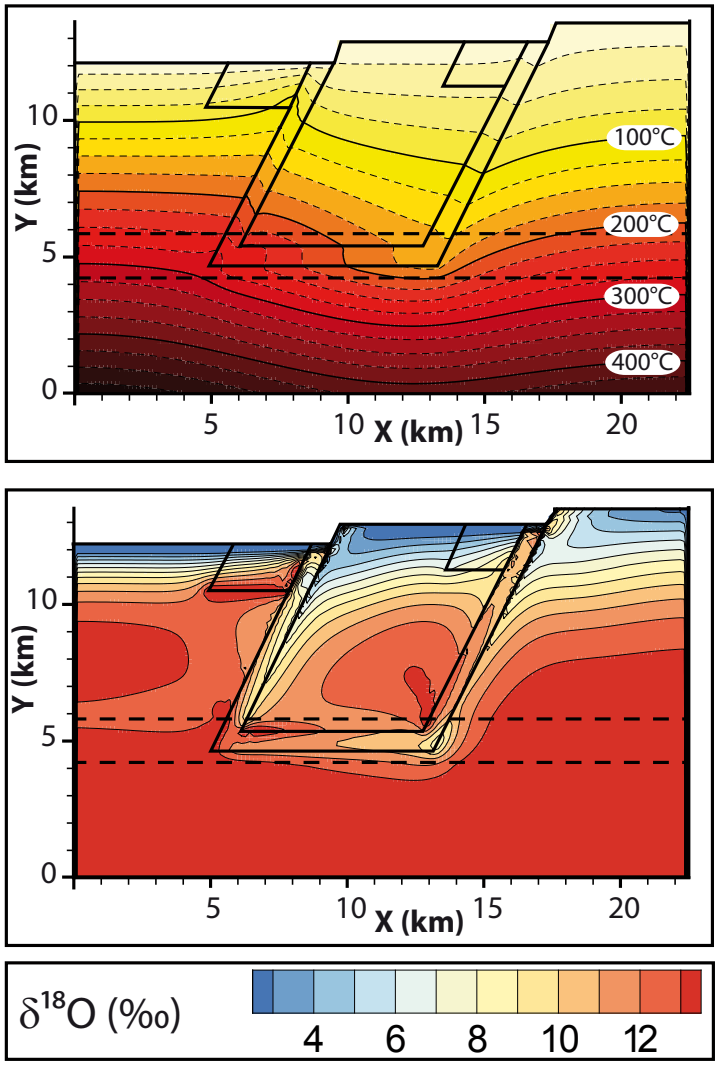

Figure 5.21: **Temperature (top) and Oxygen isotopes (bottom) results, with connected faults, using the following permeabilities: $k_{lowerplate}$ = 10^{-19} m^2, $k_{upperplate}$ = 10^{-18} m^2, $k_{shearzone}$ = 10^{-17} m^2, k_{faults} = 10^{-15} m^2, k_{basin} = 10^{-14} m^2.**

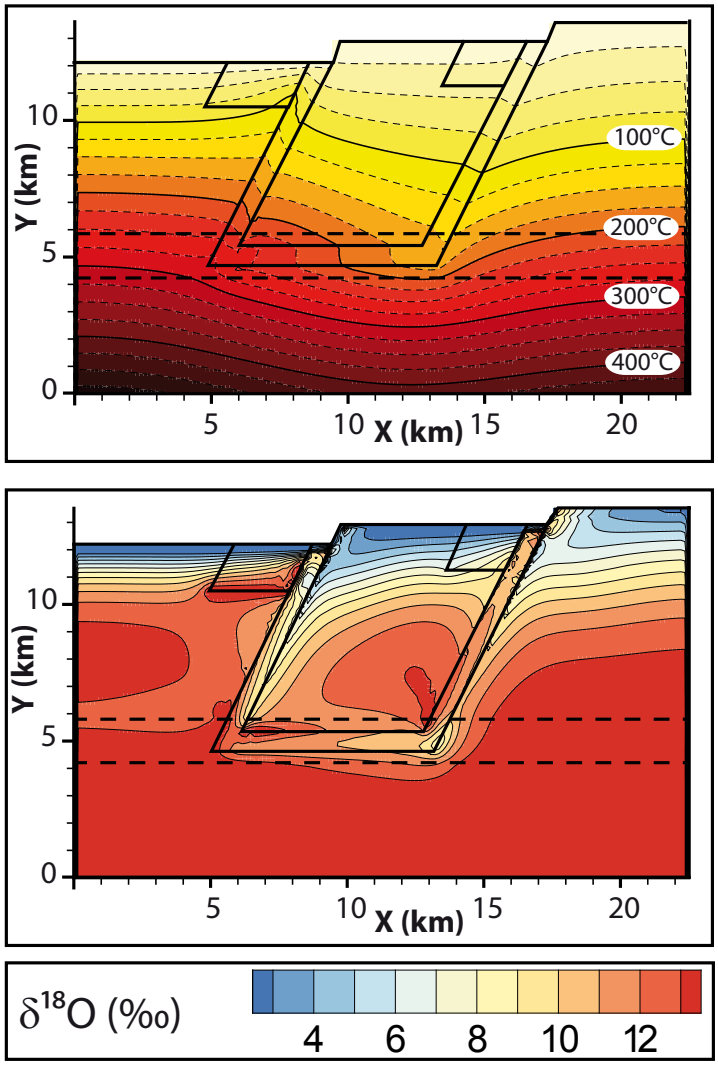

Figure 5.22: **Temperature (top) and Oxygen isotopes (bottom) results, with connected faults, using the following permeabilities: $k_{lowerplate}$ = 10^{-19} m^2, $k_{upperplate}$ = 10^{-18} m^2, $k_{shearzone}$ = 10^{-16} m^2, k_{faults} = 10^{-15} m^2, k_{basin} = 10^{-14} m^2.**

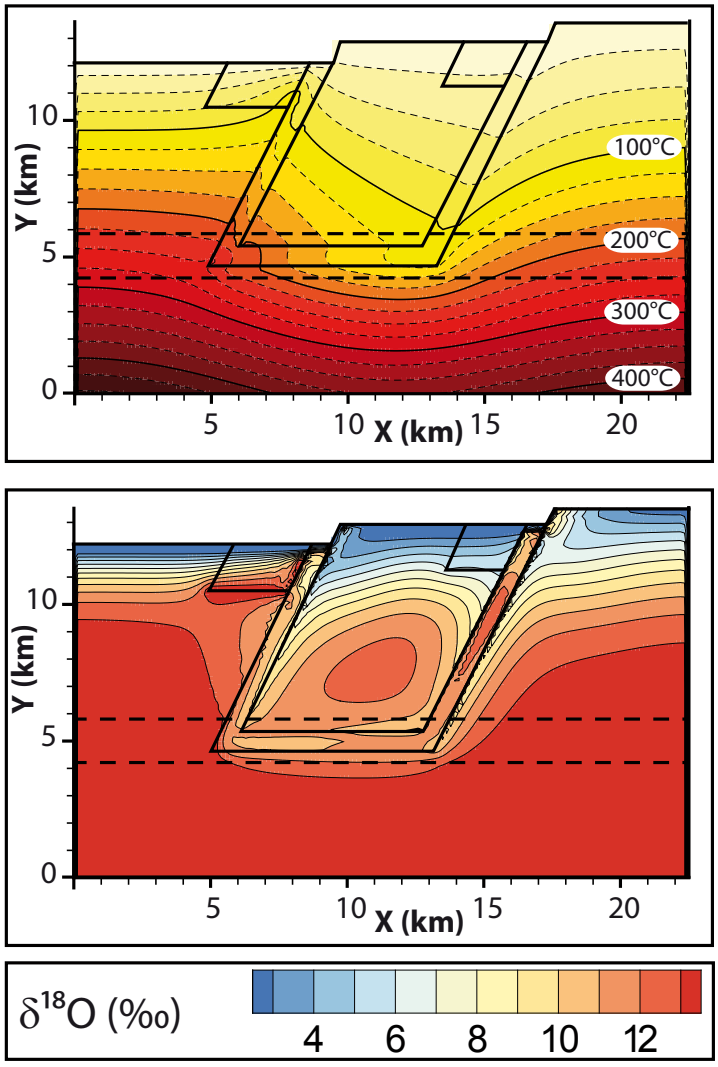

Figure 5.23: **Temperature (top) and Oxygen isotopes (bottom) results, with connected faults, using the following permeabilities: $k_{lowerplate}$ = 10^{-19} m^2, $k_{upperplate}$ = 10^{-18} m^2, $k_{shearzone}$ = 10^{-18} m^2, k_{faults} = 10^{-14} m^2, k_{basin} = 10^{-14} m^2.**

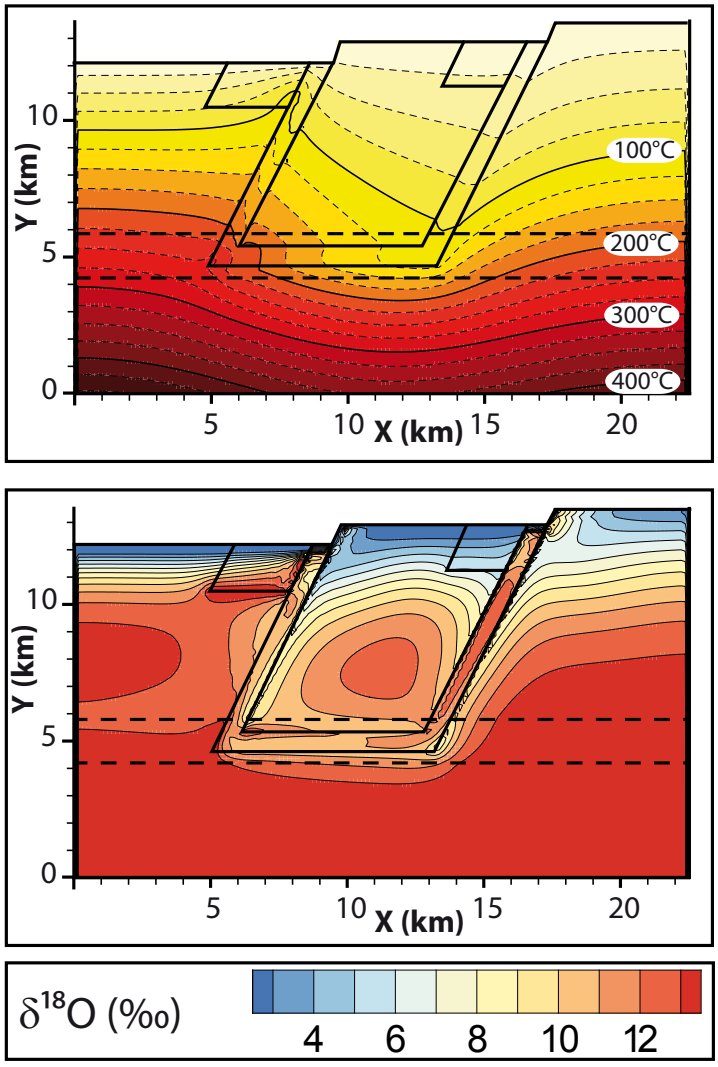

Figure 5.24: **Temperature (top) and Oxygen isotopes (bottom) results, with connected faults, using the following permeabilities: $k_{lowerplate}$ = 10^{-19} m^2, $k_{upperplate}$ = 10^{-18} m^2, $k_{shearzone}$ = 10^{-17} m^2, k_{faults} = 10^{-14} m^2, k_{basin} = 10^{-14} m^2.**

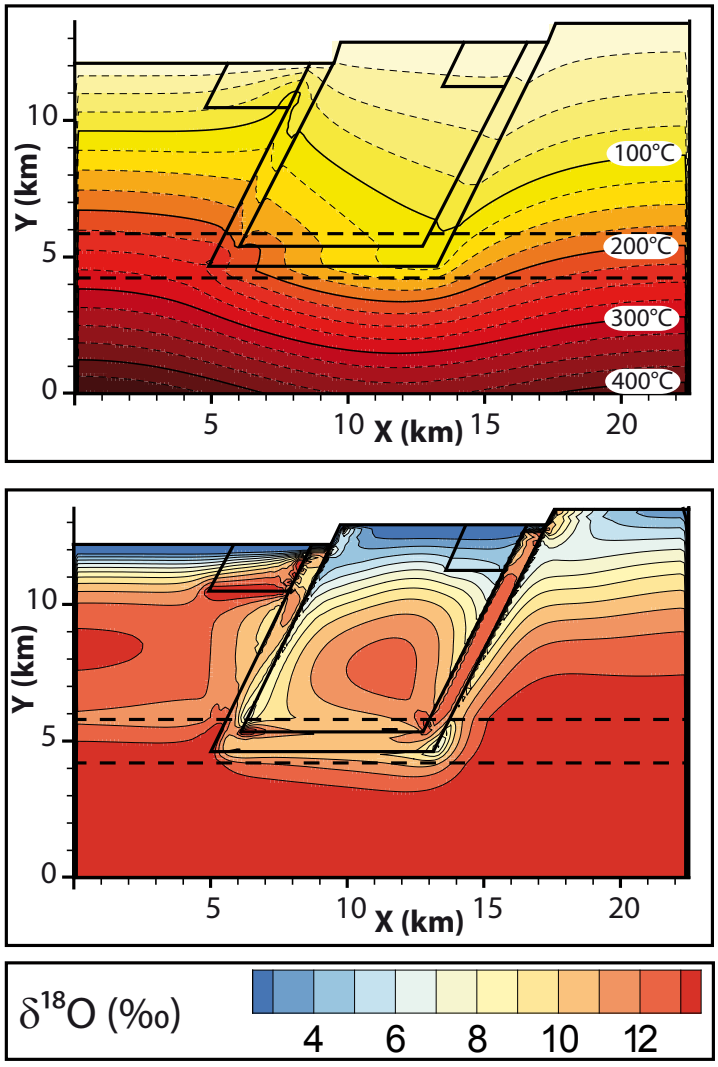

Figure 5.25: **Temperature (top) and Oxygen isotopes (bottom) results, with connected faults, using the following permeabilities: $k_{lowerplate}$ = 10^{-19} m^2, $k_{upperplate}$ = 10^{-18} m^2, $k_{shearzone}$ = 10^{-16} m^2, k_{faults} = 10^{-14} m^2, k_{basin} = 10^{-14} m^2.**

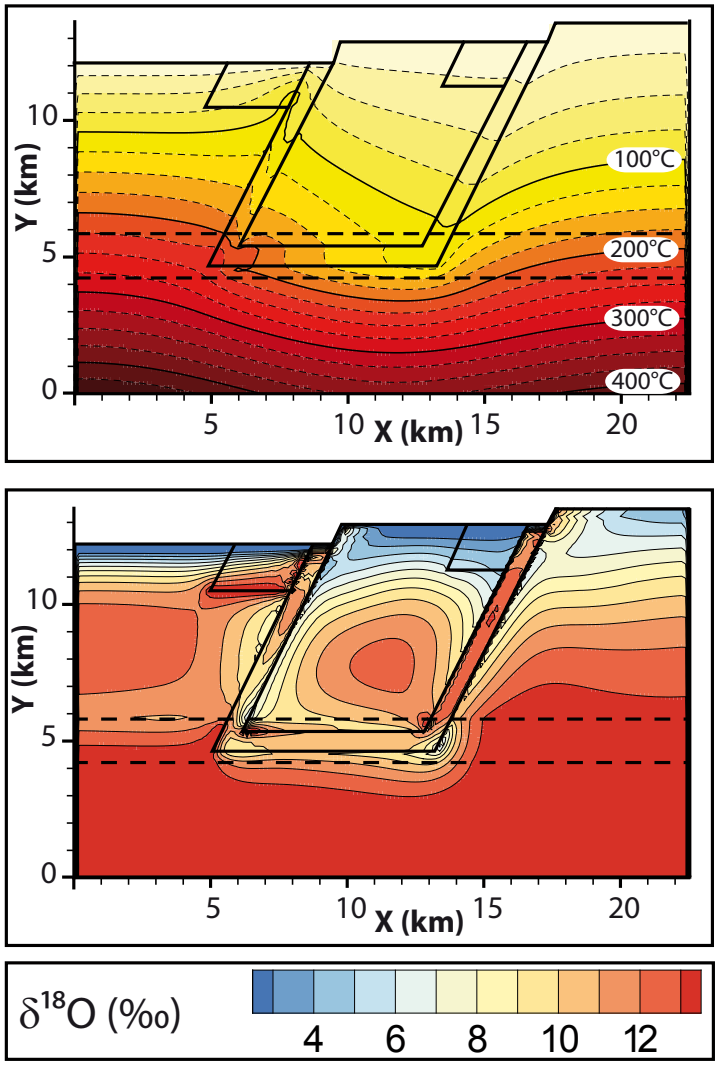

Figure 5.26: **Temperature (top) and Oxygen isotopes (bottom) results, with connected faults, using the following permeabilities: $k_{lowerplate}$ = 10^{-19} m^2, $k_{upperplate}$ = 10^{-18} m^2, $k_{shearzone}$ = 10^{-15} m^2, k_{faults} = 10^{-14} m^2, k_{basin} = 10^{-14} m^2.**

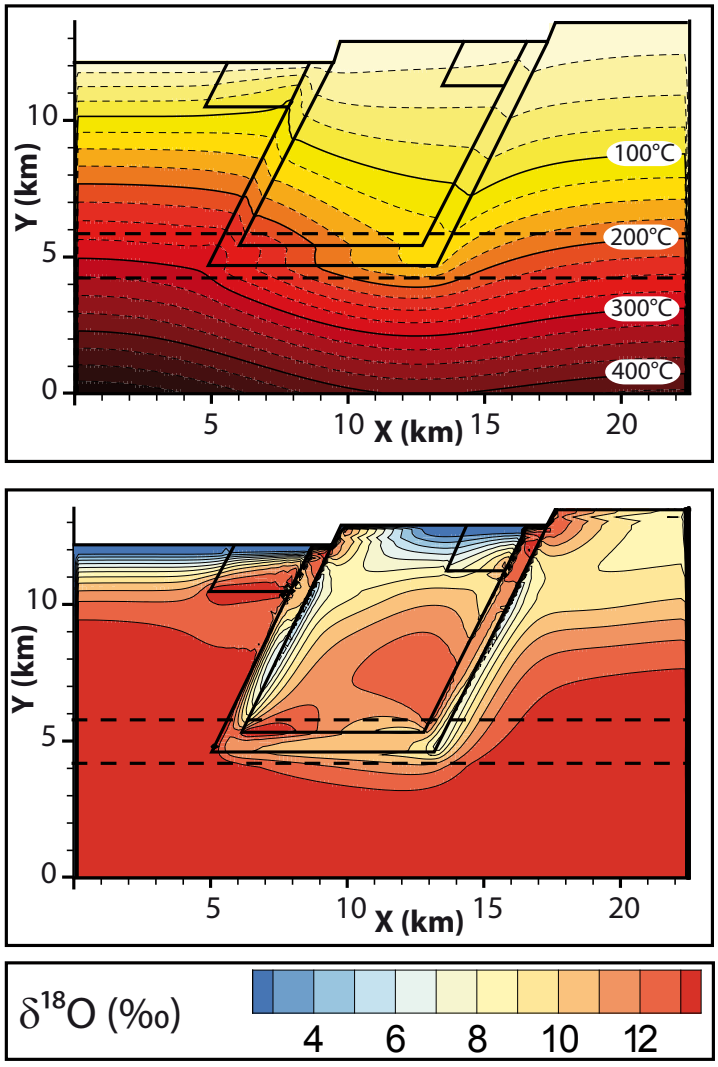

Figure 5.27: **Temperature (top) and Oxygen isotopes (bottom) results, with connected faults, using the following permeabilities: $k_{lowerplate}$ = 10^{-19} m^2, $k_{upperplate}$ = 10^{-17} m^2, $k_{shearzone}$ = 10^{-17} m^2, k_{faults} = 10^{-15} m^2, k_{basin} = 10^{-14} m^2.**

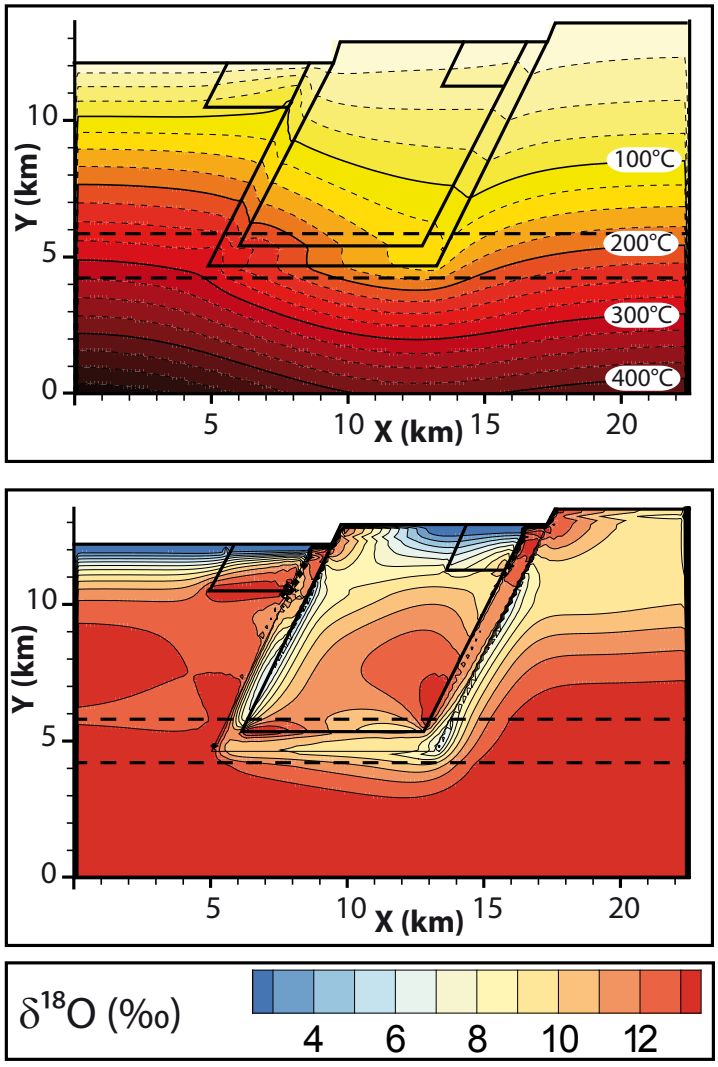

Figure 5.28: **Temperature (top) and Oxygen isotopes (bottom) results, with connected faults, using the following permeabilities: $k_{lowerplate} = 10^{-19}$ m^2, $k_{upperplate} = 10^{-17}$ m^2, $k_{shearzone} = 10^{-16}$ m^2, $k_{faults} = 10^{-15}$ m^2, $k_{basin} = 10^{-14}$ m^2.**

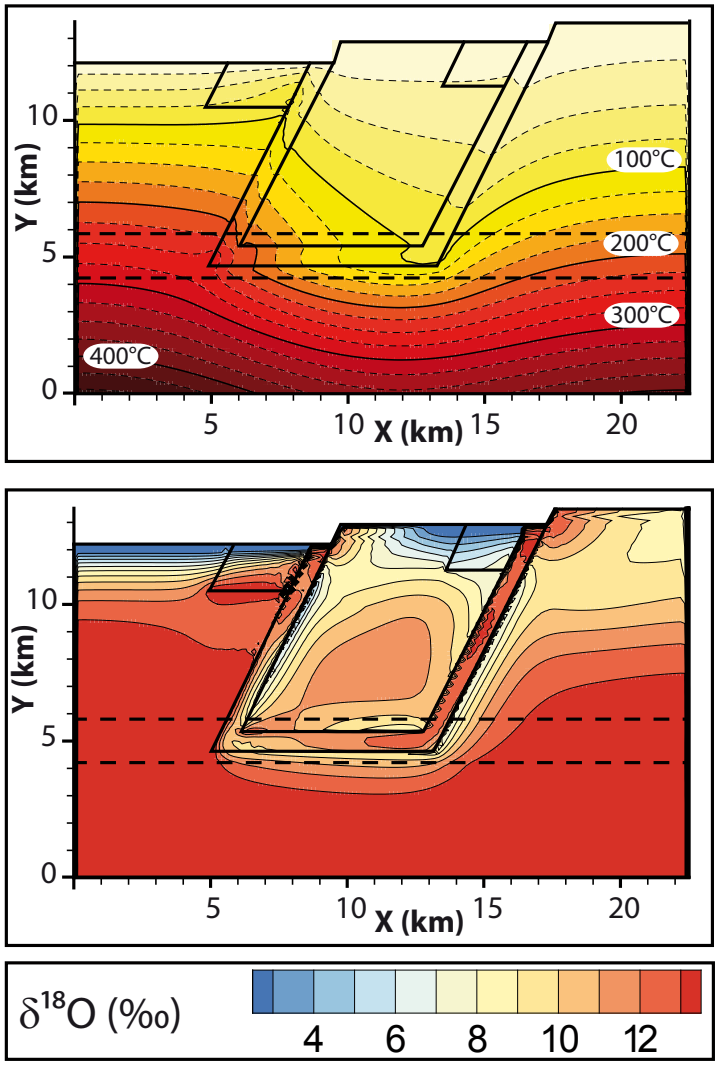

Figure 5.29: **Temperature (top) and Oxygen isotopes (bottom results), with connected faults, using the following permeabilities: $k_{lowerplate}$ = 10^{-19} m^2, $k_{upperplate}$ = 10^{-17} m^2, $k_{shearzone}$ = 10^{-17} m^2, k_{faults} = 10^{-14} m^2, k_{basin} = 10^{-14} m^2.**

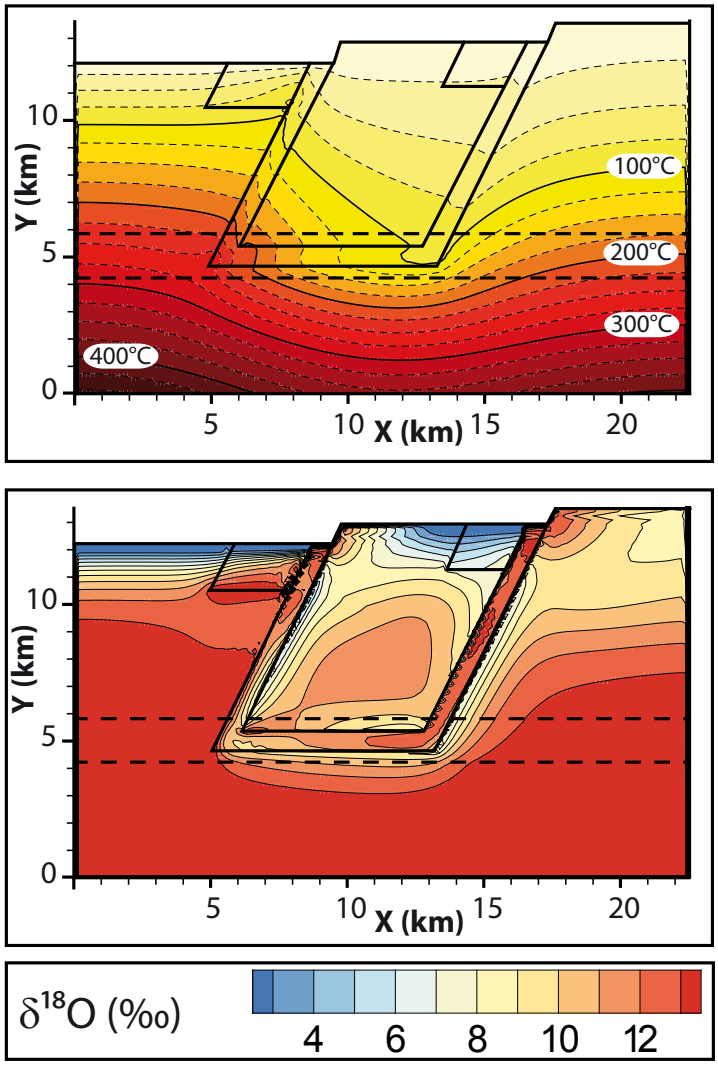

Figure 5.30: **Temperature (top) and Oxygen isotopes (bottom) results, with connected faults, using the following permeabilities: $k_{lowerplate}$ = 10^{-19} m^2, $k_{upperplate}$ = 10^{-17} m^2, $k_{shearzone}$ = 10^{-16} m^2, k_{faults} = 10^{-14} m^2, k_{basin} = 10^{-14} m^2.**

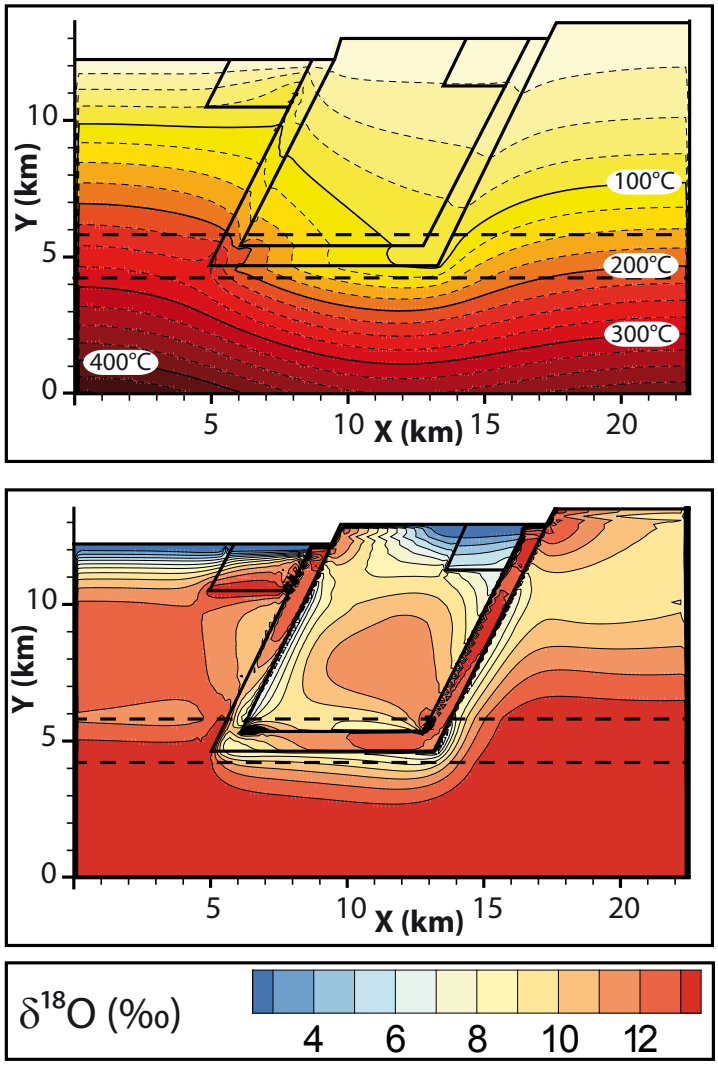

Figure 5.31: **Temperature (top) and Oxygen isotopes (bottom) results, with connected faults, using the following permeabilities: $k_{lowerplate}$ = 10^{-19} m^2, $k_{upperplate}$ = 10^{-17} m^2, $k_{shearzone}$ = 10^{-15} m^2, k_{faults} = 10^{-14} m^2, k_{basin} = 10^{-14} m^2.**

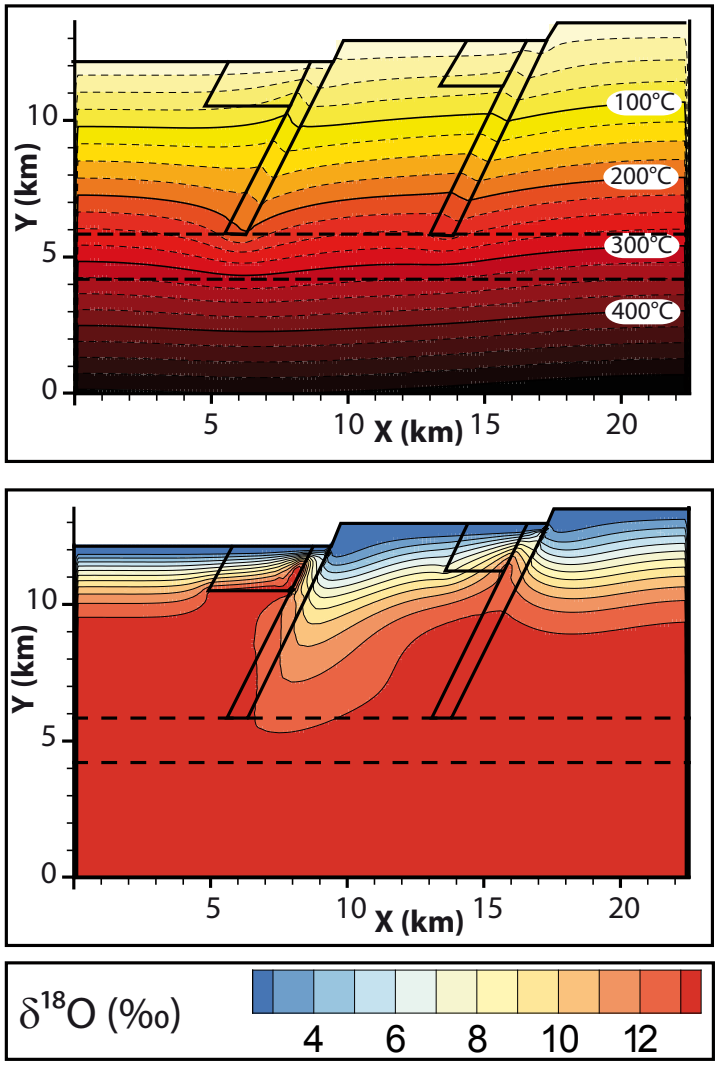

Figure 5.32: **Temperature (top) and Oxygen isotopes (bottom) results, with unconnected faults, using the following permeabilities: $k_{lowerplate} = 10^{-19}$ m^2, $k_{upperplate} = 10^{-19}$ m^2, $k_{shearzone} = 10^{-19}$ m^2, $k_{faults} = 10^{-15}$ m^2, $k_{basin} = 10^{-14}$ m^2.**

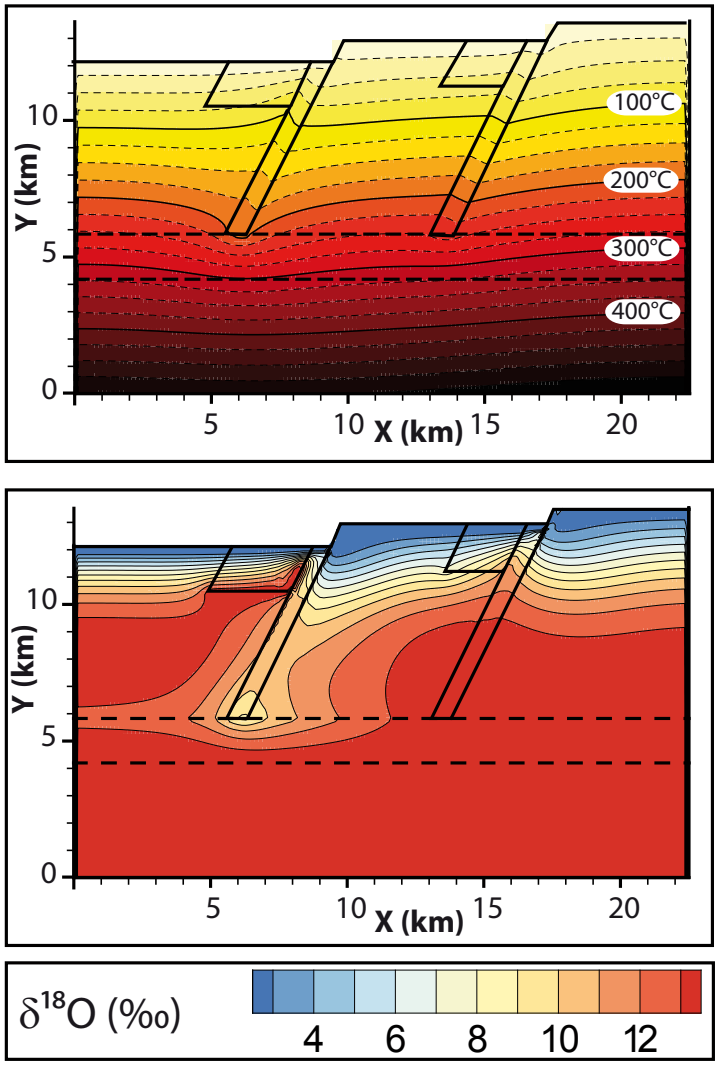

Figure 5.33: **Temperature (top) and Oxygen isotopes (bottom results), with unconnected faults, using the following permeabilities: $k_{lowerplate} = 10^{-19}$ m^2, $k_{upperplate} = 10^{-19}$ m^2, $k_{shearzone} = 10^{-18}$ m^2, $k_{faults} = 10^{-15}$ m^2, $k_{basin} = 10^{-14}$ m^2.**

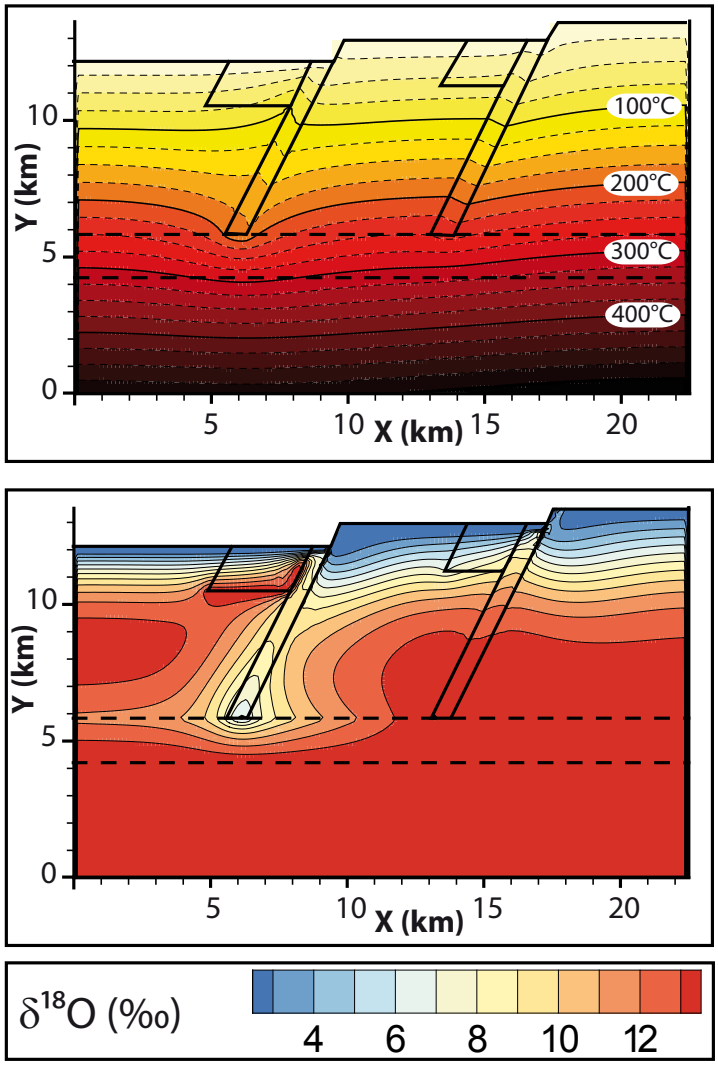

Figure 5.34: **Temperature (top) and Oxygen isotopes (bottom) results, with unconnected faults, using the following permeabilities: $k_{lowerplate}$ = 10^{-19} m^2, $k_{upperplate}$ = 10^{-19} m^2, $k_{shearzone}$ = 10^{-17} m^2, k_{faults} = 10^{-15} m^2, k_{basin} = 10^{-14} m^2.**

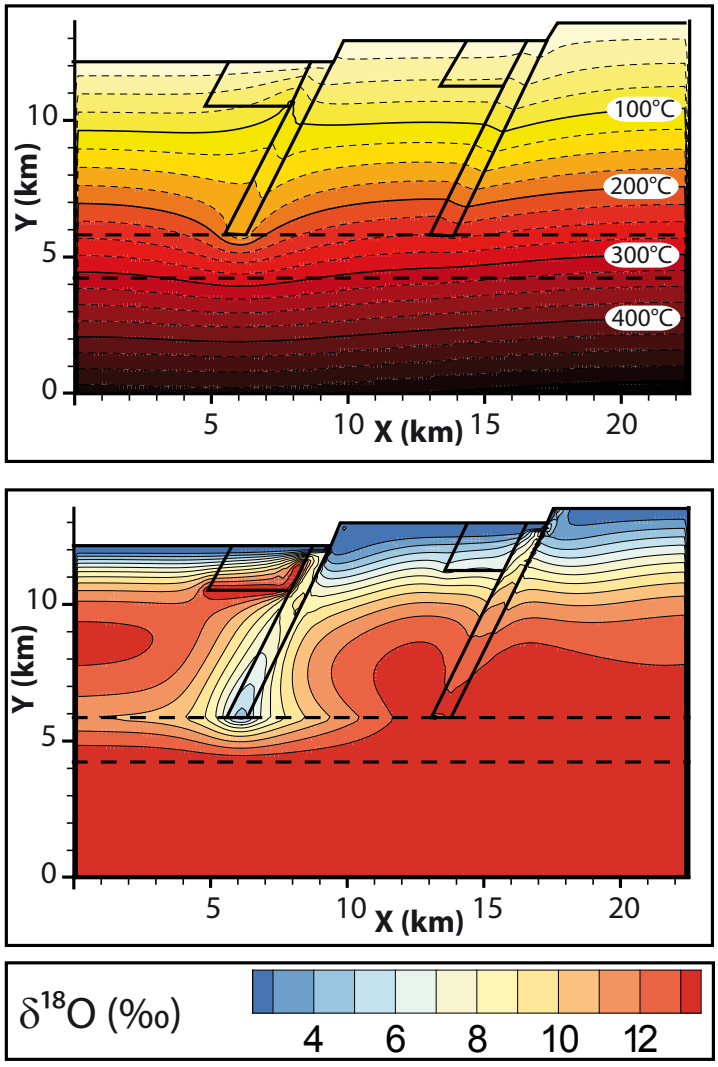

Figure 5.35: **Temperature (top) and Oxygen isotopes (bottom) results, with unconnected faults, using the following permeabilities: $k_{lowerplate} = 10^{-19}$ m^2, $k_{upperplate} = 10^{-19}$ m^2, $k_{shearzone} = 10^{-16}$ m^2, $k_{faults} = 10^{-15}$ m^2, $k_{basin} = 10^{-14}$ m^2.**

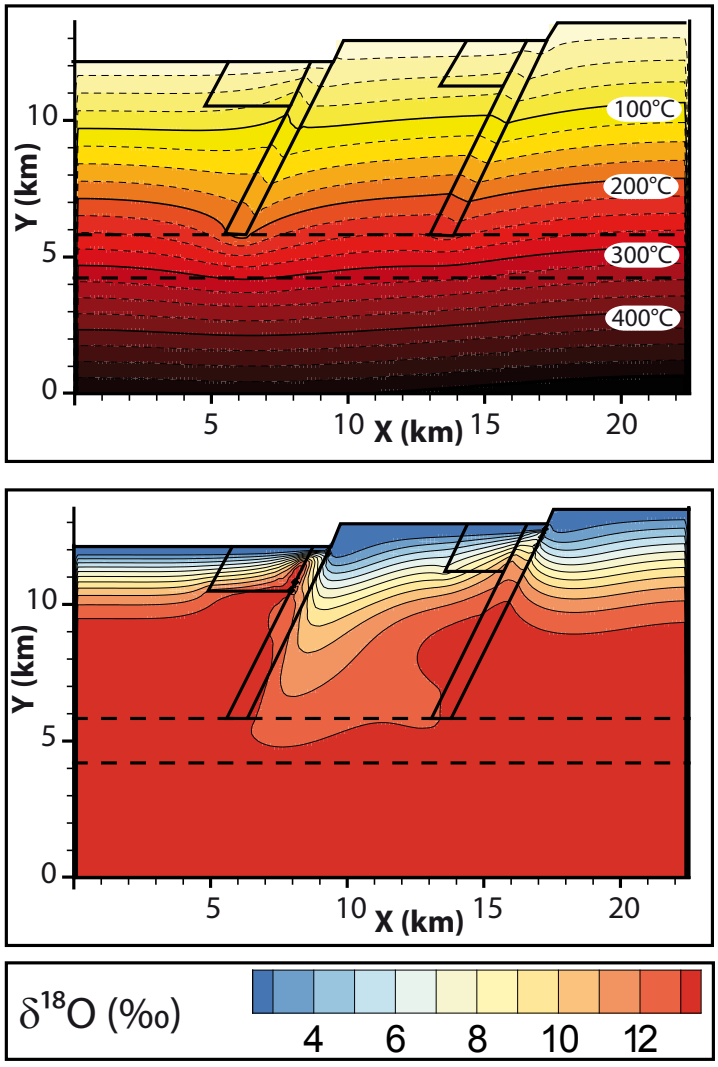

Figure 5.36: **Temperature (top) and Oxygen isotopes (bottom) results, with unconnected faults, using the following permeabilities: $k_{lowerplate} = 10^{-19}$ m^2, $k_{upperplate} = 10^{-19}$ m^2, $k_{shearzone} = 10^{-19}$ m^2, $k_{faults} = 10^{-14}$ m^2, $k_{basin} = 10^{-14}$ m^2.**

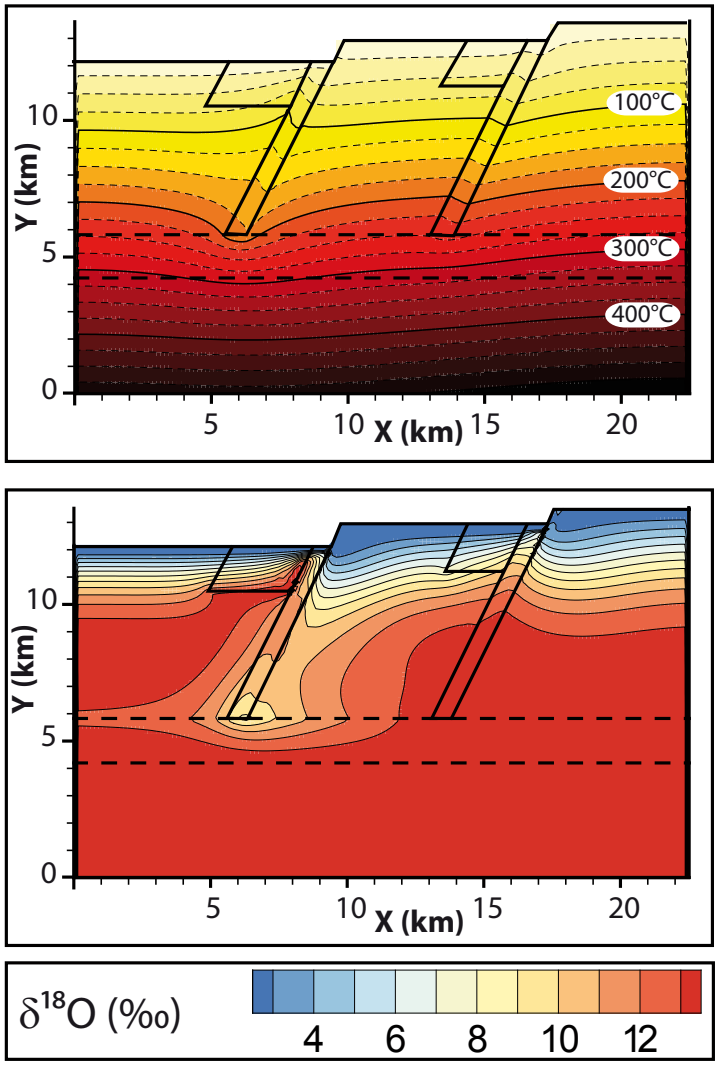

Figure 5.37: **Temperature (top) and Oxygen isotopes (bottom) results, with unconnected faults, using the following permeabilities: $k_{lowerplate}$ = 10^{-19} m^2, $k_{upperplate}$ = 10^{-19} m^2, $k_{shearzone}$ = 10^{-18} m^2, k_{faults} = 10^{-14} m^2, k_{basin} = 10^{-14} m^2.**

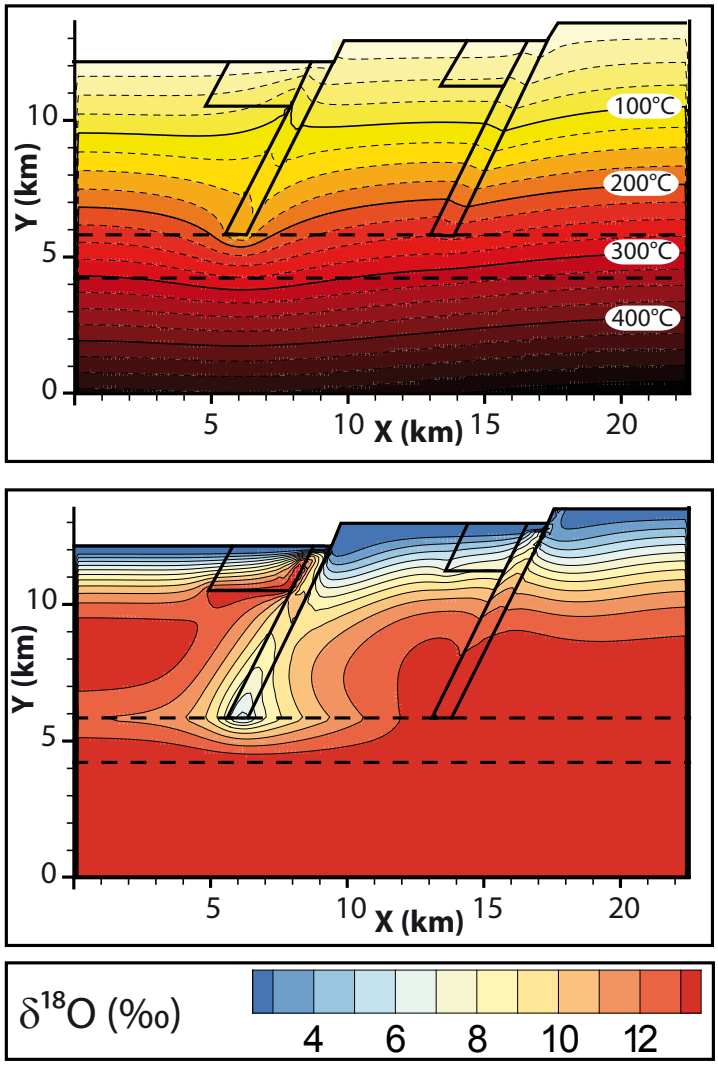

Figure 5.38: **Temperature (top) and Oxygen isotopes (bottom) results, with unconnected faults, using the following permeabilities: $k_{lowerplate} = 10^{-19}$ m^2, $k_{upperplate} = 10^{-19}$ m^2, $k_{shearzone} = 10^{-17}$ m^2, $k_{faults} = 10^{-14}$ m^2, $k_{basin} = 10^{-14}$ m^2.**

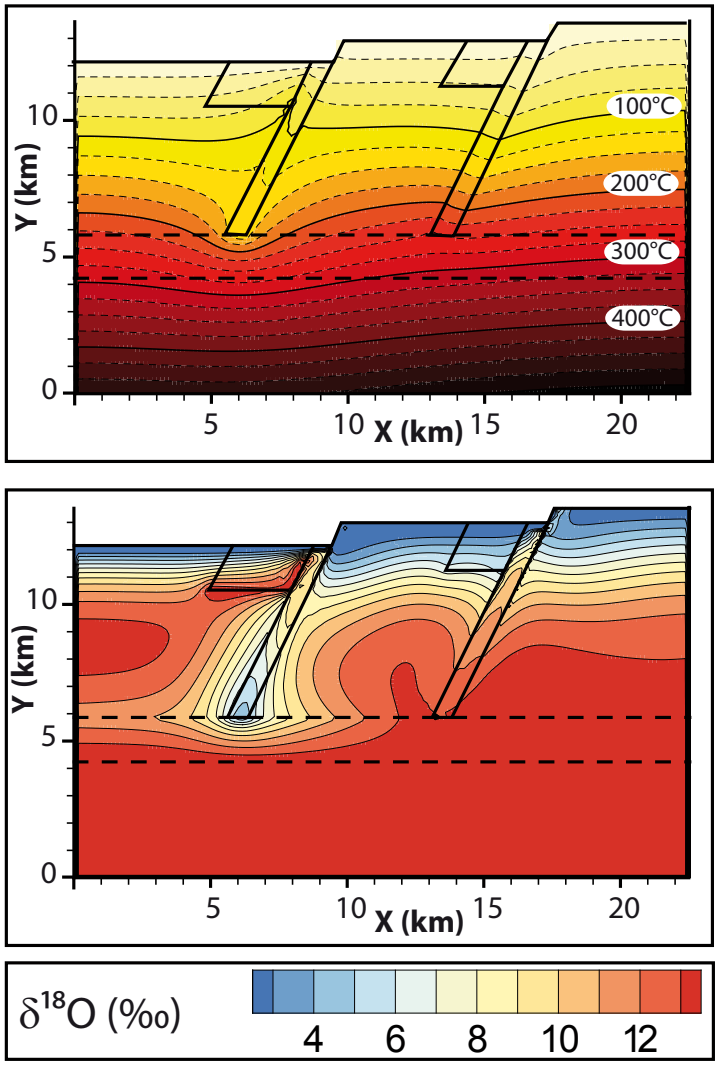

Figure 5.39: **Temperature (top) and Oxygen isotopes (bottom) results, with unconnected faults, using the following permeabilities: $k_{lowerplate}$ = 10^{-19} m^2, $k_{upperplate}$ = 10^{-19} m^2, $k_{shearzone}$ = 10^{-16} m^2, k_{faults} = 10^{-14} m^2, k_{basin} = 10^{-14} m^2.**

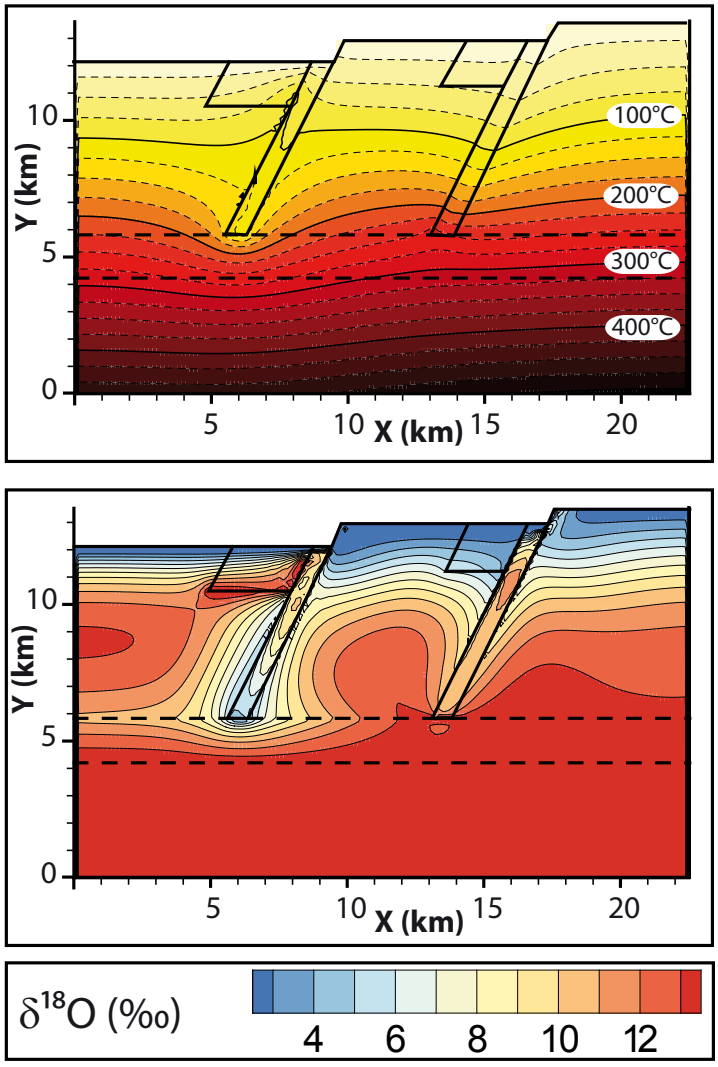

Figure 5.40: **Temperature (top) and Oxygen isotopes (bottom) results, with unconnected faults, using the following permeabilities: $k_{lowerplate}$ = 10^{-19} m^2, $k_{upperplate}$ = 10^{-19} m^2, $k_{shearzone}$ = 10^{-15} m^2, k_{faults} = 10^{-14} m^2, k_{basin} = 10^{-14} m^2.**

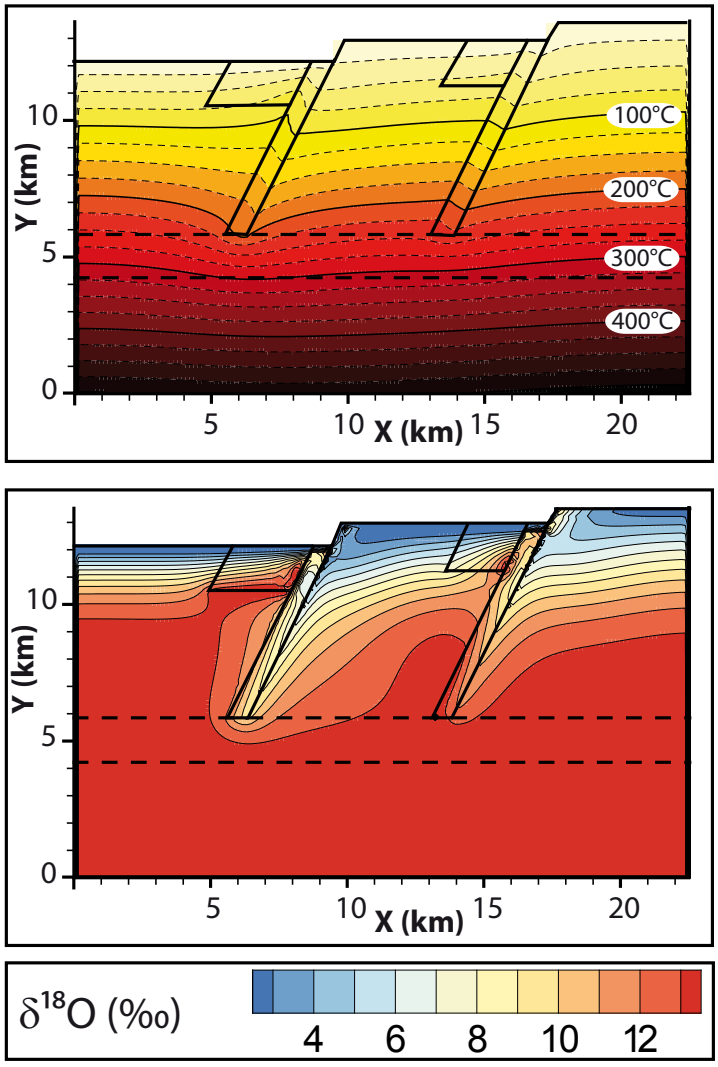

Figure 5.41: **Temperature (top) and Oxygen isotopes (bottom) results, with unconnected faults, using the following permeabilities: $k_{lowerplate} = 10^{-19}$ m^2, $k_{upperplate} = 10^{-18}$ m^2, $k_{shearzone} = 10^{-18}$ m^2, $k_{faults} = 10^{-15}$ m^2, $k_{basin} = 10^{-14}$ m^2.**

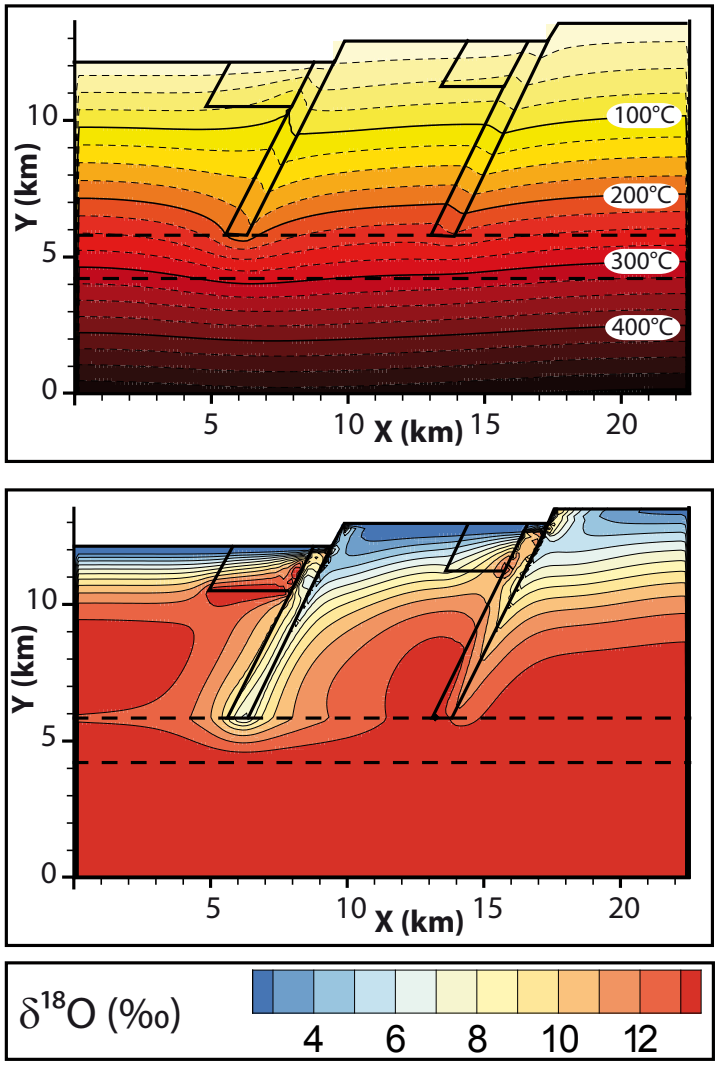

Figure 5.42: **Temperature (top) and Oxygen isotopes (bottom) results, with unconnected faults, using the following permeabilities: $k_{lowerplate}$ = 10^{-19} m^2, $k_{upperplate}$ = 10^{-18} m^2, $k_{shearzone}$ = 10^{-17} m^2, k_{faults} = 10^{-15} m^2, k_{basin} = 10^{-14} m^2.**

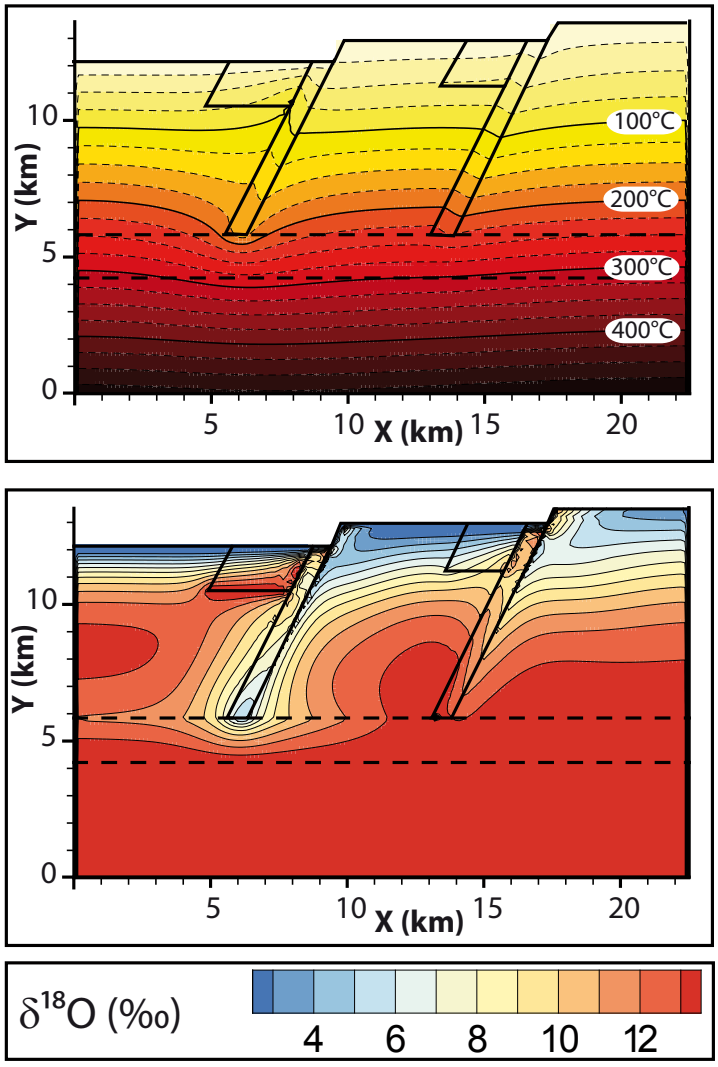

Figure 5.43: **Temperature (top) and Oxygen isotopes (bottom) results, with unconnected faults, using the following permeabilities: $k_{lowerplate}$ = 10^{-19} m^2, $k_{upperplate}$ = 10^{-18} m^2, $k_{shearzone}$ = 10^{-16} m^2, k_{faults} = 10^{-15} m^2, k_{basin} = 10^{-14} m^2.**

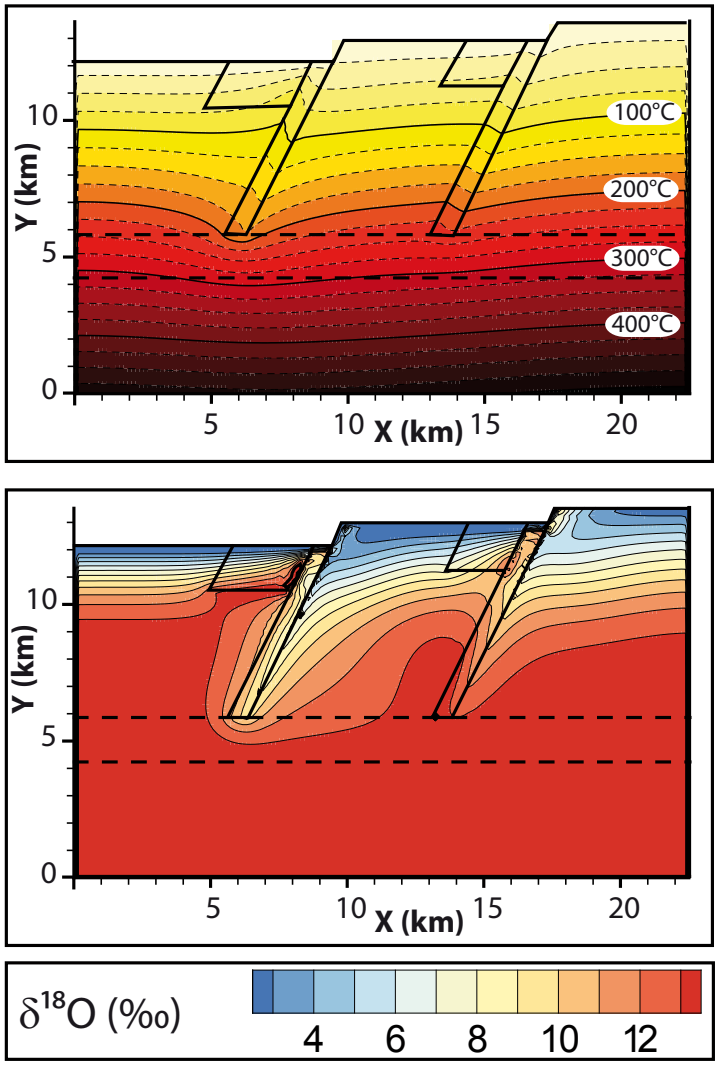

Figure 5.44: **Temperature (top) and Oxygen isotopes (bottom) results, with unconnected faults, using the following permeabilities: $k_{lowerplate}$ = 10^{-19} m^2, $k_{upperplate}$ = 10^{-18} m^2, $k_{shearzone}$ = 10^{-18} m^2, k_{faults} = 10^{-14} m^2, k_{basin} = 10^{-14} m^2.**

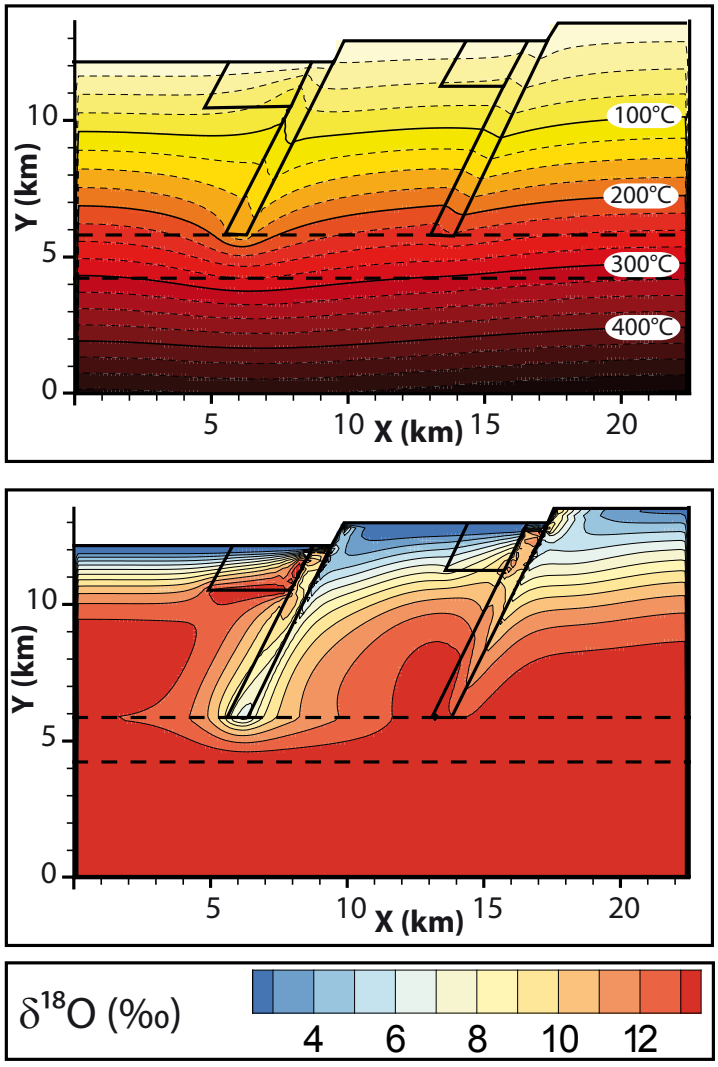

Figure 5.45: **Temperature (top) and Oxygen isotopes (bottom) results, with unconnected faults, using the following permeabilities: $k_{lowerplate} = 10^{-19}$ m^2, $k_{upperplate} = 10^{-18}$ m^2, $k_{shearzone} = 10^{-17}$ m^2, $k_{faults} = 10^{-14}$ m^2, $k_{basin} = 10^{-14}$ m^2.**

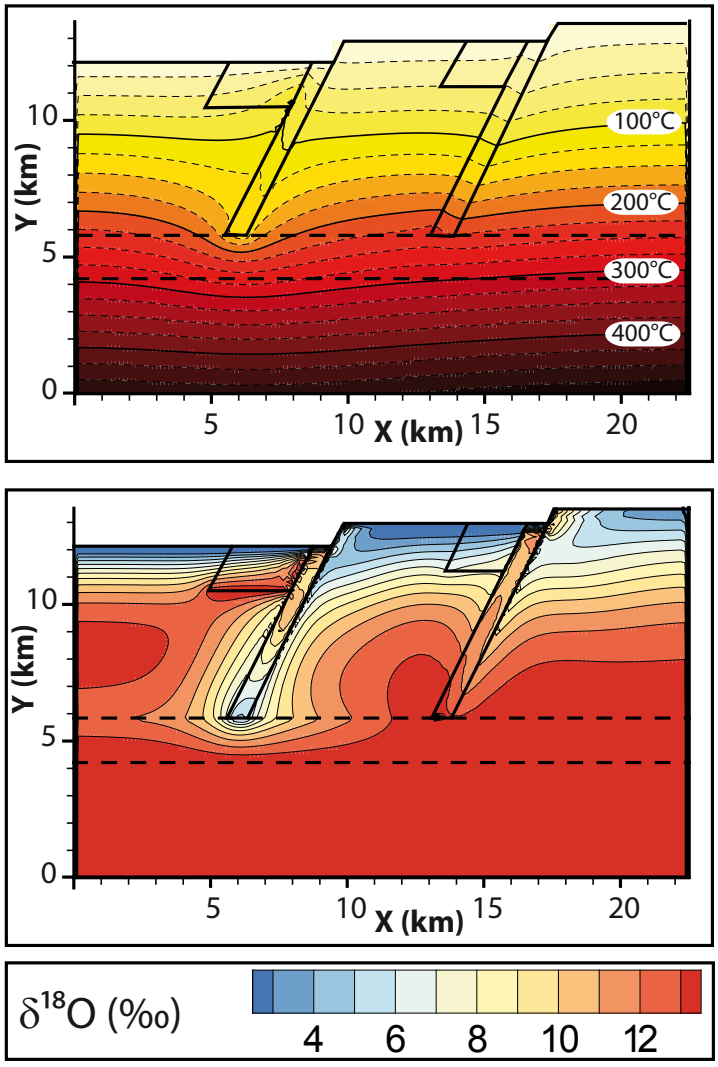

Figure 5.46: **Temperature (top) and Oxygen isotopes (bottom) results, with unconnected faults, using the following permeabilities: $k_{lowerplate}$ = 10^{-19} m^2, $k_{upperplate}$ = 10^{-18} m^2, $k_{shearzone}$ = 10^{-16} m^2, k_{faults} = 10^{-14} m^2, k_{basin} = 10^{-14} m^2.**

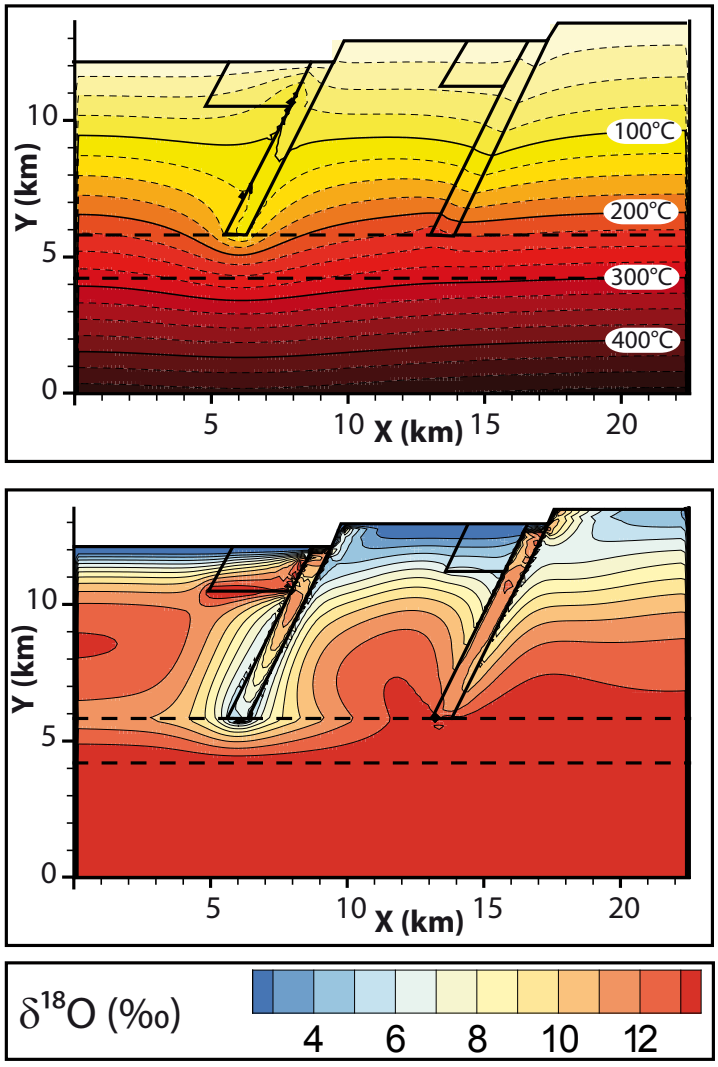

Figure 5.47: **Temperature (top) and Oxygen isotopes (bottom) results, with unconnected faults, using the following permeabilities: $k_{lowerplate} = 10^{-19}$ m^2, $k_{upperplate} = 10^{-18}$ m^2, $k_{shearzone} = 10^{-15}$ m^2, $k_{faults} = 10^{-14}$ m^2, $k_{basin} = 10^{-14}$ m^2.**

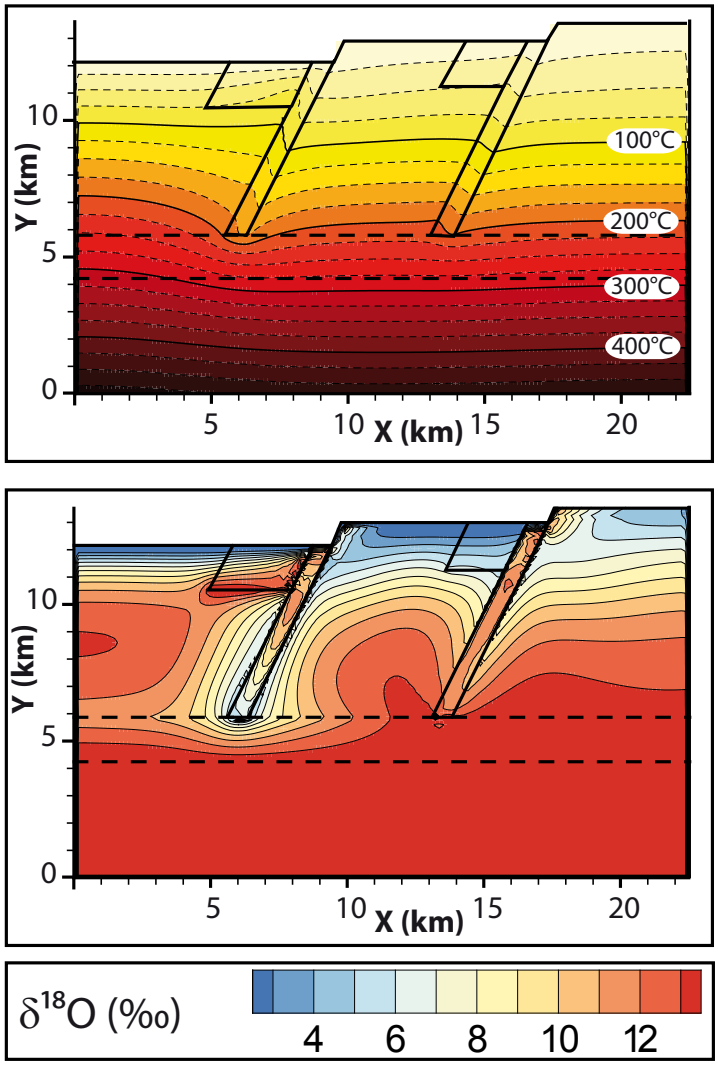

Figure 5.48: **Temperature (top) and Oxygen isotopes (bottom) results, with unconnected faults, using the following permeabilities: $k_{lowerplate}$ = 10^{-19} m^2, $k_{upperplate}$ = 10^{-17} m^2, $k_{shearzone}$ = 10^{-16} m^2, k_{faults} = 10^{-15} m^2, k_{basin} = 10^{-14} m^2.**

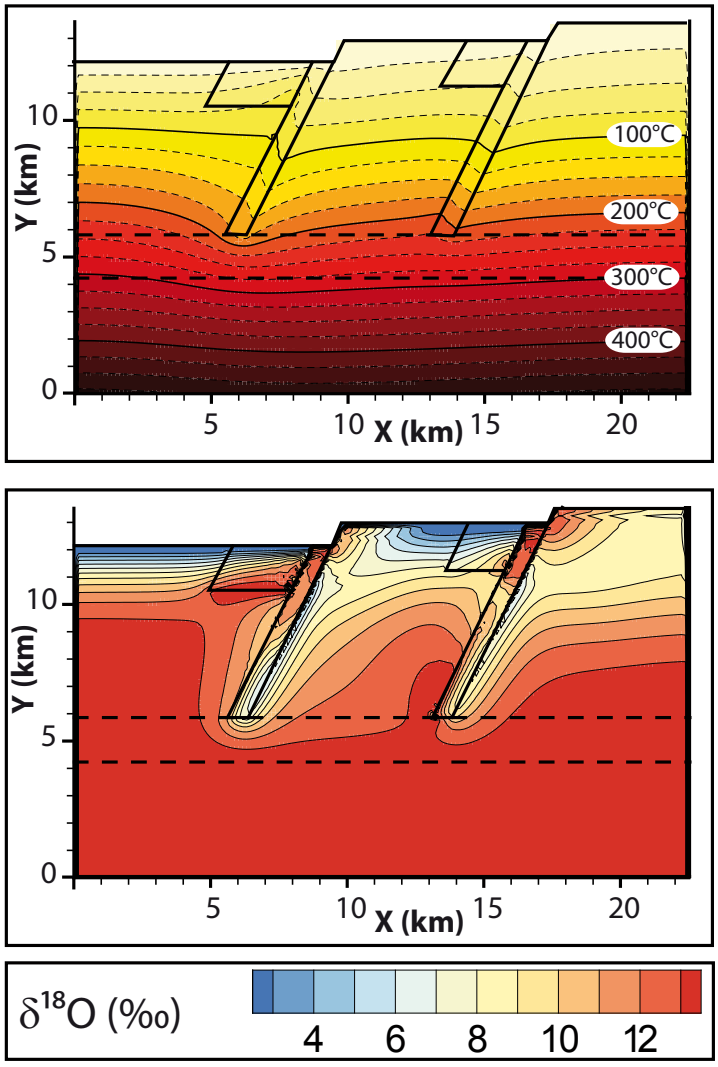

Figure 5.49: **Temperature (top) and Oxygen isotopes (bottom) results, with unconnected faults, using the following permeabilities: $k_{lowerplate} = 10^{-19}$ m^2, $k_{upperplate} = 10^{-17}$ m^2, $k_{shearzone} = 10^{-17}$ m^2, $k_{faults} = 10^{-14}$ m^2, $k_{basin} = 10^{-14}$ m^2.**

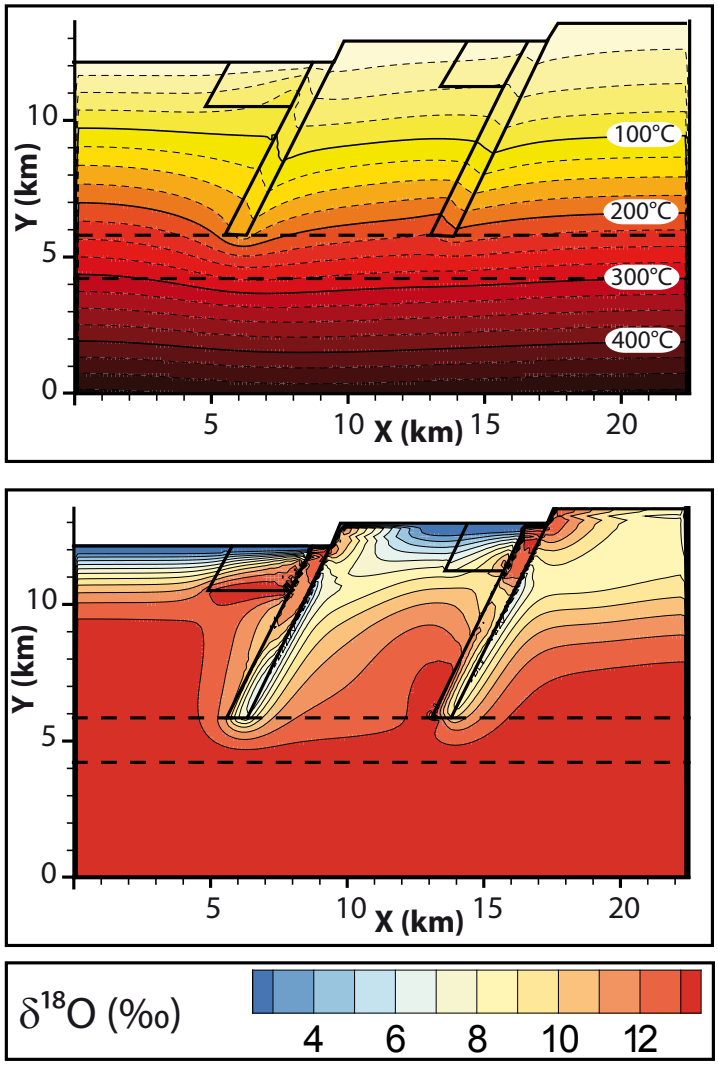

Figure 5.50: **Temperature (top) and Oxygen isotopes (bottom) results, with unconnected faults, using the following permeabilities: $k_{lowerplate} = 10^{-19}$ m^2, $k_{upperplate} = 10^{-17}$ m^2, $k_{shearzone} = 10^{-16}$ m^2, $k_{faults} = 10^{-14}$ m^2, $k_{basin} = 10^{-14}$ m^2.**

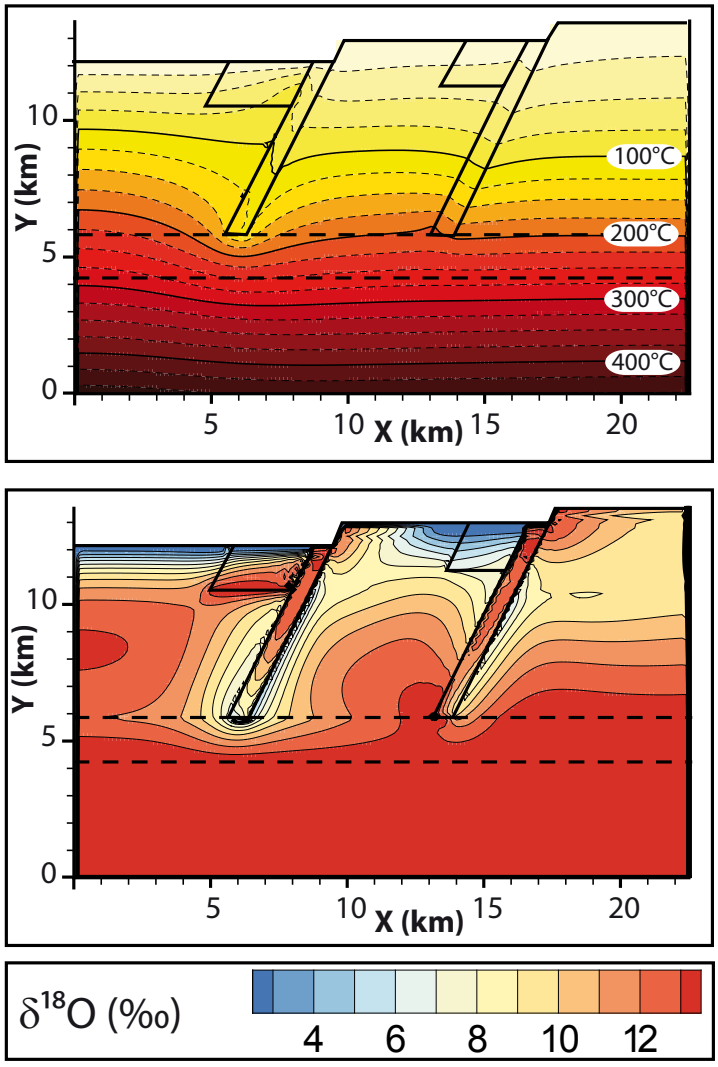

Figure 5.51: **Temperature (top) and Oxygen isotopes (bottom) results, with unconnected faults, using the following permeabilities: $k_{lowerplate}$ = 10^{-19} m^2, $k_{upperplate}$ = 10^{-17} m^2, $k_{shearzone}$ = 10^{-15} m^2, k_{faults} = 10^{-14} m^2, k_{basin} = 10^{-14} m^2.**